Selected antiretroviral and anti-tuberculosis drug combinations by non-covalent bonding

Jean Baptiste NGILIRABANGA

A dissertation submitted in fulfilment of the requirements for the degree of

Doctor of Philosophy (Pharmaceutical Science)

School of Pharmacy

University of the Western Cape

Supervisor: Professor Halima SAMSODIEN

January 06, 2021

Abstract

Selected antiretroviral and anti-tuberculosis drug combinations by non-covalent bonding

Jean Baptiste Ngilirabanga

A PhD. Pharmaceutical Sciences Thesis, School of Pharmacy, University of the Western Cape

Treatment of the human immunodeficiency virus (HIV) and tuberculosis (TB) infections have become very complicated due to the advent of drug resistance. Drug combinations offer an alternative approach to reducing the emergence of drug resistance. Pharmaceutical co-crystals have provided the pharmaceutical industry with the ability to optimise the physicochemical properties of active pharmaceutical ingredients (APIs) while preserving the biological activity. Pharmaceutical co-crystals are formed between APIs and suitable co-formers that are biologically safe or even a second or third API.

Experimentally, it is not easy to produce co-crystals and often results in other therapeutic hybrids. The objective of the work presented herein was to screen, synthesise and characterise various dual-drug co-crystals of different possible combinations of selected anti-HIV and anti-tubercular drugs as a new way of combining drugs, enhancing properties, and ultimately reduce drug resistance. Several co-crystals were produced by mechanochemical reactions using dry and liquid assisted grinding of actives and solution crystallisation in respective molar ratios. A thorough characterisation conducted confirmed the successful co-crystallisation for some samples while other combinations yielded binary eutectic mixtures (hybrids) of individual substances used. Thermal analyses by differential scanning calorimetry (DSC), hot stage microscopy (HSM), and thermogravimetric analysis (TGA) were used to investigate thermal behaviours and the initial confirmation of the possible co-crystal formation. Infrared spectrometer (FTIR) and powder X-ray diffraction (PXRD confirmed intermolecular interactions or complexation and scanning electron microscopy (SEM) confirmed the particle morphology of the co-crystals and other

Abstract

solid-state hybrids produced. An incubator/shaker and HPLC were utilised to prepare and quantify sample contents, respectively. Antimicrobial studies were partially conducted on anti-tubercular dual-API co-crystals, and eutectic mixture produced.

A total number of eighteen (18) mixed dual-API co-crystals/hybrids were synthesised. These include five confirmed co-crystals of selected antiretroviral drugs known as EFZA, NEF, NVZA2, NVZA3, EL2, and four solid dispersions confirmed as binary eutectics; NVZA1, LMZT, NL and EL1. Five dual-drug hybrids between anti-HIV/1-adamantylaimne and anti-tubercular APIs, including EFINH co-crystal and EFAD co-amorphous, INHZA, AZTPZA, and LMISO solid dispersions. Lastly, hybrids synthesised from anti-tubercular drugs include one solid dispersion INHPZA1 and three co-crystals INHPZA2, INHGA (2:1) and PGA (2:1).

Solubility evaluation of the hybrids indicated an increased amount of drugs in the co-crystals/solid dispersions compared to the untreated APIs. This suggested that dual-drug hybrids produced could exhibit an enhanced bioavailability which makes these potential therapeutic candidates for future formulation.

Keywords

HIV/AIDS, tuberculosis, infectious diseases, drug resistance, combination drug therapy, co-crystallisation, co-crystal, solid dispersions, physicochemical characterisation

Declaration

I declare that this thesis titled, "***Selected antiretroviral and anti-tuberculosis drug combinations by non-covalent bonding***" is my own work. It has not been submitted for any degree or examination at any other university, and all the sources I have used or quoted have been indicated and acknowledged by complete references.

Jean Baptiste Ngilirabanga

Signed: 

Acknowledgements

I would like to express my sincere gratitude to my supervisor, Professor Halima Samsodien, for her excellent guidance, supervision, and for creating a suitable environment for learning.

I would also like to convey my gratitude to the Pharmaceutics discipline at the School of Pharmacy for accommodating my research.

To the University of the Western Cape, I convey my sincere gratitude for offering me this opportunity of higher education.

To Stellenbosch University, Tygerberg Centre of infectious diseases, I thank you for providing a space for me to do some bioactivity experimentations.

Furthermore, I would like to extend my appreciation to the South African National Research Foundation (NRF), and the Medical Research Council (MRC) Self-Initiated Medical Research Council grant for funding this research.

Finally, and most importantly, to my family and friends for their invaluable support and contribution and for always keeping me in their prayers.

Without all of you, this work would not have been accomplished.

Dedication

To Almighty God, my family, and friends, I dedicate this work.

Table of Contents

Abstract ..... *i*

Keywords ..... *iii*

Declaration ..... *iv*

Acknowledgements ..... *v*

Dedication ..... *vi*

Table of Contents ..... *vii*

Table of figures ..... *xiii*

List of tables ..... *xxii*

List of abbreviations ..... *xxiv*

Academic outputs ..... *xxviii*

Chapter 1 Introduction *31*

1.1 Infectious diseases **31**

1.2 Drug resistance **32**

1.2.1 Drug resistance mechanisms 32

1.2.1.1 Enzymatic degradation of antibacterial drugs 34

1.2.1.2 Alteration of antimicrobial targets 34

1.2.1.3 Changes of membrane permeability 35

1.3 Drug resistance among infectious diseases **35**

1.3.1 HIV infection and drug resistance 36

1.3.1.1 Drug resistance mechanism in HIV treatment 38

1.3.2 Drug resistance in TB infection 40

1.3.2.1 The classification of drug-resistant TB (DR-TB) 41

1.4 Drug resistance among other medical conditions **42**

1.5 Drug resistance prevention principles **43**

1.6 Drug combination and antiretroviral therapy **45**

1.7 Drug combination in Anti-Tuberculosis drugs **46**

1.8 Impact of HIV/TB co-infection on current treatment **47**

1.9 Synthesis of drug substance using non-covalent approaches **47**

1.10 The aim and objective of the study **48**

1.10.1 Specific objectives 49

1.11 Significance of the study **49**

1.12 Selection of the drug candidates for the study **49**

1.13 Methodology and analytical techniques **50**

1.14 Ethical clearance **50**

Chapter 2 Co-crystal theory *51*

Table of contents

2.1 Introduction **51**

2.2 Pharmaceutical co-crystal definition **52**

2.3 Co-crystal properties **53**

2.4 Co-former selection and co-crystal design **53**

2.5 Co-crystal classification **58**

2.5.1 Other co-crystallisation outcomes 61

2.5.2 The co-crystal development pathway 62

2.5.3 Solid-state co-crystal preparation 66

2.5.3.1 Contact formation of the co-crystal 66

2.5.3.2 Solid-state grinding methods of co-crystal preparation 66

2.5.4 Extrusion 67

2.5.5 Solution-based co-crystal preparation 67

2.5.5.1 Evaporative method of co-crystallisation 68

2.5.5.2 Cooling crystallisation 69

2.5.6 Supercritical fluid methods 69

2.5.6.1 Co-crystallisation with Supercritical Solvent 69

2.5.6.2 Rapid Expansion of Supercritical Solvents 69

2.5.6.3 Supercritical Antisolvent Co-crystallisation 69

2.5.7 Miscellaneous co-crystal preparation 70

2.5.7.1 Freeze-Drying 70

2.5.7.2 Electrochemically Induced Co-crystallisation 70

2.5.7.3 Resonant Acoustic Mixing 70

2.5.7.4 Spray drying 71

2.5.7.5 Electrospray technology 71

2.6 Preference of co-crystallisation **71**

2.7 Multidrug co-crystallization (MDCs) **72**

2.7.1 Factors influencing MDC synthesis 73

2.7.2 Synthesis of Multi-Drug Co-crystals 74

2.1.1 Advantages of Multi-Drug Co-crystals 75

2.2 Conclusion **76**

Chapter 3 Materials and experimentation methods ***77***

3.1 Material sources **77**

3.2 Identification of selected compounds **77**

3.2.1 Nevirapine 78

3.2.2 Efavirenz 79

3.2.3 Zidovudine 81

3.2.4 Lamivudine 82

3.2.5 1-Adamantylamine 84

3.2.6 Isoniazid 85

3.2.7 Pyrazinamide 86

3.2.8 Glutaric acid 87

3.3 Co-crystal/solid forms preparation **88**

3.3.1 Co-crystal screening by evaporative methods 88

3.3.1.1 Co-crystal screening by single solvent evaporation 89

3.3.1.2 Co-crystal formation by binary mixtures of solvents 90

3.3.2 Co-crystal formation by vapour diffusion 90

3.3.3 Co-crystal formation by mechanochemistry 90

Table of contents

3.3.3.1 Co-crystallisation by neat/solid-state grinding 91
3.3.3.2 Co-crystallisation by liquid assisted grinding (LAG) 92

3.4 Characterisation **93**
3.4.1 Characterization by the Hot Stage Microscopy (HSM) 93
3.4.2 Differential Scanning Calorimetry (DSC) analyses 95
3.4.3 Thermogravimetric analysis (TGA) 97
3.4.4 Morphology study by scanning electron microscopy (SEM) 98
3.4.5 Characterization by Fourier Infrared spectrophotometry 99
3.4.6 Characterisation by solid state-NMR 100
3.4.7 Characterisation by Powder X-Ray Diffraction (PXRD) 100
3.4.8 Solubility evaluation by High-Pressure Liquid Chromatography 102
3.4.9 *In vitro* antimicrobial activity 102
3.4.9.1 Preparation of growth media 103
3.4.10 Other computer sources 103

3.5 Conclusion **103**

Chapter 4 Dual-drug co-crystals and eutectics of selected anti-HIV drugs: Non-covalent synthesis and characterisation ***105***

4.1 Introduction **105**

4.2 Materials and methodologies **105**
4.2.1 Materials 105
4.2.2 Co-crystal screening and preparation 106
4.2.2.1 EFZA co-crystal preparation 106
4.2.2.2 NEF co-crystal preparation 106
4.2.2.3 Binary eutectic LMZT preparation 107
4.2.2.4 NVZA solid forms preparation 107
4.2.2.5 Screening and preparation of dual drug solid forms (NVZA) 108
4.2.2.6 EL solid forms preparation 109
4.2.2.7 NL solid forms preparation 110
4.2.3 Characterization of the samples 111
4.2.3.1 Analysis by Hot Stage Microscopy (HSM) 111
4.2.3.2 Analysis by Differential Scanning Calorimetry (DSC) 111
4.2.3.3 Analysis by Thermogravimetry (TGA) 111
4.2.3.4 Morphology evaluation by Scanning Electron Microscopy (SEM) 112
4.2.3.5 Analysis by Fourier Transform Infrared Spectrophotometry (FT-IR) 112
4.2.3.6 Analysis by Powder X-Ray Diffraction (PXRD) 112
4.2.3.7 *In vitro* solubility studies 112

4.3 Results and discussions **113**
4.3.1 Efavirenz: zidovudine dual-drug co-crystal (EFZA) 113
4.3.1.1 Thermal analyses of results 113
4.3.1.2 Structural evaluation by Fourier transform infrared spectroscopy 115
4.3.1.3 Analysis of the particle morphology of EFZA dual-API co-crystal 117
4.3.1.4 EFZA analyses by Powder X-ray diffraction 118
4.3.1.5 The solid-state NMR analysis of EFZA co-crystal 119
4.3.1.6 EFZA *in vitro* solubility evaluation by HPLC 122
4.3.2 Nevirapine: efavirenz dual drug co-crystal (NEF) 125
4.3.2.1 Thermal analysis of the NEF co-crystal 125
4.3.2.2 Structural studies by infrared spectroscopy 127
4.3.2.3 Morphology studies of NEF dual-API co-crystal 129
4.3.2.4 Analysis of NEF sample by powder X-ray diffraction (PXRD) 129

Table of contents

4.3.2.5 The *in vitro* solubility evaluation of NEF co-crystal 130
4.3.3 Lamivudine-Zidovudine binary eutectic mixture (LMZT) 133
4.3.3.1 Preparation of LMZT sample 133
4.3.3.2 Thermal analyses of LMZT sample by Hot Stage Microscopy 133
4.3.3.3 Structural evaluation by infrared spectroscopy 136
4.3.3.4 Characterisation of LMZT morphology by SEM 138
4.3.3.5 Powder X-Ray diffraction analysis of LMZT sample 139
4.3.3.6 LMZT *in vitro* solubility evaluation 139
4.3.4 Nevirapine-Zidovudine solid forms and co-crystals (NVZA) 142
4.3.4.1 Thermal analyses 142
4.3.4.2 Analysis of the structure by Fourier transform infrared spectroscopy 144
4.3.4.3 Analysis of the NVZA derivative solid forms by Powder X-Rays diffraction 146
4.3.4.4 In-vitro solubility evaluation of NVZA dual-APIs solid forms 147
4.3.5 Efavirenz-Lamivudine multicomponent solid forms (EL) 150
4.3.5.1 Thermal analysis of EL solid forms by DSC and TGA 150
4.3.5.2 FTIR spectroscopic analysis of EL1 and EL2 co-crystal samples 152
4.3.5.3 Morphology of EL sample particles 154
4.3.5.4 Powder X-Rays diffraction discussion of EL solid forms 154
4.3.5.5 Solubility evaluation 155
4.3.6 Nevirapine-Lamivudine solid forms (NL) 158
4.3.6.1 The binary eutectic NL thermal analyses 158
4.3.6.2 FT-IR studies of the binary eutectic NL 160
4.3.6.3 Powder X-Ray Diffraction analysis of NL sample 161
4.3.6.4 *In vitro* solubility evaluation of the binary eutectic NL 162

4.4 Conclusion 164

Chapter 5 Dual-drug co-crystals/eutectics of selected antiretroviral and anti-tubercular drugs: Non-covalent synthesis and characterisation 165

5.1 Introduction 165

5.2 Experimentation materials and methodologies 166
5.2.1 Materials 166
5.2.2 Preparatory methods 166
5.2.2.1 Efavirenz-isoniazid co-crystal screening 166
5.2.2.1 Preparation of EFAD sample 167
5.2.2.2 Synthesis of INHZA 167
5.2.2.3 Preparation of AZTPZA sample 168
5.2.2.4 LMISO preparation 168
5.2.3 Characterization of the samples 169
5.2.3.1 Analysis by Hot Stage Microscopy (HSM) 169
5.2.3.2 Analysis by Differential Scanning Calorimetry (DSC) 169
5.2.3.3 Analysis by Thermogravimetry (TGA) 170
5.2.3.4 Morphology evaluation by Scanning Electron Microscopy (SEM) 170
5.2.3.5 Analysis by Fourier Transform Infrared Spectrophotometry (FT-IR) 170
5.2.3.6 Analysis by Powder X-Ray Diffraction (PXRD) 170
5.2.3.7 *In vitro* solubility studies 171

5.3 Results and discussions of co-crystals/eutectic mixtures 171
5.3.1 Efavirenz-isoniazid co-crystal (EFINH) 171
5.3.1.1 Thermal analysis of EFINH co-crystal 171
5.3.1.2 FTIR results of EFINH co-crystal 174
5.3.1.3 Scanning electron Microscopic analysis for EFINH adduct 176
5.3.1.4 Powder X-Ray diffraction results of EFINH co-crystal sample 176

Table of contents

5.3.1.5 Solid-state NMR results for EFINH co-crystals 177
5.3.1.6 In vitro solubility evaluation of pure EFV and INH vs EFINH co-crystal 178
5.3.2 Efavirenz-1-adamantylamine hybrid (EFAD) 181
5.3.2.1 Thermal analysis of EFAD solid form 181
5.3.2.2 Structure studies of EFAD by FTIR 183
5.3.2.3 Morphology evaluation of EFAD particles by Scanning electron microscopic 184
5.3.2.4 Powder X-Rays diffraction analysis of EFAD solid form 185
5.3.2.5 In vitro solubility evaluation of the co-amorphous solid form EFAD 186
5.3.3 Isoniazid-zidovudine binary eutectic (INHZA) 187
5.3.3.1 Thermal analyses of INHZA sample 187
5.3.3.2 Scanning Electron Microscopy analysis of INHZA 189
5.3.3.3 Structure evaluation of INHZA eutectic by FTIR 189
5.3.3.4 Powder X-ray diffraction analysis of INHZA sample 191
5.3.3.5 Solubility evaluation of INHZA vs its components AZT and INH 192
5.3.4 Zidovudine-pyrazinamide binary eutectic (AZTPZA) 193
5.3.4.1 Thermal analyses of AZTPZA sample 193
5.3.4.2 FTIR analysis of AZTPZA solid form sample 195
5.3.4.3 Powder X-ray diffraction results of the AZTPZA multicomponent sample 197
5.3.4.4 *In vitro* solubility evaluation of AZTPZA 198
5.3.5 Lamivudine-isoniazid binary eutectic LMISO 199
5.3.5.1 Binary eutectic LMISO thermal analyses 199
5.3.5.2 LMISO characterisation by FTIR 200
5.3.5.3 Analysis of LMISO by the powder X-ray diffraction 201
5.3.5.4 In vitro solubility of LMISO 202

5.4 Conclusion 203

Chapter 6 Non-covalent synthesis and characterisation of multicomponent hybrids of selected anti-tubercular drugs 204

6.1 Introduction 204

6.2 Material and experimentation 206
6.2.1 Materials 206
6.2.2 Preparatory methods 206
6.2.2.1 Dual-APIs isoniazid –pyrazinamide (INHPZA) solid forms 206
6.2.2.2 Preparation of the co-crystal between isoniazid and pentanedioic acid (INHGA) (2:1) 207
6.2.2.3 Pyrazinamide-glutaric acid co-crystal PGA (2:1) preparation 207

6.3 Co-crystallisation results and discussion 210
6.3.1 Dual-APIs isoniazid –pyrazinamide (INHPZA) solid forms 210
6.3.1.1 Thermal analysis of INHPZA1&2 solid forms 210
6.3.1.2 Particle morphology analysis by scanning electron microscopy 213
6.3.1.3 Structural evaluation by FT-IR of IHNPZA solid forms 214
6.3.1.4 Analysis by Powder X-ray diffraction 216
6.3.1.5 *In vitro* solubility evaluation of the produced materials 217
6.3.1.6 Minimal Inhibitory Concentration (MIC) Testing 219
6.3.2 Isoniazid- pentanedioic acid co-crystal (INHGA) (2:1) 219
6.3.2.1 Thermal analysis of INHGA (2:1) co-crystal 219
6.3.2.2 Structural studies of INHGA (2:1) co-crystal by Infrared spectroscopy 221
6.3.2.3 Morphology results of INHGA (2:1) co-crystal by SEM 223
6.3.2.4 Crystallographic results of INHGA (2:1) co-crystal sample 224
6.3.2.5 Solid-state NMR (SS-NMR) analysis of the local chemical environment 225
6.3.2.6 INHGA (2:1) co-crystal solubility evaluation 226

Table of contents

6.3.2.7 *In vitro* antimicrobial evaluation 227
6.3.3 Pyrazinamide-pentanedioic acid co-crystal 228
6.3.3.1 Thermal analysis of PGA co-crystal sample 228
6.3.3.2 Structural evaluation by infrared spectroscopy 231
6.3.3.3 Particle morphology by scanning electron microscope 232
6.3.3.4 Analysis of PGA sample by the powder diffraction 233
6.3.3.5 PGA Samples characterisation by solid-state NMR 234
6.3.3.6 Solubility evaluation of PGA co-crystal 235
6.3.3.7 In *vitro* antimicrobial evaluation for PGA (2:1) co-crystal 236

6.4 Conclusion 236

Chapter 7 Conclusions and future works 238

7.1 Concluding remarks 238
7.1.1 Remarks on non-covalent synthetic methods used for multicomponent solid forms preparation 239
7.1.2 Physicochemical characterisation remarks 239
7.1.3 Chapters overview 241

7.2 Future works 243

References 244

APPENDICES 285

Appendix A 285

Appendix B1 294

Appendix B2 295

Appendix B3 296

Appendix B4 297

Appendix B5 298

Appendix B6 299

Appendix B7 300

Appendix B8 301

Appendix B9 302

Appendix B10 303

Appendix C 304

Table of figures

Figure.1.1: Antibiotics bacterial resistance mechanisms (González-Bello, 2017b) 33
Figure 1.2: HIV-1 life-cycle and different inhibitory mechanisms (Source: Atta, De Seigneux and Lucas, 2019) 38
Figure.1.3: Cancer drug resistance mechanisms 43
Figure 2.1: Supramolecular synthons and their occurrence percentages based on the Cambridge Structure Database (CSD). On the left are common homosynthons; acid-acid or carboxylic acid dimer and amide-amide homosynthon or carboxamide dimer. On the right are regular heterosynthons; carboxylic acid-pyridine, carboxylic acid-carboxamide, and carboxamide-pyridine heterosynthon (Cherukuvada et al., 2016). 55
Figure 2.2: Example of O–H**…**O H-bonding between acetaminophen and oxalic acid space group P21/c shown alongside b-axis 57
Figure 2.3: Different co-crystallisation solid forms based on Cherukuvada et al. (2014) discussion 62
Figure 2.4: Co-crystal development pathway according to Duggirala et al. (2016) 63
Figure 2.5: The crystal lattice of the co-crystal between carbamazepine and para-aminosalicylic acid 68
Figure 3.1: Nevirapine molecular structure 78
Figure 3.2: Efavirenz molecular structure 80
Figure 3.3: Zidovudine molecular structure 81
Figure 3.4: Diagram of AZT metabolic pathways (Source: Veal and Back, 1995) 82
Figure 3.5: Lamivudine molecular structure 82
Figure 3.6: Diagram of lamivudine metabolism pathway (Andrade et al., 2011) 83
Figure 3.7: 1-adamantanamine molecular structure 84
Figure 3.8: Molecular structure of Isoniazid 86
Figure 3.9: Mechanisms of Pyrazinamide Action and Resistance (source: Zhang *et al.*, 2014) 87
Figure 3.10: Glutaric acid molecular structure 88
Figure 3.11: The demonstration of the crystal/co-crystal formation from solvent evaporation 89
Figure 3.12: Image demonstrating co-crystal synthesis by solid-state grinding (left) and liquid assisted grinding (LAG) (right) 92

Table of Figures

Figure 3.13: Image of the Hot Stage Microscope fully set for analysis. 94
Figure 3.14: Different information or typical transition obtained in DSC spectrum...95
Figure 3.15: A differential scanning calorimeter and Intracooler II (right).....96
Figure 3.16: The thermogravimetric analyser with a digital temperature controller...98
Figure 3.17: Scanning electron Microscopy (Auriga) 99
Figure 3.18: Spectrum 400; the FT-IR/FT-NIR spectrometer 100
Figure 3.19: D8 ADVANCE Eco – powder diffraction for powder samples.....101
Figure 4.1: The proposed molecular mechanistic for the preparation of EFZA dual-API co-crystal.....106
Figure 4.2: Molecular mechanistic for the preparation of NEF dual-API co-crystal 107
Figure 4.3: Molecular mechanistic for the preparation of LMZT eutectic mixture...107
Figure 4.4: The molecular mechanistics for the preparation of NVZA derivative solid forms. 108
Figure 4.5: Molecular mechanistic for the preparation of EL eutectic mixture.....110
Figure 4.6: Molecular mechanistic for the preparation of NL eutectic mixture 110
Figure 4.7: The HSM images for EFZA co-crystal recorded at room temperature and the temperature range over which occurred the sample of the sample (96-111°C)...113
Figure 4.8: The DSC curves of the starting materials EFV and AZT compared to the co-crystal EFZA curve showing an earlier melting transition peak. 114
Figure 4.9: The TGA and DTA curves for EFZA supramolecular co-crystal showing a total decomposition mass loss of 66.3%. 114
Figure 4.10: FTIR spectra for pure EFV and AZT compared to EFZA co-crystal. ..116
Figure 4.11: Suggested EFZA structure with probable interaction based on FTIR results 117
Figure 4.12: The SEM images of (a) pure AZT, (b) EFV-AZT physical mixture, (C) EFZA and (d) pure EFV 117
Figure 4.13: The experimental PXRD patterns of AZT, EFV, EFV-AZT physical mixture, and the co-crystal EFZA.....118
Figure 4.14: Proton MAS SSNMR experiment of AZT, EFV, and EFZA supramolecular co-crystal 119
Figure 4.15: The ^{13}C CP MAS SS-NMR experimental spectra of (a) EFV, (b) AZT (c) co-crystal EFZA.....120
Figure 4.16: ^{1}H (500 MHz) DQ MAS (35 kHz) spectra of the pharmaceutical co-crystal molecule, efavirenz- zidovudine (1:1) 122

Table of Figures

Figure 4.17: Standard calibration curves of pure AZT and EFV.....123
Figure 4.18: Solubility histogram for pure AZT and AZT in the EFZA co-crystal ..124
Figure 4.19: Solubility histogram of pure EFV vs EFV in EFZA co-crystal 124
Figure 4.20: The HSM images of NEF co-crystal recorded at room temperature (20°C), the onset of melting transition (122°C), and melting temperature (126°C).....125
Figure 4.21: The DSC thermograms for untreated EFV, NVP, and the prepared co-crystal NEF with a single melting endotherm at 125°C 126
Figure 4.22: The TGA and DTA curves of NEF co-crystal showing a total decomposition mass loss of 93% of the initial sample weight 126
Figure 4.23: FTIR spectra of pure NVP and EFV compared to the FTIR spectrum of the NEF co-crystal 128
Figure 4.24: Suggested intermolecular bonding in the NEF co-crystal based on FTIR analysis.....128
Figure 4.25: The SEM images of NVP-EFV physical mixture, NEF co-crystal, pure EFV and NVP 129
Figure 4.26: The experimental PXRD patterns for pure NVP, EFV, their physical mixture and NEF co-crystal.....130
Figure 4.27: Standard calibration curves for EFV and NVP. 131
Figure 4.28: Solubility histogram of untreated EFV and EFV in the NEF co-crystal 131
Figure 4.29: Solubility histogram of untreated NVP and NVP in the NEF co-crystal 132
Figure 4.30: The structure of lamivudine-zidovudine hydrate co-crystal [Source: Bhatt *et al.*, (2009)].....133
Figure 4.31: Diagram of HSM photographs of LMZT sample recorded at room temperature (20°C), the onset of melting at 98°C, actual melting at 105°C and decomposition at 204°C.....134
Figure 4.32: DSC curve of LMZT hybrid showing a lower melting endotherm compared to those from pure AZT and 3TC 134
Figure 4.33: TGA/DTA curves of LMZT sample showing a decomposition mass loss of ~70% over 200-300°C temperature range. 135
Figure 4.34: FTIR spectra comparing pure AZT and 3TC to the eutectic LMZT spectrum.....137

Table of Figures

Figure 4.35: The suggested LMZT structure with three prominent intermolecular bonding positions. 138
Figure 4.36: SEM micrograms of (a) AZT, (b) 3TC and (c) the LMZT sample captured at 5.00 K.X magnification, 1 µm using 5 kV of energy. 138
Figure 4.37: The experimental PXRD patterns of 3TC, AZT, and the eutectic LMZT sample 139
Figure 4.38: The standard curves for AZT and 3TC at 254 wavelengths..... 140
Figure 4.39: A solubility histogram comparing LMZT solubility to pure AZT and 3TC in buffer solutions at pH=1.2, 6.8 and 7.4 and SDS solution 141
Figure 4.40: The DSC curves of pure AZT and NVP, NVZA1, NVZA2 and NVZA3 derivative solid forms. 142
Figure 4.41: The TGA/DTA curves of NVZA1 with a total decomposition mass loss of 90.6%, co-crystal NVZA2 showing a total decomposition mass loss of 85.4% and the co-crystal form NVZA3 with a total decomposition mass loss of 95% 143
Figure 4.42: FTIR spectra of commercial NVP, AZT and their dual-drug derivative solid forms; (a) NVZA1, (b) NVZA2 and (c) NVZA3..... 145
Figure 4.43: The experimental PXRD patterns for pure AZT and NVP, their physical mixture, and their solid derivative forms (a) NVZA1, (b) NVZA2, (c) NVZA3 147
Figure 4.44: Histogram illustrating the dual co-crystallization-related solubility changes for NVP, AZT in the binary eutectic NVZA1 over a wide range of buffered media and unbuffered deionised water 148
Figure 4.45: Histograms comparing solubility of pure AZT and NVP to NVZA2 co-crystal forms at pH=1.2, 6.8, 7.4 and aqueous media..... 149
Figure 4.46: Histograms comparing solubility of pure AZT and NVP to NVZA3 co-crystal form in aqueous medium and buffer solutions at pH=1.2, 6.8 and 7.4..... 149
Figure 4.47: The DSC curves of pure EFV, 3TC, eutectic EL1 and the co-crystal EL2 samples..... 151
Figure 4.48: TGA/DTA curves of the binary eutectic EL1 showing a decomposition mass loss of ~100% and the co-crystal EL2 showing a total decomposition mass loss of 85%. 151
Figure 4.49: FTIR spectra of EFV, 3TC and EL solid forms compared 153
Figure 4.50: Suggested interactions based on the FTIR results..... 154

Table of Figures

Figure 4.51: SEM images comparing the particle morphology of EFV, eutectic EL1, the co-crystal EL2 and 3TC particles analysed with the magnification of 10.00kX and 1 μm and EHT = 5 kV. 154
Figure 4.52: The experimental PXRD patterns of pure 3TC, EFV, the binary eutectic EL1 and the co-crystal EL2 155
Figure 4.53: EFV and 3TC calibration curves 156
Figure 4.54: Solubility histograms comparing pure EFV and 3TC to their amount released by eutectic EL1 in buffer solution at pH 1.2, 6.8 and 7.4.....157
Figure 4.55: Solubility histograms comparing pure EFV and 3TC to their amount released by co-crystal EL2 in 0.1 N HCl buffer solution at pH 1.2, PBS pH 6.8 and 7.4 157
Figure 4.56: DSC graph of pure NVP, 3TC and a lower melting DSC curve of the binary eutectic NL produced.....159
Figure 4.57: The TGA/DTA curves of the binary eutectic sample (NL) with a total decomposition mass loss of 75%.....160
Figure 4.58: The FTIR spectra of NVP, 3TC and the prepared binary eutectic NL compared.....161
Figure 4.59: The experimental powder X-ray diffraction patterns for NVP, 3TC, NVP-3TC physical mixture and the binary eutectic NL.....162
Figure 4.60: Calibration curves for both NVP and 3TC.....163
Figure 4.61: Solubility histogram comparing 3TC in the binary eutectic NL to the pure 3TC in different buffer solutions and deionised water 163
Figure 4.62: Solubility histogram comparing pure NVP to the binary eutectic NL in buffered solutions (different pH) and deionised water 164
Figure 5.1: Molecular mechanistic for the preparation of EFINH co-crystal.....166
Figure 5.2: Molecular mechanistic for the preparation of EFAD amorphous solid dispersion 167
Figure 5.3: The molecular mechanistic for the preparation of INHZA 168
Figure 5.4: The molecular mehcanistics for the preparation of AZTPZA eutectic mixture 168
Figure 5.5: The molecular structures of co-formers lamivudine and isoniazid 169
Figure 5.6: HSM photographs of EFINH recorded at room temperature (20°C), Onset of melting (114°C), melting temperature (120°C) and the onset of decomposition (174°C).....172

Table of Figures

Figure 5.7: DSC curves of pure EFV, INH and the co-crystal EFINH sample showing an earlier melting transition in comparison to melting temperature of pure EFV and INH 173
Figure 5.8: The TGA/DTA curves of the EFINH co-crystal showing a single step of mass loss corresponding to its decomposition. 173
Figure 5.9: The FTIR spectra of efavirenz (EFV), isoniazid (INH) and EFINH.....175
Figure 5.10: EFINH most plausible intermolecular interactions according to the FTIR analyses 175
Figure 5.11: Scanning electron microscopy (SEM) images of efavirenz (a), EFINH co-crystal sample (b), EFV-INH 1:1 physical mixture (c) and isoniazid 176
Figure 5.12: The experimental PXRD patterns of pure INH (1), EFV (2) and the co-crystal EFINH (3) 177
Figure 5.13: EFV, INH, and EFINH co-crystal solid-state CP/MAS 13C-NMR spectra compared.....178
Figure 5.14: Solubility histogram of the commercial EFV and the co-crystal EFINH at acidic pH=1.2, (0.1N HCl), 4.5 (ammonium acetate), at pH= 7.4 (phosphate buffer solution) and deionised water 179
Figure 5.15: Solubility histogram comparing the commercial INH and INH in the co-crystal EFINH at acidic pH=1.2, (0.1N HCl), 4.5 (ammonium acetate), at pH= 7.4 (phosphate buffer solution) and deionised water 180
Figure 5.16: The HSM images of EFAD sample recorded based on thermal changes observed at indicated temperatures. 181
Figure 5.17: Figure Illustration of DSC thermograms of EFV, ADT and EFAD solid form.....182
Figure 5.18: The TGA/DTA thermograms of EFAD sample 182
Figure 5.19: FTIR spectra of pure EFV and ADT compared to EFAD solid form ...183
Figure 5.20: SEM images for EFV, EFAD, and ADT recorded at μm, 5.00 K.X and EHT = 5.00 kV.....185
Figure 5.21: The experimental powder X-ray diffraction patterns of ADT, EFV, EFAD co-amorphous and the physical mixture 185
Figure 5.22: Solubility histogram of the commercial EFV vs the co-amorphous solid form EFAD in acidic pH1.2 (0.1N HCl), pH 7.4 buffer solutions and deionised water 186

Table of Figures

Figure 5.23: The HSM photographs of INHZA sample recorded at room temperature (20°C), the beginning of a melting transition (101°C), a complete melting (106°C) and over decomposition at 232°C.....187
Figure 5.24: The DSC curve of the binary eutectic INHZA showing a melting transition at a lower temperature compared to pure INH, AZT and their physical mixture.....188
Figure 5.25: The TGA/DTA curves of the INHZA sample with two consecutive decomposition mass losses from 185 to 325°C. 188
Figure 5.26: Scanning electron microscopic images of (a) pure AZT, (b) INHZA and (c) INH particles recorded at 1 μm, 10.00 k.x. 189
Figure 5.27: The FTIR spectra of INHZA, pure INH and pure AZT compared. 190
Figure 5.28: Suggested INHZA structures with possible intermolecular interactions. 191
Figure 5.29: AZT calculated (a) and experimental (b) PXRD patterns, INH calculated (c) and experimental (d) PXRD patterns, (e) the binary eutectic INHZA and (f) INH-AZT physical mixture.....191
Figure 5.30: The solubility histograms comparing pure INH and AZT to their enhanced solubility in the binary eutectic INHZA in acidic buffer solution at pH 1.2 (0.1N HCl) and PBS at pH 6.8 and 7.4.....192
Figure 5.31: HSM photographs of the AZTPZA sample recorded at the beginning of the experiment (room temperature), the beginning of melting 101°C, a complete melting at 108°C and onset of decomposition at 130°C.....193
Figure 5.32: DSC thermograms of pure AZT, PZA and AZT-PZA physical mixture compared to the binary eutectic AZTPZA sample 194
Figure 5.33: The TGA/DTA thermograms generated from the AZTPZA sample characterised by 81% decomposition mass loss in three consecutive steps 194
Figure 5.34: The FTIR spectrum from AZTPZA sample compared to pure AZT and PZA spectra.....195
Figure 5.35: Suggested structure based on FTIR band shifting in AZTZA spectrum 196
Figure 5.36: The experimental and simulated PXRD patterns of pure PZA (a and b) and AZT (c and d), AZTPZA binary eutectic (e) and the physical mixture AZT-PZA (f). 197
Figure 5.37: Solubility diagrams comparing the concentration of untreated AZT and PZA to their concentration in AZTPZA sample at different pH environment 198

Table of Figures

Figure 5.38: The DSC curves of pure 3TC, INH, their physical mixture and the binary eutectic LMISO showing a new melting transition at a lower temperature than both starting materials and their physical mixture 199
Figure 5.39: TGA/DTA curves of the binary eutectic LMISO showing decomposition mass loss in three steps. 200
Figure 5.40: FTIR spectra of pure INH, 3TC the binary eutectic LMISO compared 201
Figure 5.41: Experimental and simulated PXRD patterns of pure 3TC and INH compared to the eutectic LMISO 201
Figure 5.42: Solubility histograms comparing in vitro solubility of pure INH, 3TC to the binary eutectic mixture LMISO at pH 1.2 (0.1 N HCl), phosphate buffer solution at pH 6.8 and unbuffered deionised water 202
Figure 6.1: The proposed molecular mechanistic for the preparation of INHPZA solid forms 206
Figure 6.2: The molecular mechanistic for the preparation of INHGA (2:1) co-crystal 207
Figure 6.3: The molecular mechanistic for the preparation of the propose PGA (2:1) co-crystal 208
Figure 6.4: The HSM images for INHPZA1 and INHPZA2 samples showing different thermal behaviours. 211
Figure 6.5: A diagram comparing DSC curves obtained from INHPZA1 and INHPZA2 solid forms and input drugs, INH and PZA 212
Figure 6.6: TGA and DTA curves of INH-PZA dual-API solid forms; (a) INHPZA1 and (b) INHPZA2 212
Figure 6.7: SEM images for (a) PZA, (b) INHPZA1, (c) INHPZA2 and (d) INH intact 213
Figure 6.8: FTIR spectra of INH, PZA and INHPZA1 powder sample 214
Figure 6.9: Diagram comparing FTIR spectra of pure INH and PZA to solvated co-crystal INHPZA2 215
Figure 6.10: The PXRD patterns for pure INH, PZA, their physical mixture, and two derivative hybrids INHPZA1 and INHPZA2 217
Figure 6.11: INH and PZA standard calibration curves with regression equations used to measure the solubility of both APIs at different pH 218
Figure 6.12: Solubility histogram of pure INH and PZA vs their binary eutectic 218

Table of Figures

Figure 6.13: HSM images for INH, GA and the co-crystal INHGA (2:1) recorded over the range 25-200°C 220
Figure 6.14: The DSC curves of pure INH, the co-crystal former GA, and the co-crystal INHGA (2:1) 221
Figure 6.15:TGA/DTA thermograms of INHGA (2:1) co-crystal 221
Figure 6.16: The FT-IR spectra of isoniazid (INH), the physical mixture, INHGA (2:1) co-crystal and pentanedioic acid (GA) 222
Figure 6.17: Suggested bonding interactions between isoniazid amide and carboxylic moieties of glutaric acid suggested based on the FTIR spectral results 223
Figure 6.18: SEM micrographs for (a) pure INH, (b) the co-former GA and (c) the co-crystal INHGA (2:1) 224
Figure 6.19: Experimental and simulated PXRD patterns of pure isoniazid and pentanedioic acid compared to the INHGA (2:1) co-crystal and INH-GA physical mixture 224
Figure 6.20: SS-NMR spectra for INH, GA and INHGA (2:1) co-crystal 225
Figure 6.21: Histogram comparing the solubility of untreated INH to INHGA (2:1) co-crystal 227
Figure 6.22: HSM images of PZA, GA and PGA (2:1) co-crystal sample 229
Figure 6.23: The DSC curves of PZA, the co-crystal former GA, and the co-crystal PGA (2:1). 229
Figure 6.24: TGA and DTA thermograms of PGA (2:1) co-crystal 230
Figure 6.25: FTIR spectra of pure pyrazinamide (PZA), PGA (2:1) co-crystal, 2:1 physical mixture, and pure pentanedioic acid (GA) 231
Figure 6.26: Suggested structure of PGA (2:1) co-crystal 232
Figure 6.27: SEM micrographs comparing the morphology of (A) pure PZA, (B) GA and (C) PGA (2:1) co-crystal 233
Figure 6.28: Experimental and calculated PXRD patterns of pure pyrazinamide and pentanedioic acid, PZA-GA physical mixture and PGA (2:1) co-crystal 233
Figure 6.29: 13C CP MAS SSNMR chemical shifting of GA (bottom), PZA (middle) vs PGA (2:1) co-crystal (top) 234
Figure 6.30: Solubility histogram comparing untreated PZA to the co-crystal PGA (2:1) in different buffered solution and deionised water 235

List of tables

Table 3.1: Basic physicochemical properties of APIs selected for this project.....104
Table 3.2: Basic physicochemical properties of a co-former selected for this project 104
Table 4.1: A summary of the most significant shifts in EFZA spectrum 116
Table 4.2: Signal shifts in EFZA ^{13}C CP MAS SSNMR spectrum vs pure AZT and EFV 121
Table 4.3: Summary of important shifts in the FTIR of the NEF co-crystal 128
Table 4.4: Basic DSC data of AZT, 3TC, LMZT, and the physical mixture 135
Table 4.5: Main bands identified in the spectrum of pure drugs AZT and 3TC and their respective positions in the of LMZT sample 137
Table 4.6: Summary of IR shifts found in different NVZA co-crystals and the eutectic mixture 145
Table 4.7: Summary of characteristic peaks in the FTIR spectra of EFV, 3TC, the eutectic EL1 and the co-crystal EL2 and their assignments 153
Table 4.8: The summary of essential DSC data of NVP, 3TC and eutectic NL.....159
Table 5.1: Summary of the main spectral band shifting detected in the EFINH spectrum vs their original band positions 175
Table 5.2: Shifts of the main bands identified in the spectrum of EFAD vs pure EFV and ADT.....184
Table 5.3: Summary of spectral changes detected in INHZA spectrum as a result of weak interactions between INH and AZT 190
Table 5.4: DSC thermal data of the individual drugs AZT, PZA, and the AZTPZA and AZT-PZA mixture (physical mixture).....194
Table 5.5: Summary of different FTIR band shifting in AZTPZA spectrum vs original band positions in AZT and PZA spectra.....196
Table 6.1: The prominent IR spectral band positions in pure INH and PZA spectra and their respective positions in the spectra of the multi-component solid forms INHPZA1 and INHPZA2 216
Table 6.2: MICs of INH and PZA (controls) and INHZA solid forms against M tuberculosis stains 219
Table 6.3: The FTIR shifts detected in the spectra of INH, GA and their co-crystal INHGA (2:1).....223

List of Tables

Table 6.4: Isotropic chemical shifting due to the INHGA (2:1) co-crystal 226
Table 6.5: MICs of INH (control) and INHGA (2:1) against M tuberculosis stains .227
Table 6.6: Thermal properties for pure PZA, GA, and the co-crystal PGA (2:1) from DSC.....230
Table 6.7: Summary of all shifts in wavelength in both PGA (2:1) sample.....232
Table 6.8: MIC of PGA (2:1) co-crystal against M tuberculosis.....236

List of abbreviations

DR: Drug resistance is when a microorganism mutates and becomes insensitive to a drug designed to kill it (a drug that was effective previously).

BP: Bacterial protein is a target for antimicrobial drugs to which they bind.

HIV/AIDS: Human immunodeficiency virus Acquired immunodeficiency syndrome; this is one of the deadliest viruses. It spread through certain body fluids, specifically targeting the host's immune system (the CD4 cells). If not treated, the infection can progress into AIDS.

TB: Tuberculosis; a bacterial infection caused by *Mycobacterium tuberculosis*. It mainly targets the lungs

MDR-TB: multidrug resistance TB; infection is resistant to isoniazid (INH) and rifampicin (RMP) the most important drug members of the first-line treatment regimen

API: Active Pharmaceutical Ingredient is an active substance in every pharmaceutical product. The formulation combines this with other excipients to make a final product.

DNA: Deoxyribonucleic acid, the hereditary material in humans and almost all other organisms

NRTI: Nucleoside reverse transcriptase inhibitors (NRTIs) block reverse transcriptase**;** and HIV enzyme used by this HIV to convert its RNA into DNA (reverse transcription). The process of blocking this reverse transcription prevents HIV from replicating in the host cells.

NNRTI: Non-nucleoside reverse transcriptase inhibitors (NNRTIs) also block "**reverse transcriptase";** an HIV enzyme used by this HIV to convert its RNA into DNA (**reverse transcription**). They bind non-competitively to this enzyme and prevent the conversion of the viral RNA to DNA.

WHO: The World Health Organization is a specialized agency of the United Nations that is concerned with international public health. It was established on April 7 1948

DSC: Differential Scanning Calorimetry (DSC) is a popular thermal analysis instrument used to measure melting temperature, heat of fusion, latent heat of melting,

reaction energy and temperature, glass transition temperature, crystalline phase transition temperature and energy, precipitation energy and temperature, denaturalization temperatures, oxidation induction times, and specific heat or heat capacity…

HSM: Hot Stage Microscopy is a thermal microscopic analytical tool used to observe thermal changes in a sample under the microscope.

SS-NMR: Solid-state Nuclear Magnetic Resonance

^{1}H-CP-MAS SS-NMR: Proton-cross polarization-magic angle spin solid-state NMR

^{13}C-CP-MAS SS-NMR: ^{13}Ccross-polarisation-magic angle spin solid-state NMR

CP-HETCOR SSNMR: The cross-polarization heteronuclear correlate solid-state NMR

1H-DQ-BABA-SSNMR: Proton double-quantum back to back solid-state NMR

FT-IR: Fourier Transform Infrared Spectroscopy; a technique that is used to obtain an infrared spectrum of absorption, emission, photoconductivity, or Raman scattering of a solid, liquid, or gas.

PXRD: Powder X-ray Diffraction; a rapid analytical technique primarily used for phase identification of a crystalline material and can provide information on unit cell dimensions of powdered samples.

SXRD: Single X-ray Diffraction; is a non-destructive analytical technique which provides detailed information about the internal lattice of crystalline substances, including unit cell dimensions, bond-lengths, bond-angles, and details of site-ordering

CSD: The Cambridge Structural Database; a repository and a validated and curated resource for the three-dimensional structural data of molecules generally containing at least carbon and hydrogen, comprising a wide range of organic, metal-organic and organometallic molecules.

B.P.: boiling point; also known as saturation temperature is the temperature at which the vapour pressure of a liquid equals the external pressure surrounding the liquid.

List of abbreviations

M.P.: melting point; chemically referred to as a temperature at which solid and liquid forms of a pure substance exist in equilibrium.

ADT: 1-adamantylamine; an antiviral and antiparkinsonian drug previously used in salt form for the treatment of influenza A. the drug is also potent towards different neuro disorders.

EFV: Efavirenz; one of the popular non-nucleoside reverse transcriptase inhibitors (NNRTIs), used in combination with other anti-HIV drugs in current treatment.

NPV: Nevirapine; a non-nucleoside reverse transcriptase inhibitor (NNRTI), used alternatively to EFV, in combination with others to manage HIV infection.

3TC: Lamivudine; an anti-HIV and anti-hepatitis drug that works by reducing the number of viruses in the host blood. The drug belongs to the inhibitors of the reverse transcriptase.

AZT: Zidovudine (azidothymidine), a known HIV reverse transcriptase inhibitor. The drug is also used as a preventive diagnosis immediately after suspected exposure to the virus.

GA: *L*-glutaric acid (also known as pentanedioic acid) is one of many dicarboxylic acids used as co-crystal formers in different co-crystals.

INH: Isoniazid; a key member of first-line anti-tubercular drugs used in a combined treatment regimen.

PZA: Pyrazinamide; an anti-tubercular drug used in combination with others in the first-line treatment regimen of TB

EFZA: The co-crystal of two inhibitors of reverse transcriptase efavirenz and zidovudine

NEF: A dual drug co-crystal obtained from nevirapine and efavirenz

NVZA: Nevirapine: zidovudine solid-state hybrids

EFAD: A solid-state hybrid produced by mechanochemical reaction efavirenz: 1-adamantylamine

List of abbreviations

ADZT: A solid-state hybrid resulted from mechanochemical grinding of 1-adamantanamine and zidovudine

NL: Nevirapine-lamivudine co-crystal by grinding method

LMZT: a eutectic mixture of lamivudine and zidovudine

EFINH: A dual drug co-crystal synthesized from efavirenz and isoniazid

INHPZA: Co-crystal and/or a eutectic mixture of isoniazid and pyrazinamide

INHGA: A co-crystal of isoniazid with glutaric acid as a co-crystal former

PGA: A co-crystal that was produced from Pyrazinamide and glutaric acid as a co-former.

Academic outputs

Part of this research was published internationally

Research paper: Dual-drug co-crystal synthesis for synergistic in vitro effect of three key first-line antiretroviral drugs

Jean Baptiste Ngilirabanga[1], Marique Elisabeth Aucamp[1], Paulo Pires Rosa[2], and Halima Samsodien[1]

[1]*School of Pharmacy, University of the Western Cape, 7535 Cape Town, South Africa*

[2]*Faculty of Pharmaceutical Sciences, State University of Campinas, Sao Paulo, Brazil*

Ngilirabanga, J.B., Rosa, P.P., Aucamp, M., Kippie, Y. and Samsodien, H., 2020. Dual-drug co-crystal synthesis for synergistic in vitro effect of three key first-line antiretroviral drugs. *Journal of Drug Delivery Science and Technology*, 60, p.101958. https://doi.org/10.1016/j.jddst.2020.101958

Research paper: Mechanochemical synthesis and physicochemical characterization of isoniazid and pyrazinamide co-crystals

Jean Baptiste Ngilirabanga[1], Marique Elisabeth Aucamp[1], Paulo Pires Rosa[2], and Halima Samsodien[1]

[1]*School of Pharmacy, University of the Western Cape, 7535 Cape Town, South Africa*

[2]*Faculty of Pharmaceutical Sciences, State University of Campinas, Sao Paulo, Brazil*

Ngilirabanga, J.B., Aucamp, M., Rosa, P.P. and Samsodien, H., 2020. Mechanochemical Synthesis and Physicochemical Characterization of Isoniazid and Pyrazinamide Co-crystals With Glutaric Acid. *Frontiers in chemistry*, *8*.

doi.org/10.3389/fchem.2020.595908

List of abbreviations

Review paper: Pharmaceutical co-crystals: An alternative strategy for enhanced physicochemical properties and drug synergy

***Jean Baptiste Ngilirabanga**, Halima Samsodien[*]*

School of Pharmacy, Faculty of Science, University of the Western Cape, Cape Town, Bellville 7535, South Africa.

Published: Nano Select

Article DOI: 10.1002/nano.202000201

Research paper: Zidovudine-lamivudine eutectic (LMZT): Mechanochemical synthesis, characterization and solubility evaluation

Jean Baptiste Ngilirabanga, Marique Elizabeth Aucamp, Halima Samsodien*

School of Pharmacy, Faculty of Science, University of the Western Cape, Bellville 7535, South Africa.

Published: ***Journal of Drug Delivery Science and Technology***

Part of this research was presented locally and internationally

XXXVI Congresso de Iniciacao Clientifica Unicamp Campinas Brazil held on 17-19 October 2018

Title: **Solubility study of drugs and development of dissolution tablets assay.**

Giulia Paschalis*, Jean Baptiste Ngilirabanga**, Halima Samsodien**, Paulo C. P. Rosa*.

**Unicamp – Campinas Brazil, **University of the Western Cape – South Africa*

Category: Oral presentation

The First Conference of Biomedical and Natural Sciences and Therapeutics (CoBNeST) at Spier Estate Stellenbosch South Africa, 7-10 October 2018

Title**: Synthesis and characterization of dual drug supramolecules of three Reverse Transcriptase Inhibitors; Efavirenz, Nevirapine, and Zidovudine for drug resistance**

List of abbreviations

Category: Oral presentation under the Academy of Pharmaceutical Sciences of South Africa (APSSA) presentations

Chapter 1 Introduction

Resistant causative organisms of infectious diseases such as the human immunodeficiency virus/acquired immunodeficiency syndrome (HIV/AIDS) and tuberculosis (TB) impact significantly on therapeutic outcomes of administered medication. This presents a major challenge to manage these diseases. To combat this problem, it is necessary to examine alternative strategies to overcome resistance by developing new derivatives of active entities. These should be therapeutically efficient, cost-effective, and be formulated with patient adherent qualities.

1.1 Infectious diseases

Genetic analysis and other technologies such as molecular clocks, phylogeographic analyses of archaeological and paleontological discoveries reflect that infectious diseases date back to the Palaeolithic period. This shows that pathogens have existed since 10 000 to 2.5 million years (Trueba, 2014). Other theories suggest that different infections and pathogens arose during the "new stone age"/Neolithic period or later from domestic animals and rodents by human's close contact (Trueba, 2014).

An infection is defined simply as an invasion of a host (human or animal) by pathogens such as bacteria or viruses. According to the World Health Organisation (WHO), infectious diseases are the second largest cause of death, globally, after cardiovascular diseases, accounting for approximately 26% of all deaths (Günthard et al., 2014).

The road to the discovery of proper treatment for infections began with Alexander Fleming, a German scientist who first discovered the first-ever antibiotic from *Penicillium notatum*. Prior to this, **Salvarsan** also known as ***Arsphenamine***, was the first chemical used to treat syphilis by another German physician Paul Ehrlich and his team (K. J. Williams, 2009). Since then, different antibiotics have been developed with bactericidal and bacteriostatic activity as well as broad and narrow spectrum ones.

Despite the extensive efforts by various researchers, infectious diseases continue to pose a global threat aggravated by the appearance of drug resistance which significantly impacts the current treatment strategies but also; making it impossible to control the infection. Apart from the common cold, HIV and TB are most prominent (Zaffiri et al., 2012).

1.2 Drug resistance

Drug resistance (DR) is a major global threat and the main reason for infection treatment failure (Tenover, 2006; World Health Organization, 2014). According to WHO, DR is defined as the ability of microorganisms such as bacteria, viruses, and others, to grow in the presence of drugs designed to cure the infection by rendering them ineffective (World Health Organization, 2014).

DR leads to a significant reduction or complete suppression of drug effectiveness which typically results in a medical failure to cure a disease. Further, when DR occurs, pathogens replicate despite the presence of a potential therapeutic drug, either by changing its mechanisms of action to the point that the treatment assigned is no longer effective (World Health Organization, 2014).

1.2.1 Drug resistance mechanisms

DR is classified as "active" when it occurs as a result of a specific evolutionary pressure to adopt a counter-attack mechanism against an antibiotic or class of antibiotics and "passive" when it occurs as a consequence of general adaptive processes of a pathogen that has nothing to do with a given class of antibiotics. A typical example is that of a Gram-negative bacterial outer membrane which imparts a broad barrier to entry (Wright, 2005, 2016). The term "***Superbugs***" is referred to pathogens that are resistant to most of the antimicrobials. According to Rekha B., resistance refers to a load of bacteria that are not inhibited by the usually achievable systemic concentration of an agent with a normal dosage schedule and/or fall in the minimum inhibitory concentration ranges (Bisht et al., 2009).

DR claims several lives that would have otherwise been saved. According to the WHO report 2019, approximately seven hundred thousand (700000) people worldwide die every year due to DR. Considering this number, two hundred thirty thousand (230000) is the annual approximated number of multidrug resistance-related deaths (World Health Organization, 2019).

The antibiotic/ antimicrobial resistance (AR) occurs via three fundamental mechanisms namely enzymatic degradation of antibacterial drugs, alteration of bacterial proteins that are antimicrobial targets, and changes in membrane permeability to antibiotics (Dever

& Dermody, 1991; Tenover, 2006; Wright, 2016). An in-depth analysis reveals that antibiotic resistance can further be classified as either plasmid-mediated or maintained on the bacterial chromosome (Dever & Dermody, 1991). A few examples of how antimicrobial resistance (AR) is manifested include the most commonly known resistance mechanism of the penicillins and cephalosporins which is mediated by antibiotic hydrolysis caused by the bacterial enzyme β-lactamase (Dever & Dermody, 1991). The expression of chromosomal β-lactamase can either be induced or steadily repressed by exposure to β-lactam drugs.

Another resistance mechanism known in several classes of antibiotics, including the later three classes of antibiotics in addition to the β-lactam drugs, is a reduced penetration ability of an antibiotic (Dever & Dermody, 1991).

The resistance of bacteria to available drugs also threatens the pharmaceutical industry, which continuously invests time, money and takes risks in dealing with sometimes harmful biological and chemical substances to bring about medicines. Bacteria have biochemical and genetic mechanisms enabling them to ensure the evolution and spread of antibacterial resistance genes. The worst-case scenario is when an infection is caused by multiple resistant bacterial strains.

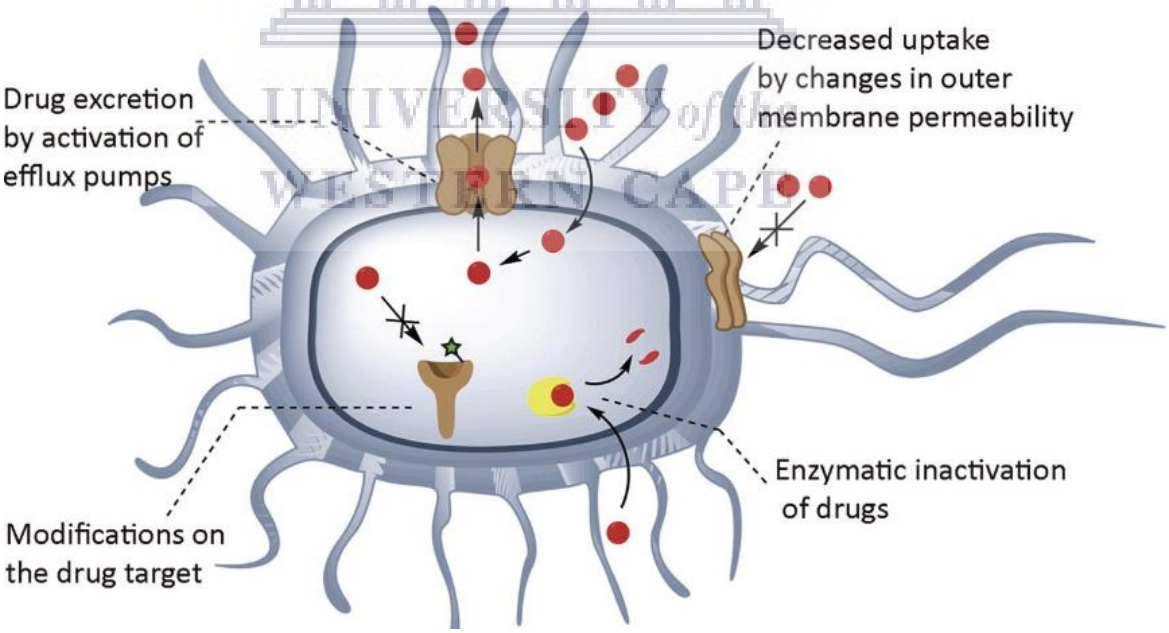

Figure.1.1: Antibiotics bacterial resistance mechanisms (González-Bello, 2017b)

Resistance to certain groups of antibiotics is very high (up to 100%), due to the non-critical use of antibiotics of such groups. Jovanovic et al. suggested that this development of resistant bacterial strains may soon lead to insufficiency or a complete

lack of effective antibiotics. The war against evolution and widespread antibiotics resistant genes is real and we all need to participate. A unique main factor that can be exercised to slow down this outbreak is to properly use available antibiotics (Jovanović et al., 2008).

1.2.1.1 Enzymatic degradation of antibacterial drugs

Enzymatic degradation of antibacterial drugs is related to what Wright et al. detailed in enzymatic strategies of antibiotic inactivation (**Figure.1.1**) (Gatch et al., 2013; Gonzalez, 2015; Wright, 2005).

These strategies include:

Hydrolysis during which, cleavage of the target bonds, without which there will be no interaction between the drug-target, causing loss of antibiotic activity accordingly.

Enzymes amidases, esterases, etc., are known to obstruct the binding process before the drug reaches the target site.

Hydrolysis occurs due to the interference of macrolide-resistant enzymes (macrolide esterases) with protein synthesis. This is a mechanism used by bacteria to successfully resist some antibiotics. They act by emanating enzymes that deteriorate and inhibit important properties of the drugs (bacteriostatic and bactericidal properties).

1.2.1.2 Alteration of antimicrobial targets

The antimicrobial targets are also known as bacterial proteins (BP) to which antibiotics are bound. Modification of these BPs leads to an altered structure on which a drug will partially bind or completely fail to bind. This, in turn, creates a way of spontaneous mutations in a gene(s) encoding the target. The rising of these mutations is a common source of alteration in one or more sequences of amino acids, mainly in the putative binding site of the target protein (Gonzalez, 2015).

Enzymes known as transferases constitute a large group of enzymes that act by covalently modifying the structure of the antibiotic exposed to them, resulting in an impaired binding ability to the target and a total loss of activity expected. Examples given include acyltransferases, phosphotransferases, thioltransferases, nucleotidyltransferases, ADP-ribosyltransferases, and glycosyltransferases (Munita & Arias, 2016; Vázquez-Laslop & Mankin, 2018; Wright, 2005).

Other enzymatic mechanisms of resistance include the use of redox and lyases enzymes responsible for antibiotic oxidation on the one hand and the formation of double bonds

and ring closure by cleaving carbon-carbon, carbon-oxygen, carbon-nitrogen, and carbon-sulfur bonds on the other hand (Gonzalez, 2015; Wright, 2005).

1.2.1.3 Changes of membrane permeability

"Changes in membrane permeability to antibiotics" is a resistance mechanism commonly known in Gram-negative bacteria due to their increased protection. The chemical modification (change in chemical structure) of the phosphatidylglycerol caused by bacterial enzymes from anionic to cationic or zwitterionic form, leads to increased bacterial resistance against polycationic antimicrobial drugs. Targeting and inhibiting these enzymes would be a shield against the development of this type of bacterial resistance. It is crucial to remember that many antimicrobial drugs are cationic (Epand et al., 2016). Among the antimicrobial agents targeting the cell wall, there are the *β*-lactam antibiotics such as penicillin and cephalosporin that inhibit cell wall synthesis.

1.3 Drug resistance among infectious diseases

DR particularly AR is well recognised as a major setback in the current treatment of infectious diseases, hospital management (more extended hospitalisation), and development of communities (Marston et al., 2016; Organization & others, 2014; Tenover, 2006; Wright, 2005). Presently, DR is familiar with its effects on the treatment of various bacterial, fungal, parasitic, and viral infections and treatment of chronic diseases such as cancer, diabetes and particularly, on the treatment of complex conditions such as HIV and TB.

HIV and TB infections are known to be the two top killers. Today, their treatment has become very complicated by the appearance of drug resistance, also known as drug tolerance; the primary cause of unsuccessful treatment (Julian Davies and Dorothy Davies, 2010).

AR is a serious clinical concern in the chemotherapeutic treatment of an infection. For decades, various common bacterial pathogens have become increasingly resistant to the drugs (antibiotics) used for their treatments, consequently, reducing the disease control abilities and increasing the mortality rates accordingly. The substantial and often unnecessary use of antibiotics is seen as a practice that encourages the proliferation of resistant mutant strains of bacteria while suppressing the susceptible strains (Homer et al., 2000). Drug resistance is not only popular in infectious diseases but also in cancer

treatment and other diseases. The inability of disease to respond to a specific medicine mainly results from the host factors such as a reduced or poor solubility and poor absorption of the drug, rapid metabolism, and excretion of a drug which results in low levels of serum and poor tolerance of drug effects (Gottesman, 2002).

1.3.1 HIV infection and drug resistance

It is believed that HIV infection originated from African primates. The first HIV-1 infected people were bush-meat hunters (Gao et al., 1999; Sharp & Hahn, 2011). The source was the contact with infected primates, but the trigger of the attention to the virus was its discovery among USA young homosexuals in 1981 and other populations including the users of injectable drugs and haemophiliacs (Sharp & Hahn, 2011). It is only in 1983 that HIV was identified as a causative agent of the pandemic known as AIDS (Ammaranond & Sanguansittianan, 2012; Barré-Sinoussi et al., 1983). The advent of this pandemic brought many problems in society; hindering, therefore, the progress to the development of communities and aggravating the existing challenges including socioeconomic problems faced daily (Buchacz et al., 2010). These problems are associated with an increase of opportunistic infections and other diseases such as TB which increase the rate of mortality worldwide.

African nations and Southern Africa particularly hold the first place with regards to having a high rate of HIV infection worldwide (70.8%). AIDS is the progression of HIV infection to a stage where several reductions in T-cells weakens the immunity system of infected individuals, making them vulnerable to various infectious diseases (Gao et al., 1999).

The WHO worldwide estimation revealed that approximately 46 million persons were living with HIV by the year 2004. Sixteen thousand people acquired the virus every day in the same year. However, the number of infected people globally at the end of 2018 was 37.9 million [32.7–44.0 million] (UNAIDS, 2019).

According to research, the two types of HIV (HIV-1 and HIV-2) genetically different, were introduced to humans through multiple interspecies transmissions from simian immunodeficiency virus (SIV) (Gao et al., 1999). Due to its lower viral load, HIV-2 is less transmitted and generally restricted to West Africa. On the other hand, HIV-1 is known to its widespread (Lemey et al., 2003) and a tremendous number of people died from it.

The development of anti-HIV compounds started, and the first anti-HIV drugs were protease inhibitors viz, indinavir, and ritonavir. However, the first treatment option approved by the U.S. Food and Drug Administration (FDA) was Zidovudine (AZT) in 1987. The clinical experience revealed that over 40% of all patients treated singly by the above two compounds (indinavir and ritonavir) experienced the emergency of resistance within 24 weeks (Greco et al., 1995). Even though promises initially were seen, a rapid increase in resistance was also experienced in the monotherapy with AZT (Boyer et al., 2015). Regardless of many years of research, no vaccine nor cure is available as yet (Walker & Burton, 2008). The advent of antiretroviral therapy (ART) for the treatment of HIV and the prevention of AIDS, has been a great achievement in the history of science and technology. ART therapy showed a dramatic impact on reducing HIV morbidity and mortality, (Jacobson & French, 1997; Murphy et al., 2001; Palella Jr et al., 1998) and its intervention was very distinct in the history of medicine. Today, the use of ARVs enables the reduction of both plasma and tissue-related viral load.

The worldwide estimated number of new HIV infections decreased from 2.7 million in 2008 to 2.3 million in 2012, the lowest number of infections since 1990, where 3.5 million people were acquiring HIV infection every year (UNAIDS, 2013). This number was quite significant to show how HIV treatment and prevention precautions have improved by the use of ARVs.

The actual known reverse transcriptase inhibitors (RTIs) are classified into two categories namely the nucleoside analogue RT inhibitors (NRTIs) and non-nucleoside analogue RT inhibitors (NNRTIs) (Arnold et al., 1996; De Clercq, 1995; Ding Jianping, Kalyan Das, Yu Hsiou, Wanyi Zhang, Edward Arnold, Prem NS Yadav, 2018; Jianping Ding Kalyan Das, 1997; Tantillo et al., 1994). The former category, NRTIs comprises the inhibitors that are analogue to normal deoxynucleoside triphosphates whereas the latter category, NNRTIs consists of inhibitors that function by binding at a common site, approximately 10 Å away from the polymerase active site (Arnold et al., 1996; J Ding et al., 1995; Kohlstaedt et al., 1992; Ren Jingshan, Robert Esnouf, Elspeth Garman, Donald Somers, Carl Ross, Ian Kirby, 1995; Smerdon et al., 1994).

Despite the use of ARVs and their impact on the lives of HIV-infected people and the management of the disease in general, resistance remains a challenge and the main

reason for treatment failure. Additionally, several other setbacks are associated with ARTs use. These include but not limited to severe side effects attributed to the high doses required to achieve a therapeutic effect, inadequate drug concentration at the site of action, and or the poor bioavailability of some antiretroviral drugs.

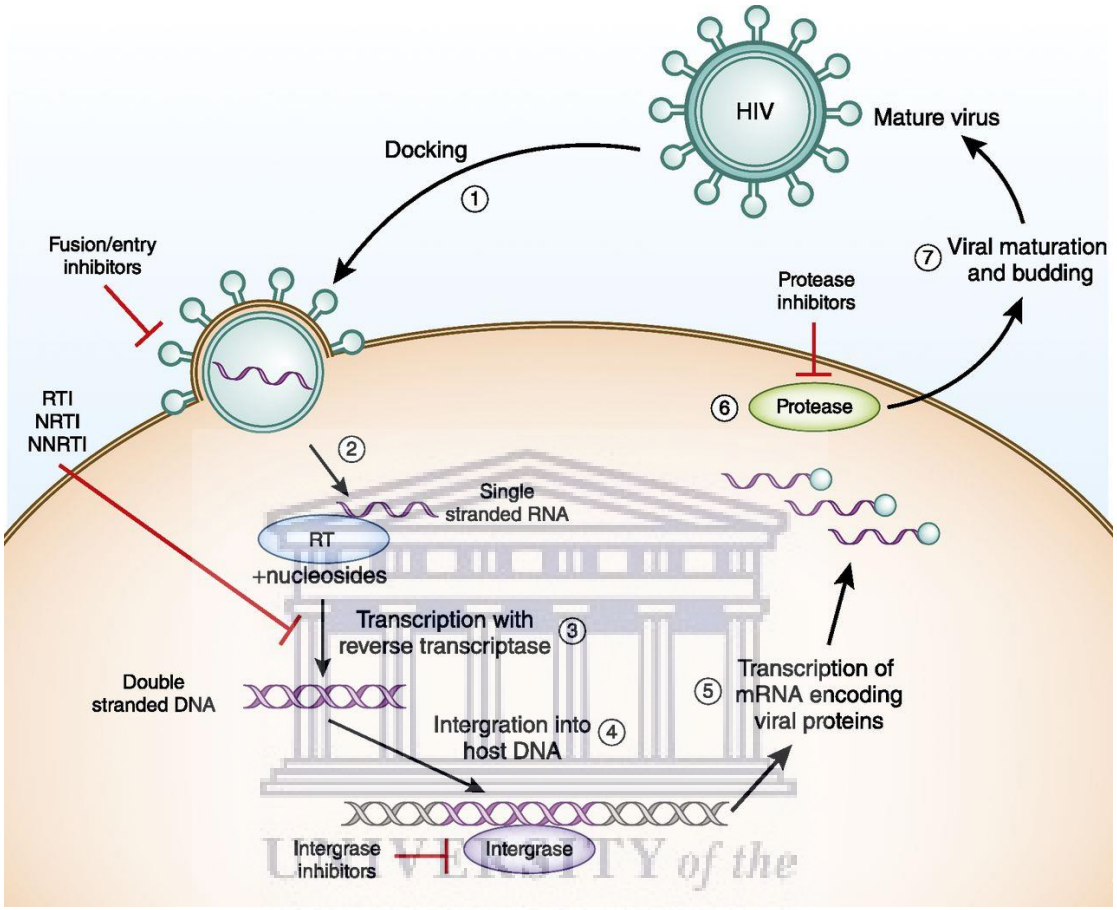

Figure 1.2: HIV-1 life-cycle and different inhibitory mechanisms (Source: Atta, De Seigneux and Lucas, 2019)

1.3.1.1 Drug resistance mechanism in HIV treatment

Like other RNA viruses (retroviruses), HIV uses all possible mechanisms of genetic variations to survive. This results in high rates of mutation during the replication process. Due to error-prone reverse transcriptase, the circulating viruses in the infected subject are represented by a swarm of related viral variants called quasispecies (Coffin, 1995).

This error-prone RT does not have proofreading activity and engages in frequent transfers of strands during reverse transcription, causing persistent recombination effects together with high viral replication rates (Coffin, 1995; Domingo & Holland, 1997).

This resistance of HIV to the treatment either taken individually or in combination is its fundamental strategy to survive. This is the reason why every step in its life cycle (**Figure 1.2**) serves as a potential target for therapeutic mediation. There are different ways the virus can enter the host. The primary vector is the contact with infected blood or other body fluids such as sperms and the commonly known HIV transmission way being through sexual activities. Details on HIV transmissions have been reported (Bobat & Archary, 2017; Capriotti, 2018; Cohen et al., 2011, 2016; "HIV Transmission," 2003; Hollingsworth et al., 2008; Naidoo, 2020; Patel et al., 2014; Shaw & Hunter, 2012).

RT is the enzyme necessary for the transformation of a single-strand viral ribonucleic acid (RNA) into double-strand linear DNA that is integrated into the host cell chromosomes. HIV uses this enzyme to multiply. For HIV multiplication, the retroviral RT with the catalytic activities of RNA-dependent DNA polymerization forms an RNA:DNA hybrid followed by RNase H degradation of the RNA strand from RNA:DNA hybrids and DNA-dependent DNA polymerization to generate a double-strand viral DNA (dsDNA), also capable of replication like other normal DNA (Coffin, 1995).

The NRTIs-binding site of RT is dynamic since, upon binding of the NNRTI, the RT modifies its conformation to accommodate the NNRTI forming a nonnucleoside inhibitor-binding Pocket (NNIBP). However, research indicated that despite major chemical differences among the first generation NNRTIs, they all bind to the very flexible, hydrophobic binding pocket (NNIBP) located in an adjacent position to the polymerase active site, mainly through energetically favourable positions (Jianping Ding et al., 1998; Kohlstaedt et al., 1992). Therefore, indicating that binding to the RT enzyme is dependent on a conformational fit, instead of a slight structural change (Miller, 2002).

Research also showed that NNRTI resistance is linked to over 40 possible amino acid substitutions occurring mainly at the NNIBP. These mutations affect NNRTI binding indirectly by hampering access to the pocket or by directly altering the size, shape and polarity on different areas of the pocket. However, mutations are primarily noted at either the Tyr181 or Tyr188 amino acids within the NNIBP. It is, in fact, these alterations that confer a high level of resistance to NNRTIs. These specific amino acids

change the avert affinity of a specific NNRTI for the binding site, ultimately resulting in drug resistance (Das et al., 2004).

Even though combination therapy using ARVs by targeting the viral enzymes RT and protease in an attempt to inhibit viral replication completely, there is evidence that multidrug-resistant strains may still emerge. Hence, a quest for new strategies is highly needed to prevent viral replication. To overcome HIV-1 RT mutant strains, major structural changes are required that will incur increased flexibility for the already flexible NNIBP. Slight modifications in structure (such as angle changes or isomeric forms) will not meet the required flexibility of the RT enzyme (Das et al., 2004).

1.3.2 Drug resistance in TB infection

Today, tuberculosis (TB) is one of the biggest challenges worldwide, affecting mainly the most impoverished populations. Even if asymptomatic, one-third of the population worldwide is infected by latent *mycobacterium tuberculosis*, the bacteria causing TB and serve as a stock for the pathogen, and this makes the control of the disease more complicated. Only about 10% of them develop active disease during their lifetime. The WHO reported an estimation of 8.6 million TB infections, of which 1.3 million deaths reported in 2012 were TB associated. Three hundred twenty thousand is the number of deaths attributed to TB among HIV infected people (World Health Organisation, 2013), (Baddeley, A; Dean, A; Monica-Dias, H; Falzon, D; Floyd, K; Garcia, 2013), (Organization et al., 2012). This number clearly indicates how heavy this burden is to the public.

The first anti-tuberculosis drug used was streptomycin. However, strains resistant to this drug were identified only a few months later. The emergence of these resistant strains evolved the introduction of TB treatment using more than one drug over 18 to 24 months. The arrival of rifampicin in 1970 significantly improved TB treatment and reduced the course to a period of 6 months. The problem arose in 1990 with reports of multidrug-resistant TB (MDR-TB) and was further aggravated by the emergence of extensively drug-resistance (XDR-TB) in 2006, which by definition is resistance to the first-line and second-line drugs (Shah et al., 2007). In addition to isoniazid and rifampicin, these strains are resistant to at least one of the fluoroquinolone drugs and an injectable agent (WHO, 2016).

The appearance of these resistant strains had completely transformed TB treatment into a nightmare that requires management with extended treatment courses and sometimes

impossible to control using available medications (Gandhi et al., 2006; Kim et al., 2007; Migliori et al., 2007; Shah et al., 2007). Further, the emergency of multidrug-resistant (MDR)-TB and an increase of wide-spread extensively drug-resistant TB (XDR-TB) worsened the situation and created additional complications to the control, prevention, and treatment of TB infection (Zumla et al., 2012).

1.3.2.1 The classification of drug-resistant TB (DR-TB)

Even though the classification of DR-TB is generally based on key actives of the treatment regimen, extended classification of DR-TB includes the following subdivisions: the mono-resistance (resistance to one anti-tuberculosis drug), poly-resistance (which is referred to as resistance to more than one anti-TB drug other than isoniazid and rifampicin), multidrug-resistance (resistance to isoniazid and rifampicin) and extensive drug resistance (XDR-TB is the resistance to isoniazid and rifampicin, any fluoroquinolone and to at least one of three injectable second-line drugs viz, capreomycin, kanamycin, and amikacin).

According to the WHO report 2008, poor management of the supply, under-investment in TB control, and the quality of anti-tuberculosis drugs are the leading causes of the MDR-TB (World Health Organization, 2009). Poor-quality control during the drug manufacturing process is one of the most important causes of an increased prevalence of substandard and counterfeit medications such as fixed-dose combinations (FDC). These, in turn, lead to MDR-TB, toxicity, increased morbidity, and mortality in TB-infected patients (World Health Organization, 2009).

The probability of drug resistance for previously treated patients was over 4-fold while MDR-TB was 10-fold higher than for untreated patients. This significantly indicated how strong drug resistance is associated with previous treatment (Organization, 2008). Therefore, treatment of the newly infected patients and previously treated ones should be different. Currently, some drugs used against the spread of drug-resistant TB are more toxic and so have less potential and should be taken for a longer period (18 months or longer). Further, the *Tuberculosis* strains resistant to all antibiotics named totally drug-resistant (TDR)-TB was recently reported and increased worries (Migliori et al., 2012; Udwadia et al., 2012; Velayati et al., 2009) not only in the population but also in current TB treatment strategies; knowing that there is no proper treatment whatsoever available yet. Furthermore, XDR-TB is virtually untreatable using the current available anti-TB drugs (first and second-line treatments). The second-line drugs are last in line

used in TB treatment. Moreover, there are no third-line drugs reported to date. The mortality rate of XDR-TB is over 90%, and it is the leading cause of death (60-70%) in HIV/TB infected patients, according to WHO, 2006. This opens windows for researches and syntheses of new classes of anti-TB chemical structures are needed (Nayyar & Jain, 2005). Therefore, alternative strategies capable of offering the treatment with better therapeutic effects, reduced toxicity, and short courses of treatment, are highly needed.

1.4 Drug resistance among other medical conditions

Unfortunately, the phenomenon of DR has been identified in different medical conditions other than bacterial infections such as TB and HIV infections discussed above. Typical examples include a complicated case of cancer where the treatment is compromised through the complex process which, available drugs undergo to attain and deliver their therapeutic effects.

Like in bacterial infections, different mechanisms summarized in **Figure.1.3** are involved in cancer resistance; a reduced activation drug modification, partial degradation, or complexation of the drug with other molecules or proteins leads to the appearance of drug resistance.

Resistance to cancer treatment also occurs as a result of target alteration. Modification in the structure of the target protein alters how cancer cells respond to the drug and mutations in the target molecule results in a decreased activity anticancer treatment. It is also important to mention that mechanisms of drug resistance vary from one medical condition to another. However, some of these mechanisms such as drug efflux are known in cancer as well as microbial treatment. Other mechanisms through which the current cancer treatment is compromised include the DNA mutations and drug inhibition and degradation caused by metabolic changes. Drug efflux promotes cancer drug resistance by enhancing efflux which consists of pumping anticancer drugs out of cancer cells, therefore reducing the accumulation of the drug. The DNA damage, another factor that promotes multidrug resistance in cancer treatment, has been attributed to some of the chemotherapy drugs (Wu et al., 2014). The repair of the damaged DNA is a process that takes place after treatment in response to chemotherapy drugs that either directly or indirectly damage DNA. These DNA damage response (DDR) mechanisms have a clear role in anticancer intrinsic drug resistance (Wu et al., 2014).

Harmful crosslinks have been seen during the cancer treatment with chemotherapy drugs that contain platinum; a typical example of a mechanism that sometimes leads to apoptosis. The nucleotide excision repair and homologous recombination are responsible for this resistance (Housman et al., 2014; Wu et al., 2014). Other mechanisms such as Epithelial-Mesenchymal Transition and Metastasis and cell death inhibition were also detailed (Du & Shim, 2016; Housman et al., 2014).

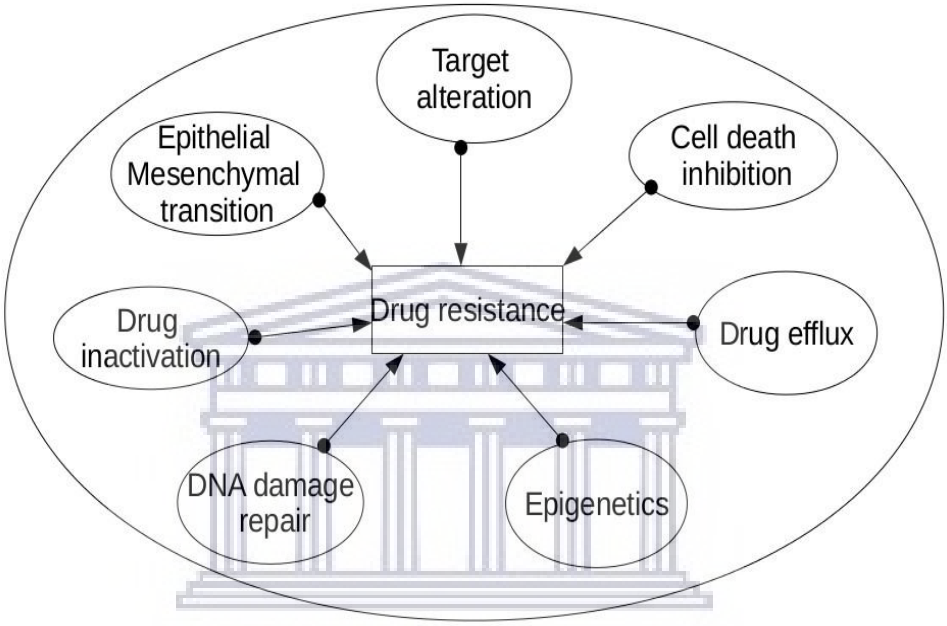

Figure.1.3: Cancer drug resistance mechanisms

Methods to overcome resistance to β-lactam antibiotics include the development of new antibiotics that are stable to β-lactamase attack and the co-administration of β-lactamase inhibitors with β-lactam drugs. Resistance to methicillin, which is stable to gram-positive β-lactamase, occurs through the alteration of an antibiotic target protein, penicillin-binding protein 2. Production of enzymes that alter antibiotic and synthesis of the bacterial target that are insensitive to an antibiotic is the primary resistance mechanism for the classes of antibiotics, such as trimethoprim, sulphonamides, aminoglycosides, chloramphenicol, and quinolone drugs (Dever & Dermody, 1991).

1.5 Drug resistance prevention principles

Physicians often prescribe combinations of medicines for the treatment and management of different medical conditions. Drug combinations generally provide an effective cure when compared to the single drug dosage forms and are often used for multiple targets. This makes drug combinations highly important (Calzolari et al., 2008;

Zinner et al., 2009). Due to this, there is an extensive increase in interest among academic researchers as well as pharmaceutical industries in developing drugs combined into single dosage forms. Drug combinations are not a new strategy in the history of medicine and pharmaceutical sciences. Generally, mixing several drugs at various doses imparts a more efficient result than single-drug remedies (Calzolari et al., 2008; Zinner et al., 2009).

Hans-Georg Breitinger indicated that with regard to the concept of the drug combination, combined forces or agents could add up, by not interacting with each other, but producing greater results or could simply lead to the less effective outcome on the other hand. The combination therapy approach has been used in the treatment of several cardiovascular diseases. Different examples include acute coronary syndrome (Al-Zakwani et al., 2011) and pulmonary arterial hypertension (B. Mukherjee & Howard, 2011).

Literature according to Herrick & Million, 2007 suggests that since several approved new chemical entities (NCEs) are in decline, reformulating the already known and tested drugs into fixed-dose combinations may provide pharmaceutical companies with an opportunity to develop new drug products and maximise returns (Herrick & Million, 2007).

Currently, the Fixed-Dose combinations (FDC) approach is one of the drug combination strategies attempted. FDCs are now available on the market. Oral drugs taken individually for the treatment of certain diseases are now formulated in one tablet (FDC) instead, therefore, reducing the pill load, and with no addition of side effects, thereby offering better compliance to the patience, simplification of prescription, reduced chances of drug resistance development and low programmatic costs (Bangalore et al., 2007; Blomberg et al., 2001; Hong, 1989; Thipparaboina et al., 2016; Walker & Burton, 2008) as well as a better anti-TB therapy delivery (WHO, 2013).

An improved pharmacological profile is the main objective of innovation in the pharmaceutical area. Combining the active ingredients with complementary therapeutic activity has been considered potential in providing therapeutic regimens in various fields of disease.

Fixed-dose combination therapy relies on a new technology flexible for formulating multilayer tablets (Abdul & Poddar, 2004; Desai et al., 2013), allowing the immediate and continuous release in a single dosage unit through separate layers (Mandal & Pal,

2008). This technology also allows the co-existence of incompatible drugs in a single dosage unit, in which they are incorporated into two layers, separating them and minimizing their interactions at the interface of the two layers.

However, the multiple excipients required in FDC maintain an undesirable large dosage form (Desai et al., 2013). Further, the delamination of the layer during the tablet compression or storage or due to an elastic mismatch increases the risk by creating different degrees of relaxation between two layers (Podczeck, 2011).

1.6 Drug combination and antiretroviral therapy

Franco Maggiolo and Sebastiano Leone reported that the use of the Highly Active Antiretroviral Therapy (HAART) might be very important in the control of the HIV epidemic due to its population-based dimension (Maggiolo & Leone, 2010). The use of this combination significantly changed the deadly HIV infection from an incurable disease to a manageable chronic illness. In the report according to Julio Montaner, HAART has not only reduced community viral load but also reduced the new HIV detections per year in the Canadian province (Montaner et al., 2010). However, it has been identified that there is the possibility of residual virus replication during this successful HAART therapy (Martinez-Picado et al., 2000).

The antiretroviral drug combinations (also known as cocktails), targeting viral enzyme RT and protease at the same time; have been used in the attempt to completely eradicate HIV replication. The diagnosis strategy HAART (Stephenson, 1997; Van Vaerenbergh et al., 2002) showed a substantial impact on saving the lives of many HIV-infected people. Nonetheless, an increase of ART drug resistance during the HAART use was reported in different areas. At least 10-15% of patients on ART treatment in Europe (Bannister et al., 2008; Booth & Geretti, 2007; Pillay & Porter, 2006; Vercauteren et al., 2009; Yerly et al., 2007) and the USA (Wheeler et al., 2010) carry viruses with at least one drug resistance mutation. The mutations in the HIV genome are causative agents of drug resistance and responsible for HIV treatment failure. These mutations also affect the immune response to the ART by reducing the HIV viruses' vulnerability to the treatment.

The rate of replication of HIV is very high (109 to 1010 virions per person per day). Together with error-prone polymerase, it is very easy for HIV to develop mutations. These mutations modify virus vulnerability to ARVs. Further, resistance to one ARV drug often imparts a decrease or a complete loss of susceptibility to others and

sometimes to all drugs of the same class (Coffin, 1995; Ferguson et al., 2002; Lloyd et al., 2014; Smyth et al., 2012).

1.7 Drug combination in Anti-Tuberculosis drugs

Due to the emergence of drug resistance in monotherapy treatment, combining antitubercular drugs was suggested as a way that can improve the treatment outcomes and suppress resistance. A typical example is the combination of isoniazid and streptomycin in the TB treatment which was further enhanced by the introduction of rifampicin later in 1970 for the suppression of resistance shown by the use of individual drugs.

Today, a standard treatment for active TB includes a combination of rifampicin, isoniazid, ethambutol, and pyrazinamide to be taken for two months after which, follows a four months course of treatment by only rifampicin and isoniazid. This provides a cure with high rates of approximately 90% in HIV-negative patients (Morris, 2009; Who, 2010).

A large number of tablets that a patient must take; usually 9 to 16 tablets per day for two months during the initial treatment, followed by 3 to 9 tablets per day for four months during a continuation phase, constitute a huge burden. However, with the application of FDCs, treatment becomes much easier, with 3 to 4 tablets per day.

Nevertheless, a reduced bioavailability was reported in rifampicin used in FDC than when individually or separately administrated among other anti-TB drugs in a combination (Laserson et al., 2001). This happens owing to the chemical reaction with isoniazid in the gastric acid environment. The reaction is favoured by the presence of pyrazinamide and ethambutol playing the role of catalytic agents (Bhutani et al., 2005; Prasad et al., 2006).

Apart from the drug combinations prescribed by physicians, chemically, one can distinguish two categories in drug combination due to whether the process was technically performed by mixing drugs in a single dosage form, the process known as drug cocktail or non-covalent interactions also known as supramolecular chemistry, a very important field of chemistry recognized by Donald J. Cram, Jean-Marie Lehn, and Charles J. Pedersen also awarded Nobel Prize for Chemistry in 1987 for their works in this particular area (Bhutani et al., 2005).

1.8 Impact of HIV/TB co-infection on current treatment

Additionally, to the other social problems aggravated by the transmission of HIV, it is evident that infection by HIV significantly increased the rate of not only new mycobacterium tuberculosis (MT) infections but also favoured the activation of latent infection (Patrick J. Brennan, Douglas B. Young, 2008).

A consistent increase in TB infections was in past years, attributed to an increase in HIV infections (Currie et al., 2003). Nearly two-thirds of TB diagnosed patients also have HIV infections (Currie et al., 2003; B. G. Williams & Dye, 2003). In addition to this, several studies reported TB as a causative agent for the progress of HIV infection to AIDS illness (Toossi et al., 2001). Furthermore, the effective treatment of TB in HIV/TB co-infected people is complicated by multidrug interactions. These interactions arise because of rifampin's potential to induce hepatic cytochrome CYP450 enzyme; a plasma concentration reducing agent for co-administered drugs metabolized through this pathway (Lienhardt et al., 2010) A typical example of consequences these interactions cause is the acquired rifampin resistance development reported among HIV-infected patients on advanced immunosuppression treated with twice a week rifampin or rifabutin based regimens (CDC, 2003). Therefore, new regimens that are safe, well-tolerated, effective in a short period and amenable to the routine programmatic condition are urgently needed. Designing new derivatives is one of the suggested solutions (Wechter et al., 1975). Despite the pressure by this quick development of drug resistance, the actual speed and effort put into this process is not enough considering the pace at which drug resistance is spreading (González-Bello, 2017b); Gonzalez, 2015).

1.9 Synthesis of drug substance using non-covalent approaches

Drug discovery has always been referred to by different scientists as an invention, creation, or synthesis of a potential therapeutic active compound. Drug discovery is an expensive, interdisciplinary and time-consuming process. It involves the identification of candidates and synthesis, characterisation, screening, and assays of their therapeutic efficiency.

The use of natural extracts for medical intention goes back to thousands of years. It is only in the 1900s with the discovery of penicillin and the introduction of synthetic organic chemistry that drug discovery has shown a significant evolution. Until 1990 synthetic chemistry remained unchanged until new approaches known as combinatory

chemistry (Chorghade, 2006). In the last few years, traditional drug discovery has evolved into a strategy called the "reductionist target-based approach". This focuses on the identification and validation of small molecules having specific activity against a specific target; (usually a protein) that has a crucial function for the phenotype of the disease.

Traditional drug discovery is a three-stage process; target identification and validation, lead identification and lead optimisation/prioritisation. Understanding of the disease mechanism using cellular and genetic approaches is crucial to identify potential drug targets. The knowledge about the aetiology of the disease and whether there are certain disease properties or phenotypes (Sawyer, 2006) may be considered as potential targets. HIV replication within T-cells is a typical example of disease targetable characteristics. The lead identification process focuses on measuring the activity of compounds towards the target identified through a set of assays specifically designed to evaluate the effect of a drug candidate on disease state improvement.

The last stage is lead optimization which simply refers to the clinical trials of the candidate where *in* vitro and *in* vivo cell-based studies are performed before being approved for further development and marketing.

Apart from traditional approaches of drug synthesis mainly based on screening compound libraries, complementary methods of computer-based molecular design (Leach, 2001) and combinatory chemistry (Balkenhohl et al., 1996) are the routine methods employed today in the lead identification and the development phases of drug design. This fulfils the idea according to Jürgen Drews that drug discovery in the 20th century was driven by chemistry in the guide through pharmacology and clinical sciences. Today, the new basics are provided by biology where molecular genetics, genomic sciences, and informatics are specifically driving forces in the generation of new pharmaceuticals (Strohl, 2000).

During the last few years, the synthesis and design of new compounds via non-covalent interactions have evolved as an alternative approach to produce entities of a wide range of utilities. The approach is based on the use of intermolecular interactions such as hydrogen bonds to generate desired supramolecules.

1.10 The aim and objective of the study

The study aimed to explore the possible combinations of the selected clinically relevant pharmacologically active drug substances, expecting the beneficial modulation of

physicochemical properties, biological activity, and pharmacokinetics of the newly modulated entities for the management of drug resistance.

The principal objective of this study was to monitor the drug resistance by the development and synthesis of new complexes from the selected ARVs and anti-TB drugs; through drug combination by co-crystallisation.

1.10.1 Specific objectives

- Screening for and non-covalently synthesise different dual-API co-crystals of selected drug candidates.
- Solid-state characterise different hybrids prepared, using a variety of analytical techniques such as Differential scanning calorimetry (DSC), hot stage microscope (HSM), thermogravimetric analysis (TGA), powder X-ray diffraction (PXRD), scanning electron microscope (SEM), and the solid-state NMR.
- Evaluate the *in vitro* solubility of the all self-assembly hybrids produced using HPLC quantification methods.

1.11 Significance of the study

The loss of efficiency of different antibiotics/anti-HIV drugs due to drug resistance is of great concern. Microorganisms are now able to replicate in the presence of the drug. Drug resistance still emerges in some combination therapy regimens and is the main cause of treatment failure in some cases. In an attempt to prevent this threat and eradicate pathogen replication completely, alternative treatment strategies are highly needed. In this study, we use the non-covalent approach of drug combination as a way to optimize the efficiency of drugs and overcome different treatment difficulties. This approach may not only exhibit a tremendous impact on drug resistance but also contribute to the drug efficacy restoration.

1.12 Selection of the drug candidates for the study

For this study, four antiretroviral drugs; nevirapine, lamivudine, efavirenz, and zidovudine were selected from the ARV regime guidelines found in the South African Standard Treatment Guideline (SASTG) in the Primary Health Care System (Bhatt et al., 2008, 2009a). The anti-tuberculosis drugs; isoniazid and pyrazinamide considered as first-line anti-TB drugs were selected for their potential activity against *M.Tuberculosis* and were used for co-crystals formation as well. In addition to these,

amantadine free base was also selected due to the antiviral and neurodegenerative activities of the amantadine ring.

1.13 Methodology and analytical techniques

Techniques such as co-precipitation (solvent evaporation), dry grinding, solvent-assisted grinding, freeze-drying, vapour diffusion, sublimation, were employed to prepare different combination systems (Bannister et al., 2008) for co-crystallisation.

A variety of analytical techniques were used to characterise the prepared products.

Thermo-analysis was conducted on a differential scanning calorimetry (DSC), Hot Stage Microscopy (HSM) and Thermogravimetric analysis (TGA). Powder X-ray diffraction (PXRD), Fourier-Transform Infra-Red Spectroscopy (FTIR), Scanning Electron Microscopy analysis (SEM) and the Cambridge Structural Database (CSD) was used for structural elucidation. Solubility studies were performed on the synthesized compounds.

Finally, *in vitro* antimicrobial activity of the newly formed anti-tuberculosis compounds was evaluated.

1.14 Ethical clearance

No ethical clearance was required to conduct this study since no human or animal studies were required to achieve the aims and objectives of this study.

Chapter 2 Co-crystal theory

This chapter describes the concept of co-crystallisation as a systematic approach to enhance the physicochemical properties of active substances, targeting pharmaceutical co-crystals. The history of co-crystallisation is explored; offering a few clear and concise definitions of the concept. Then pharmaceutical co-crystals are highlighted, and several key issues including design strategies, preference over other techniques and methods are discussed. The chapter ends with particular emphasis on multidrug co-crystals, demonstrating the use of co-crystallisation as a tool not only to enhance physicochemical properties of drugs but also synthesise multidrug pharmaceutical co-crystals and other hybrids with synergistic benefits.

2.1 Introduction

Less than 1% of active pharmaceutical ingredients (APIs) reach the market because of poor biopharmaceutical properties among which solubility plays a key role (Qiao et al., 2011). Poor physicochemical properties of APIs such as chemical stability, dissolution, hygroscopicity, and solubility impact therapeutic efficacy (Bavishi & Borkhataria, 2016). This, in turn, leads to treatment failure and the development of different side effects, if not monitored. Poor physicochemical properties affect not only the performance of a drug substance but also impact formulation strategies and other post-formulation processes such as absorption, distribution, metabolism, and excretion, which may lead to adverse effects and toxicity (Garnero et al., 2017; R. Maheshwari et al., 2018; Van Hoogevest et al., 2011). Pharmaceutical scientists strive to find a better strategy to improve the properties of the APIs owing to their therapeutic potency, without compromising their chemical identity. Various methods have been developed and used to enhance the physical properties of pharmaceutical ingredients. Commencing with a supramolecular perspective, these include the formation of the amorphous state, polymorphs, hydrates, salts, solvated forms of drugs and the formation of pharmaceutical co-crystals/complexes (Karagianni et al., 2018b).

A co-crystal is a single crystalline material consisting of at least two molecular components usually solid at room temperature and present in a definite stoichiometric ratio (Daingade et al., 2019). A broad definition as per the Indo-US meeting in 2011 refers to co-crystals as single-phase solid crystalline materials composed of at least two

different molecular and/or ionic compounds that are neither solvates nor simple salts and exist in a stoichiometric ratio. Other co-crystal definitions as per different authors were reported (Schultheiss & Newman, 2009a).

According to different literature, co-crystal formation enables the modification of fundamental physicochemical properties of pharmaceuticals such as solubility and stability towards better thermal stress, humidity stress, dissolution rate and compressibility (Aher et al., 2013; Babu & Nangia, 2011; Bethune et al., 2011; Bolla et al., 2013; Good & Rodriguez-Hornedo, 2009; Goud et al., 2012; Hickey et al., 2007; Jones et al., 2006; Sanphui et al., 2011; Shan & Zaworotko, 2008; Tao et al., 2012; Thakuria et al., 2013; Trask et al., 2005; Vangala et al., 2011; Vishweshwar et al., 2003). Henceforth, the co-crystal formation of drug substances offers a great opportunity to develop drug products with better physicochemical properties without changing the pharmacological properties of the API. Due to this, there has been a very intense desire to design co-crystals for different applications which eventually make co-crystallisation a preferred technique in pharmaceutical sciences (Najar & Azim, 2014; A. V Yadav et al., 2009). Other physical properties such as hygroscopicity, stability, crystallinity, particle size, flow, filterability, density, and taste, which may be changed as well, preferably improved by co-crystallisation, leading to a better therapeutic effect (Childs et al., 2007). Interestingly, even though Friedrich Wohler solved the first co-crystal structure in 1844, it is only in the present century that co-crystals have attracted much attention.

2.2 Pharmaceutical co-crystal definition

Based on the definition given in section **Error! Reference source not found.**, a co-crystal is a multi-component molecular complex non-covalently bonded, in which one molecule is neutral and the second component is termed the co-former. A "pharmaceutical co-crystal" is made of an API and a co-former. The latter is either an ionic or a neutrally safe inactive chemical selected from the Generally Regarded as Safe substance (GRAS) list mostly provided by the United States Food and Drug Association list (FDA), or it could be another API (Smith et al., 2013; Sun, 2013). Both co-crystal components are solid at ambient temperature and present in known stoichiometric amounts (Aakeröy & Salmon, 2005). Co-crystallisation of the API with pharmaceutically acceptable co-crystal formers has gained increasing attention due to

the abilities of this approach to achieve a complex without altering the chemical structure or nature of both drug components (Asija et al., 2013).

2.3 Co-crystal properties

Properties of a co-crystal depend mostly on the selected co-former (Fukte et al., 2014; Nauha, 2012) and the types of intermolecular interactions formed during the co-crystallization process. This is one of the advantages of co-crystal synthesis over other techniques used to improve the physicochemical properties of the drug substance (Nauha, 2012) among which salt formation, micronization, and amorphisation are found.

Pharmaceutical co-crystal formation involves APIs forming non-covalent bonds with co-formers or other APIs. The presence of either hydrogen donor or acceptor groups on molecules forming a co-crystal is fundamental because the best donor generally associates with the best acceptor in the crystal structure (Remenar et al., 2003; Vinesh et al., 2013).

The hydrogen donors or acceptors are functional groups such as amide, primary and secondary amine, carboxylic acid, hydroxyl groups, thioester, thiazole, and others. Different properties of a co-crystal such as melting point, physical and chemical stability, solution stability and crystallinity, dissolution and bioavailability, have been thoroughly discussed in the literature (Karagianni et al., 2018b; Jean Baptiste Ngilirabanga, 2014; Schultheiss & Newman, 2009b).

2.4 Co-former selection and co-crystal design

The selection of a co-crystal former compatible with an API is a crucial step in the co-crystal design but also one of the challenges faced during the co-crystal formation process. The general strategy used in co-former selection is by trial and error also known as a tactless approach during which a number of the pre-determined pharmaceutical library of acceptable compounds (drugs found in General Regarded as Safe (GRAS) FDA list of drugs) are used in the co-crystallisation attempt.

A co-crystal is considered strategically on the following basis: when a co-former has a complementary functional group(s), that can join to the drug candidate through supramolecular synthons by means of intermolecular interactions (Fukte et al., 2014). Properties (mainly physical and chemical) of the produced co-crystal depend on the co-

crystal former used. This makes the selection of co-crystal former a paramount step in the co-crystal synthesis process. When the co-crystal former is selected from the US-FDA GRAS list any drug excipient, neutral, acid or base, is safe according to this list and can be considered. Further, pharmaceutically accepted salts are also used as co-formers (Schultheiss & Newman, 2009b) and result in multicomponent salts or co-crystal salts where there is a partial transfer of proton and formation of intermolecular interactions at the same time.

A co-crystal former may also be another active pharmaceutical ingredient (API). However, the selection of such substances should fulfil certain criteria, with the intention to improve properties and biological activity of either or both active(s) in the co-crystal system. APIs with polymorphic properties have been used as co-crystal formers. Such combinations offer better stability to the system components. This is one of the techniques used to prevent unwanted polymorphs which most of the time come with serious effects in terms of drug performances (Aitipamula et al., 2009). Compounds which crystallize with more than one molecule in the crystallographic asymmetric unit (Z 0 >1) have also been suggested as good co-crystal formers (Aitipamula et al., 2009). Amorphous compounds are another class of drugs that have been proven relevant as co-crystal formers due to their enhanced solubility profiles (Anil Kumar Kruthiventi, Saikat Roy, Rajesh Goud, Iqbal Javed, Ashwini Nangia, 2009).

Despite their poor bioavailability, nutraceuticals which by definition refer to food or part of food that provides medical or health benefits and an ability to prevent and be used as a treatment of a disease can also be used as co-formers (Nasri et al., 2014; Télessy, 2018). Therapeutic effects associated to these drugs is a target for solid-state chemists and when co-crystallised with APIs would enhance physicochemical properties, stability, solubility as well as bioavailability of drug product (co-crystal or hybrid) and generate priceless and cost-effective synergistic hybrids, being affordable and easily attainable (Sinha et al., 2015). This also reflects their structures offering robust supramolecular synthons (Thipparaboina et al., 2016). This substantial degree of freedom to select co-formers and the subsequent diversity of the co-crystals has made co-crystallisation very attractive as a method to fine-tune properties of APIs.

A few examples of such drugs that have been previously used in co-crystal formation have been reported (Thipparaboina et al., 2016). In addition to the synergistic effects of nutraceutical-API combinations, these drugs may also play a crucial role in interconnecting APIs in a multi-drug crystal lattice. The use of nutraceuticals has been reported; flavonoids and vitamins are examples of nutraceuticals investigated and used as co-crystal drug candidates to enhance physicochemical properties and bioavailability (Sekhon, 2012). Systematically, the choice of co-former is usually based on a supramolecular approach, according to Thakuria *et al.*, 2013.

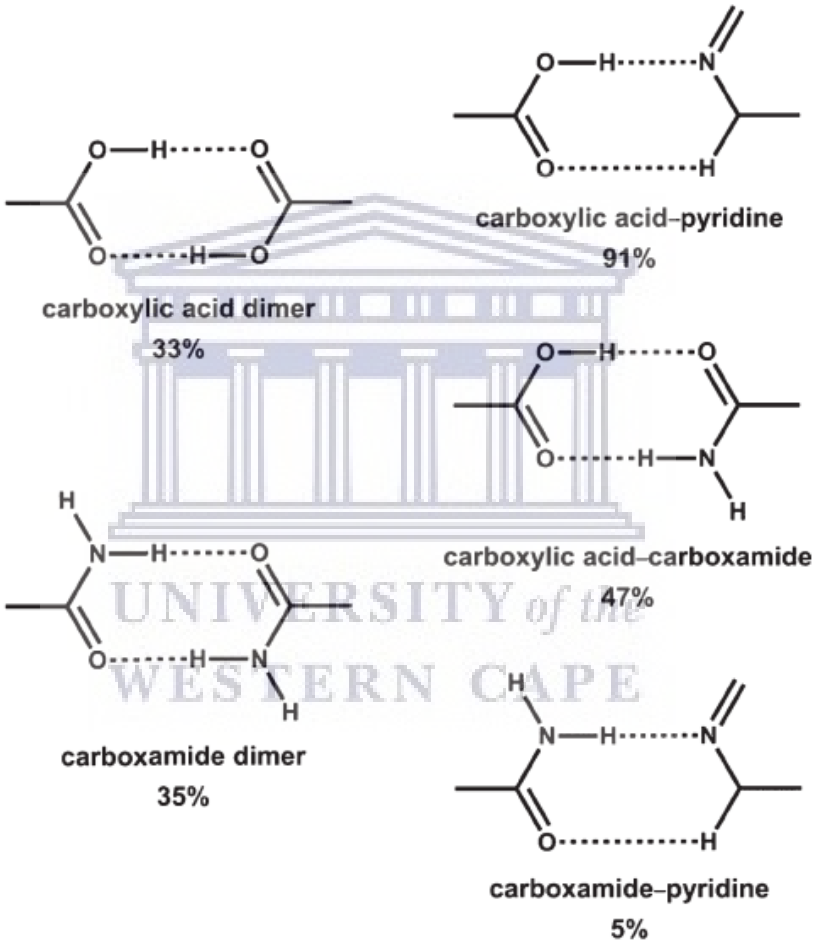

Figure 2.1: Supramolecular synthons and their occurrence percentages based on the Cambridge Structure Database (CSD). On the left are common homosynthons; acid-acid or carboxylic acid dimer and amide-amide homosynthon or carboxamide dimer. On the right are regular heterosynthons; carboxylic acid-pyridine, carboxylic acid-carboxamide, and carboxamide-pyridine heterosynthon (Cherukuvada et al., 2016)**.**

According to Duggirala *et al.* (2016), property optimisation of drug substances was the main goal of crystal engineering scientists in the co-crystal design. Authors established

that the design and synthesis of co-crystals rely exclusively on the presence of supramolecular synthons. It has been demonstrated that co-crystals with strong hydrogen interactions are designed based on the supramolecular synthons approach. These supramolecular synthons are referred to as structural units within supermolecules that can be formed and/or assembled by known or conceivable synthetic operations involving intermolecular interactions. In a crystal system, supramolecular synthons are the smallest structural units within which is encoded all information inherent in the mutual recognition of molecules to yield that crystal (or solid-state supermolecules) (Friščić & Jones, 2010; D. S. Reddy et al., 1996).

Just like the known reactants to make specific covalent bonds, the choice of a synthon which is likely to form during a crystallisation process is crucial. Examples of such synthons are depicted in **Figure 2.1**. A crystal structure is simplified as a network in which molecules are seen as nodes and molecule synthons as connectors of those molecules (Desiraju, 1995; Desiraju & others, 2001; D. S. Reddy et al., 1996). In most cases, hydrogen bonds (H-bonds) due to their strength and directionality compared to other intermolecular forces are involved in synthons. However, this doesn't withstand the contribution of various other intermolecular forces such as halogen bonds, π–π interactions in aromatic structures, stacking interactions and van der Vaal interactions as these contribute to the final results of crystallisation (Nauha, 2012) as well as a significant role in the co-crystal formation (Vinesh et al., 2013).

A very good understanding of synthons is also paramount for a better selection of co-crystal formers. The co-crystal design also requires a good understanding of the intermolecular interactions. Intermolecular interactions as described by Dunitz (2009) are the fundamental basis of supramolecular chemistry. He also described these weak interactions as what keeps the organic world together (Dunitz & Gavezzotti, 2009), (Thakur et al., 2015). Interactions such as hydrogen bonding, π–π stacking, electrostatic, hydrophobic, charge transfer, metal coordination, halogen bonding, and metallophilic interactions interconnect molecules in the lattice via different supramolecular synthons discussed in the previous paragraphs. Molecular recognition (which is a necessary complementarity between molecules forming an aggregate) is compulsory in this formation and stabilisation of supramolecular systems. In such entities, these interactions are like bridges between molecular building blocks (Albrecht, 2007).

Among these interactions, ***H-bond*** is predominant and most explored mainly due to its directionality. Its natural existence (ubiquitous), from just a drop of water, DNA to large supramolecular assemblies (Aakeröy & Sinha, 2018)(Bhattacharya et al., 2018). According to the IUPAC Recommendations 2011, H-bonds are attractive interactions between a hydrogen atom from a molecule or molecular fragment X–H in which X is more electronegative than H, and an atom or a group of atoms in the same or a different molecule, in which there is evidence of bond formation (Arunan et al., 2011). The commonly known strong hydrogen bonding in solid materials such as co-crystals is O–H···O, N–H···O or O–H···N; **Figure 2.2** illustrates this type of interactions. The weak hydrogen bonding, include C–H···O, C–H···N, and N–H···π.

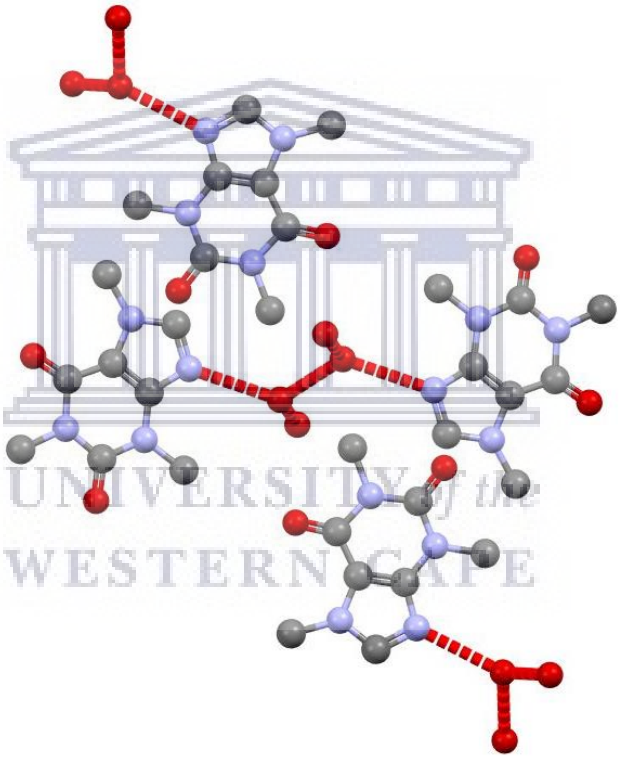

Figure 2.2: Example of O–H...O H-bonding between acetaminophen and oxalic acid space group P21/c shown alongside b-axis

Attraction dispersive and (or) inductive forces between molecules promote the formation of interaction known as "***Van der Waals***". These forces are responsible for the formation of solid dispersions.

Molecules containing halogens such as Fluorine tends to form halogen bonding interactions during the self-assembling process. According to Desiraju *et al.* (2013), a ***"halogen bond***" occurs when there is evidence of a net attractive interaction between

an electrophilic region associated with a halogen atom in a molecular entity and a nucleophilic region in another, or the same, molecular entity. The halogen bond is also characterised by its directionality, strength, polarity, hygroscopicity, donor-atom dimension and its tunability (Andree et al., 2018).

Other intermolecular interactions include **C–H···π** weak bond that plays an additional or secondary role in molecular recognition, therefore reinforcing interactions such as hydrophobic effects. An example of how important this kind of interaction is seen in the non-polar hydrocarbon encapsulation. These hydrocarbons are accommodated and in the capsule-like host and tumbled by C-H···π bonding forces (Matsuno et al., 2018). The type of hydrogen bonding and other interactions between molecules in the co-crystal is determined by the type of supramolecular synthons available.

Furthermore, an API with abundant hydrogen bonding sites and molecular flexibility may be manipulated by a proper choice of solvent to form a specific form of crystal possessing a different arrangement and conformation to the original crystal lattice (Bhatt et al., 2008). In fact, the change of molecule arrangement in the crystal lattice leads to modified solid-state properties affecting its solubility, dissolution, stability and ultimately bioavailability. Therefore, different crystal forms can lead to changed biological activity (lower or higher than desired) (Sekhon, 2012). For co-crystals produced by solution crystallisation methods, two components must have similar solubility in a chosen solvent; otherwise, it is unlikely to produce a co-crystal. This is because the difference in solubility will lead to the precipitation of the least soluble part, leaving the other component in the solution (Aakeröy & Sinha, 2018).

2.5 Co-crystal classification

Even though co-crystal classification should primarily depend on the useful nature of component drugs, scientists and researchers approach this issue by overseeing the content of the structure rather than their utility. This is due to the diversity of co-crystals and their wide range of uses which include but not limited to medicinal or pharmaceuticals, mineral, agrochemistry, engineering, crystallography, and energy (Braga et al., 2010; Karimi-Jafari et al., 2018).

Based on factors such as the number of component molecules in the crystal structure and presence in the structure of an ion, polymorph, water, or solvent, one can divide co-crystals into two main classes:

Class 1 includes "**binary co-crystals**"; the two components single solid crystalline substances designed based on hydrogen bonding propensity, supramolecular synthons, Hansen solubility parameters, pKa values (Sandeep & Arun, 2018). Typical examples of this type are pharmaceutical co-crystals where one structural component is an active pharmaceutical ingredient and the second being a co-former selected from the United States Food and Drug Administration (US-FDA) list of generally regarded as safe (GRAS) drugs. The binary co-crystal class is further divided into two groups depending on whether molecules in the crystal lattice are hydrogen or halogen-bonded (Aakeröy & Sinha, 2018).

"**Ternary** and **quaternary co-crystals**" respectively composed of three and four neutral drugs arranged in a definite stoichiometry in their crystal structures. Using isoniazid and nicotinamide, Aitipamula *et al.*, 2013 produced two tertiary co-crystals using fumaric and succinic acid. In both cases, hydrogen bonding occurs via pyridine-acid synthons (Aakeröy & Salmon, 2005; Sandeep & Arun, 2018). Synthesis of such multi-component solids provides an opportunity to explore the combination of drugs usually administered separately, aiming at different targets or drugs having synergistic effects. Other examples of this type were reported in a book by Aakeröy & Abhijeet S. Sinha, (2018).

The second class of co-crystals includes **Polymorphic co-crystals**: Investigation on different polymorphic forms of a particular compound is common in solid-state pharmaceuticals and solid-state chemistry. Investigating polymorphism is crucial during drug development because polymorphic forms exhibit different physical and chemical properties. The future or safety post-manufacturing of a drug formulation depends on how well this step was explored. Just like any other chemical entities, identifying all possible forms during the development of a co-crystal is paramount.

Even though co-crystallisation has been attributed to reducing polymorphism propensity (Sekhon, 2012; A. V Yadav et al., 2009), polymorphic co-crystals have been reported (Aitipamula et al., 2014). Different polymorphic co-crystals of the same drug exhibit different physicochemical properties (Babu et al., 2008). Polymorphism in co-

crystals is promoted by different factors, among which co-crystallised drugs belonging to families with a polymorphic history or use of polymorphic co-formers (Lemmerer et al., 2013) being the primary. Compounds that exhibit polymorphism also enable the formation of heteromeric intermolecular interaction with co-former molecules (target molecules) over monomeric interactions and allow the existence of different molecules in the same crystal lattice, theoretically making them possible good co-crystallising agents (Aakeröy & Salmon, 2005). However, only practically, this can be proven.

It is therefore important to investigate these aspects with vigilance as the outcomes may be catastrophic for a pharmaceutical company if an unwanted polymorph is formulated. An example of co-crystal polymorphism was observed when a chloroform solution of caffeine and glutaric acid was allowed to evaporate slowly and two polymorphs having different morphologies rods (form I) and blocks (Form II) were produced (Trask et al., 2005).

Salt co-crystals: Before the introduction of co-crystals, the salt formation was among the approaches used to modify the physical properties of APIs. This is evidenced by statistics approximating that over half of the medicines on the market are administered in salt forms (Schultheiss & Newman, 2009a). Salt formation suffers from the limitation that only compounds/APIs with an ionisable site are fit to be processed.

Formation of co-crystals involving ionic substances was introduced after the discovery of polymorphic forms (neutral and zwitterion forms) of piroxicam-4-hydroxybenzoic acid co-crystal (1:1, v/v). Different salt co-crystals, also known as ionic co-crystals, have been reported (Wang et al., 2018). Salt/ionic co-crystals were also previously synthesised and identified using bis(1-adamantylaminium) carbonate with neutral mono and dicarboxylic acids as co-crystal formers (Jean Baptiste Ngilirabanga, 2014).

Solvated/hydrated co-crystals constitute another type of co-crystals in which solvent/water molecules are part of a crystal structure. In some cases, these guest molecules are what keeps a crystal together, and collapse upon desolvation or solvent/water molecule removal. Different examples of such co-crystals have been reported (Bhatt et al., 2009b; Lange & Sadowski, 2016).

2.5.1 Other co-crystallisation outcomes

Co-crystallisation doesn't always produce co-crystals, solid forms such as eutectic mixtures, salts, hydrate/solvates, ionic liquids, solid dispersions, solid solutions and supramolecular gelators can sometimes result from the co-crystallisation process (Sathisaran & Dalvi, 2018). Factors such as the nature of the components, environment (solvents, temperature, pH) contribute to the occurrence of these adducts (Cherukuvada et al., 2016).

Hydrate/solvate formation commonly occurs when water/solvent molecules are incorporated into the crystal lattice (Healy et al., 2017). The presence of this may significantly contribute to molecular networks within a crystal and sometimes these entrapped solvent molecules are what hold the crystal molecules together (this is the case of polymorphic solvates when solvent molecules are an integral part of the crystal structure) and the crystal collapses upon desolvation which eventually results in a disordered system known as a solid amorphous form (Boothroyd et al., 2018). Alternatively, the solvent molecules fill the voids in the crystal and can be easily removed by desolvation without affecting the crystal structure. This is the case of pseudopolymorphic solvates (Byrn et al., 2017). A particular example is that of caffeine where hydration maintains the order in both its polymorphic crystals. Before co-crystallisation with water, molecules in both polymorphs lacked order (Cherukuvada et al., 2016). The Cambridge Structural Database (CSD) indicates the solvation ubiquity of 43% among organic crystals reported (Groom et al., 2016).

It sometimes happens that instead of a co-crystal, drugs (i.e. APIs) combined via co-crystallization result in what is known as eutectic mixtures (**EM**) (Zaini et al., 2015) or solid dispersions. **Eutectic Mixtures** (EM) are multi-component solids that are recently gaining much interest of researchers in the pharmaceutical field. EM are obtained as a result of the failed co-crystal formation. Due to an increased number of researches in pharmaceutical co-crystals, several pharmaceutical eutectics are likely to increase even more (Sathisaran & Dalvi, 2018).

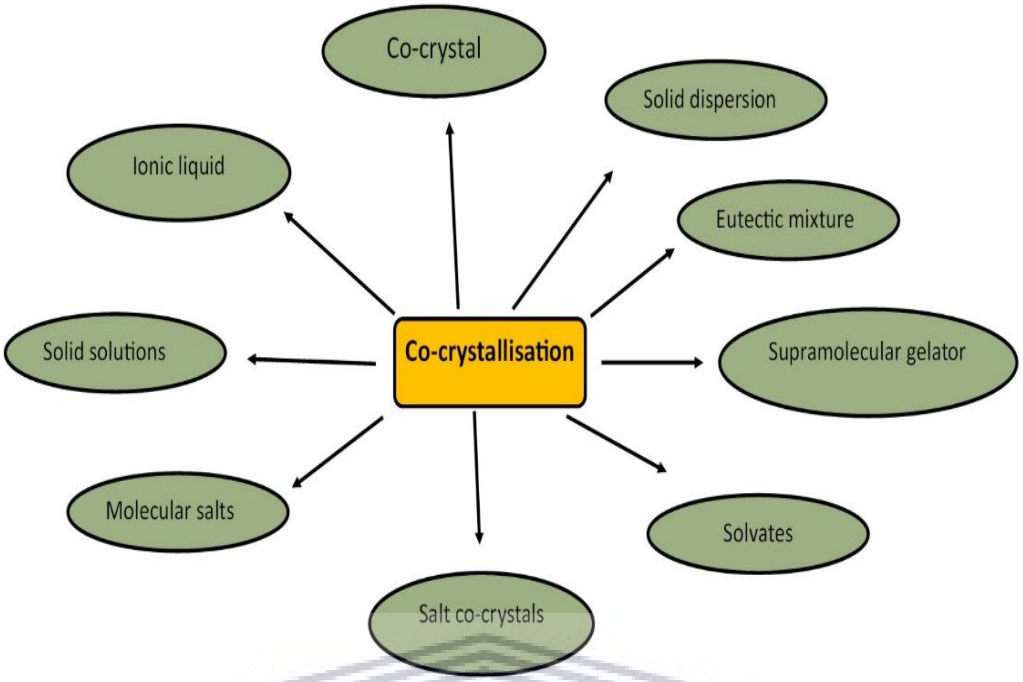

Figure 2.3: Different co-crystallisation solid forms based on Cherukuvada et al. (2014) discussion

Based on the definition according to Cherukuvada and Nangia, (2014), **EMs** are conglomerates of solid solutions in which similar molecules are held together by strong cohesive interactions whereas unlike ones are bound by weak adhesive forces. However, this class of multicomponent solids lacks a distinct crystal structure despite the above interactions binding their molecules together. Instead, their crystalline nature resembles that of parent compound combinations (this can be easily justified by the similarities between diffraction patterns). Furthermore, eutectics are thermally characterised by lower melting points than that of their drug components intact and they present themselves as important in enhancing the physicochemical properties of the drug components (API(s) in case dual drug) as their co-crystals counterparts (Cherukuvada & Nangia, 2014). Other solid forms which may be resulted from co-crystallisation but which won't be discussed here include those summarised in **Figure 2.3**.

2.5.2 The co-crystal development pathway

The development pathway of pharmaceutical co-crystals has been encompassed into eight stages (**Figure 2.4**) (Duggirala et al., 2016).

Co-former identification: Initially, a complementary co-former to a drug molecule candidate is selected from a library (dependant on the type of co-crystal to be synthesised). In the case of pharmaceutical co-crystals, the co-former is selected from a generally regarded as safe (GRAS) list provided by the FDA and Everything Added to Food in the United States (EAFUD) list approved by the FDA (Frestedt, 2018; Nutrition, 2009).

Discovery: A stage during which co-crystal synthesis is carried out. Methods such as slow solvent evaporation, slurry mediated transformation and mechanical grinding (both neat and solvent-drop or liquid assisted) are used. Other methods used during co-crystal screening are also identified (Duggirala et al., 2016).

Characterization: A stage during which physical and chemical properties are assessed is carried out using different techniques. Differential scanning calorimetry (DSC), thermogravimetric analysis (TGA), infrared and Raman spectroscopy, powder X-ray diffraction (PXRD), single-crystal X-ray diffraction (SCXRD), and solid-state nuclear magnetic resonance (ss-NMR), are used to characterise novel co-crystals (Izutsu et al., 2016; Pindelska et al., 2017).

Properties: This was described as a stage during which further steps would be decided.

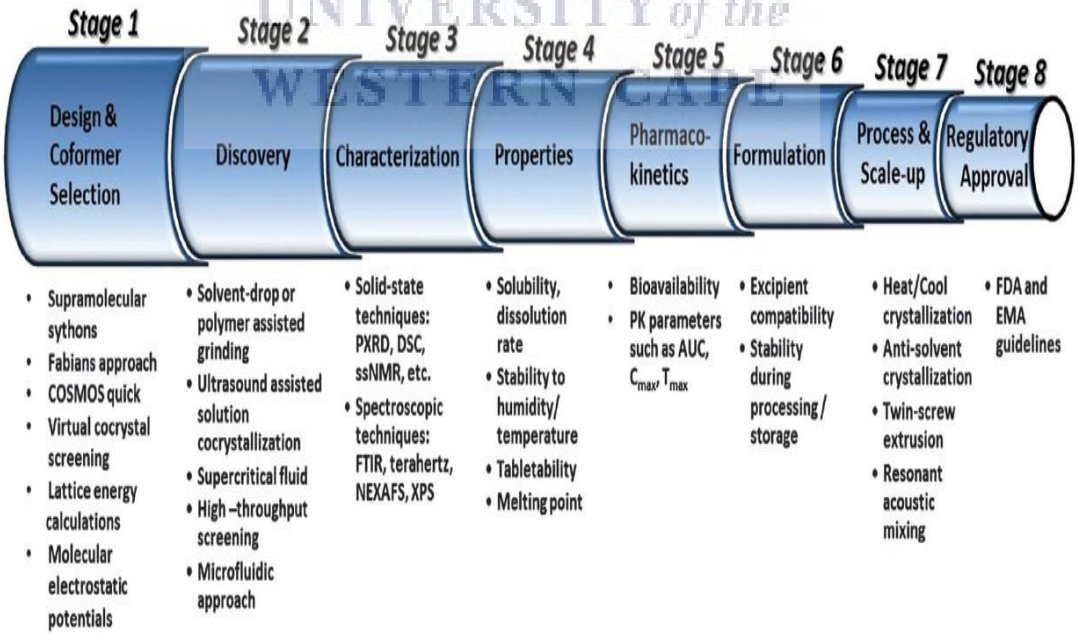

Figure 2.4: Co-crystal development pathway according to Duggirala et al. (2016)

Evaluation of pharmacokinetics: Evaluating pharmacokinetics (Pk) of a drug is a crucial step in drug development. The drug performance and drug-action site flow are explored during this stage. It is based on this that the route of drug administration and the dose for any medication is determined. Pk is often defined as a study of processes such as drug absorption, distribution, metabolism, and elimination from a patient's body. Changes in physicochemical properties which supramolecular systems such as co-crystals deliver, result from changes in thermodynamics of APIs. These, in turn, affect not only drug bioavailability but also the Pk of a drug through processes outlined in the previous paragraph (timely exploring but not limited to the drug quantity (concentration) in biological fluids, tissues, and excreta (Shan et al., 2014).

Different studies witnessed improved pharmacokinetics of APIs by co-crystallisation. Of these, the study according to Dooner *et al.*, 2019, reported increased pharmacokinetics of both APIs in Tramadol-Celecoxib co-crystal. Other examples include those highlighted by Duggirala *et al.* (2016). Therefore, evaluating the Pk of a new drug substance and new delivery systems such as the co-crystal is an important step in the development process of a drug.

Formulation: The formulation of a co-crystal in a dosage form is not a straight forward process. Held together by hydrogen bonds co-crystals stability in the presence of excipients that also contain hydrogen bonding groups becomes a major concern and presents a great risk. Choosing the right excipients is paramount to minimise the possible source of interactions with the co-crystal (Duggirala et al., 2016).

The stability of co-crystals into formulation is of major concern. This is because co-crystals are stabilised by H-bonds and the risks associated with the use of excipients already containing H-bonds are high, especially those excipients designed to enhance properties of a drug in the formulation.

Further, pharmaceutical co-crystals, having enhanced physicochemical properties, behave differently from their pure API. Regardless of the H-bonds-dependant stability, it requires an adjustment and manipulation of the excipients, the amount of API required to produce the same activity, and a change of the formulation method where necessary (Duggirala et al., 2016; Panzade et al., 2017).

Additionally, more studies are needed to address issues encountered during pharmaceutical co-crystals formulation. The use of examples to explore the implication of co-crystal in the formulation stage doesn't draw a steady conclusion. Nonetheless, different examples have been used to explore risks associated with the formulation of pharmaceutical co-crystals (Duggirala et al., 2016).

Process and Scale-up: Scale-up of the co-crystal produced by traditional solution methods of co-crystallisation such as solvent evaporation and slurry, present challenges. Good quality co-crystals are obtained from solution crystallisation, a method usually used to purify chemical substances such as APIs. Not only is there a problem of solvent cost and solubility of the individual component but also the tendency to crystallise which is different for these components to reduce the chances of reproducing the same co-crystals with the desired yields (Gagnière et al., 2011).

For many co-crystals prepared using simple and common solid-state approaches known as mechanochemical approaches, there are challenges with required high mechanical stress and the difficulty in achieving a homogeneous final product for larger-scale processes. Nonetheless, alternative methods such as extrusion (twin-screw) and resonant acoustic mixing can help prepare large volumes and only require the addition of small amounts of solvent during the process (Chavan et al., 2018; Duggirala et al., 2016; Malamatari et al., 2017).

Finally, there is regulatory approval and patenting stage during which a co-crystal undergoes different evaluations for patenting purposes. Initially, intellectual property protection must be ensured. Pharmaceutical co-crystals fulfil three primary criteria for issuing a patent. These are a novelty, non-obviousness, and utility (the drug substance has pharmacological activity and/or improved performance vs the corresponding single component drug substance) and so can be patented (Duggirala et al., 2016; Steed, 2013a).

Co-crystallisation methods

There are different methods used successfully for co-crystal preparation. Some of these have been used for decades while others were recently introduced following the intensive growth in co-crystal applications and commercialisation. Karimi-Jafari *et al.*, 2018, reviewed old as well as new co-crystallisation methods.

Conventional methods such as solvent evaporation, slow cooling evaporation, vapour diffusion can be grouped into solution crystallisation, whereas other methods include grinding (either solid-state, or liquid-assisted), slurry conversion, melt crystallisation, hot-melt extrusion, and spray crystallisation. With new advances in technology, different methods are now available and summarised in five classes according to Karimi-Jafari *et al.* (2018): solid-state, solution-based, supercritical fluid and miscellaneous co-crystal preparation.

2.5.3 Solid-state co-crystal preparation

Solid-state methods use different mixing exercises and manipulation of target drug and the co-former in their powder or crystalline form to produce co-crystals. Partial wetting of the samples may be required for some of these methods (Karimi-Jafari et al., 2018; Trask & Jones, 2005).

2.5.3.1 Contact formation of the co-crystal

This is a spontaneous formation of the co-crystal upon gently mixing the API and co-former without any physical application of force. According to Maheshwari et al. (2009), such spontaneity requires changes in free energy evaluated from solubility and equilibrium constants (C. Maheshwari et al., 2009). Various examples have been given. Results obtained were not all in agreement with thermodynamics of the samples, it was then indicated that the co-crystallization rate can also be affected by other factors such as diffusivities, molecular mobility, molecular interactions and surface interactions (C. Maheshwari et al., 2009) in addition to high temperature and relative humidity (Karimi-Jafari et al., 2018).

2.5.3.2 Solid-state grinding methods of co-crystal preparation

The most popular solid-state methods; dry (neat) grinding (DG) and liquid-assisted grinding (LAG) have been widely used in co-crystal preparation. Both DG and LAG are what constitute solid-state grinding also known as mechanochemistry; a method developed as an alternative to solution-based methods of co-crystal preparation. This method is simple, green, reproductive, clean, reliable and yield is imminent which is advantageous over solution-based methods (Abidi et al., 2017; Braga et al., 2013)

Dry grinding (DG) uses pressure generated manually (using a mortar and pestle) or by mechanical forces created by an automated ball mill to combine the target drug and the co-former. Usually, sample preparation using this technique is carried out at room

temperature. Where an automated ball mill is used, the temperature must be monitored and recorded to address any changes if any and reported. Despite its effectiveness, simplicity and other advantages, DG is associated with failure or incomplete conversion to co-crystal and possible generation of unstable amorphous form as a result of crystal defect (Friscic & Jones, 2009; J. L. Howard et al., 2018; Karimi-Jafari et al., 2018).

Liquid-assisted grinding **(LAG)** refers to grinding assisted by the addition of a very small amount of solvent to the mixture at the beginning and during the grinding process. The solvent places a catalytic role, therefore accelerates and promote the formation of the co-crystal. Different co-crystals have been produced using LAG (Friscic & Jones, 2009; Karimi-Jafari et al., 2018).

2.5.4 Extrusion

Extrusion, a relatively new method uses a twin-screw extruder to simultaneously mix and pressing the starting material or a mixture of starting materials through a die under a controlled environment. Unlike Hot melt extrusion which involves melting the samples and mixing at high temperatures (Gajda et al., 2019; Sarabu et al., 2019), here the process is maintained below the melting temperature of either content of the sample being processed (Karagianni et al., 2018a). Different co-crystals were reported to have been produced by the Twin-screw extrusion method (Karimi-Jafari et al., 2018).

2.5.5 Solution-based co-crystal preparation

The co-crystal preparation from solution requires supersaturation of the target drug and co-former; followed by the nucleation process, then the crystal growth. Good care and conditions must be established to ensure the thermodynamic stability of the co-crystalline suspension (sample containing solution).

Apart from the conventional methods outlined at the beginning of this section, solvent-mediated and precipitation can also be used to produce co-crystals. Further, the majority of co-crystals reported in the Cambridge structural database were produced by solution co-crystallisation. (Karimi-Jafari et al., 2018; Leyssens & Ter Horst, 2017) A particular example is that of carbamazepine (CBZ) an anticonvulsant with para-aminosalicylic acid (PASA) an antitubercular (**Figure 2.5**).

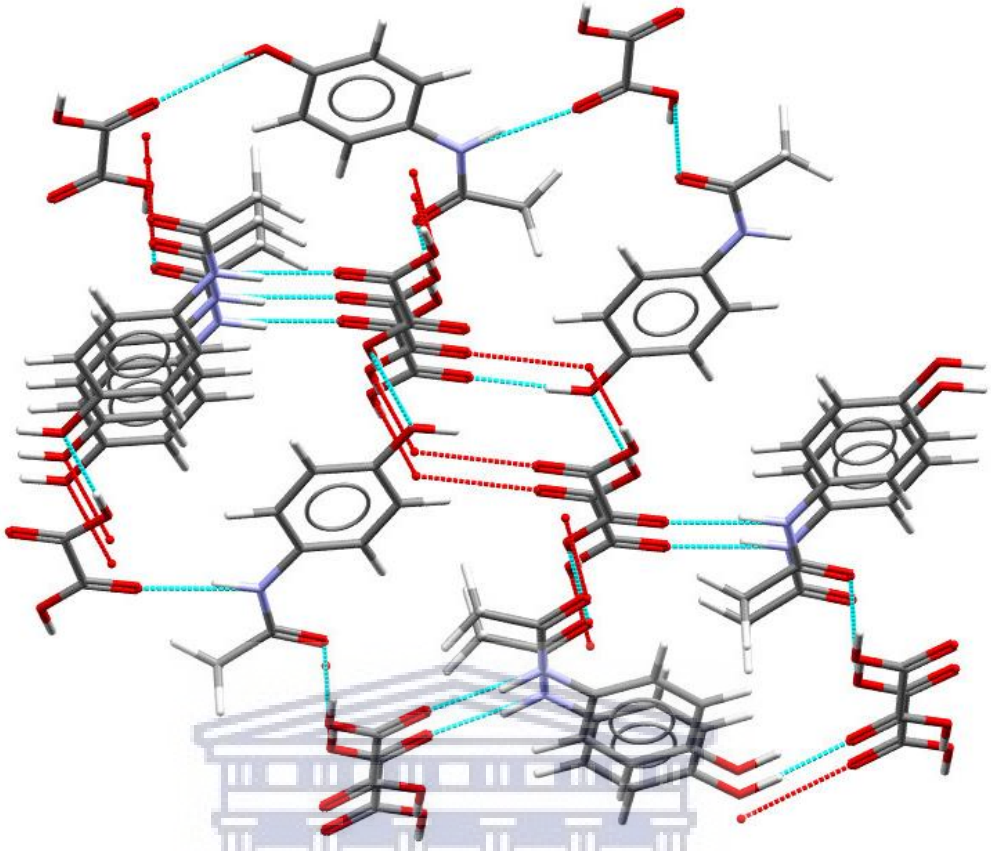

Figure 2.5: The crystal lattice of the co-crystal between carbamazepine and para-aminosalicylic acid

2.5.5.1 Evaporative method of co-crystallisation

Evaporative co-crystallisation has been widely used to produce co-crystals. The super-saturation is achieved as solvent volume reduces upon evaporation, which in turn increases the concentration of co-crystalline mixtures in the solution. This is an effective and preferred method to produce good quality single crystals fit for single X-ray diffraction. Atmospheric conditions (temperature and pressure) must remain constant throughout the experiment to ensure reproductivity, reliability of the co-crystal product and consistency between batches (Karimi-Jafari et al., 2018; A. R. Kumar et al., 2019).

The high evaporation rate leads to accelerated co-crystallisation. However, this was associated with the formation of unstable/metastable crystals. Consequently, slow evaporation of the solvent is recommended.

2.5.5.2 Cooling crystallisation

Cooling crystallisation is another solution method of co-crystal preparation. Supersaturation required for co-crystal growth is achieved by cooling the co-crystalline solution. A drop-in temperature decreases the solubility of both co-formers, leading to precipitation tendency and subsequent co-crystal growth. Among co-crystals produced via CC are co-crystals of carbamazepine/nicotinamide obtained from ethanol.

2.5.6 Supercritical fluid methods

Supercritical fluid technology has been successfully used to produce co-crystals, using supercritical carbon dioxide (CO_2).

2.5.6.1 Co-crystallisation with Supercritical Solvent

During the use of this technique, the API and the co-former are suspended as a slurry in liquid or supercritical CO_2, using the solvent power of supercritical CO_2 and not that of toxic organic solvents. First the thermodynamic of CO_2 is controlled to fine-tune its density as well as solvent power. This, in turn, allows the control over co-crystallisation between components of the co-crystal (Karimi-Jafari et al., 2018).

The application of this technique was shown an increased rate of co-crystallisation. This is due to an intense mass transfer by convection which is promoted by stirring co-crystal components in CO_2 slurry, which in turn offers a complete co-crystallisation and results in a highly pure co-crystal (Karimi-Jafari et al., 2018).

2.5.6.2 Rapid Expansion of Supercritical Solvents

This method consists of saturation of the supercritical fluid (supercritical CO_2) with an API and co-former before the depressurisation of the CO_2phase through a nozzle into a drying chamber at atmospheric pressure. Unfortunately, this method requires that API and co-former be solubility in supercritical CO_2 while the majority of pharmaceutical molecules present low solubility (Karimi-Jafari et al., 2018).

2.5.6.3 Supercritical Antisolvent Co-crystallisation

This method uses supercritical CO_2 as an antisolvent for the co-crystallisation process. On the contrary to a rapid expansion of supercritical solvent, this method requires that API and the co-crystal former have reduced solubility in supercritical CO_2 to allow precipitation of two as one co-crystal structure. Once in a vessel, the CO_2 dissolves in

the used solvent, leading to simultaneous volume expansion and reducing the solubility of that solvent, therefore resulting in precipitation.

Using its two techniques, such as batch gas antisolvent during which the solution contained both API and co-crystal former, is saturated with CO_2 in a high-pressure vessel until co-crystallisation takes place. The second technique is a semicontinuous supercritical antisolvent process during which an API-co-former solution is forced through a nozzle into a highly pressurized vessel containing supercritical CO_2 (Karimi-Jafari et al., 2018).

2.5.7 Miscellaneous co-crystal preparation

Among the miscellaneous method of co-crystal preparation, there is the use of high-power CO_2 laser to irradiate powder blends of cocrystal formers, which then promote recrystallization to a cocrystal. This method is known as "***laser irradiation***". It is assumed that the rearrangement of co-formers molecules, as well as nucleation, occur in a vapour phase. This is because it was seen that co-crystallisation can only take place if co-crystal formers sublimate enough (Karimi-Jafari et al., 2018).

2.5.7.1 Freeze-Drying

Also known as lyophilisation has been wildly used in preserving a variety of products including pharmaceuticals. The material solution is frozen at a controlled (reduced) surrounding pressure to allow the frozen water in the material to sublime. This method has potentially been used to prepare solid-state co-crystal forms (Sonali R. Devne, Vidya N. Kapse, 2019).

2.5.7.2 Electrochemically Induced Co-crystallisation

Electrochemically Induced Co-crystallisation is another miscellaneous method that uses electrochemistry to incite co-crystallisation by creating a conducive environment for the process (pH adjustment to neutral and generate necessary local forces).

2.5.7.3 Resonant Acoustic Mixing

Co-crystal preparation relies on the acoustical transfer of mechanical energy to a wetted powder mixture (drug-co-former). This form of energy transfer encourages the intimate mixing of the components, therefore increasing chances for co-crystal formation (Am Ende et al., 2014; Michalchuk et al., 2018).

2.5.7.4 Spray drying

Spray drying is a well-known method used to produce dry powder from solutions, emulsions and suspensions. The advanced technology which allows a highly-controlled environment and use of hot steam air to rapid evaporation of the used solvent, the method is very fast and produces pure co-crystals when compared to other solution co-crystallisation methods. For this reason, spray drying is among the most preferred method for preparation and scale-up (Alhalaweh & Velaga, 2010). The method has been widely used in the production of amorphous solid dispersions. This method can also and has been used to prepare co-crystal (Alhalaweh et al., 2013; Karimi-Jafari et al., 2018).

2.5.7.5 Electrospray technology

This method leads to liquid atomisation using electrical forces where the liquid flows out a capillary nozzle at high electric potential, and then the liquid is forced by the electric field into a dispersion of fine and highly charged droplets. After drying, the resulted particles are collected using a charged powder collector.

All these methods have been thoroughly discussed with examples (Karimi-Jafari et al., 2018).

2.6 Preference of co-crystallisation

The scientific need for using the co-crystallisation process as a potential tool to enhance the desired properties of drug substances has recently increased significantly due to the benefit of this approach over a variety of other techniques outlined at the beginning of this chapter. Further, the uniqueness with respect to the structure and properties, of each product of co-crystallisation (novelty), a variety of solid forms that can be resulted from this approach (non-obviousness), each of them exhibiting unique physicochemical properties (utility) based on which different application may be evaluated. Simplicity and the greenness of co-crystallisation confer this a remarkable method (Cherukuvada et al., 2016).

Additionally, co-crystallisation around an API increases the protection of its intellectual property (IP), by reducing the risks and industrial crisis in case the drug loses its effectiveness over time while on the market (reducing the risk of costly litigation and market erosion) (Sekhon, 2009).

Co-crystallisation also stabilises drugs known to exhibit polymorphism issues (Thakuria & Sarma, 2018). The latter being the ability of a substance to present itself in different crystalline forms (also known as polymorphs) characterised by the same chemical composition (same substance) but different physicochemical properties, structure arrangements (molecules are joined and arranged differently in lattices) (Karagianni et al., 2018b).

It is mandatory to know that the formation of hydrogen bonds during the co-crystal screening is dependent on the molecular complementarity of the co-crystal formers and plays an important role in structure directions due to the molecular flexibility they offer. It is from this supramolecular concept where the idea of drug-drug co-crystallisation comes. This concept of drug-drug co-crystallisation will be discussed in subsequent sections (Fábián, 2009; Hutchins, 2018).

Assisted by the Cambridge structure database crystal engineering helps the understanding of intermolecular forces involved in hydrogen bonding between molecules (organic mostly). The presence of functional groups that engage in hydrogen bond formation makes the molecular nature of drugs a key factor in the co-crystallisation process. This factor also makes all APIs immanently prone to the co-crystal formation (Shan & Zaworotko, 2008).

2.7 Multidrug co-crystallization (MDCs)

Multiple drugs combination in a single dosage form for oral administration has become a popular drug development strategy mainly due to its abilities to boost the treatment effect and improvement of disease management. The advantage gained from this is also reflected in patient adherence and reduction of product development costs. Such benefits and much more can also be obtained from combined drugs in the pharmaceutical co-crystals (Žegarac et al., 2014).

Despite their potential as recognised by different solid-state scientists, not much attention has been given to them, only a little is found in the literature. However, with the present increase of complex medical conditions and increased pressure in the discovery of new APIs, these hybrids are of utmost importance.

Drug-drug or multidrug co-crystallisation is the relatively unexplored technique for the design of solid APIs, and according to the literature, the use of this technique may

produce co-crystals with potential applications in terms of drugs combination and improved properties for further development (Thipparaboina et al., 2016). Hence, for Bhupinder, the idea of developing a multiple-drug co-crystal is reflected in recent publications and patent applications (Bhatt *et al.*, 2008; Aitipamula, Chow and Tan, 2009; Peterson *et al.*, 2010; Cheney *et al.*, 2011; Lee, Zhang and Flanagan, 2011).

According to Thipparaboina *et al.* (2016), multidrug co-crystals are dissociable solid crystalline supramolecular complexes comprising two or more therapeutically effective components in a stoichiometric ratio within the same crystal lattice, and wherein the components may predominantly interact via non-ionic interactions and rarely through hybrid interactions (a combination of ionic and non-ionic interactions involving partial proton transfer and hydrogen bonding) with or without the presence of solvate molecules. This definition was reconstructed based on FDA guidelines according to which co-crystals are dissociable multi-component solid crystalline supramolecular complexes composed of two or more components within the same crystal lattice wherein the components are in a neutral state and interact via non-ionic interactions.

The multidrug co-crystals implement the patent eligibility criteria such as non-obviousness, novelty, and utility for pharmaceutical development (Ghadi, 2014), (Drozd et al., 2017). According to Ghadi, (2014), there was no record of multidrug co-crystals in the literature. However, this statement was later changed and now, due to an increased interest of researchers on these adducts, the number of reports is evolving in the literature (Thipparaboina et al., 2016).

A more explicit definition of multidrug co-crystals takes into consideration the growing literature on salt/co-crystal hybrids and ionic co-crystals thus includes hybrids interactions. Benefits such as offering potential advantages of synergistic, additive effects, enhanced solubility and dissolution of at least one of the drug components as well as bioavailability are associated with these solid-state materials. Furthermore, MDC due to intermolecular interactions can stabilise unstable components (Sekhon, 2012; Thipparaboina et al., 2016).

2.7.1 Factors influencing MDC synthesis

It is familiar that the co-crystallisation process often yields complex hybrids other than co-crystals intended. The same phenomenon is likely to increase when attempting to prepare MDCs. According to Ghadi, (2014), combining two drugs may result in either

a mixture or a co-crystal in a specific ratio. In cases where a co-crystal is formed, improvements in physicochemical properties and performance of at least one drug component of the co-crystal system may be observed. Alternatively, in the case where another supramolecular hybrid is produced, characterisation should be conducted to determine its usefulness.

Different factors are to be considered when attempting to synthesise MDCs:

- Like normal drug-co-former co-crystals, the successful production of MDCs depends on the method used. Mechanochemistry is likely to be the best, simplest and cost-effect method to prepare MDCs.

- A deep understanding of both components ensures a successful co-crystal formation. The compatibility of the MDC system components should be established. Both drugs must possess complementary functional groups necessary for intermolecular interactions.

- Many active pharmaceutical ingredients (APIs) with exploitable functional groups that are readily available for hydrogen bonding can be considered.

- A diversity of methods available to synthesize co-crystals can be used, some of which will be discussed in the methodology chapter of this thesis.

- Possibilities of co-crystal formation with ionic drugs. This factor favours co-crystallisation over the salt formation and,

- Finally, the need for that particular co-crystal on the market motivates the search, screening and production processes.

2.7.2 Synthesis of Multi-Drug Co-crystals

Generally, MDCs are synthesised the same way as normal single drug co-crystals, and conventional methods used are similar (Thipparaboina et al., 2016). Some of the traditional methods for co-crystal formation also applied to MDCs synthesis are; simple distillation, solvent evaporation, cooling crystallisation, co-grinding, liquid-assisted grinding, slurry crystallisation, melting, and sonic crystallisation. The successful application to MDCs of these methods has been justified by a growing number of these hybrids in the literature (Thipparaboina et al., 2016). Some of these methods were used in this work and therefore, are discussed in Chapter 3 section 3.3.

2.1.1 Advantages of Multi-Drug Co-crystals

MDCs offer potential advantages of synergistic benefits in addition to enhancing solubility, dissolution as well as bioavailability offered by normal co-crystals. Multidrug co-crystallization as a subset of co-crystallisation provides not only the opportunity to modify the physicochemical properties of a drug substance but also the new strategies for the development of combination therapies. MDCs, due to the intermolecular interactions, can stabilise unstable components, (Thipparaboina et al., 2016) therefore, reducing the occurrence of drug resistance and related side effects.

Even though the production of MDCs follows the same crystallographic procedures, there are other factors to consider in order to successfully produce MDCs. Firstly, in-depth knowledge of both drug components of the co-crystal is paramount to address the purpose of the product co-crystal desired. Other factors include but are not limited to co-crystallisation conditions as well as methods used particularly, in pharmaceutical co-crystal production, the compatibility of two drugs, differential solubility and variations in dose must be considered (Thipparaboina et al., 2016).

Examples of multi-drug co-crystals synthesised through this approach include three anti-TB drugs, isoniazid (INH) and pyrazinamide (PZA) key-members of the first-line treatment and 4-aminosalicylic acid, the second-line anti-TB drug. Both INH and PZA were co-crystallized by PAS and two complexes resulted. The first complex is anhydrous formed between INH and PAS with a 1:1 stoichiometric ratio. The second complex was a monohydrate resulted from co-crystallising PZA and PAS (Grobelny et al., 2011). Other reported combinations such as molecular complexes of theophylline from its co-crystallisation with 5-fluorouracil and barbital have also been discussed in the literature (Thakuria & Sarma, 2018).

The co-crystallisation of meloxicam, a non-steroidal anti-inflammatory and aspirin resulted in a co-crystal showing a reduced time required to reach the human therapeutic concentration compared with the parent drug, meloxicam (Cheney et al., 2011). The co-crystal of acetaminophen and theophylline in a 1:1 ratio showed a better dissolution rate than that of the physical mixture of these drugs. Other examples include Dapsone which due to its potential therapeutic activity, was co-crystallised by different active substances (Bucar et al., 2014; Fernandes et al., 2015; Jiang et al., 2014; Surov et al., 2014).

The MDR Entresto (Chavan et al., 2018) comprising of valsartan; an angiotensin II receptor antagonist used in the management of hypertension and sacubitril; a neprilysin inhibitor, was the first to be approved by the US FDA for the treatment of heart failure.

2.2 Conclusion

With an intense demand for new medications, an increase of drug resistance among available medications, the desire to discover new, co-effective, and patient-friendly compounds, compel researchers to explore different alternatives one of them being fine-tuning physicochemical properties of known APIs. Co-crystallisation has recently evolved as a better approach to promising new chemical entities. Based on a growing number of publications, co-crystals have gained potential applications in the pharmaceutical industry and other fields of chemistry and physics such as agrochemistry, catalysts, food industry, energy, etc.

Co-crystallisation does not only enhance the essential properties of APIs but also plays an important role in combination therapy where APIs can be combined in a single co-crystal for multi-target purposes. Typical examples of these include HIV, TB and cancer treatments that require high doses and therefore, involve the administration of many drugs at once in order to achieve the necessary doses.

Even though co-crystal formation is not always successful, the resulted multi-component adducts (MDC) come with even better properties than that of the co-crystal counterpart. The diversity of these solid-state materials that can be effected under different circumstances from co-crystallisation justify the influence of this approach in protecting the intellectual property of a drug.

Assisted by the CSD, crystal engineering helps the understanding of intermolecular forces involved in hydrogen bonding between molecules (organic mostly). The presence of functional groups that engage in hydrogen bond formation makes the molecular nature of drugs a key factor in the co-crystallization process. This factor also makes all APIs immanently prone to co-crystal formation (Shan & Zaworotko, 2008).

Chapter 3 Materials and experimentation methods

This chapter presents materials used in this study and a description of all the analytical techniques (laboratory and computational) applied to critically analyse the various chemical products.

Initially, a brief discussion of selected drug substances consisting of material source, chemical structures, and the physicochemical properties is given, then the mode of action of each candidate is summarised. Selected candidates can be grouped into two categories: the first one is made of antiviral drugs for the treatment and prevention of HIV/AIDS and amantadine and the second group consists of anti-tuberculosis drugs. The chapter also gives a full description of the experimentation for the preparation and the physicochemical characterisation of different solid forms of selected candidates. Thermal, spectral, morphological, diffraction, chromatographic as well as computational analytical methods were collectively utilized in this research.

3.1 Material sources

Anti-retroviral drugs efavirenz (EFV), nevirapine (NVP), zidovudine (AZT), lamivudine (3TC) were obtained as a generous donation from ASPEN Pharmacare (Cape town) and were used as received. Adamantyl-1-amine (ADT), isoniazid (INH), pyrazinamide (PZA) and glutaric acid (GA) were purchased from Sigma-Aldrich Chimie GmbH (Steinheim, Germany) and were also used without further purification. All solvents used were all purchased from Sigma-Aldrich Chimie GmbH (Steinheim, Germany) as well. Where necessary dilution was made has been indicated.

3.2 Identification of selected compounds

As mentioned in chapter 1, considering the speed of HIV replications and the number of errors and cross-species transmissions that can occur, interfering with viral growth requires different strategies. Due to this, a variety of anti-HIV drugs were developed and are available in different classes such as ***fusion inhibitors*** which interfere with attachment and fusion of the virus into the cell-host via an envelope glycoprotein complex. This envelope is made of a total of 161 subunits that mediate the entry process and facilitate the fusion to the host (Eggink et al., 2010). Other inhibitors include: ***protease inhibitors*** and ***reverse transcriptase inhibitors (RTIs)*** grouped into

nucleoside (NRTIs) and ***non-nucleoside reverse transcriptase inhibitors (NNRTIs)***. Antiviral drugs selected for this study include two NRTIs, Zidovudine (AZT) and Lamivudine (3TC), two NNRTIs, Nevirapine (NVP) and Efavirenz (EFV), and 1-adamantylamine (ADT).

3.2.1 Nevirapine

NVP (**Figure 3.1**) is a well-known NNRTI used in combination with other drugs in a single regimen, alternatively to EFV, for the treatment of HIV infection and AIDS. NVP belongs to the chemical class of dipyridodiazepinone and is known to an IUPAC name of 11-cyclo-propyl-5,11-dihydro-4methyl-6H-dipyrido(3,2-b:2',3'-e) (1,4) diazepin-6-one.

Approved in 1996 by the US-FDA, the drug was marketed as Viramune®. NVP binds directly to reverse transcriptase (RT), blocking the RNA-dependent and DNA-dependent DNA polymerase activities, thus disrupting the enzyme's activities.

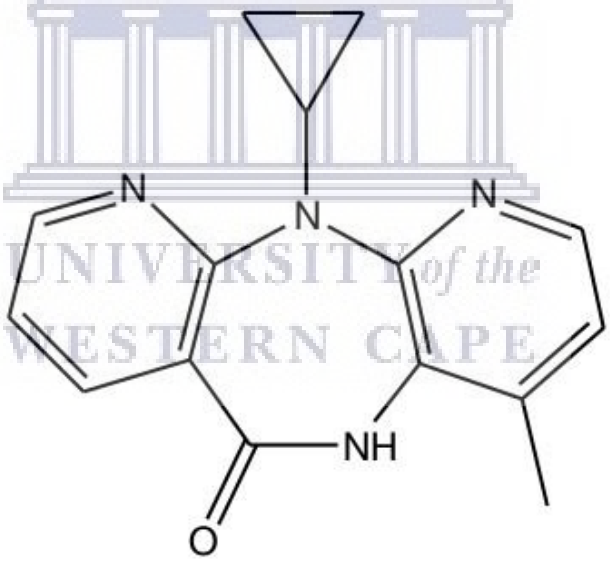

Figure 3.1: Nevirapine molecular structure

According to the biopharmaceutics classification system (BCS) by the FDA, the drug belongs to a class II drug (high permeability and low solubility). The aqueous solubility of NVP at pH = 7 and at 37°C is very low (0.1 mg/mL). NVP has shown the ability to form different polymorphs. Three polymorphs and several solvated forms of NV were isolated using different recrystallisation methods (Chadha et al., 2010a).

Alternative modes of self-association such as co-crystallisation are possible due to the presence of a rigid conformational amide functional group in the NVP molecule. The crystallization normally occurs via dimeric or catemeric synthons (Chadha et al., 2010a; B Reguri & Chakka, 2006; Buchi Reguri & Chakka, 2004; Stieger et al., 2010).

According to Caira et al. (2012), the butterfly-like shape of the NVP structure is essential in binding to the reverse transcriptase site. Worries on whether co-crystallising NVP would result in altered conformation flexibility of the molecule have been investigated and proven otherwise since insignificant change occurs upon co-crystallisation, thus having no impact on the binding abilities of the drug to the inhibitor enzyme.

NVP is one of the poorly water-soluble antiretroviral drugs. It is known to exhibit a limited dissolution rate which subsequently leads to low and variable bioavailability. It is for this reason that NVP is classified as a Class II drug according to the Biopharmaceutical Classification System (BCS) (Raju et al., 2014). NVP has shown the ability to form crystals with different carboxylic acid and other carbonyls. Five co-crystals of nevirapine have been reported (Caira et al., 2012).

Just like other NNRTIs, NVP is vulnerable to the development of resistance. It is known that one mutation causes high-level resistance to all first-generation NNRTIs. NVP noncompetitively inhibits HIV-1 RT DNA polymerization reactions. However, this statement is contradicted by the changes in inhibition constants depending on the identity and sequence of template or primer substrate used during the assay (polymerase assay) (Sluis-Cremer & Tachedjian, 2008).

3.2.2 Efavirenz

Efavirenz (EFV); also, chemically known as ((4S)-6-chloro-4-(2-cyclopropylethynyl)-4(trifluoromethyl)-2,4-dihydro-1H-3,1-benzoxazin-2-one (**Figure 3.2**) is a potent non-nucleoside inhibitor (NNI) of the human immunodeficiency virus (HIV) type 1 transcriptase. EFV is used as part of first-line antiretroviral therapy. Despite its poor aqueous solubility and high permeability thus a BCS class II drug, EFV remains one of the drugs of choice and part of the highly active antiretroviral therapy (HAART). EFV is commercially available as Sustavine® or Stochine®, supplied by the pharmaceutical company Bristol-Myers Squibb (Gatch et al., 2013).

EFV is a lipophilic crystalline solid and a derivative of benzoxazinone. The drug has a solubility of 0.9 μg/mL and a low intrinsic dissolution rate of 0.037 mg/cm^2/min (da Costa et al., 2012). Approved by US-FDA in 1998, EFV demonstrates its high potent non-nucleoside inhibitory activity against HIV-1 reverse transcriptase by suppressing viral multiplication and prevent damage of related cells even at nanomolar concentrations (De Gomes et al., 2013).

EFV is currently used clinically in a single tablet dosage along with integrase and protease inhibitors administered once daily (as a fixed-dose combination). This is an immensely desired and compliant HIV-1 treatment known according to De Gomes *et al.*, (2013).

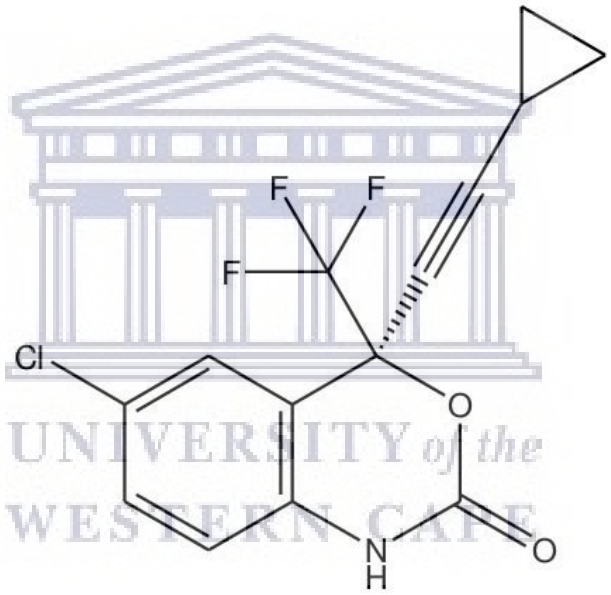

Figure 3.2: Efavirenz molecular structure

EFV co-crystallization is not very well documented despite its well-known ability to solve aqueous solubility-related problems that such a drug may encounter (De Gomes et al., 2013; Mahapatra et al., 2010). Co-crystallising EFV with the highly aqueous soluble co-formers would enhance its solubility profile.

Generally, NNRTIs inhibit the replication of HIV in the early stages. However, NNRTIs such as EFV have shown to inhibit the replication at a later stage of the viral replication. Despite the differences structurally, all NNRTs interact with HIV-1 RT by binding to a single site on the p66 subunit of the HIV-1 RT p66/p51 heterodimer also

known as NNRTI binding pocket situated approximately 10 Å from the RT DNA polymerase active site and 60 Å from the RT RNase H active site (Sluis-Cremer & Tachedjian, 2008).

3.2.3 Zidovudine

Zidovudine (**Figure 3.3**) is one of the anti-HIV agents used individually or in combination with other agents. The drug is known to the IUPAC name of 1-[(2R,4S,5S)-4-Azido-5-(hydroxymethyl)oxolan-2-yl]-5-methylpyrimidine-2,4-dione or azido-deoxythymidine (AZT).

Available on the market under the brand name of Retrovir®, AZT was the first drug approved by the US for the treatment of HIV infections and AIDS on 19 March 1987. AZT falls under the category of NRTIs due to its inhibition to RT, the enzyme used by HIV to synthesise the viral DNA. This viral DNA is key to the multiplication of HIV. The use of AZT remarkably reduces (but does not suppress) the replication of HIV and restores the immune system. It is also assumed to intervene in the prevention of HIV transmission from a mother to a child during the birth or in case of injury. Due to the resistance to HIV, AZT is used in combination with other anti-HIV drugs in a regimen known as HAART.

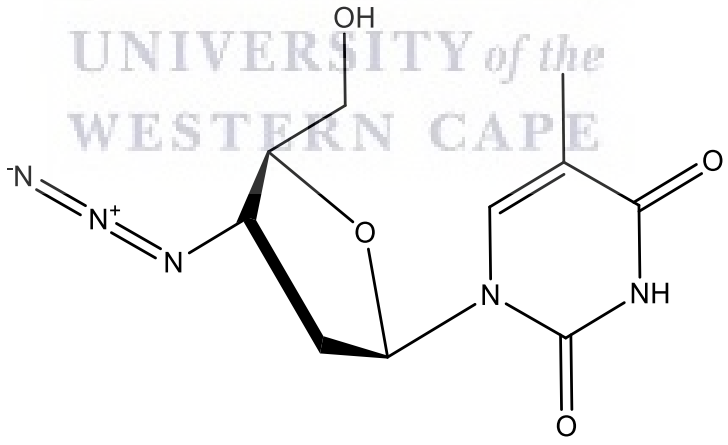

Figure 3.3: Zidovudine molecular structure

This information on physical and chemical properties was extracted from Sigma Aldrich Material Safety Data Sheet (MSDS).

Zidovudine is known to have metabolic pathways, namely phosphorylation (**Figure 3.4**) during which AZT reacts with different enzymes to reach its active stage (Veal & Back, 1995).

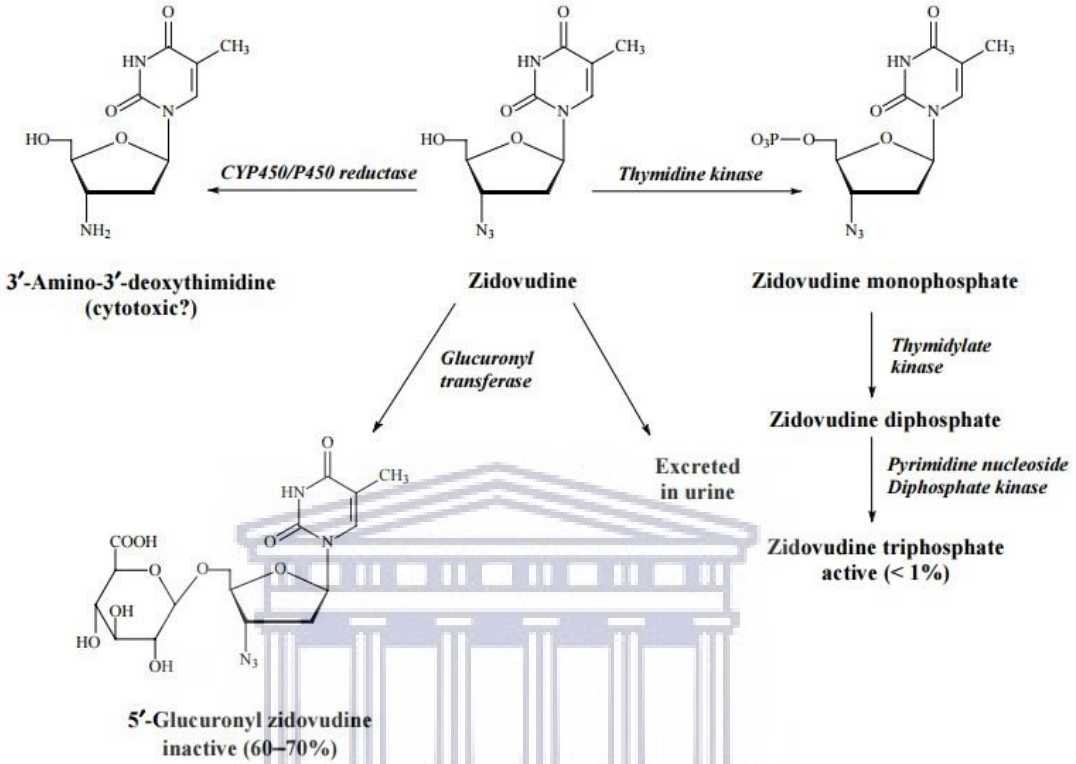

Figure 3.4: Diagram of AZT metabolic pathways (Source: Veal and Back, 1995)

3.2.4 Lamivudine

Lamivudine (**Figure 3.5**) with an IUPAC name of 2-deoxy-3-thiacytidine (3TC) is a synthetic nucleoside analogue (dideoxynucleoside) that is used for the treatment of HIV by inhibiting the replication and chronic hepatitis B viral infections. Like AZT, 3TC only becomes active through the metabolism process of phosphorylation (**Figure 3.6**) (Andrade et al., 2011).

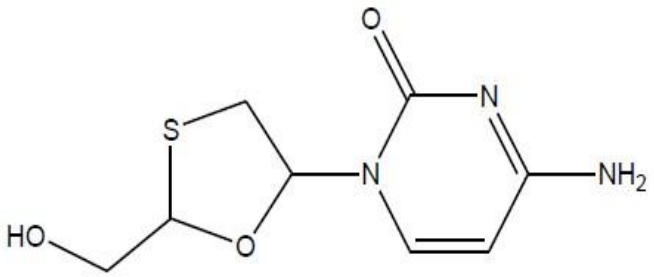

Figure 3.5: Lamivudine molecular structure

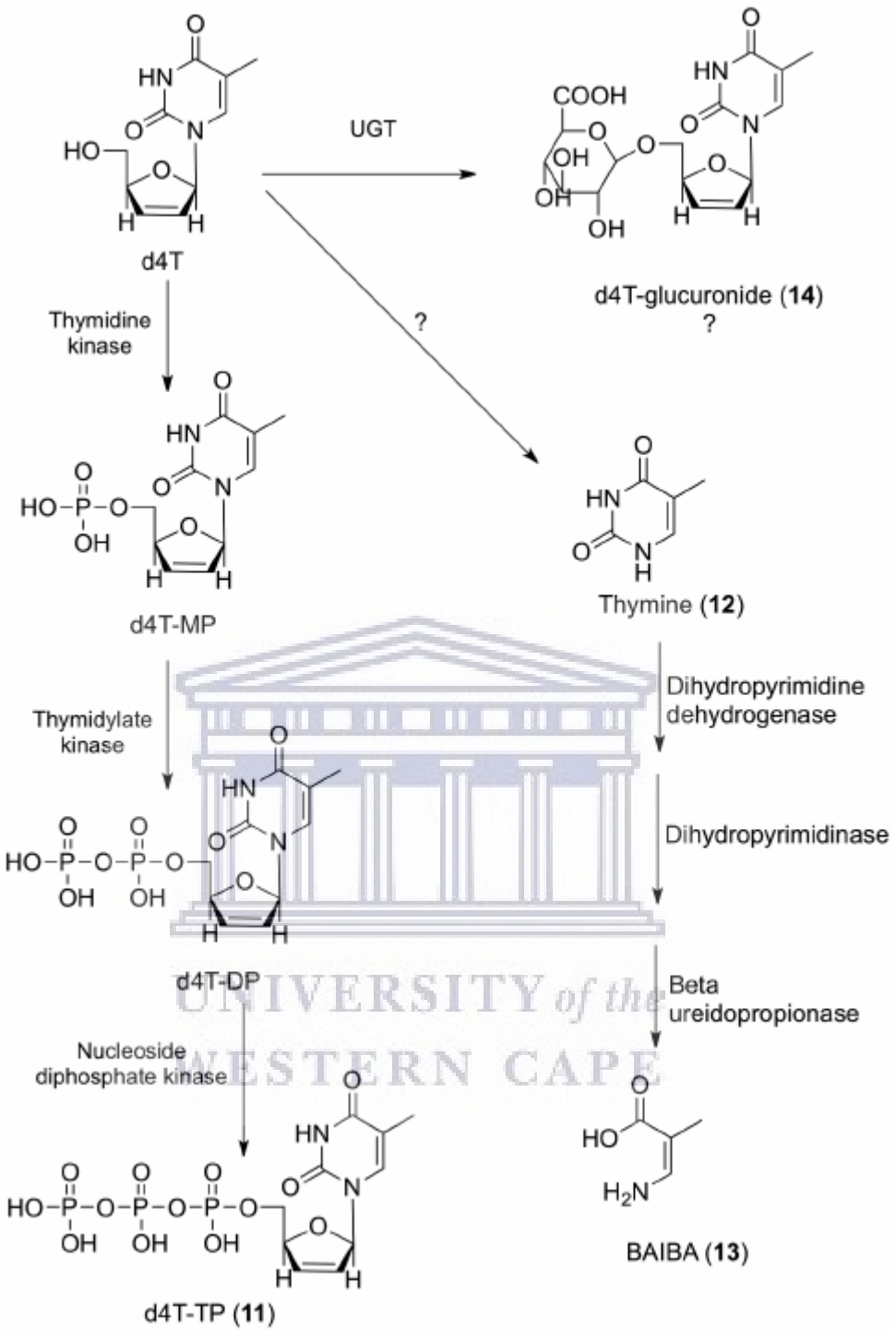

Figure 3.6: Diagram of lamivudine metabolism pathway (Andrade et al., 2011)

The mechanism produces a 5'-triphosphate which inhibits the HIV enzyme, the reverse transcriptase which; by using host cell endogenous nucleosides as substrates, catalyses the formation of a complementary DNA from a single-stranded HIV RNA. The chain termination is induced by the absence of 3'-Hydroxyl group (on which 3',5'-phosphodiester linkages are made) due to the incorporation of the active triphosphate on RT binding site instead of the normal endogenous triphosphate. 3TC inhibits HIV

replication also by interfering with reverse transcriptase, thereby reducing the viral load and significantly the mortality rate.

3CT is also known to exist in different polymorphic forms (forms I, II, and III) among which polymorph I and II were reported (Chadha, Saini, et al., 2012; Harris et al., 1997), polymorph III was later reported in 2007 by Singh (Singh, G. P., S. Dhananjai, M. B. Saini, 2007). Due to this polymorphism phenomenon, a number of 3TC polymorphic co-crystals have been identified in the literature (Bhatt et al., 2008; Sekhon, 2012). Generally, carboxylic acid-aminopyridine synthons were involved in co-crystal formation.

3.2.5 1-Adamantylamine

1-Adamantanamine (ADT) (**Figure 3.7**) is commonly found in the literature in its hydrochloride salt form. The rate of activity of the free base compared to the salt forms might differ because the solubility of the freebase and salt form is very different. ADT trade names are Amantadine®, Midantan® and Symmetrel®. ADT-HCl salt was once used for its antiviral activity in the prevention and the early-stage treatment of influenza A.

The drug is known to increase the dopamine levels in the central nervous system (CNS); for this reason, it is often applied in medication for the treatment of dementia, Parkinson's disease, Alzheimer's diseases, stroke, hypoxic brain afflictions, and neuro infections (Hay, 1989; Kampman et al., 1996; Kornhuber et al., 1995).

A caged structure of this drug and the presence of an amine group confer to the molecule the special chemical property of a diamond-like structure (Kornhuber et al., 1995).

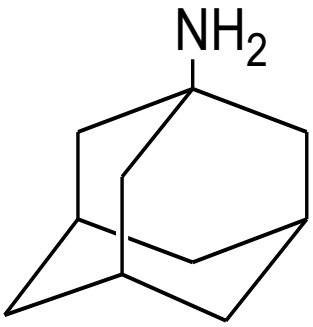

Figure 3.7: 1-adamantanamine molecular structure

The system is rigid but strain-free, demonstrating that there is no angle or torsional strain present. Consequently, it is a highly stable structure.

1-adamantanamine hydrochloride (ADT-HCl) inhibits replication of the influenza group A virus, containing the M2 protein. The M2 protein functions as an ion channel and prevents exposure of the viral hemagglutinin to low intracellular pH to which it is sensitive.

The apparent antiviral activity of ADT-HCl results from the ability of the drug to prevent viral penetration into the host cell by blocking ion channel proteins existing in the virion lipid envelope of the group A viruses or suppressing the uncoating process (Blázquez et al., 2016; Davies et al., 1964; Staničová et al., 2001).

The antiparkinsonian activity is less known, although it is also related to the ability of 1-adamantanamine to block neuromuscular transmission, which may, however, depend on its capacity to increase the synthesis and release of dopamine (Blázquez et al., 2016; Hubsher et al., 2012). ADT-HCl is also believed to be effective against the dengue virus (Koff et al., 1980; Lin & Chen, 2016).

3.2.6 Isoniazid

Isoniazid (**Figure 3.8**), chemically known as isonicotinylhydrazide (INH) is an antibacterial drug used in the first-line treatment of TB infections since 1952. It is used in the prevention and treatment of both latent and active TB.

INH is inactive (a prodrug), the *in vivo* activation by KatG, which is an enzyme with catalase and peroxidase activities. The process leads to inhibition of mycolic acid synthesis; a long-chain fatty acid-containing component of the mycobacterial cell wall (Lei, Wei, and Tu, 2000). The activated inhibitors are known to exhibit their activity on two target enzymes; enoyl-acyl carrier protein reductase (InhA) and β-ketoacyl-Acyl carrier protein synthase. Further, it was also reported that the activation of INH inside the mycobacterium tuberculosis by oxidation with manganese (iii) pyrophosphate which is a chemical model of the KatG protein, generated four isomeric adducts that are effective against InhA, an essential enzyme in mycolic acid biosynthesis which was fully characterized in detail by (Broussy et al., 2003).

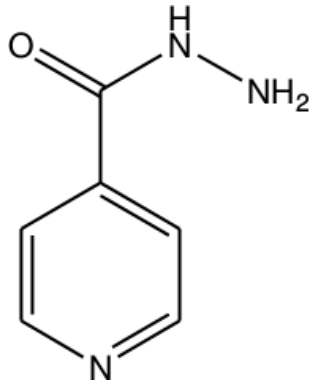

Figure 3.8: Molecular structure of Isoniazid

INH has been co-crystallised with different dicarboxylic acids as co-crystal formers. Some of these are found in the literature according to Swapna, Maddileti and Nangia, (2014).

3.2.7 Pyrazinamide

Pyrazinamide is an antitubercular drug known to a UIPAC name of pyrazine -2-carboxamide (PZA). PZA is always used in combination with other anti-tubercular drugs, specifically during the first months of treatment to shorten the regimen duration. It was reported that the ability of PZA to destroy semi-dormant tubercle bacilli in acidic pH environments which survived other anti-TB drugs, shortens the duration of treatment to 6 months (Zhang et al., 2003).On the other hand, its absence in the first-line treatment regimen makes the duration of the treatment longer up to nine months or more. Even though the title drug is naturally bacteriostatic, it was also found to be bactericidal in the presence of active *Mycobacterium tuberculosis* (Gunasekaran & Sailatha, 2009; Zhang et al., 2003). PZA among isoniazid and rifampicin, the first-line drugs for the treatment of TB infection is also considered as a keystone in modern TB therapy.

The mechanism of action of PZA is summarised in **Figure 3.9**. According to Zhang et al. (2003), the process begins with PZA entering tubercle bacilli by passive diffusion where it is converted to pyrazinoic acid (POA) by pyrazinamidase /nicotinamidase encoded by the pncA gene. POA then reaches the cell surface through passive diffusion and a weak (deficient) efflux mechanism. At acid pH, the protonated POA (HPOA) enters the cell by passive diffusion, in a pH-dependent manner and then accumulates to high levels intracellularly and kills bacteria using different mechanisms including disruption of membrane energy production, inhibition of translation, possibly inhibition

of pantothenate and CoA biosynthesis, and other mechanisms which are not yet identified.

PZA is a paradoxical and unconventional drug due to its strange properties. It is active against non-growing and old bacilli. This is the absolute opposite of other antibiotics that actively inhibit young growing bacteria. PZA is active only under acidic conditions, practically inactive in near-neutral pH 7. PZA activation is obtained from an increased acidity generated during active inflammation and slow conversion into its active form; POA by the bacterial nicotinamidase/ pyrazinamidase (PZase) (Zhang et al., 2003).

Different co-crystals have been prepared from PZA with different co-crystal formers including active substances such as diflunisal a non-steroidal anti-inflammatory substance (Abourahma et al., 2011; Évora et al., 2011; Grobelny et al., 2011; Rajbongshi et al., 2018).

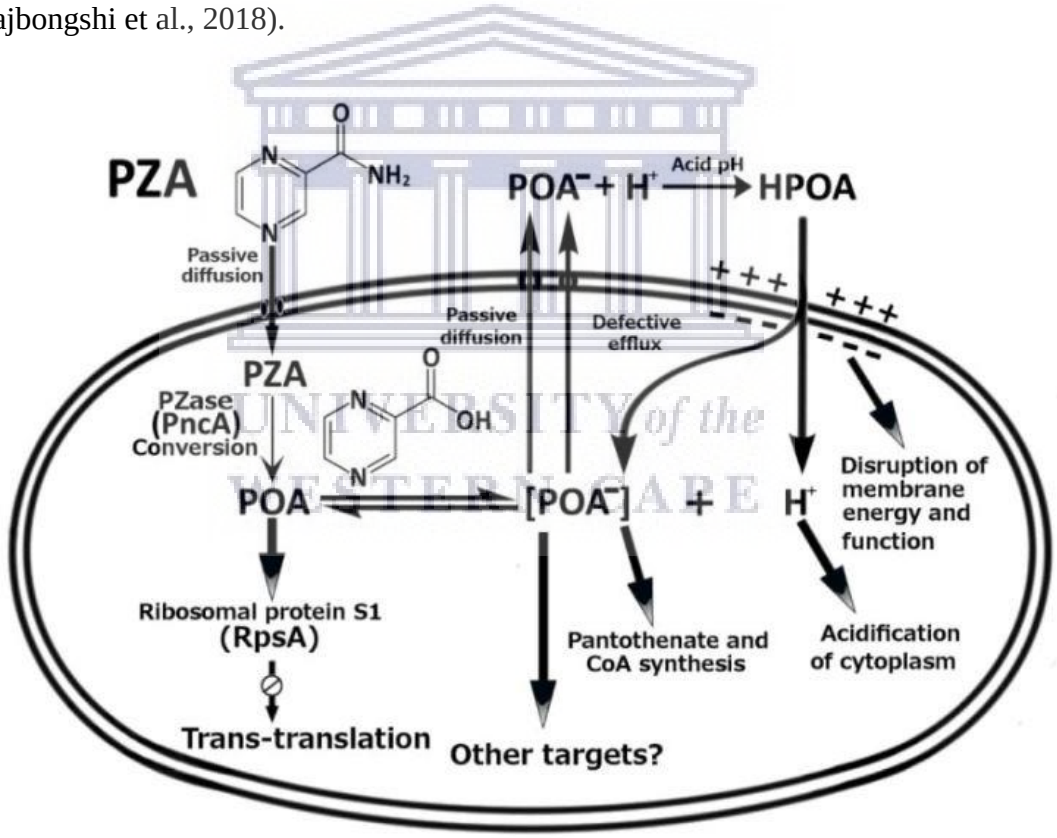

Figure 3.9: Mechanisms of Pyrazinamide Action and Resistance (source: Zhang *et al.*, 2014)

3.2.8 Glutaric acid

Glutaric acid (Figure 3.10) is one of dicarboxylic acid safe according to the US-FDA GRASS list and widely used as a co-former in different pharmaceutical co-crystals to

enhance physicochemical properties such as solubility and dissolution behaviours. The wide use of carboxylic acids such as Glutaric acid also reflects their carboxyl moieties readily available to form hydrogen bonding with amino moieties present in different APIs (Caira et al., 2012) (Luo & Sun, 2013) (Jung et al., 2015) (Samsodien et al., 2017).

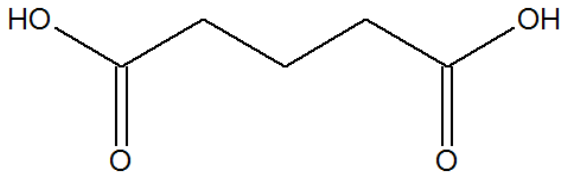

Figure 3.10: Glutaric acid molecular structure

3.3 Co-crystal/solid forms preparation

There are different methods to prepare multicomponent solid-state materials. Particularly for co-crystal synthesis, solution crystallisation methods such as solvent evaporation are methods of preference due to the high purity of the product. However, it is not always possible to successfully produce a co-crystal using these methods. In that case, mechanochemical reactions via neat grinding, and/or solvent-assisted grinding (Friscic & Jones, 2009) are used as co-crystallisation methods. The co-crystallisation process involves the formation of intermolecular interactions between a drug of choice and a selected co-crystal former. Both solution and solid-state methods have been explored in the attempt to form co-crystals of the above selected APIs.

3.3.1 Co-crystal screening by evaporative methods

The evaporative method of co-crystallisation, also known as co-crystallisation from solution involves dissolving powder or crystalline samples into different solvents and letting evaporation take place while growing crystals (Ghadi, 2014). Advantages of synthesising co-crystals from these evaporative methods include:

There is a fast transformation by the liquid phase present, eschewed components thermal stress and consideration of the solubilities of the components during the experimental design. Other important points to note are that almost any solvent can be utilized for co-crystal screening and synthesis regardless of its boiling point. There is a high chance for co-crystal formation due to the maximum activity of the co-crystal components in solution and the possibility for the formation of a thermodynamically stable solid-state.

Furthermore, the methods adhere to the unexpected outcomes in terms of stoichiometries of the binary compound and offer an easy way to manage experiments because any change of the precipitate relative to the thermodynamically stable form of the pure drug substance reveals the formation of a binary compound (Rager & Hilfiker, 2010).

Despite their advantage over mechanochemistry, these methods are expensive and time-consuming, and as discussed in chapter 2, the correct choice of solvent is, in fact, paramount. Exposure to some solvents used during these experiments may be dangerous and may cause long-term effects. **Figure 3.11** demonstrates the solution co-crystallisation steps; the first beaker contains the co-crystallising solution in which a drug was completely dissolved and filtered while the second beaker contains a solution with crystals precipitated at the bottom after co-crystallisation occurred.

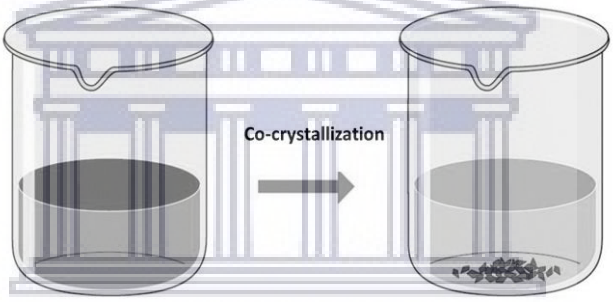

Figure 3.11: The demonstration of the crystal/co-crystal formation from solvent evaporation

3.3.1.1 Co-crystal screening by single solvent evaporation

During this evaporative method, stoichiometric amounts of two-parent compounds were dissolved in the necessary volume (e.g. 2 mL) of solvent. With temperatures kept below the melting point of the lowest melting constituent and about 10^{o}C below the appraised boiling point of the solvent system, the two samples were separately dissolved in the solvent while being stirred with a magnetic stirrer on a hot plate until the powders were completely dissolved. The two solutions were then mixed in the vial containing the smaller quantity and extracted using a syringe. The solution was then filtered through a 0.45 μm micro-filter and transferred to a clean and labelled vial and closed with Parafilm®. A few holes were made in the parafilm® using needles, to facilitate solvent evaporation.

3.3.1.2 Co-crystal formation by binary mixtures of solvents

Solvent evaporation using mixtures of solvents has been proven useful where the use of one solvent fails to produce the desired co-crystal.

In this research, co-crystal screening was also carried out by the slow evaporation method using a mixture or mixtures of solvents in several stoichiometric ratios. The stoichiometric amounts of the compound and co-crystal formers are dissolved in a known volume of a binary mixture of solvents. Samples were dissolved separately in the respective solvent systems, stirred with a magnetic stirrer while on a hot plate until the powders were completely dissolved. All temperatures were kept below the melting point of the lowest melting component and approximately 10^{o}C below the estimated boiling point of the solvent system. The two solutions are then mixed in the vial with the lesser amount of solvent, stirred, extracted via a syringe and filtered from the syringe through a 0.45 μm micro-filter and transferred to a clean and labelled vial and closed with Parafilm®. The parafilm® was perforated using needles to facilitate solvent evaporation. The solution is left undisturbed for a reasonable period of time, allowing the evaporation process to take place desirably.

3.3.2 Co-crystal formation by vapour diffusion

A solution of the solute and co-former in a stoichiometric amount was prepared using a so-called good solvent (solute and co-former soluble solvent) and was placed in a small vial that was stored in another big container, containing a small amount of a miscible, volatile non-solvent.

The bigger container was tightly closed. The sample preparation was left for a reasonable time to allow diffusion of the non-solvent vapour phase into the solution of the small vial creating equilibrium in vial contents. As the equilibrium was reached, saturation or super-saturation was achieved. The solubility of the compound in a precipitant used in such a technique should be as low as possible (much less than 1 mg/ml), and the precipitant (the solvent in which the compound is poorly soluble) should be miscible with the solvent and the saturated solution in the small vial.

3.3.3 Co-crystal formation by mechanochemistry

Mechanochemistry is the transformation (chemical and physicochemical) of substances during the aggregation caused by mechanical energy. Moreover, by definition, mechanochemical reactions are chemical reactions induced by mechanical energy. This

approach has long been used for the synthesis of different solids, including metallic alloys. The approach was introduced by Faraday earlier in 1820. Other works on the development of this method include Ostwald's who established the position of mechanochemistry within the chemistry framework and compared four branches namely electrochemistry, mechanochemistry, photochemistry and thermochemistry (Jones & Eddleston, 2014). Quinhydrone was the first organic co-crystal by mechanochemical reactions using solid-state grinding, produced by Friedrich Wöhler in 1844.

This approach presents several advantages, such as simple process, ecological safety and the possibility of obtaining a product in the metastable state. Among co-crystallization techniques, the application of mechanochemical technology in the pharmaceutical field has recently gained extensive attention and has been successfully used for the production of pharmaceutical co-crystals, solid dispersion, eutectic mixtures and other important solid forms including but not limited to the amorphous form (Jones & Eddleston, 2014).

3.3.3.1 Co-crystallisation by neat/solid-state grinding

Co-crystallisation by grinding is a very popular method that uses mechanical energy to induce the chemical reactions between the two co-crystal formers. According to the literature, this method efficiently promotes hydrogen bonding and when compared to other methods, solid-state grinding (SSG) also shows different advantages such as being simple, quick, environment-friendly and does not require the use of solvent or heat (Douroumis et al., 2017).

Neat or dry grinding consists of mixing stoichiometric amounts of crystal components and grinding them either manually using a mortar and pestle or mechanically **Figure 3.12** (Ghadi, 2014; Jayasankar et al., 2006). Several pharmaceutical complexes/co-crystals have been successfully synthesised by neat grinding (Friscic & Jones, 2009; Yun Hu et al., 2014).

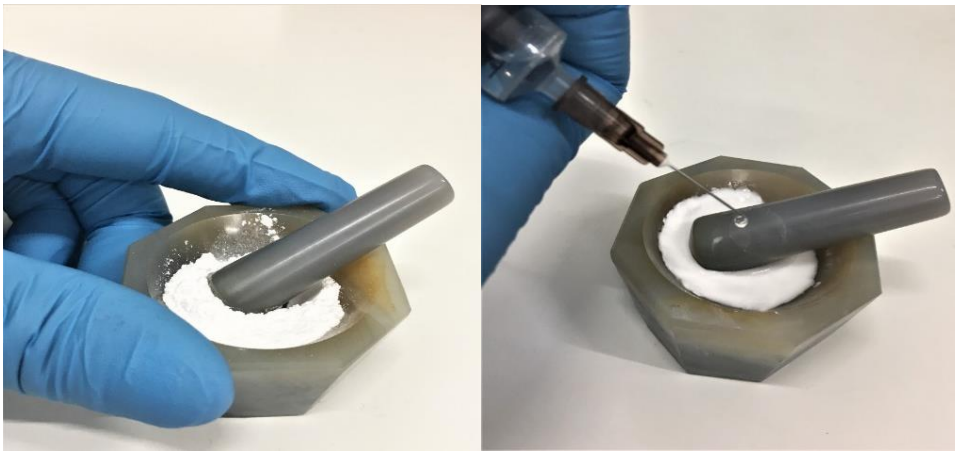

Figure 3.12: Image demonstrating co-crystal synthesis by solid-state grinding (left) and liquid assisted grinding (LAG) (right)

In this work, co-formers were accurately weighed in different molar ratios and were transferred in a marble mortar, ground manually with a pestle for at least 30 minutes period of time. The resulted powders were subsequently characterised using various methods as found in the characterization section.

3.3.3.2 Co-crystallisation by liquid assisted grinding (LAG)

The LAG is an auspicious method widely used to synthesise co-crystals. In this method the mechanochemical reactions use the addition of a small amount of suitable solvent to the ground mixture (API and co-former) at the beginning of milling, to accelerate the process of the co-crystal formation (**Figure 3.12**). This method was reported to synthesise co-crystals even more efficiently than neat grinding (Friić, 2010),(A. Mukherjee et al., 2018). Just like solid-state grinding, the LAG method offers an additional opportunity to explore non-crystalline materials and drugs whose differences in solubility limits other solution co-crystallisation methods.

Furthermore, the LAG/solvent-drop grinding method avoids excessive use of crystallisation solvent. Hence, compared to solution crystallisation methods such as solvent evaporation; it can be regarded as a green process. The solvent-drop grinding method could also prove useful for polymorph control and selective polymorph transformation as previously reported (Braga et al., 2013; Hasa et al., 2015; Karimi-Jafari et al., 2018).

3.4 Characterisation

3.4.1 Characterization by the Hot Stage Microscopy (HSM)

Thermal microscopy, also known as the hot stage microscopy, combines microscopy and a thermal analyser to enable the understanding of and characterise materials as a function of temperature and time. Otto Lehman was the first to use this technique in the 1880s, and it was introduced in the pharmaceutical field by Maria Kuhnert-Brandstatter; the first researcher to use thermal microscopy in the characterisation of pharmaceutical compounds (Stieger et al., 2012).

For the characterisation of active pharmaceutical ingredients, this technique allows:

- The observation of any changes in the physical appearance of the sample.
- The economic analysis of a very small amount of analytical samples. The method is relatively inexpensive in terms of instrumental setup which comprises of a heating stage with a sample holder and a suitable light polarizing microscope which is sometimes coupled with a gaseous atmosphere controller and a system that enables the image/ video to be captured, measurements of observations and temperature to be determined.

With the use of HSM observations of the physical changes are made possible. These include compound morphology, gas evolution (in solvated samples), solid-solid transformations, the interaction between different compounds, dissolution of one compound in another, sublimation and/or evaporation, vapour deposition, melting or liquefaction upon heating (solid-liquid transformations), solidification upon cooling, crystal growth and its rate and decomposition (Stieger et al., 2012).

The use of this thermo-microscopic technique allows the observation of different thermal events while heating or cooling the sample crystal or powder on a hot stage.

Figure 3.13: Image of the Hot Stage Microscope fully set for analysis.

In this research, a Linkam TP92 temperature control unit connected to a Linkam THMS 600 hot stage (**Figure 3.13**) was used to heat samples at a controlled rate. Observations and visual characterisation were made possible using a real-time Sony Digital Hyper HAD colour video camera, fitted to a Nikon SMZ-10 stereoscopic microscope. Images were recorded and analysed by the Soft Imaging system Essential Stream®. This interconnected system proves to be very useful and allows distinguishing new solid phases such as polymorphs (transition from one form to another can be easily observed), co-crystals and/or complexes, amorphs (which recrystallise due to their instability), and desolvation of solvated crystals can be detected over the heating process. Further, sublimation and physical vapour deposition can be observed under microscopy during the HSM analysis.

HSM results and the DSC analysis were correlated to TGA analyses that were also performed to assess % solvent content in samples. During the heating process on the HSM, the appearance of bubbles coming from the sample in an inert medium (e.g. silicone oil), usually indicated a solvent loss. Other thermal changes such as polymorphic transition and decomposition were indicated by colour changes in the sample being analysed.

3.4.2 Differential Scanning Calorimetry (DSC) analyses

Understanding thermal behaviours during drug discovery and development is an essential step in the supramolecular synthesis. DSC analysis plays a remarkable role in the process of drug development. DSC is one of the most common thermal analysis (TA) techniques, which has been widely used to evaluate the thermal stability of a variety of substances (Abd-Elghany & Klapötke, 2018). Today, it is not easy to find substances which have not yet been studied

The wide range of DSC applications of which some are shown in **Figure 3.14** and its capabilities in different fields make this instrument a very useful tool. Those applications include but are not limited to the determination of the characteristic temperatures such as melting, crystallisation, polymorphic transitions, reactions, glass transition), melting, crystallization, transformation, and reaction heats (enthalpies), the crystallinity of semi-crystalline substances, decomposition, thermal stability, oxidative stability, degree of curing in materials such as resins, adhesives, purity determination of low molecular mass compounds, specific heat and compatibility between components (Abd-Elghany & Klapötke, 2018).

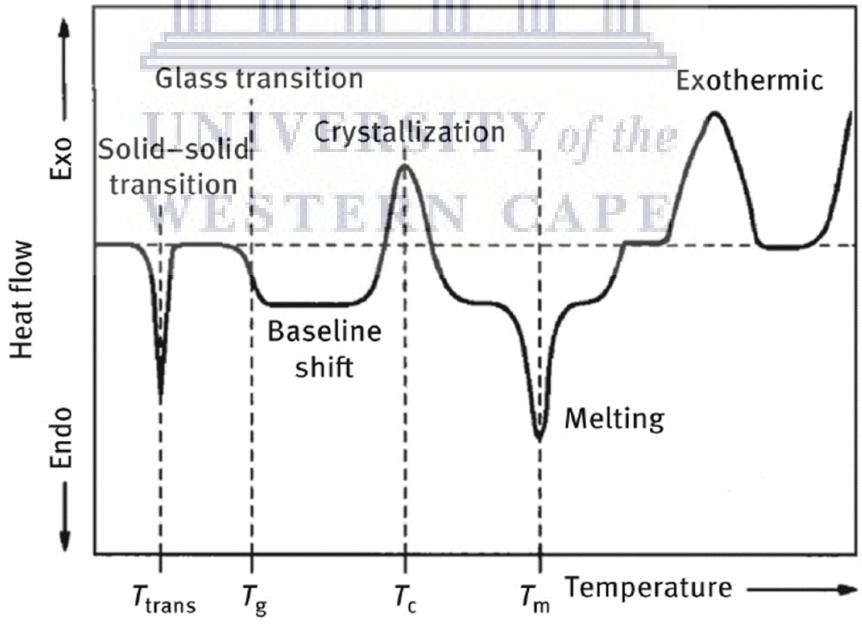

Figure 3.14: Different information or typical transition obtained in DSC spectrum

Different events may occur during thermal analysis by DSC (**Figure 3.14**.), some of which are endothermic and others exothermic. Interpretation of these and deduction of

what exactly is happening can be very tricky and requires a basic understanding of thermodynamics.

In this research, an 8000 Perkin-Elmer DSC (**Figure 3.15**) (Waltham, USA), incorporating a cooling system was used at a scanning rate of 10^{o}C per min, under N_2 gas (99.8%) purged with a flow rate of 20 mL/min. DSC traces were recorded from room temperature to 20^{o}C above the melting point of the drug being analysed. Sample sizes were in the range of 1-4 mg for all compounds. Crystalline samples were taken from the vial, dried on filter paper, and crushed to appropriate particle size, and sealed in an aluminium pan.

A sealed and empty pan was used as a reference. The DSC analyser was calibrated by measuring the onset temperatures of the melting of indium (m.p. 156.6^{o}C) and zinc (m.p. 419.5^{o}C) while the heat flow was calibrated from the enthalpy of melting of indium (28.62 J/g). Endothermic and exothermic peaks appearing in the DSC graphs were analysed in terms of their onset temperatures, the temperature range of the peak (determined from the first derivative of the trace), and the enthalpy of the peak (measured in J/g). Various endothermic and exothermic peaks observed in the DSC trace are associated with various thermal behaviours and were interpreted in correspondence with HSM to be associated with solvent loss, phase changes in the sample, and decomposition.

Figure 3.15: A differential scanning calorimeter and Intracooler II (right)

3.4.3 Thermogravimetric analysis (TGA)

Thermogravimetric analysis (TGA) is another TA widely used in research and development of different substances and engineering materials. TGA has recently been used in quality control and assurance of different raw materials. TGA changes in the mass of the sample are measured as a function of temperature and time under controlled atmospheric conditions and temperature program. Loss of mass during TGA experiments may occur due to the presence of volatile components such as absorbed moisture, residual solvents, or low molecular mass additives or oligomers that generally evaporate, decompose, oxidate, etc. In general, TGA generates information such as composition, the extent of cure, and the thermal stability of the samples (Prime et al., 2008).

However, A TG thermogram graphically shows the sample mass change vs temperature or time. These changes are unique from one compound to another. Like DSC, some of the common applications of the TGA in pharmaceutical sciences include the characterisation of the physicochemical properties of crystalline solids (single or multi-components) and the detection and identification of polymorphic forms, solid dispersions, and other polymeric dosage forms. TA techniques are also used to investigate the effects of lyophilisation as well as develop optimal lyophilisation formulations and cycles.

In this work, a 4000 Perkin-Elmer PC thermal system (Waltham, USA) was used (**Figure 3.16**). Calibration of the instrument was performed using three different references; Alumel (m.p. = 154.2°C), Perk alloy (m.p. = 596.00°C) and iron (m.p. = 780°C) at 1 and 2°C/min. The samples analysis was carried out over a temperature range between 30°C – 400°C at a predetermined heating rate of 10°C/min. Samples were continuously purged by a stream of dry (99.8%) nitrogen gas (20 mL/min), and solvent stoichiometry of the compounds was determined from the percentage mass loss.

The TGA was used to measure the mass loss of samples as a function of temperature and the decomposition of desolvated materials. An empty ceramic crucible was weighed first inside the instrument to re-zero the weighing scale of the instrument. The sample (crystalline or powder) was then placed into the crucible, and the weight was recorded. The programmed TG technique was carried out over a temperature range between 30°C and 400°C at a predetermined heating rate of 10°C per minute. Samples

were continuously purged by a stream of dry nitrogen gas, and the solvent stoichiometry of the compounds, as well as decomposition, was determined from the percentage mass loss.

Figure 3.16: The thermogravimetric analyser with a digital temperature controller

3.4.4 Morphology study by scanning electron microscopy (SEM)

Scanning electron microscopy (SEM) is one of the most versatile analytical tools used to analyse a wide range of materials, including pharmaceuticals. The instrument is equipped with its powerful electron microscope that produces high-resolution images of the specimen. The sample is struck with a beam of high energy electrons focussed on one spot resulting in an emission of secondary high energy electrons (backscattered) which then generate images of the best quality. Diffracted secondary electrons are used to determine the structure of the sample exposed (Goldstein et al., 2017).

Its applications also include the use of energy-dispersive X-ray spectroscopy (EDS) to acquire elemental maps or spot chemical analyses. Phase discrimination is based on the mean atomic number, compositional maps using transition metals, and rare earth metals. Additionally, when equipped with diffracted backscattered electron detectors, SEM can be used to examine crystallographic orientation in many materials and microfabric (Goldstein et al., 2017).

Morphology of individual pure drugs and the synthesised co-crystals were conducted using an AURIGA Field Emission High-Resolution Scanning Electron Microscope

(HRSEM), Zeiss (Germany) (**Figure 3.17**). Powder samples were mounted onto aluminium stubs using carbon tape. The energy (kV) used for images was 5 kV and 20 kV for EDS. The lament current was set at 2,359 amps. Carbon tabs were placed on the aluminium stubs to hold samples. Working distance (WD) for images is displayed on each image. SmartSEM 90 and AZTEC software were used for imaging and EDS, respectively.

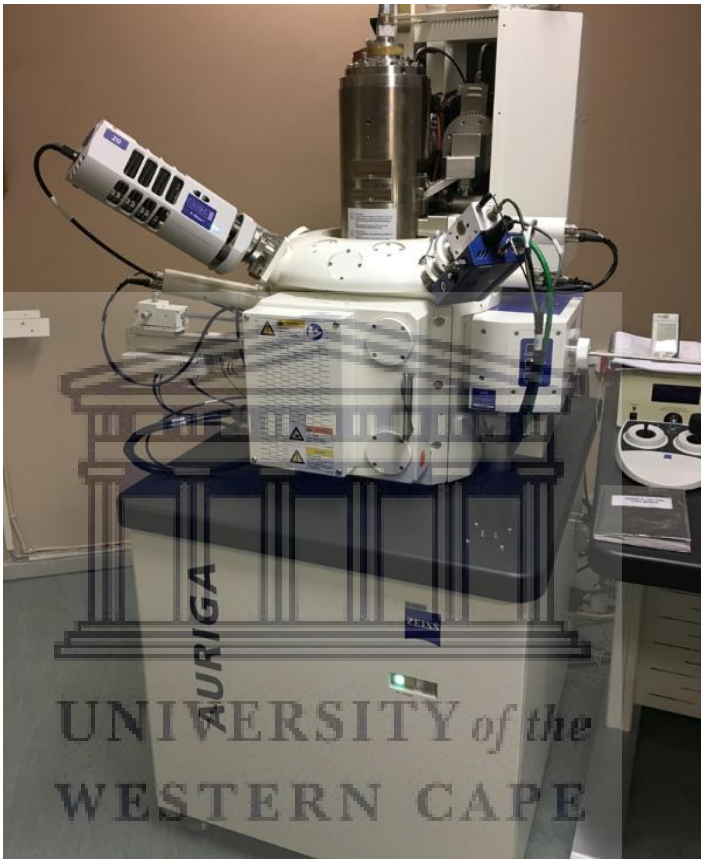

Figure 3.17: Scanning electron Microscopy (Auriga)

3.4.5 Characterization by Fourier Infrared spectrophotometry

Infrared spectra of the parent drugs and the co-crystals or other solid-state sample products were obtained using a Perkin-Elmer 100 FTIR instrument (**Figure 3.18**) fitted with UATR and controlled with Spectrum® software version 6.3.5.0176 for the analysis of samples.

Samples were analysed mostly in a powder form or crystalline form over the range of 600-4000 cm^{-1} at a spectral resolution of 2 cm^{-1}. The percentage of transmittance was recorded against frequency. This analytical technique was used to investigate different

functional groups in samples and to prove the existence of intermolecular interactions during the co-crystal/complexation processes.

Figure 3.18: Spectrum 400; the FT-IR/FT-NIR spectrometer

3.4.6 Characterisation by solid state-NMR

NMR is one of the most powerful spectrometric techniques used for structure analysis of compounds due to its ability to access information of the chemical structure at a molecular level.

3.4.7 Characterisation by Powder X-Ray Diffraction (PXRD)

single-crystal X-ray diffraction provides direct, complete, and accurate structural information on molecular and supramolecular structures. However, the applicability of this method is always limited to the requirement of good quality and single-sized crystal, which is not always possible to find. Due to this restriction and the increasing interest in mechanochemical syntheses of powder co-crystals and other solid-state multicomponent samples, powder X-ray diffraction (PXRD) has proven to be a powerful non-destructive method (Karki et al., 2007).

In this work, the PXRD was used to determine the characteristic patterns of crystalline materials. New materials species such as polymorphs, complexes, and co-crystals can be identified using this technique. This technique is particularly used in the absence of good quality crystals suitable for single crystal structure determination.

The PXRD in this work was used to confirm new phases and co-crystal formation. Changes in diffracted patterns occur due to changes in the crystal lattice, and this is the key to the identification of newly formed materials.

The PXRD data were identified and recorded using a D8 Advance powder X-ray diffractometer (Bruker AXS GmbH, Germany) with Cu K radiation (= 1.54056). The tube voltage and current applied were 35 kV and 40 mA, respectively. A V20 variable slit was used. Samples were placed on the sample holder, which has 1 mm thickness and 1.5 cm in diameter. With a scan rate of 2°per min, the sample scan was performed in a continuous scan in locked coupled mode, within a range of 2θ 5° to 50°. OriginPro 8.5 was used to plot PXRD patterns.

Powder patterns of ground samples were recorded on a D8 Advance (**Figure 3.19**) with Ni-filtered CuKα radiation (λ = 1.5406 Å) produced at 40 kV and 40 mA. Samples were packed in aluminium or glass sample holders and step scans of 0.034° 2θ, with 0.5 seconds counting times, in the range 4-50° 2θ.

Figure 3.19: D8 ADVANCE Eco – powder diffraction for powder samples

3.4.8 Solubility evaluation by High-Pressure Liquid Chromatography

Different methods have been designed and used based on the nature of the active substances being evaluated. Generally, three HPLC systems Agilent and Perkin Elmer and Azula, have been used at determined acquisition parameters.

Four buffer solutions were prepared from different proportions of hydrochloric acid, monobasic potassium phosphate (0.2 M), and sodium hydroxide (solution 0.2 M), as follows: pH 1.2 (HCl 0.1N), pH 4.5 (Acetate), pH 6.8 (KH_2PO4 and NaOH), pH 7.4 (KH_2PO4 and NaOH).

Excess amounts of the individual drugs and their respective co-crystals/solid hybrids were added to USP aqueous buffer solutions at HCl 0.1M, pH 4.5 (acetate), pH 6.8 (phosphate), and pH 7.4 (phosphate) and water. The incubator shaker was used to keep samples at 37°C during the test with the agitation of 100 rpm for 48 hours (until achieving the equilibrium condition). After this period, samples were immediately filtered (0.45 µm PVDF syringe filter) and diluted in a volumetric flask with the corresponding media and analysed in HPLC.

APIs in different co-crystals/complexes were quantified using three different HPLC systems; an Agilent HPLC system setting with FXBPump (Flexar Binary Pump), an automated injector equipped with a UV detector (LC 200a Series PDA Detector), and a Flexar autosampler. Due to the nature of the samples, different acquisition methods were used. A reversed-phase Supelco Discovery HS C_{18} HPLC column 15 cm x 4 mm, 5μm was utilized. Injection volume was 10 µL, and absorbance of elution was recorded at the necessary wavelength following suitable dilutions. It is worth noting that elution, flow rates, column and mobile phases are subjected to change based on drug substances or products being evaluated.

3.4.9 *In vitro* antimicrobial activity

The in *vitro* antibacterial activity of the antitubercular drugs produced co-crystals, and other solid forms were assessed by tube dilution method against both *Mycobacterium tuberculosis* (Mtb) H37Rv (ATCC 27294) and pan-susceptible clinical isolate strains. Pyrazinamide was used as a standard antimycobacterial drug.

The stock solution of 62.5 mg/ml concentration for each test and standard drugs was prepared using 100% dimethyl sulfoxide (DMSO), then brought to a working solution

of 8445.9 µg/mL by diluting the stock solution by 1:7.4 with 100% DMSO. Two further 1:10 dilutions were made from the working solution to give 844.6 µg/mL and 84.5 µg/ml, respectively.

3.4.9.1 Preparation of growth media

Growth media were prepared by adding dehydrated medium (19 g) to purified water (900 ml) containing glycerol (15 ml). The mixture was stirred well to dissolve and autoclaved at 121°C for 10 min. Oleic acid-albumin catalase (100 ml) was aseptically added to the medium after cooling to 45°C. No adjustment for pH was made.

3.4.10 Other computer sources

The Cambridge Structural Database (CSD) Conquest 2.0.1 and Mercury 4.1.3 were used to search for relevant structures reported in this work. CSD which was initially known as the computer-based file that contains information on bibliography and literature abstracted data relevant to the molecular crystal structure now contains a complete record of all published organic and metal-organic small-molecule crystal structures with more than 800 000 CSD entries (Groom et al., 2016). ACD/ChemSketch® and ChemDraw Ultra 12.0 were utilized to draw different structures relevant to the dissertation. Furthermore, software such as Origin Pro 8.5 and IBM SPSS statistics 25 was used to process different graphs in this work

3.5 Conclusion

APIs discussed in this chapter were selected due to their potential activity against HIV and tuberculosis except 1-adamantylamine that was included due to its antiviral activity against influenza A. A short history, properties, and the mechanism of action were briefly discussed. Furthermore, the ability to co-crystallisation and where applicable, some examples of co-crystals synthesized from the above APIs were highlighted. **Table 3.1** and **Table 3.2** summarise the basic properties of all APIs above and the GRAS co-former. The chapter also introduces experimentation that involves co-crystal screening and preparation, and characterisation of results.

Table 3.1: Basic physicochemical properties of APIs selected for this project

APIs	Melting point	Molar mass (g/mol)	Physical state	Structure	Aqueous Solubility
Nevirapine	247°C	266,29	Crystalline	$C_{15}H_{14}N_4O$	Poor
Efavirenz	136°C	315,67	Crystalline	$C_{14}H_9ClF_3NO_2$	Insoluble
Zidovudine	122°C	267,24	Crystalline	$C_{10}H_{13}N_5O_4$	Soluble
Lamivudine	178°C	229.26	Crystalline	$C_8H_{11}N_3O_3S$	Soluble
Amantadine	192°C	151.25	Crystalline	$C_{10}H_{17}N$	Sparingly
Isoniazid	171°C	137.14	Crystalline	$C_6H_7N_3O$	Soluble
Pyrazinamide	192°C	123.12	Crystalline	$C_5H_5N_3O$	soluble

Table 3.2: Basic physicochemical properties of a co-former selected for this project

GRAS co-former	Melting point	Molar mass (g/mol)	Physical state	Structure	Aqueous Solubility
Glutaric acid	98°C	132.12	Crystalline	$C_3H_6(COOH)_2$	soluble

Chapter 4 Dual-drug co-crystals and eutectics of selected anti-HIV drugs: Non-covalent synthesis and characterisation

This chapter expounds on the preparation procedures and discusses the results of the co-crystallization experiments of the selected four antiretroviral drugs. The physicochemical characterization of each successfully produced solid-state hybrid is conclusively discussed herein.

4.1 Introduction

Preformulation, as a very important step in drug development, provides an insight into the physical and chemical properties of a drug, properties that could affect the performance of a drug and/or affect later stages of drug development, before subjection to the compounding process. Exploring the co-crystallisation aspect of supramolecular chemistry is growing at a high pace with regulatory bodies favouring the use of this approach due to its extraordinary way of enhancing properties.

Co-crystal formation as a crystal engineering approach is used to enhance the properties of crystalline drugs. As discussed in section **2.4** of **Chapter 2**, a co-crystal is formed between at least two components; one being a neutral/ionic drug and the other one being a Generally Regarded as Safe (GRAS) listed drug, also known as a co-crystal former. Particularly, pharmaceutical co-crystals are produced between active pharmaceutical ingredients (APIs) and a safe co-crystal former.

4.2 Materials and methodologies

4.2.1 Materials

As part of the co-crystallization process, four anti-HIV (human immunodeficiency virus) drugs, i.e. two nucleoside reverse transcriptase inhibitors (NRTIs) lamivudine (3TC) and zidovudine (AZT) and two non-nucleoside reverse transcriptase inhibitors (NNRTIs) efavirenz (EFV) and nevirapine (NPV); were selected due to their potential inhibitory activity on the reverse transcriptase protein. These active substances were

donated by Aspen Pharmacare Pharmaceutical company (7 Fairclough Rd, Holland Park, Port Elizabeth, 6001 South Africa) and were used as received.

4.2.2 Co-crystal screening and preparation

4.2.2.1 EFZA co-crystal preparation

Dry grinding (DG) and liquid assisted grinding (LAG) methods were used to prepare the EFZA samples (Error! Reference source not found.). The screening process was carried out by taking both actives in different stoichiometric ratios (1:1, 1:2, 1:3, 2:1, 3:1) into a marble mortar and were co-ground physically using a pestle. The grinding process was performed for at least thirty minutes to ensure a complete co-crystallisation.

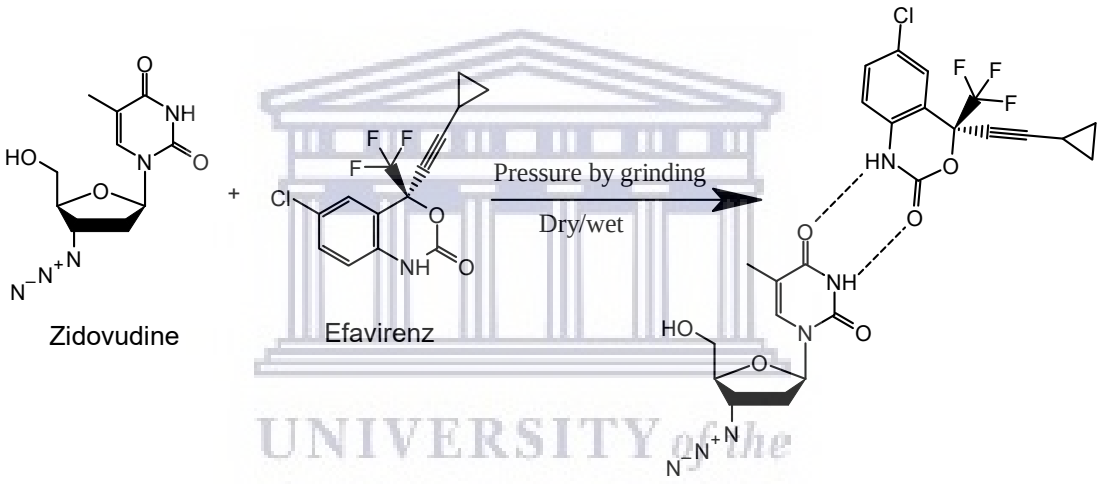

Figure 4.1: The proposed molecular mechanistic for the preparation of EFZA dual-API co-crystal

Where solvent was used, a dropwise addition was done throughout the grinding process. Furthermore, an equimolar amount of both APIs was slurred in methanol overnight. Samples were then characterised to identify, evaluate their different behaviours, and confirm their nature. Supporting information on the screening process has been included in Appendix A. Based on the preparative methods; EFZA prepared in a 1:1 molar ratio by solid-state co-grinding method achieved the following positive co-crystal results. The experiments were repeated to ensure that samples are reproducible.

4.2.2.2 NEF co-crystal preparation

A dual-API co-crystal between EFV and NVP was prepared by solid-state grinding (**Figure 4.2**). Equimolar amounts of APIs (EFV = 0.118 g) and (NVP = 0.1g) were

ground in a mortar using a pestle for the minimum period of thirty minutes. The sample was immediately analysed or stored in an airtight container before analysis. The sample's reproducibility was ensured by repeating the experiment twice. Other experiments done during the screening exercise were included in **Appendix A**.

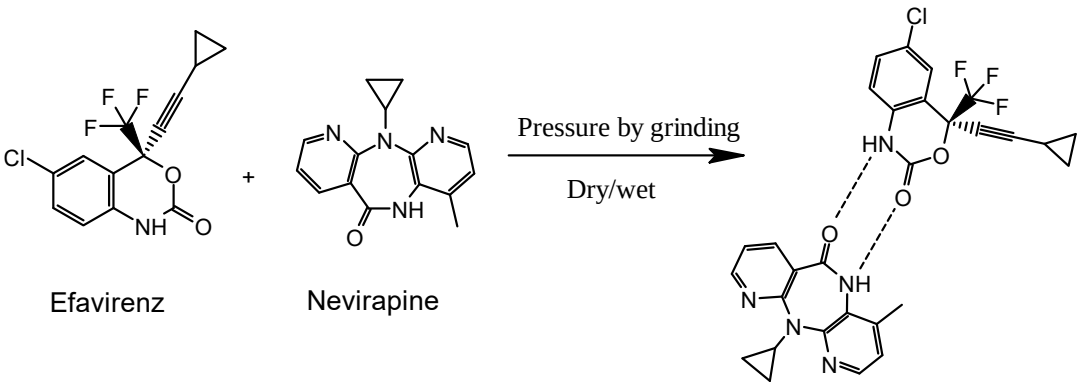

Figure 4.2: Molecular mechanistic for the preparation of NEF dual-API co-crystal

4.2.2.3 Binary eutectic LMZT preparation

For the sample preparation of LMZT, the accurate amounts of the two drugs [AZT (0.2mg) and 3TC (0.17mg)] in a 1:1 stoichiometric ratio, were placed in a mortar and the mixture was co-milled using a pestle (**Figure 4.3**) for thirty minutes. The resulted white crystalline powder was kept in the sealed glass polytop vial for further characterised.

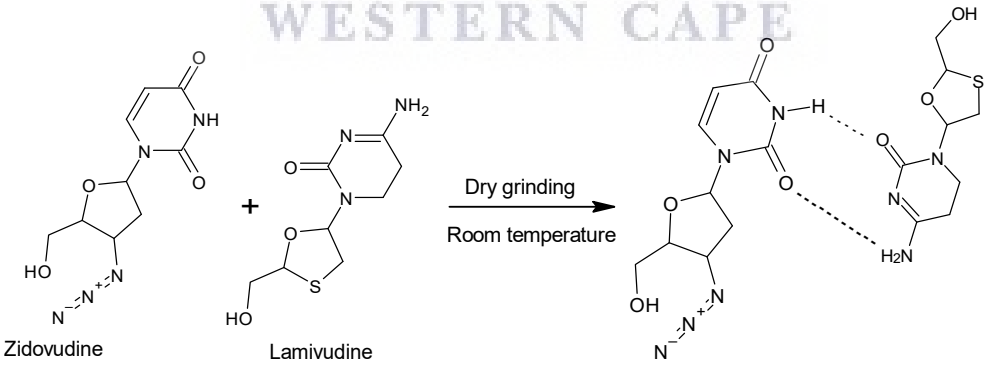

Figure 4.3: Molecular mechanistic for the preparation of LMZT eutectic mixture

4.2.2.4 NVZA solid forms preparation

Different approaches were used to screen for co-crystals between NVP and AZT, two antiretroviral drugs belonging to different classes of the reverse transcriptase inhibitors. Co-crystal preparation techniques such as solid-state grinding and solution

crystallisation have been explored. Co-crystallisation of nevirapine (NVP) with Zidovudine (AZT) relies on the complementarity of their functional groups based on which the following structure was estimated (**Figure 4.4**). To the best of our knowledge, there is no dual drug co-crystal reported on these APIs.

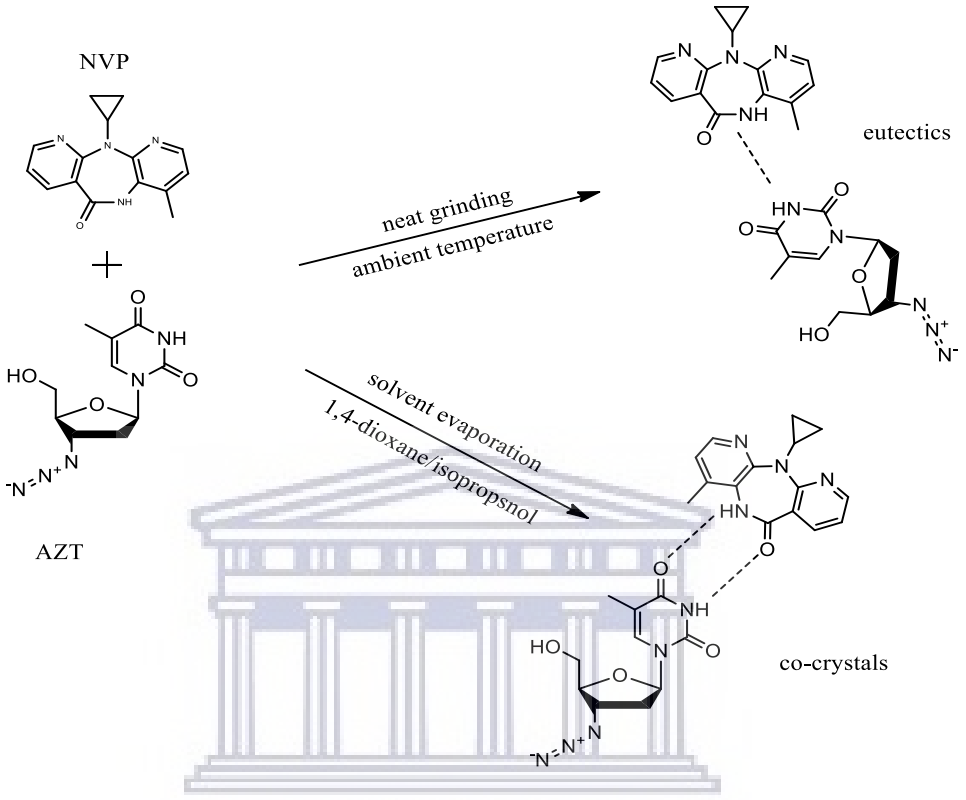

Figure 4.4: The molecular mechanistics for the preparation of NVZA derivative solid forms.

4.2.2.5 Screening and preparation of dual drug solid forms (NVZA)

Initially, the co-crystal screening was carried out using grinding methods. 1:1, 1:2, 1:3 and 2:1 stoichiometric ratio of starting materials NVP and AZT were co-milled manually in a marble mortar for about thirty minutes using a pestle. The resulted powder samples (**NVZA1**) were stored in airtight containers for further characterization.

Co-crystallisation was also attempted by dissolving different stoichiometric ratios of pure NVP and AZT in a variety of solvents. From the solvent evaporation method;

Firstly, the crystal sample was prepared by dissolving 1:1 and 2:1 stoichiometric amount of the active substances in 2 mL of 1,4-Dioxane in separate polytop vials. Using the magnetic stirrer, both mixtures (drug + solvent) were continuously stirred at

predetermined rpm and elevated temperature to 10°C below 1,4-Dioxan B.P., until clear solutions were obtained. The two solutions were subsequently mixed and stirred for about ten minutes, filtered (0.45 μm), and stored in a clean polytop vial sealed with a perforated parafilm® to allow controlled evaporation at room temperature. The crystalline powder sample (**NVZA2**) was scratched out of crystallization vial and characterised immediately.

NVZA2 was further obtained by dissolving the equimolar mass of input materials (AZT and NVP) in a known amount of propane-2-ol using a magnetic stirrer, at elevated temperature (10°C below propane-2-ol B.P.), filtered using nylon filters (0.45) and covered with perforated parafilm paper. Finally, the sample was placed in a stable environment to evaporate at room temperature. A resulted crystalline powder sample was analysed immediately.

A new derivative solid form (**NVZA3**) was produced by the slurry method. Both input material in a 3:1 molar ratio was accurately weighed and transferred into the separate polytop vials, then an amount of 1,4-dioxane was added to each. The suspensions were stirred on the hot plate using a magnetic bar, with the temperature raised to 50°C. Obtained clear solutions were combined and stirred for an additional 5 minutes, and filtered and slurred at 20°C for two days. The powder sample named **NVZA3** was collected and stored in an airtight container for subsequent analyses.
Unfortunately, no crystals of good quality obtained for single x-ray diffraction. Due to this, there was no structure elucidated. All samples were produced in triplicate to ensure reproducibility and analysed according to methods described in section **4.2.3**.

4.2.2.6 EL solid forms preparation

A physical co-crystal screening performed using different methods revealed that two types of solid forms were produced depending on the ratio used. Stoichiometric ratios such as 1:1, 3:2, 1:2, 1:3, 2:5 and 1:4 were used in the preparation attempt of **EL** dual-API co-crystal. Different mixtures of EFV and 3TC were prepared according to the above molar ratios, and then co-ground physically using an agate mortar and a pestle for thirty minutes (**Figure 4.5**). The powder samples obtained were stored in sealed vials and characterized later. All samples and the starting materials EFV and 3TC were analysed using a series of characterisation techniques described in section 4.2.3.

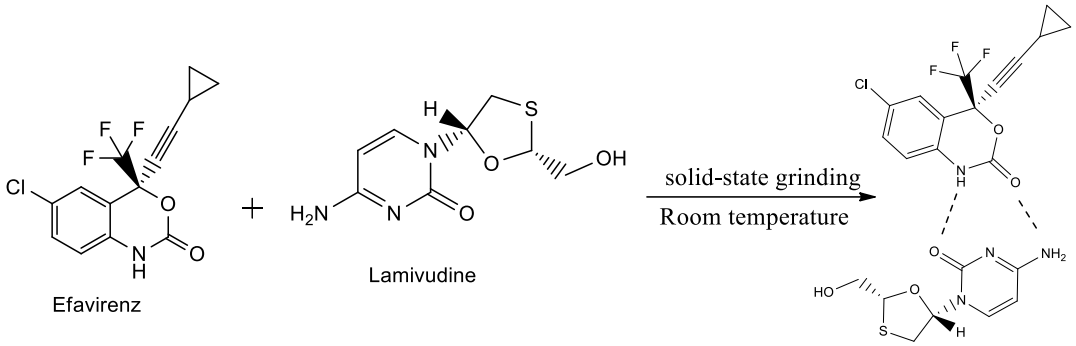

Figure 4.5: Molecular mechanistic for the preparation of EL eutectic mixture

4.2.2.7 NL solid forms preparation

The neat or solid-state grinding approach (**Figure 4.6**) was used in the attempt to produce a co-crystal between NVP and 3TC. A mixture of parent drugs in different molar ratios; 1:1 (NVP=2mg; 3TC=1.7mg), 2:1, 2:3, 3:1 and 4:1 were accurately weighed in a marble mortar and manually co-ground for 30 minutes using a pestle. The powder samples produced were kept in sealed polytop vials prior to analyses to avoid any contamination. Samples were characterised using a series of complementary analyses, from thermal, particle morphologies to structural analyses and in-vitro solubility evaluation.

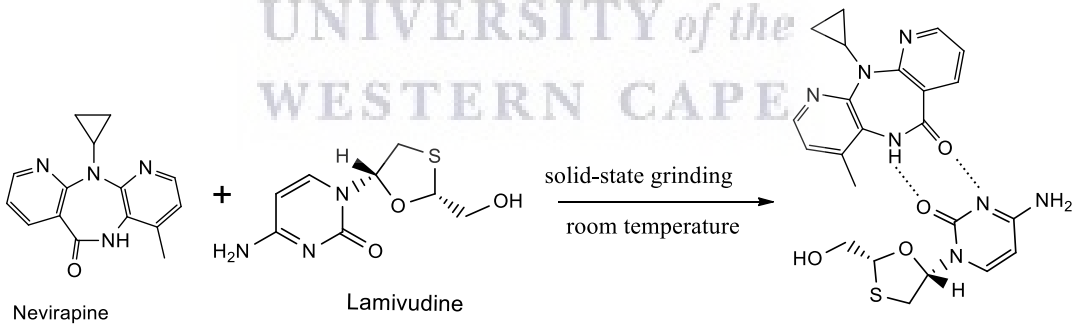

Figure 4.6: Molecular mechanistic for the preparation of NL eutectic mixture

After a complete analysis, it was confirmed that a binary eutectic named **NL** was produced using (1:1 and 2:3) molar ratios. The co-crystallisation attempts by solution crystallisation in solvents such as propane-2-ol, butanol, acetonitrile, acetonitrile-methanol, ethanol and methanol were unsuccessful. A full experimentation report is given in Appendix A. all samples were reproduced three times.

4.2.3 Characterization of the samples

A full characterization was carried out for obtained samples vs their starting materials. Thermal analysis using the Hot Stage Microscopy, Differential scanning calorimetry, and thermogravimetric analyses. Sample morphologies were evaluated using Scanning electron Microscopy, while structural information and molecular identities of samples were obtained from Fourier infrared spectroscopy and the powder X-ray diffraction. In vitro solubility of samples was measured using PHLC.

4.2.3.1 Analysis by Hot Stage Microscopy (HSM)

Thermo-microscopic analyses were performed with an optical microscope Olympus (SZX-ILLB200) equipped with a Linkam temperature-controlled stage (THMS600/720), connected to a T95-PE system controller (Linkam Scientific Instruments Ltd., Tadworth, Surrey, UK). Images were recorded with an Olympus UC30 camera attached to the specified microscope (Olympus Optical, Japan) using Stream Essentials software. Samples were heated over a temperature range of 30 C - 350°C at a constant heating rate of 10°C/min, with samples submerged in silicon oil. The hot-stage was calibrated using USP melting point standards.

4.2.3.2 Analysis by Differential Scanning Calorimetry (DSC)

DSC analyses were performed using a DSC 8000 Perkin Elmer instrument (Waltham, USA), incorporating a cooling system. Samples (2.5 - 5 mg) were crimped in the aluminium pans sealed with pierced lids. The instrument was calibrated by measuring the onset temperatures of the melting of indium (m.p. 156.6 ^{o}C) and zinc (m.p. 419.5 ^{o}C) while the heat flow was calibrated from the enthalpy of melting of indium (28.62 J/g). The samples were heated to 20-30 °C above the melting range of the most thermally stable, at a heating rate of 10°C/min. All analyses were performed under continuous pure (99.8%) dry nitrogen purging with a flow rate of 20 mL/min) and were reproducible.

4.2.3.3 Analysis by Thermogravimetry (TGA)

A Perkin-Elmer 4000 PC thermal system (Waltham, USA) was used. Calibration of the instrument was performed using three different references; Alumel (m.p. = 154.2 °C), Perk alloy (m.p. = 596.00 °C) and iron (m.p. = 780 °C) at 1 and 2°C/min. The samples analysis was carried out over a temperature range between 30 °C – 400 °C at a predetermined heating rate of 10°C/min. Samples were continuously purged by a

stream of dry (99.8%) nitrogen gas (20 mL/min) and solvent stoichiometry of the compounds was determined from the percentage mass loss.

4.2.3.4 Morphology evaluation by Scanning Electron Microscopy (SEM)

The morphology of individual pure drugs and co-crystal samples were conducted using an AURIGA Field Emission High-Resolution Scanning Electron Microscope (HRSEM), Zeiss (Germany). Powder samples were mounted onto aluminium stubs using carbon tape. Energy (kV) used for images was 5 kV and 20 kV for EDS. The lament current was set at 2,359 amps. Carbon tabs were placed on the aluminium stubs to hold samples. Working distance (WD) for images is displayed on each image. SmartSEM 90 and AZTEC software were used for imaging and EDS, respectively.

4.2.3.5 Analysis by Fourier Transform Infrared Spectrophotometry (FT-IR)

Infra-red spectra of the individual drugs and the co-crystal samples were obtained using a Perkin-Elmer 100 FTIR instrument (Waltham, USA) fitted with UATR and controlled ® with Spectrum software version 6.3.5.0176 for the analysis. Analyses of powder or crystalline samples were done over the range of 650-4000 cm^{-1} at a spectral resolution of 2 cm^{-1}.

4.2.3.6 Analysis by Powder X-Ray Diffraction (PXRD)

PXRD data were recorded on a D8 Advance powder X-ray diffractometer (Bruker AXS GmbH, Germany) with CuKαradiation (Cu-$K\alpha_1$= 1.54056 Å). The tube voltage and current applied were 35 kV and 40 mA, respectively. A V20 variable slit was used. Samples were placed on the sample holder which has 1 mm thickness and 1.5 cm in diameter. With a scan rate of 2°per min, the sample scan was performed in a continuous scan in locked coupled mode, within a range of 2θ5°to 50°. Origin Pro 8.5. was used to plot PXRD patterns.

4.2.3.7 *In vitro* solubility studies

Excess amounts of the individual drugs zidovudine and lamivudine and their respective co-crystals were added to USP aqueous buffer solutions at pH 1.2 (0.1M hydrochloric acid), 0.2M potassium phosphate buffer (pH 6.8 and pH 7.4, and 0.1% SDS. The mixtures were continuously shaken in an incubator shaker at 37 °C (± 0.5 °C) and 100 rpm for 24/48 hours. Samples were filtered using 0.20 μm PVDF syringe filters and analysed using an HPLC. Individual APIs, and co-crystals/eutectic mixtures were

quantified using an Agilent HPLC system setting with FXBPump (Flexar Binary Pump), an automated injector equipped with a UV detector (LC 200a Series PDA Detector), and a Flexar autosampler. Isocratic/gradient elution was specific for each analysis and was applied at a flow rate of 1 mL/min. Two reversed-phase columns; Luna C_{18}HPLC 250 mm x 4.6 mm, 5μm and a supercol 150 mm x 4.6 mm, 5μm were used. Injection volume was 10 µL and absorbance of elution was recorded at a specified nm following suitable dilutions. All analyses were conducted in triplicate.

4.3 Results and discussions

4.3.1 Efavirenz: zidovudine dual-drug co-crystal (EFZA)

4.3.1.1 Thermal analyses of results

Thermal analysis was initiated by observing thermal behaviour using HSM (**Figure 4.7**). With the sample submerged in silicone oil, and the temperature raised steadily, thermal changes were observed and recorded on HSM comparatively to the DSC results. A melting transition was observed in the temperature range between 96°C and 105°C. No other identifiable changes occurred until decomposition of the sample.

Figure 4.7: The HSM images for EFZA co-crystal recorded at room temperature and the temperature range over which occurred the sample of the sample (96-111°C)

DSC has been proven to be a reliable, rapid tool used to confirm co-crystal formation (Saganowska & Wesolowski, 2018). From the DSC curve, it was observed that not only did the melting transition in EFZA co-crystal shift to a lower temperature in comparison to both individual APIs melting points, the intensity of the melting endotherm also changed accordingly. While pure AZT and EFV exhibited sharp melt endotherms at 121°C and 139°C, respectively (**Figure 4.8**), the melting transition for EFZA was confirmed by a single endotherm at 98°C (onset = 95.6°C). This was the initial

indication of the possible interactions between the co-formers and change in the crystal lattice of one drug in the presence of the other. Both HSM and DSC analyses were conducted in triplicate.

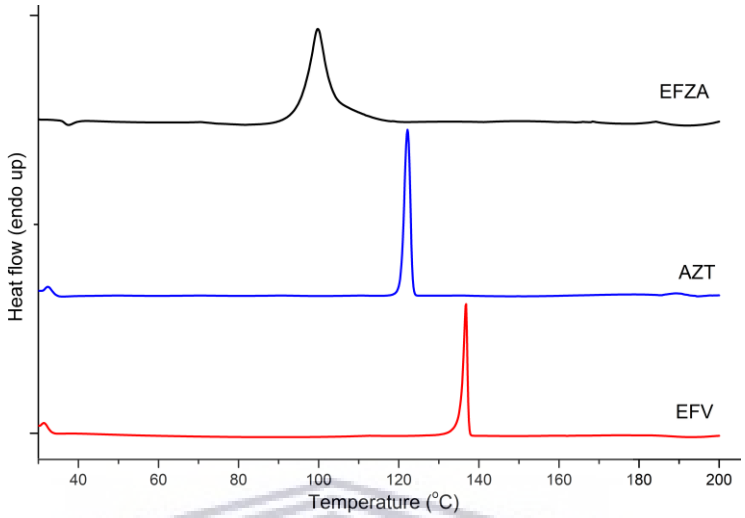

Figure 4.8: The DSC curves of the starting materials EFV and AZT compared to the co-crystal EFZA curve showing an earlier melting transition peak.

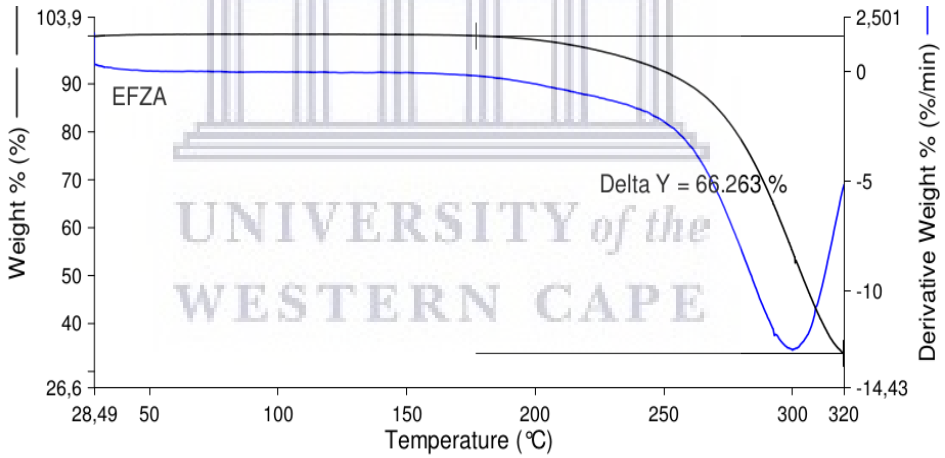

Figure 4.9: The TGA and DTA curves for EFZA supramolecular co-crystal showing a total decomposition mass loss of 66.3%.

The absence of any guest molecules in the sample was confirmed by thermogravimetric analysis (TGA). The TGA/DTA curves presented in **Figure 4.9** show no mass loss before the melting range and confirm the absence of any volatile guest molecules in the EFZA co-crystal sample. One step of mass loss is observed in the TGA curve over 190°C, suggesting the sample's degradation with a total loss of approximately 66.3%. This affirmation is consistent with the HSM analysis and the absence of additional

endotherms in the DSC curves. The TGA/DTA curves of both APIs are included in Appendix C.

4.3.1.2 Structural evaluation by Fourier transform infrared spectroscopy

FTIR is a useful technique for the identification of drug substances. A careful perusal of characteristic stretch vibrations of different functional groups enables researchers to identify molecules' structural information. With this, it is also possible to detect variations due to factors such as interactions with other molecules present. However, a complete structure elucidation requires the use of additional non-destructive techniques such as powder X-ray diffraction (PXRD) and solid-state NMR (SSNMR).

The FTIR spectra of AZT, EFV and EFZA, are depicted in **Figure 4.10**. In this work, spectral studies assessed the possible intermolecular interactions between EFZA co-crystal components EFV and AZT. *Ab initio*, pure drugs were analysed and used as a reference since their characteristic peaks agreed with spectra from literature.

The characteristic bands at 3314 cm^{-1} and 1742 cm^{-1} were attributed to N–H and C=O stretching vibration of the pyrimidine moiety in the EFV spectrum. The peak at 3095 cm^{-1} was assigned to N–H stretching vibration and 2250 cm^{-1} to C–H stretch while C–F stretching peaks at 1495 cm^{-1}. These characteristic peaks are in agreement with the analysis by Reddy *et al.* (2015).

In the AZT spectrum, all IR peaks agree with the previously reported data (Bansal et al., 2013; De O. Porfírio et al., 2015). The O–H/N–H stretch vibration peaked at 3460 cm^{-1}, aromatic stretch C–H at 3155 cm^{-1} and the peak at 1668 cm^{-1} was assigned to stretching C=O vibration of imide carbonyl. Further, the absorption band at 2081 cm^{-1} was due to a stretching azide N=N=N–C (Bansal et al., 2013).

The FTIR spectrum for EFZA was carefully examined (**Figure 4.10**, **Table 4.1**) in terms of various changes in frequencies. It was found that AZT peak at 3460 cm^{-1} (O–H stretch) had shifted to 3463 cm^{-1}, and band at 3176 cm^{-1} (N–H) shifted significantly from 3155 cm^{-1} while C=O stretch at 1668 cm^{-1} also shifted to 1684 cm^{-1}. On the other hand, the EFV absorption peak at 3095 cm^{-1} (C–H) subsides in the EFZA spectrum.

The EFV C=O stretching at 1742 cm^{-1} had shifted slightly to 1740 cm^{-1} and C–F stretch at 1495 cm^{-1} had shifted to 1497 cm^{-1}. The AZT C–N=C stretching at 2081 cm^{-1} had

also shifted slightly to 2084 cm^{-1}. Shifts and other changes originally not found in parent drugs' spectra, were referred to as consequences of intermolecular bonding between EFV and AZT. Furthermore, these changes were an indication that a newly derivatized entity had been supramolecularly formed. **Figure 4.11** presents the suggested best intermolecular bonding based on FTIR results. Analysis was done in triplicate.

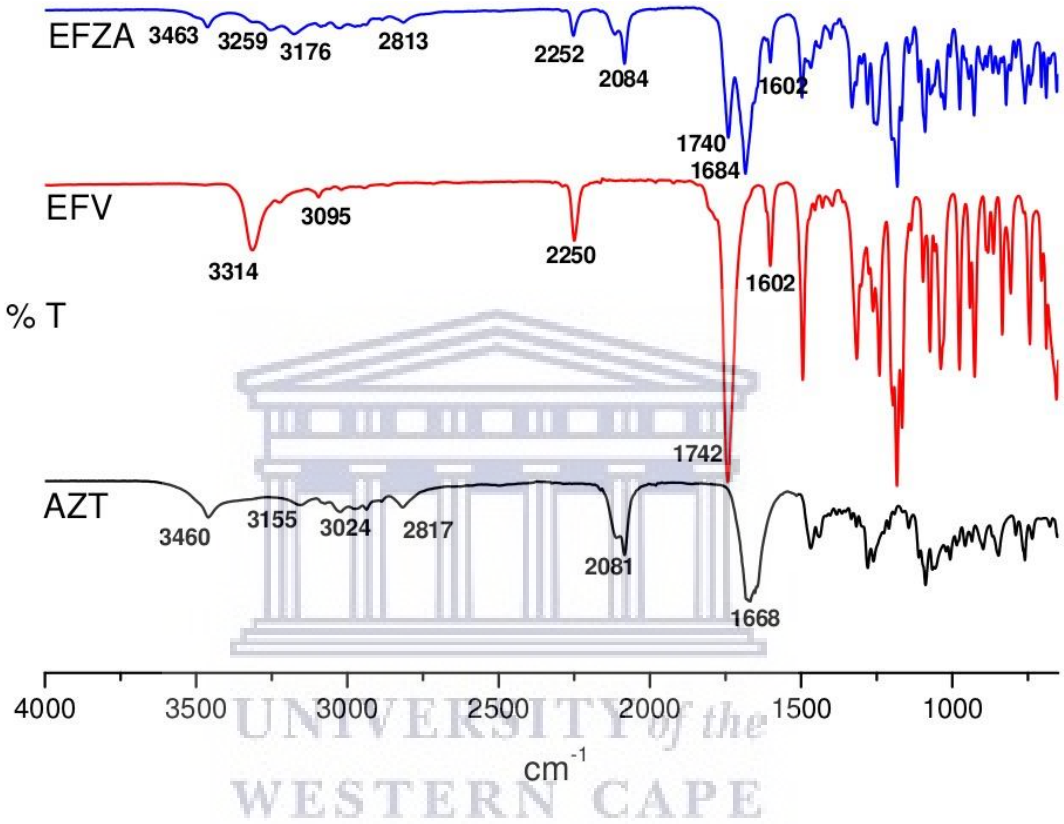

Figure 4.10: FTIR spectra for pure EFV and AZT compared to EFZA co-crystal.

Table 4.1: A summary of the most significant shifts in EFZA spectrum

Comments	AZT	EFV	EFZA
Carbonyl stretch C=O		1746 cm^{-1}	1740 cm^{-1}
Carbonyl stretch	1668 cm^{-1}		1684 cm^{-1}
Pyrimidinic stretching N–H	3155 cm^{-1}		3176 cm^{-1}
Hydroxyl stretch O–H	3460 cm^{-1}		3463 cm^{-1}
Strong stretching N–H		3314 cm^{-1}	Disappears
Aromatic ring C–H		3095 cm^{-1}	Disappears

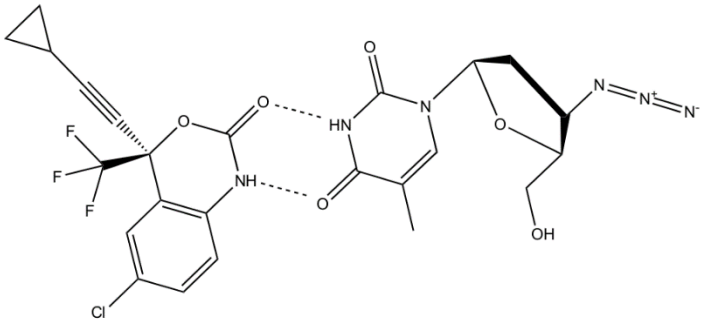

Figure 4.11: Suggested EFZA structure with probable interaction based on FTIR results

4.3.1.3 Analysis of the particle morphology of EFZA dual-API co-crystal

Morphology analyses were performed for active substances AZT, EFV, and EFZA co-crystal through SEM analyses. SEM micrographs are presented in **Figure 4.12**.

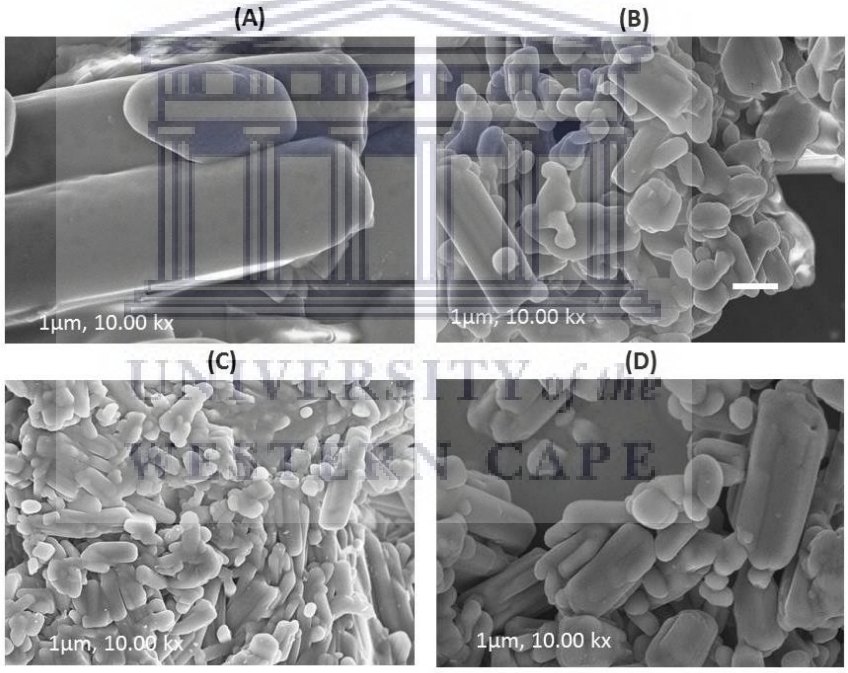

Figure 4.12: The SEM images of (a) pure AZT, (b) EFV-AZT physical mixture, (C) EFZA and (d) pure EFV

Particles of EFZA co-crystal (**Figure 4.12**c) showed very distinct morphologies from that of individual APIs. Pure EFV exhibited a polyhedral rod-shaped morphology (**Figure 4.12**d) while the AZT sample showed an irregularly shaped crystal habit with smooth surfaces. A physical mixture of two actives EFV and AZT showed particles of varied shapes inherited from individual drugs (**Figure 4.12**b). The EFZA co-crystal

sample is made of irregular particles with soft edges, increased uniformity/homogeneity, and reduced size due to milling exercise (**Figure 4.12**c).

4.3.1.4 EFZA analyses by Powder X-ray diffraction

Powder X-ray diffraction (PXRD), a non-destructive and preferable tool for identifying new phases of powdered samples, was used to ensure the co-crystal formation. PXRD patterns of EFV, AZT, EFZA sample and the physical mixture are shown in **Figure 4.13**.

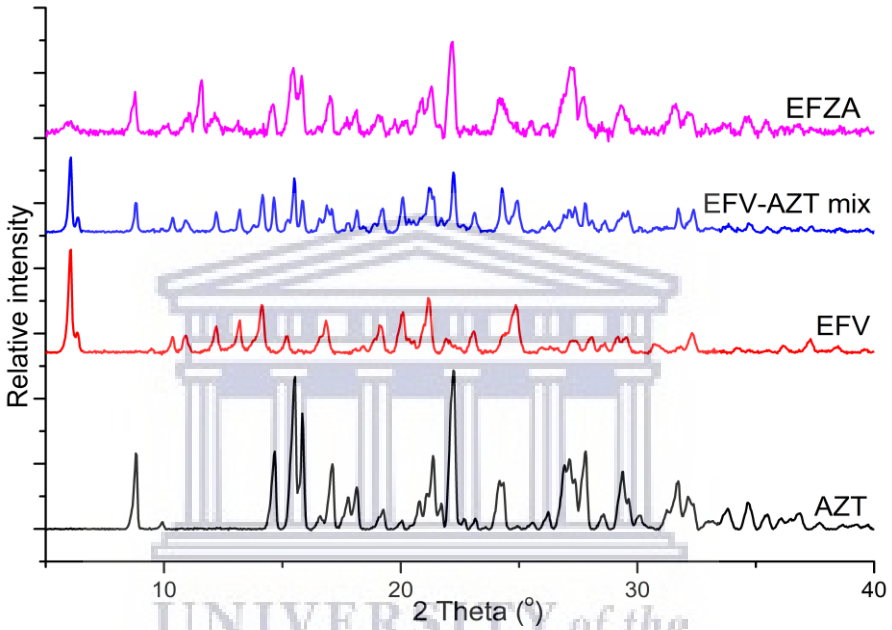

Figure 4.13: The experimental PXRD patterns of AZT, EFV, EFV-AZT physical mixture, and the co-crystal EFZA

The PXRD pattern of EFV has very sharp intense characteristic diffraction peaks at 2θ 6.00°, 14.12°, 21.10°, and 24.86°, medium peaks at 2θ 12.16°, 13.1°, 16.83°, 19° and small peaks at 2θ 10.3°, 10.83°, 15.15°, 21.84°, 23.00°, 27.1°, 27,9°, 29°, 32.27°, and 37.27°. AZT has three intense characteristic diffraction peaks at 2θ 15.49°, 15.83°, 22.18° and medium peaks at 2θ 8.84°, 14.67°, 17.1°, 21.39°, 27.12°, 27.77°, 29.35° and small peaks at 2θ 18.13°, 24.2°, 31.68°. Compared to pure APIs diffraction parameters, EFZA exhibited a PXRD pattern characterised by intense and very distinct diffraction peaks at 2θ 11.55° and 27.15°, confirming the new phase. The PXRD pattern also shows other less intense peaks with different shapes than diffraction peaks found in both AZT and EFV patterns (**Figure 4.13**).

4.3.1.5 The solid-state NMR analysis of EFZA co-crystal

Solid-state NMR (SS-NMR) is a powerful, non-invasive, and non-destructive analytical technique used to assess chemical, structural, and physical properties of solid-state pharmaceuticals. This technique is quite useful in providing vital information at the atomic level or even deeper. Such information on the local environment inside the crystal lattice and molecular mobility (Park et al., 2009), cannot be easily obtained from other powerful analytical techniques such as X-ray diffraction (Xu et al., 2016).

EFZA co-crystal sample was subjected to an in-depth characterization using 1D and 2D SSNMR methods to confirm the molecular association and other structural elucidation features such as hydrogen bonding (Vogt et al., 2009). The numbering of the co-crystal formers was used to discuss experimental results. For the 1D experiment, the 1H-MAS SSMNR and 13C CP-MASS SSNMR experiments were conducted. Different experiments have been conducted for the best resolution and interpretation of the sample. The assignments shown are concerning the numbering scheme for EFV and AZT displayed below.

Initially, the 1H MAS SSNMR analysis was carried out, and then spectral changes detected in the EFZA spectrum were compared to the pure drugs AZT and EFV spectra. Such anisotropic chemical shifting occurred among only two 1H peaks between 15 and -3 ppm (**Figure 4.14**) was attributed to the hydrogen bond formation between bridging protons.

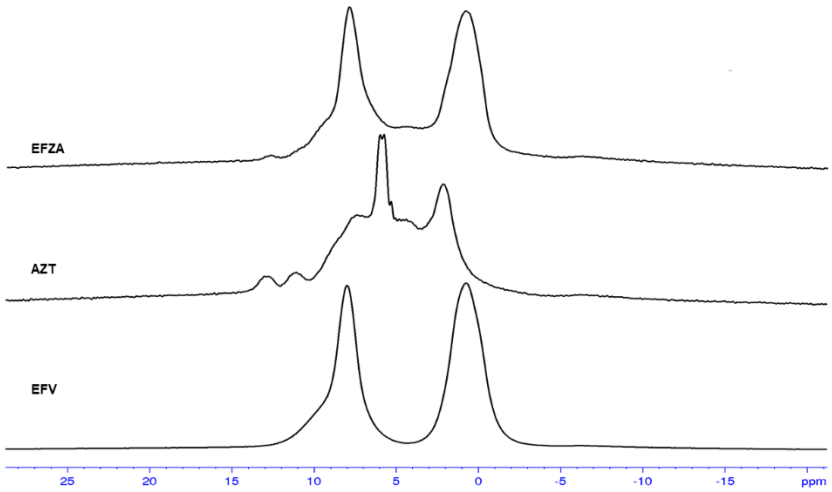

Figure 4.14: Proton MAS SSNMR experiment of AZT, EFV, and EFZA supramolecular co-crystal

The ^{13}C CP MAS solid-state NMR spectra of EFV, AZT, and EFZA co-crystal are shown in **Figure 4.15**. Similarly to the FTIR results, the ^{13}C CP MAS SSNMR spectrum of EFZA co-crystal shows the significant shifting of peak positions (see **Table 4.2**) as a result of co-crystallisation between EFV and AZT. The spectrum also indicated that the crystal lattice of EFZA co-crystal contains one molecule of each starting material (i.e., ratio 1:1) bound to one another by weak hydrogen bonding interactions.

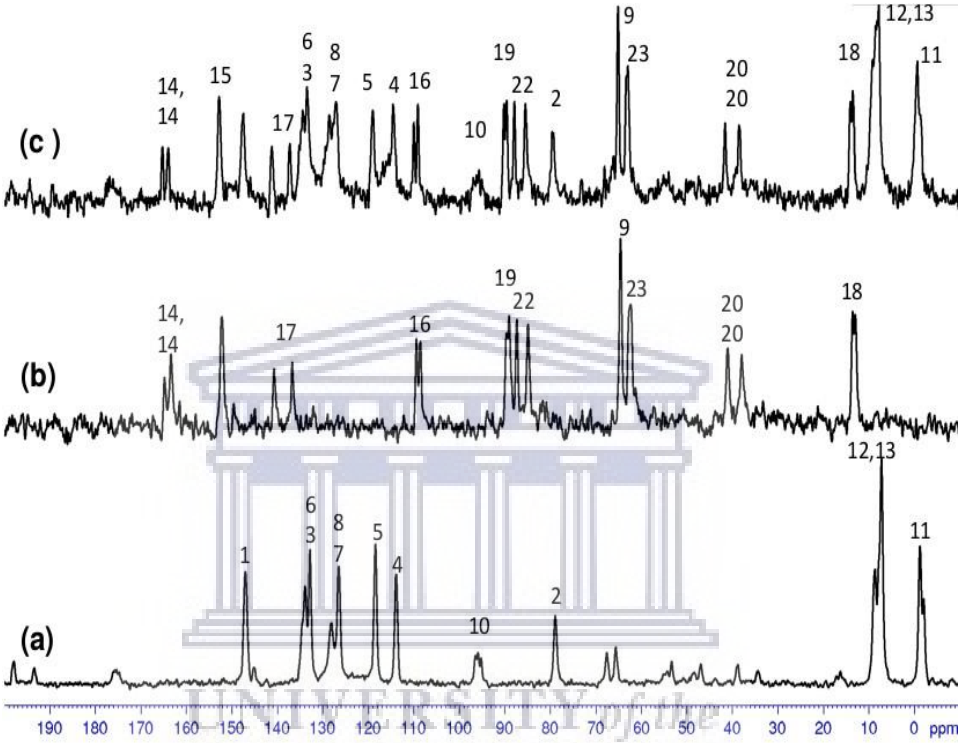

Figure 4.15: The ^{13}C CP MAS SS-NMR experimental spectra of (a) EFV, (b) AZT (c) co-crystal EFZA

The CP-HETCOR solid-state NMR spectrum of EFZA co-crystal can be found in **Appendix C** (**Supporting figure 6)**.

The ^{1}H DQ back-to-back solid-state NMR (^{1}H DQ BABA SSNMR) spectrum of EFZA is shown in **Figure 4.16**. This experiment aimed to identify proton proximities to detect and predict the possible H-bonding locations and the structure of EFZA. The results suggested interactions between pyrimidines of both drugs. However, it is deplorable that the most crucial part of this exercise; ^{15}N CP MAS SSNMR necessary for a complete structure determination could not be performed.

Table 4.2: Signal shifts in EFZA ^{13}C CP MAS SSNMR spectrum vs pure AZT and EFV

EFV C13 shifts	AZT C13 shifts	EFZA C13 shifts
146.99		147.47
78.86		79.54, 79.25
133.88		135.14, 134.40
113.85		115.44, 114.49
118.4		118.99
132.8		133.46
128.09		129.74, 128.53
126.47		127.05
65.57		66.10, 65.06
96.42, 95.84, 95.17		*
-2.09		-0.75
8.6		8.1
7.13		7.76
	163.36, 164.75	163.93, 165.21
	152.17	152.76
	136.68	137.18
	109.38, 108.51	109.97,109.05
	13.47, 12.93	13.44, 13.95
	89.62, 89.02, 87.29	90.17, 89.56
	37.88	38.48, 41.57
	*	141.18
	84.85	85.42
	64.51, 62.31	62.93

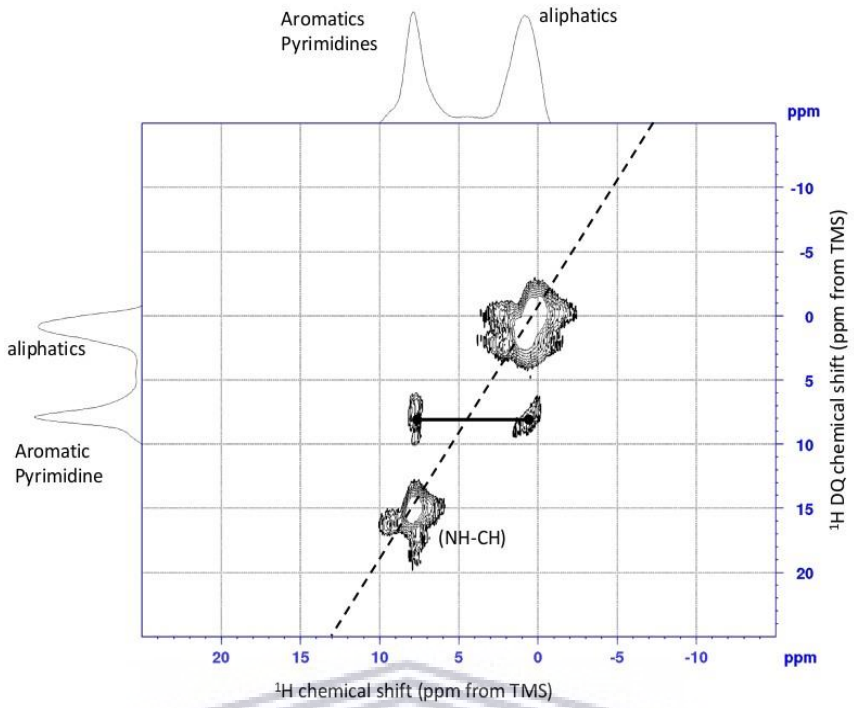

Figure 4.16: ^{1}H (500 MHz) DQ MAS (35 kHz) spectra of the pharmaceutical co-crystal molecule, efavirenz- zidovudine (1:1)

4.3.1.6 EFZA *in vitro* solubility evaluation by HPLC

A gradient elution, using a flow rate of 1 mL/min was applied as follows: Methanol 85% (aq.): sodium phosphate monobasic buffer solution (pH=3.6) 0 to 1 min (35:65), 1 to 2 min (35:65), 2 to 3 min (10:90), 3 to 4 min (10:90), and 4 to 5 min (90:10). A reversed-phase Supelco Discovery HS C18 HPLC column 5 cm x 4.5 mm 3 µm was used. Injection volume was 10 µL, and absorbance of eluting was recorded at 255 nm following suitable dilutions.

For the standard calibration, the R-Square equal to 0.99985 and 0.999909 was found for AZT and EFV, respectively (**Figure 4.17**).

Solubility evaluation for the pure drugs and the co-crystal was performed in triplicate (3 injections per vial) in different buffered solutions; at pH=1.2 (0.1N HCl), sodium acetate buffer solution at pH=4.5, potassium phosphate buffer solution at pH=5.8 or 6.8 and pH=7.4, and unbuffered aqueous solution (deionised water). Descriptive statistical data analysis revealed that the solubility of both APIs in the co-crystal had significantly increased.

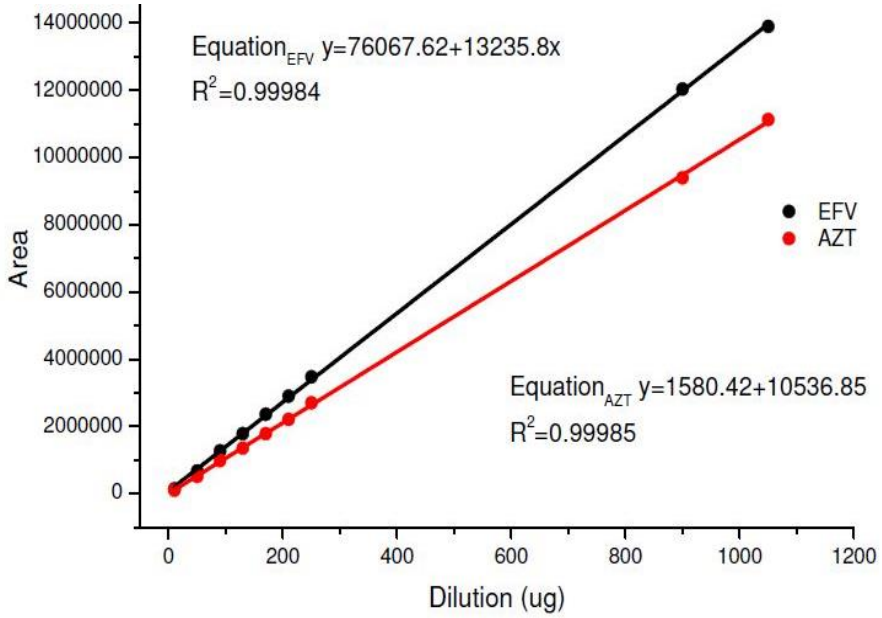

Figure 4.17: Standard calibration curves of pure AZT and EFV

Solubility measurements for pure AZT and its contents in EFZA co-crystal were taken at pH= 1.2, 4.5 ,5.8, 6.8, 7.4 and water. At both pH 4.5 and 5.8, EFZA showed a 3-fold increase in AZT solubility in the presence of EFV compared to its pure form and 2-ford at pH = 1.2, 6.8, 7.4 and water (**Figure 4.18**). This is due to increased lattice energy by co-crystallisation, leading to a higher apparent solubility (Ranjit & Sarma, 2018). AZT did not show any pH-dependent solubility profile.

EFV is a highly hygroscopic drug, and just like NVP, it is a weakly basic and known to exhibit poor aqueous solubility and oral bioavailability. This type of drug is also known to have a pH-dependant solubility profile (Hamed et al., 2016) and prefers a lower pH due to its ionization and solubilisation. Thus, the solubility of pure EFV increased steadily with an increase in pH values (1.2-7.4). Ionisation at lower buffered pH values may lead to reduced solubility, which could be the case here.

EFV showed a significant solubility increase in EFZA co-crystal across the pH range of pH environments (**Figure 4.19**). A 3.3 and 4.5-times solubility increase was recorded at pH = 1.2 and 4.5, while 6.9, 2.6 and 1.2-times increase in solubility was measured at pH=5.8, 6.8 and 7.4, respectively. Finally, in an unbuffered medium such as water, a 2.2-times increase of EFV in EFZA co-crystal was observed. Additionally, the higher solubility of this co-crystal reflects its reduced thermal stability (melting point) in

comparison to both starting materials as confirmed by the DSC analysis (Bethune et al., 2009), (Luo & Sun, 2013).

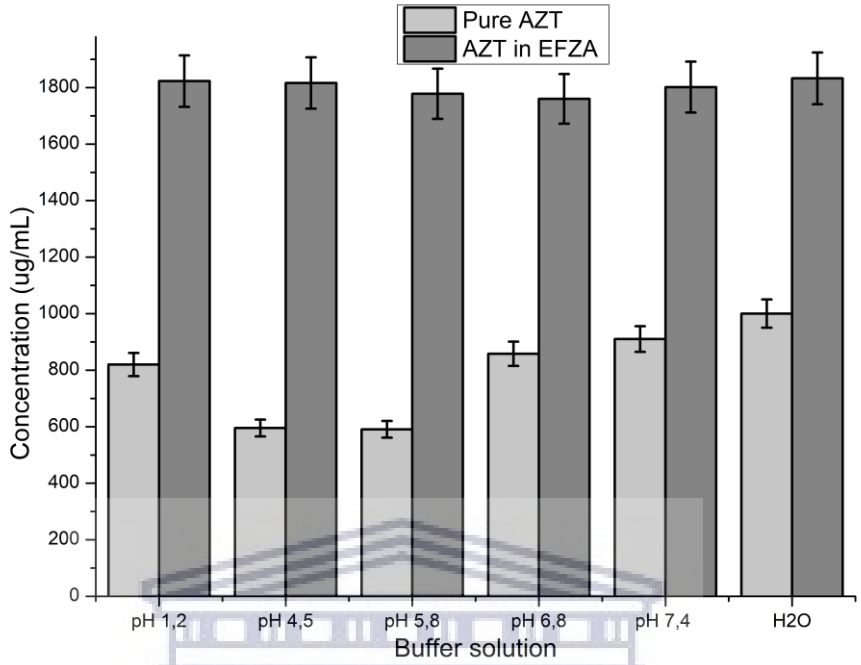

Figure 4.18: Solubility histogram for pure AZT and AZT in the EFZA co-crystal

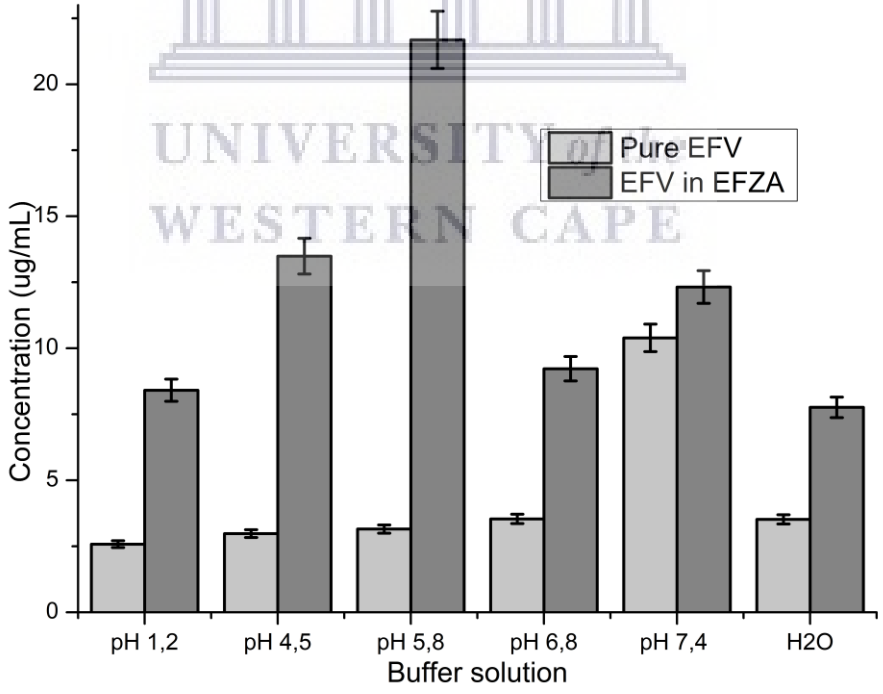

Figure 4.19: Solubility histogram of pure EFV vs EFV in EFZA co-crystal

To conclude, EFZA co-crystal was successfully produced using the solid-state co-grinding method and fully characterised. The co-crystal demonstrated a significant

increase in solubility for both APIs across pH range (1.2-7.4) and in unbuffered aqueous solution.

4.3.2 Nevirapine: efavirenz dual drug co-crystal (NEF)

As physical grinding continues to be one of the most common traditional methods used in co-crystals preparations, many co-crystals, and other solid-state hybrids are being investigated and produced. This is due to the benefits it offers over other solution-based co-crystallisation methods detailed in different pieces of literature (Braga et al., 2013; James & Friščić, 2013b, 2013a).

4.3.2.1 Thermal analysis of the NEF co-crystal

Thermo-microscopic analyses were initially conducted on the HSM, and thermal changes in the sample were recorded from room temperature to the decomposition of the sample. Based on HSM images are presented in **Figure 4.20**, a new melting transition was detected in temperature ranging from 123 to 128°C.

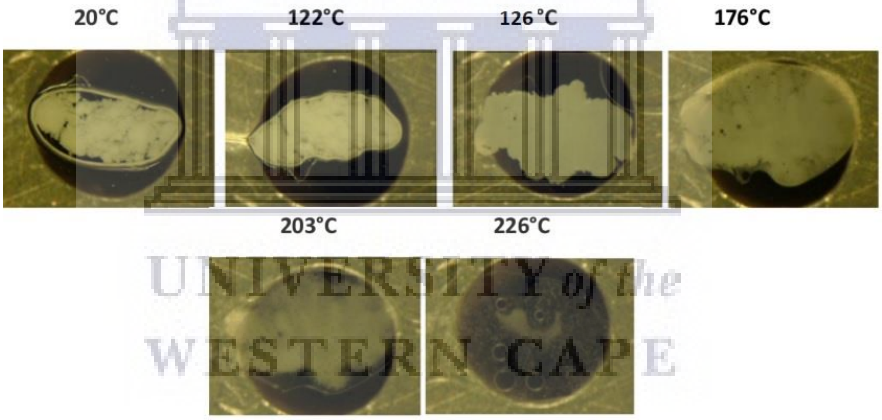

Figure 4.20: The HSM images of NEF co-crystal recorded at room temperature (20°C**), the onset of melting transition (122**°C**), and melting temperature (126**°C**)**

From the DSC thermograms presented in **Figure 4.21**, it is clear that the melting peak in the co-crystal NEF shifts to a lower temperature than both individual drugs melting points. Pure EFV and NVP exhibited sharp melt endotherms at 139°C and 244°C respectively, while DSC thermogram of NEF showed a melting endotherm at 125°C with an onset at 123°C.

The TGA ensured the absence of any volatile guests of the sample. The analysis was carried out according to the method described in section **4.2.3.3**. The TGA/DTA curves

resulting from the NEF co-crystal sample (**Figure 4.22**) are characterised by a single step of mass loss attributed to the sample's degradation.

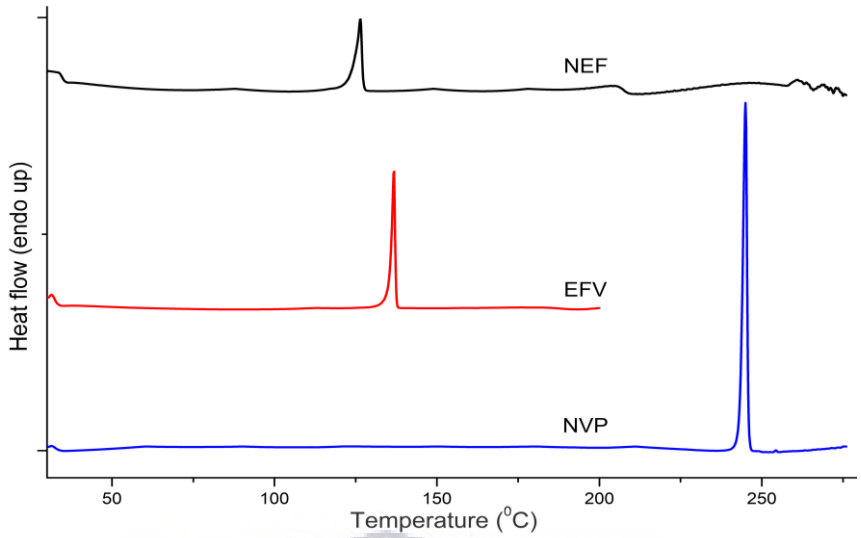

Figure 4.21: The DSC thermograms for untreated EFV, NVP, and the prepared co-crystal NEF with a single melting endotherm at 125°C

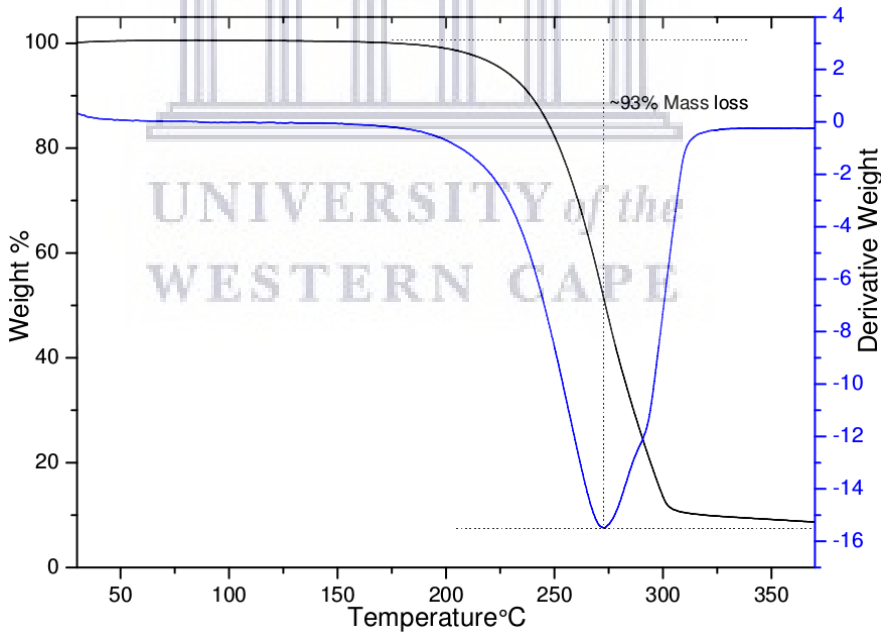

Figure 4.22: The TGA and DTA curves of NEF co-crystal showing a total decomposition mass loss of 93% of the initial sample weight

The TGA/DTA curves showed no mass loss prior to the melting temperature (0.0% mass loss); thus, indicating the absence of possible guest molecules (solvent inclusion). The result further justified a single endotherm in the DSC curve and the absence of air bubbles over the heating process during the HSM analysis. A total mass loss of

approximately 93% was recorded, thereby concluding the co-crystal degradation. The TGA/DTA curves of the individual starting materials EFV and NVP have been included in Appendix C (**Supporting figure 2** and **Supporting figure 3**)

4.3.2.2 Structural studies by infrared spectroscopy

Infrared spectroscopy offers valuable structural information, particularly hydrogen bonding between organic compounds. For this reason, FTIR was used to characterize the NEF powder sample.

Starting materials NVP and EFV were analysed first; then the co-crystal sample was compared to them. Based on studies found in (Chadha et al., 2010b; Samsodien et al., 2017; Sarkar et al., 2008) assignment of the FTIR peaks for the individual NVP was carried out while FTIR peaks of EFV were also assigned based on the research according to Reddy *et al.*, 2015.

In **Figure 4.23**, the NVP spectrum displayed peaks at 3185 cm^{-1} and 1641 cm^{-1}, respectively assigned to N–H and C=O stretch of the carboxamide moiety. The band at 3062 cm^{-1} appeared because of the stretching vibration of C–H. The FTIR spectrum of EFV showed peaks at 3313 cm^{-1} and 1742 cm^{-1} respectively attributed to N–H and C=O stretching vibration of the pyrimidine moiety. The band at 3094 cm^{-1} was assigned to N–H stretching vibration while alkynyl C≡C–H peaks at 2250 cm^{-1} (N. P. Reddy et al., 2015).

The changes and shifts identified in the NEF spectrum include EFV peak at 3313 cm^{-1} assigned to N–H stretch that significantly shifted to 3321 cm^{-1} and reduced intensity while its stretch C=O at 1742 $^{-1}$ shifted slightly to 1745 cm^{-1}. The C-H stretch at 3095 cm^{-1} is missing in the NEF spectrum, and aromatic C=C stretch at 1602 cm^{-1} also shifted slightly to 1600 cm^{-1}. On the other hand, the NVP C–H stretch at 3062 cm^{-1} shifted to 3068 cm^{-1} whereas its N-H stretch significantly subsided. Accordingly, the C=O stretch at 1641 cm^{-1} shifted to 1646 cm^{-1}. These changes suggest interactions occurring between NVP and EFV, thus confirming NEF co-crystal formation (**Figure 4.23**).

Despite the FTIR spectrum of NEF co-crystal showing both APIs peaks which confirmed the presence of both in the new phase, identified spectral shifting proved that interactions between functional groups exist. Predictably, based on changes in peak

intensities and shifts (**Table 4.3**), it was suggested that potential hydrogen bonding took place between NVP carboxamide N–H and C=O with carbonyl (C=O stretch) and the N–H stretch of EFV cyclic amide (**Figure 4.24**).

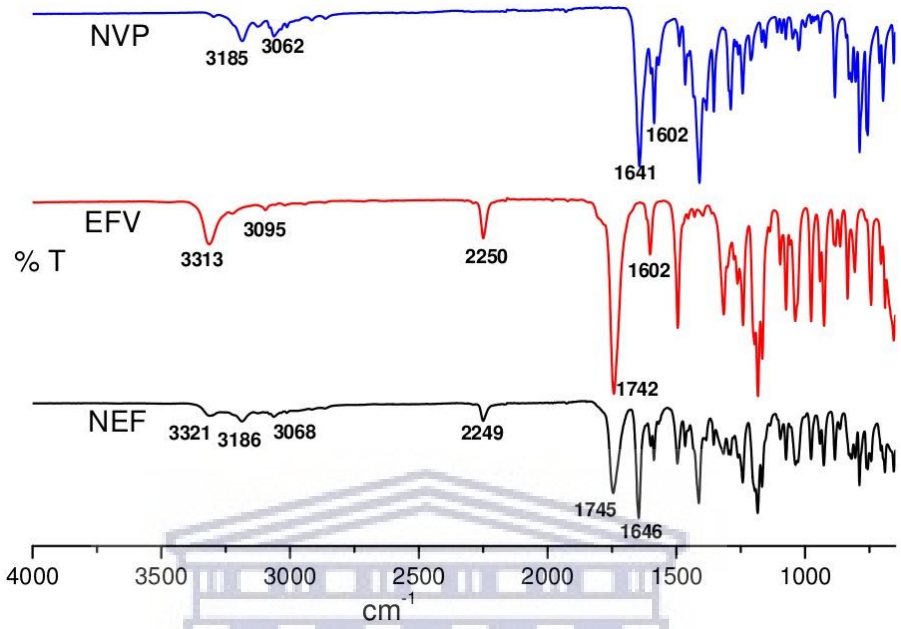

Figure 4.23: FTIR spectra of pure NVP and EFV compared to the FTIR spectrum of the NEF co-crystal

Table 4.3: Summary of important shifts in the FTIR of the NEF co-crystal

Comments	NVP	EFV	NEF
Carbonyl stretch C=O		1742 cm-1	1745 cm-1
Carbonyl stretch C=O	1641 cm-1		1646 cm-1
Aromatic ring C–H	3062 cm-1		3068 cm-1
Stretching N–H		3313 cm-1	3321 cm-1
Aromatic ring C–H		3095 cm-1	Disappears

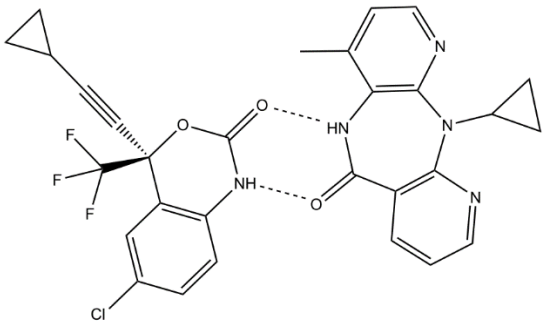

Figure 4.24: Suggested intermolecular bonding in the NEF co-crystal based on FTIR analysis

4.3.2.3 Morphology studies of NEF dual-API co-crystal

Solid phases exhibit size differences and crystal habits. SEM analysis enabled the understanding of these properties. The SEM micrograms of individual APIs, the physical mixture and the co-crystal are shown in **Figure 4.25**. Untreated NVP exhibited crystal habits with irregularly-shaped particles and smooth surfaces while EFV exhibited polyhedral rod-shaped particles. On the other hand, the NEF co-crystal exhibited irregular, smooth, and more homogeneous and compact than the physical mixture of the starting materials.

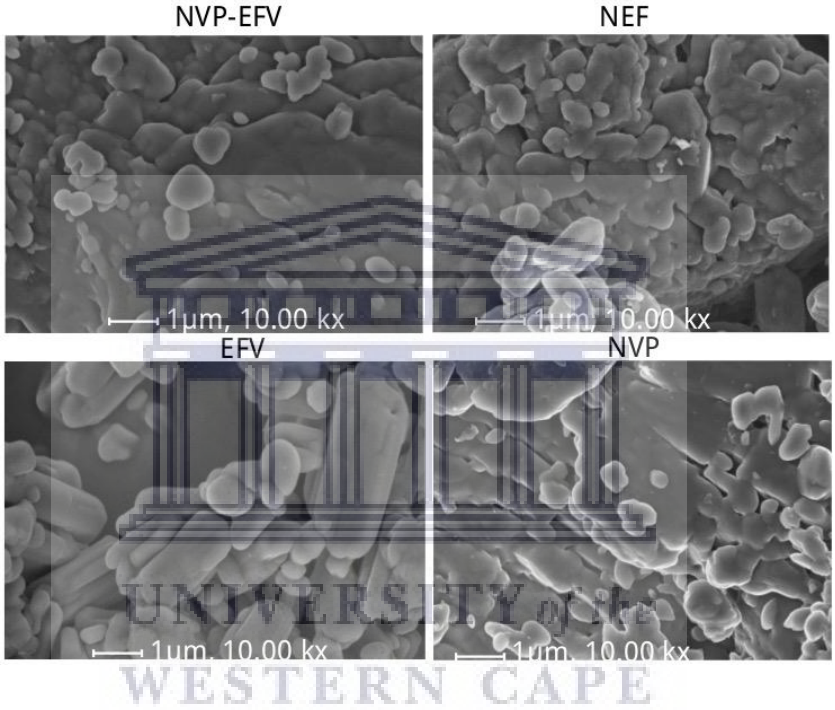

Figure 4.25: The SEM images of NVP-EFV physical mixture, NEF co-crystal, pure EFV and NVP

4.3.2.4 Analysis of NEF sample by powder X-ray diffraction (PXRD)

The PXRD patterns generated from EFV, NVP, and NEF co-crystal are shown in **Figure 4.26**. Untreated NVP exhibited characteristic diffraction peaks at 2θ 13°, 13.4°, 18.96°, and 25.44°. Other medium-sized peaks appear at 2θ 9.18°, 17.17°, 20.64°, 22.5°, 23.11°, and 26.4°. The PXRD pattern of EFV is characterised by very sharp, intense characteristic diffraction peaks at 2θ 6.00°, 14.12°, 21.10°, and 24.86°, medium-sized peaks at 2θ 12.16°, 13.1°, 16.83°, 19° and small peaks at 2θ 10.30°, 10.83°, 15.15°, 21.84°, 23.00°, 27.1°, 27,9°, 29°, 32.27°, and 37.27°. NVEF exhibited a distinct PXRD pattern from the individual drugs patterns, with characteristic diffraction peaks

at 2θ 11.68°, 13.36°, 17.24°, 27.36°, and 31.72°; ensuring the new phase and confirm that NEF is indeed a co-crystal.

Furthermore, the co-crystal was also confirmed by changes in the local molecular environment as indicated the ^{13}C solid-state NMR spectrum of the co-crystal NEF. Spectra were included in Appendix C **(Supporting figure 7**).

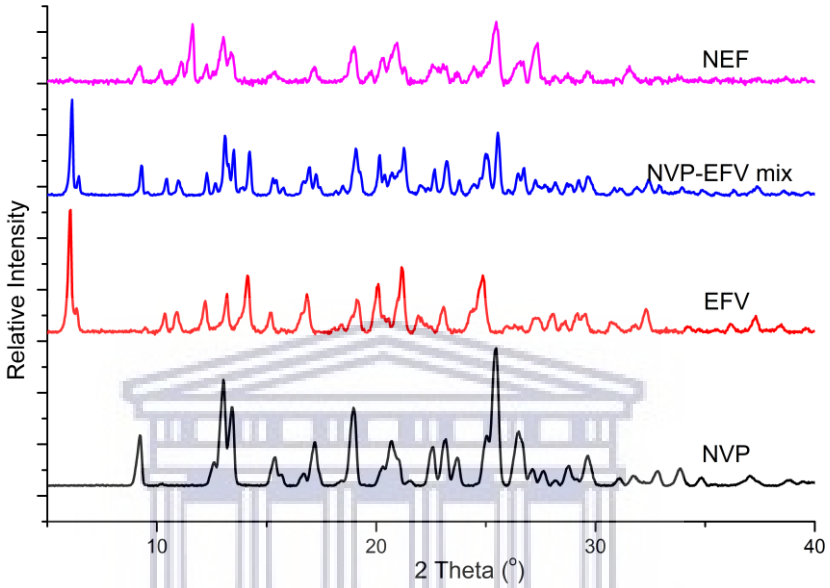

Figure 4.26: The experimental PXRD patterns for pure NVP, EFV, their physical mixture and NEF co-crystal

4.3.2.5 The *in vitro* solubility evaluation of NEF co-crystal

Solubility studies were carried out by adding an excess amount of individual drugs EFV, NVP and the prepared co-crystal to distilled water and aqueous USP buffered solutions at pH 1.2 (0.1M hydrochloric acid), pH 4.5 (acetate), pH 6.8 (phosphate), and pH 7.4 (phosphate). The suspensions were continuously stirred in a shaker at 37 ± 0.5 °C and 100 rpm for 48 hours.

Samples were then filtered using 0.20 µm PVDF syringe filters and analysed using a reverse-phase HPLC method described in section **4.3.1.6**. Standard calibration indicated R^2 = 0.99997 for EFV and 0.99909 for NVP. **Figure 4.27** illustrates the standards calibration curves of both EFV and NVP and regression equations used to calculate the amount of each drug in samples.

As discussed in section **4.3.1.6**, EFV and NVP are weakly basic drugs characterised by their poor aqueous solubility and oral bioavailability. Weakly basic drugs exhibit a pH-

dependant solubility profile (Hamed et al., 2016). Thus, it was observed that EFV solubility in both pure and NEF co-crystal forms increases with pH (**Figure 4.28**).

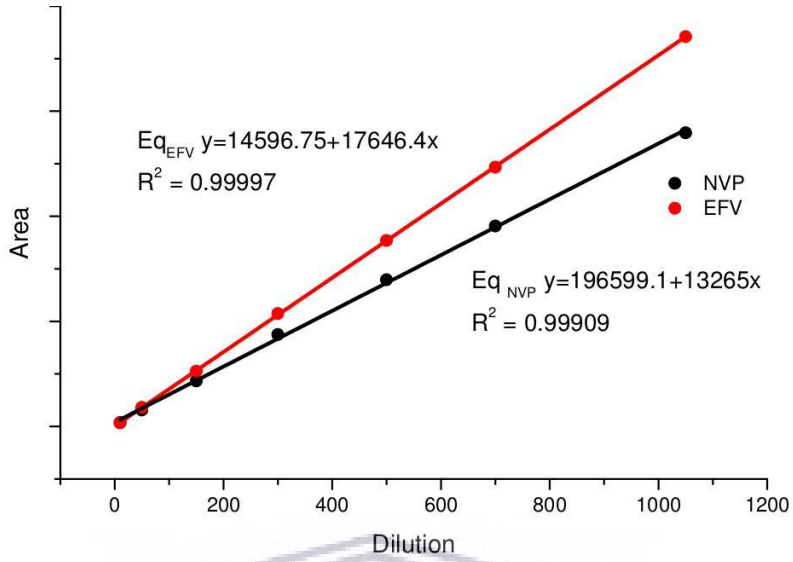

Figure 4.27: Standard calibration curves for EFV and NVP.

NVP is a lipophilic drug known for its poor aqueous solubility which significantly affects its bioavailability. Solubility data revealed that pure NVP solubility is inversely proportional to pH, exhibiting higher solubility at ≤ pH 2. This is consistent with the previous publication (Kuminek et al., 2016).

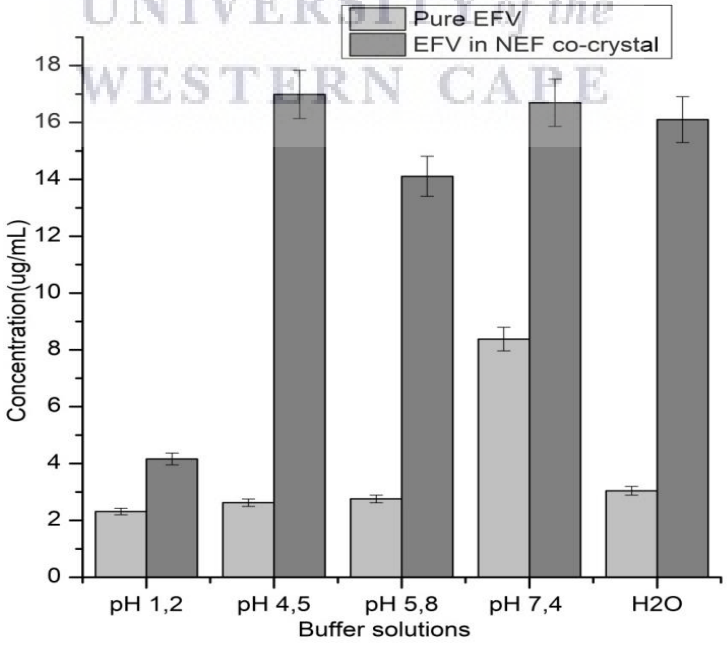

Figure 4.28: Solubility histogram of untreated EFV and EFV in the NEF co-crystal

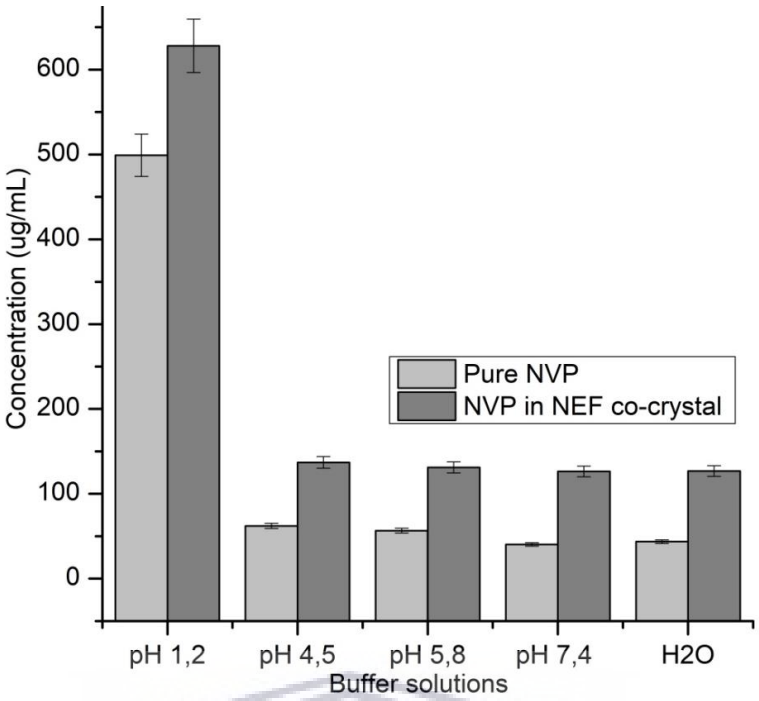

Figure 4.29: Solubility histogram of untreated NVP and NVP in the NEF co-crystal

NVP, in its dual-API co-crystal with EFV, also inherited the same pH-dependant solubility. The solubility increase was evident throughout the pH range of 1.2 -7.4. However, a weak solubility difference was observed from pH 4.5 to pH 7.4 and unbuffered aqueous solution (deionised water), suggesting a poorer effect of pH on co-crystal solubility (**Figure 4.29**). Nonetheless, the co-crystal NEF showed a significantly higher solubility compared to both pure APIs.

For EFV solubility in NEF co-crystal, an increase by 2-fold, 6.6-fold, 5.6-fold, 2.5-fold and 6.6-fold were respectively measured at pH= 1.2, 4.5, 5.8, 7.4 and deionised water while NV solubility in the same co-crystal was increased by 1.3, 2.2, 2.3, 3.1 and 3-fold, respectively at pH values 1.2, 4.5, 5.8, 7.4 and deionised water. The co-crystal's reduced thermal stability further justifies the solubility increase by this co-crystallisation (Bethune et al., 2009), (Luo & Sun, 2013).

4.3.3 Lamivudine-Zidovudine binary eutectic mixture (LMZT)

4.3.3.1 Preparation of LMZT sample

According to the study previously conducted on the co-crystal forming abilities of the two drugs (Bhatt et al., 2008), where AZT and 3TC were screened against different co-crystal formers, the dual-API co-crystal formation attempt between AZT and 3TC, using solution co-crystallisation, resulted in a hydrate (**Figure 4.30**). Nonetheless, the present study focuses on the co-crystal preparation via mechanochemical reactions (or grinding methods).

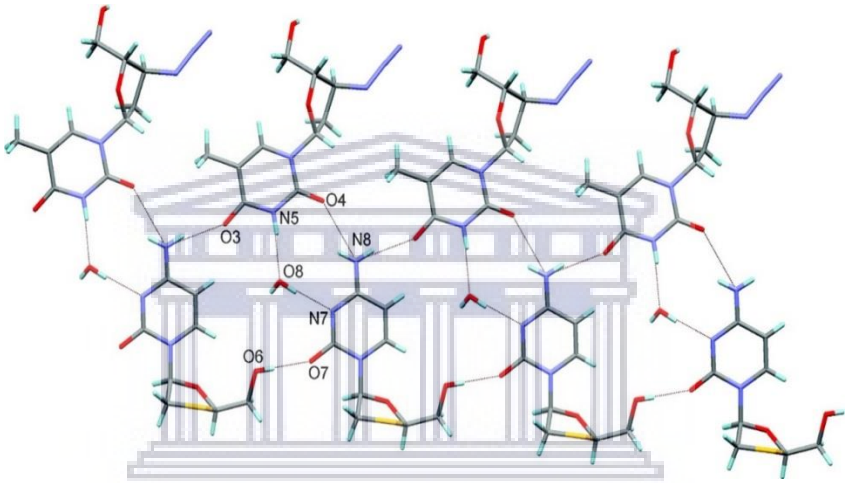

Figure 4.30: The structure of lamivudine-zidovudine hydrate co-crystal [Source: Bhatt *et al.*, (2009)]

Physical grinding as one of the most common traditional methods widely used in co-crystal preparations, was explored due to the benefits it offers over other solution-based methods of co-crystallization such as simplicity, time efficiency, safety, cost-effectiveness, and other benefits (Braga et al., 2013; James & Friščić, 2013b, 2013a).

4.3.3.2 Thermal analyses of LMZT sample by Hot Stage Microscopy

The HSM photographs of the LMZT sample are portrayed in **Figure 4.31**. The analysis was performed as previously described in section 4.2.3.1. Data collection was achieved over a 30-350°C temperature range. The LMZT sample started melting at 105°C. This melting transition is lower than both AZT and 3TC, which melted at 121°C and 175°C, respectively (HSM images for the starting materials not included here). No air bubbles

observed prior to the melting temperature. The decomposition of the sample was characterised by explosive bubbling at around 205°C.

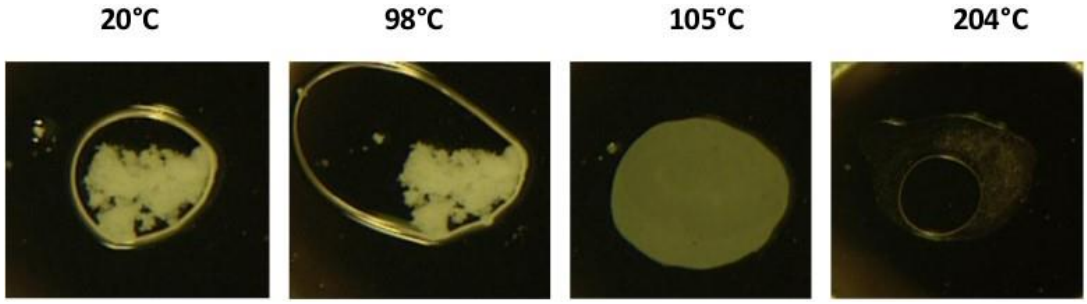

Figure 4.31: Diagram of HSM photographs of LMZT sample recorded at room temperature (20°C), the onset of melting at 98°C, actual melting at 105°C and decomposition at 204°C.

The DSC analysis was carried out on APIs, their physical mixtures, and the milled sample. The DSC curves are depicted in **Figure 4.32**, and the basic DSC details for the LMZT sample, starting materials and their physical mixture, are summarised in **Table 4.4**. According to the DSC analysis, melting points for AZT and 3TC occurred at 122°C and 177°C respectively. This is consistent with the previous publication (Araújo et al., 2010) and correlates well with the HSM observed changes. On the other hand, the LMZT sample melted over 103-110°C temperature range as indicated by a single endotherm peaking at 109°C and onset of 103°C (**Figure 4.32**). Both HSM and DSC results confirmed a new melting transition and LMZT as a possible binary eutectic mixture.

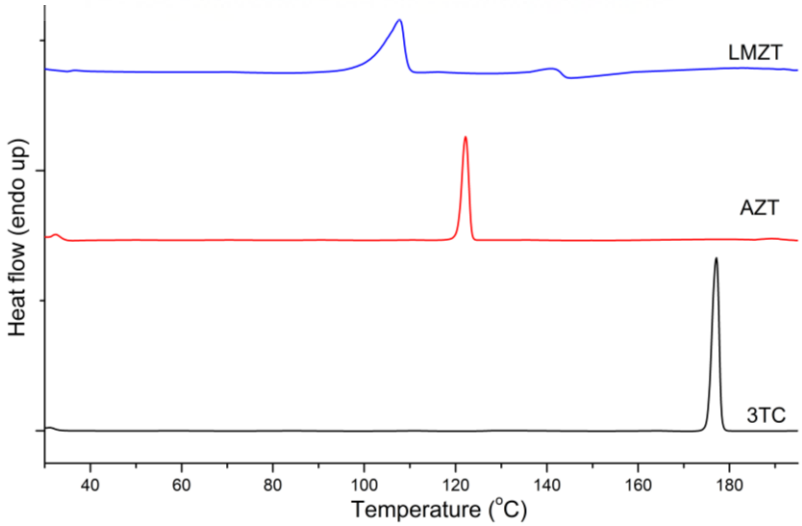

Figure 4.32: DSC curve of LMZT hybrid showing a lower melting endotherm compared to those from pure AZT and 3TC

Like AZT, the LMZT sample showed a broad decomposition exothermic peak in the DSC curve between 200-245°C. This is also consistent with the sample discolouration observed in the same range during the HSM analysis.

Table 4.4: Basic DSC data of AZT, 3TC, LMZT, and the physical mixture

Material	Onset (°C)	m.p. (°C)	Delta H (jg^{-1})	Peak area (mJ)
AZT	120.61	122.17	135.62	542.48
3TC	175.32	177.17	119.98	299.96
LMZT	103.60	108.83	2.32	69.67
Physical mixture	112.09	117.33	135.62	542.48

To confirm the absence of any volatile substances and degradation of the sample, TGA was performed under a neutral environment, at a predetermined heating rate of 10°C/min, following a TGA method described in section 4.2.3.1. The TGA measurements were done over 30-370°C temperature range and the TGA/DTA curves of the LMZT sample are shown in **Figure 4.33**.

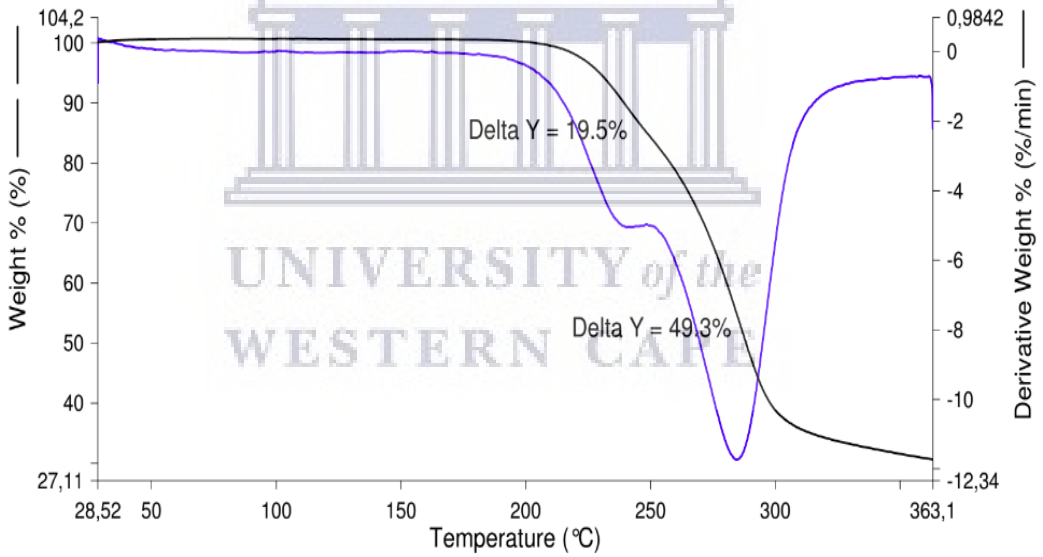

Figure 4.33: TGA/DTA curves of LMZT sample showing a decomposition mass loss of ~70% over 200-300°C temperature range.

Based on the TGA/DTA results, there was a negligible mass loss (~0.0%) in the LMZT sample before its decomposition onset at 205°C, therefore, concluding that there are no volatile guest molecules in the LMZT structure. The decomposition occurred in steps. Initially, 19.5% mass loss was calculated over 205-250°C temperature range, followed by a second mass loss of 50% between 250°C and 325°C.

4.3.3.3 Structural evaluation by infrared spectroscopy

FTIR spectra of AZT, 3TC, and LMZT are presented in **Figure 4.34**. The spectral data from the individual APIs matched the ones reported previously (Pandey et al., 2016). FTIR spectrum from the LMZT milled sample was analysed by comparing the shifts and other changes in functional groups bands w.r.t the parent compounds.

Analysis of the FTIR spectra based on the key intensity shifts compares 3TC and AZT to LMZT. It is also important to note that only peaks in functional groups region in the FTIR spectra have been assigned owing to this characterization. The FTIR spectrum of 3TC peaked at 3324 cm^{-1} and 3196 cm^{-1}, respectively and the two peaks were ascribed to an amino N−H and hydroxyl O−H stretching, in agreement with (Pandey et al., 2016). Minor differences observed could be due to different instrumentation, sensibility, and purity of samples. Peaks at 3075 cm^{-1} and 2883 cm^{-1} belong to the C−H stretching of cytidine whereas C=O and C=C stretching show doublet peaks at 1648 cm^{-1} and 1635 cm^{-1} respectively.

FTIR spectrum of AZT showed peaks at 3459 cm^{-1} and 3150 cm^{-1} that correspond to N−H and O−H respectively. The FTIR peaks at 3024 cm^{-1} and 2813 cm^{-1} were respectively attributed to stretching =C–H of the pyrimidine ring and C-H and the band peak at 2081 cm^{-1} was assigned to asymmetric N_3 stretching of azido group. FTIR peak at 1671 cm^{-1} was due to the pyrimidine carbonyl C=O stretching.

FTIR spectrum of the LMZT sample displayed all FTIR peaks inherited from both pure drugs 3TC and AZT, with minor band shifting. The 2813 cm^{-1} assigned to C−H overlapped with the 3TC peak at 2833 cm^{-1} and slightly shifted to 2815 cm^{-1} in the LMZT spectrum. The AZT peak with maxima at 2081 cm^{-1} (azido N_3) had slightly shifted to 2083 cm^{-1}. Furthermore, there was an intense band shifting of AZT pyrimidinic C=O, from 1669 cm^{-1} to 1683 cm^{-1} in the spectrum of the LMZT sample. Thus, confirming the possible intermolecular bonding with 3TC. The 3TC O-H stretching peak at 3198 cm^{-1} also shifted slightly from 3195 cm^{-1}.

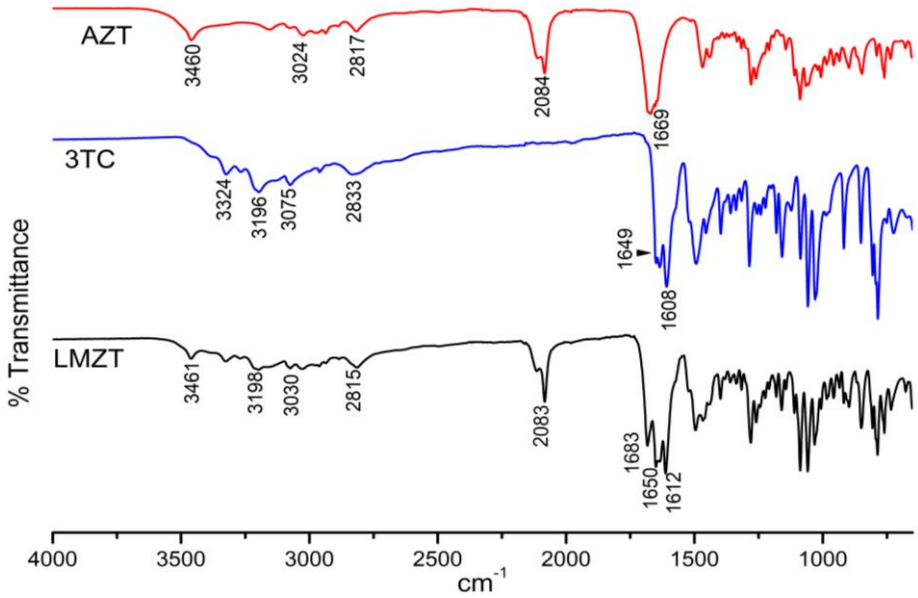

Figure 4.34: FTIR spectra comparing pure AZT and 3TC to the eutectic LMZT spectrum

These FTIR band shifts identified in the LMZT confirmed intermolecular bonding between AZT and 3TC and the formation of a new entity although inconclusive. **Table 4.5** summarises all shifts and other changes identified in the LMZT spectrum in comparison to the starting materials.

Table 4.5: Main bands identified in the spectrum of pure drugs AZT and 3TC and their respective positions in the of LMZT sample

F(x) groups	AZT	3TC	LMZT	Assignment
O–H	3460 cm^{-1}		3461 cm^{-1}	Hydroxyl
C–H	3024 cm^{-1}	3075 cm^{-1}	3030 cm^{-1}	Stretch asymm. alkyl
C–H	2817 cm^{-1}	2833 cm^{-1}	2815 cm^{-1}	stretching alkyl
N=N+	2084 cm^{-1}		2083 cm^{-1}	Azido moiety
C=O	1669 cm^{-1}		1683 cm^{-1}	stretching carbonyl
		1635 cm^{-1}	1650 cm^{-1}	cytidine carbonyl
N–H		3324 cm^{-1}		Amino
O–H		3196 cm^{-1}		Hydroxyl

Based on the FTIR results confirming the interaction between AZT and 3TC, the following structure (**Figure 4.35**) was suggested.

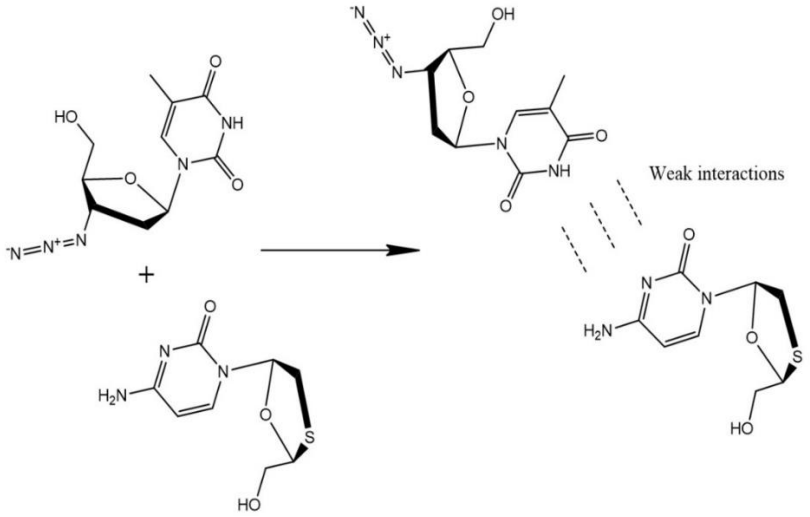

Figure 4.35: The suggested LMZT structure with three prominent intermolecular bonding positions.

4.3.3.4 Characterisation of LMZT morphology by SEM

From SEM analysis, it is observed in **Figure 4.36** that the AZT sample showed an irregular shaped crystal habit with smooth surfaces (**Figure 4.36**a).

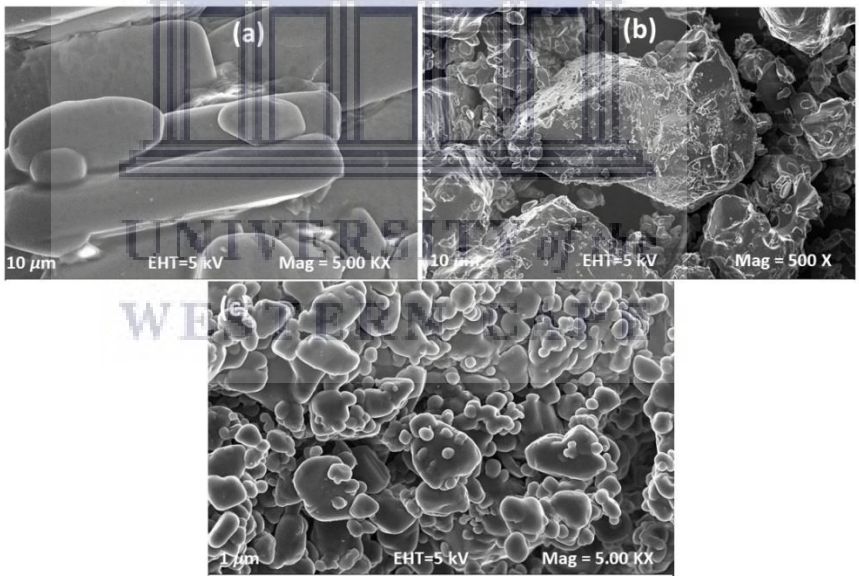

Figure 4.36: SEM micrograms of (a) AZT, (b) 3TC and (c) the LMZT sample captured at 5.00 K.X magnification, 1 µm using 5 kV of energy.

The most stable polymorphic form (form-II) of 3TC was used in this experiment. This polymorph used in powder form exhibits prismatic crystals when recrystallized (Chadha, Arora, et al., 2012). Despite this, the 3TC powder sample appears to have lost its original crystal habit and exhibited large irregular particles (**Figure 4.36**b). The

LMZT sample showed round particles and very small in size compared to both APIs (**Figure 4.36**c).

4.3.3.5 Powder X-Ray diffraction analysis of LMZT sample

The powder X-ray diffraction (PXRD) is a non-destructive method to confirm new phases such as co-crystals. The patterns from the LMZT sample and the pure drugs are displayed in **Figure 4.37**. 3TC PXRD pattern showed characteristic peaks at 2θ =13.23°, 17.38°, 20.50°, 21.29°, 24.79°, 26.33°. The diffraction peaks for AZT are found at 2θ=8.8°, 14.63°, shouldered peak at 2θ = 15.53°and 15.83°, 17°, 21.36°, 22.21°, 24.14°, 27°, 27.77°, 29.32°, and 32.65°.

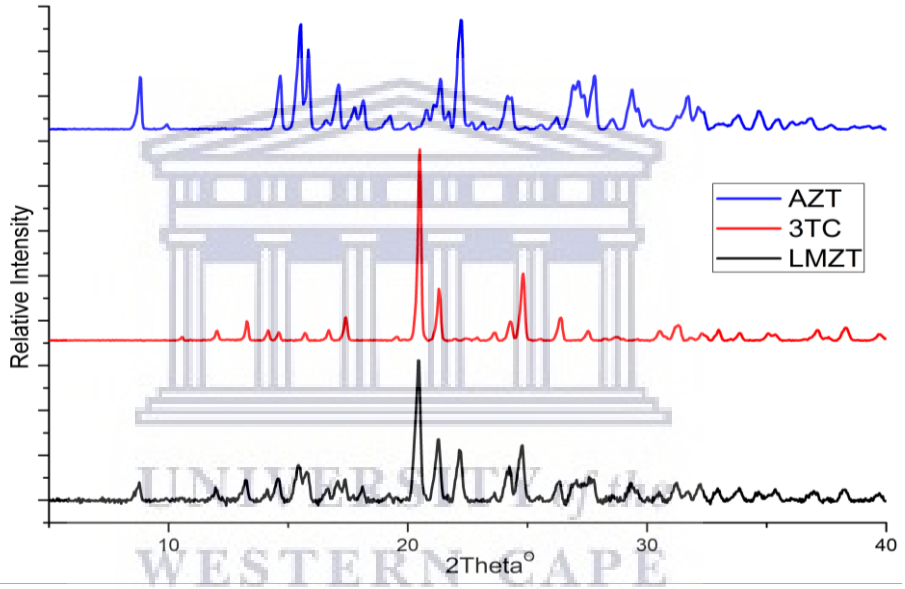

Figure 4.37: The experimental PXRD patterns of 3TC, AZT, and the eutectic LMZT sample

From the LMZT diffraction pattern the main peaks are identified at 2θ value 8.77°, 13.23°, 14.57°, 15.42°, 20.43°, 21.25°, 22.21°, a double shoulders peak at 24.24 and 24.79°. From these data, it is clear that only minor changes took place. The LMZT pattern inherited peaks from AZT and 3TC, confirming the thermal analyses findings that LMZT is indeed a eutectic mixture rather than a new co-crystal. Compared to AZT and 3TC's PXRD patterns, the LMZT pattern shows a reduced crystallinity.

4.3.3.6 LMZT *in vitro* solubility evaluation

Evaluating the physicochemical properties such as solubility of the active substance is an important step in the pharmaceutical development process. If not monitored the

impact on drug formulation, bioavailability, storage, and dosage form itself can be detrimental.

In vitro solubility evaluation was carried out by dissolving an excess amount of individual drugs and the binary eutectic produced LMZT in different buffer solutions at pH 1.2, 6.8, 7.4 and sodium dodecyl sulfate (SDS) solution. The mixtures were agitated for 24 hours, using an incubator shaker, and then filtered. After necessary dilutions, a Perkin Elmer HPLC was used to quantify the amount of both APIs in the eutectic LMZT sample and compared to the concentration of individual drugs in the same buffer solutions.

A Perkin Elmer HPLC system setting with FXBPump (Flexar Binary Pump), an automated injector equipped with a UV detector (LC 200a Series PDA Detector), and a Flexar autosampler. Gradient elution, using a flow rate of 1.0 mL/min was applied as follows: Methanol 85% (aq.): phosphate buffer solution (pH=3.6) 3 min (70:30), 1 min (35:65), 3 min (0:100), 2 min (0:100), 2 min (70:30) and 2 min (70:30). A reversed-phase Supelco Discovery HS C_{18} HPLC column 15 cm x 4 mm, 5μm was used. Injection volume was 10 µL and absorbance of elution was recorded at the necessary wavelength. The standard calibration curves (Figure 4.33) were plotted and R squared (R2) = 0.9989 for AZT and 0.9988 for 3TC were obtained.

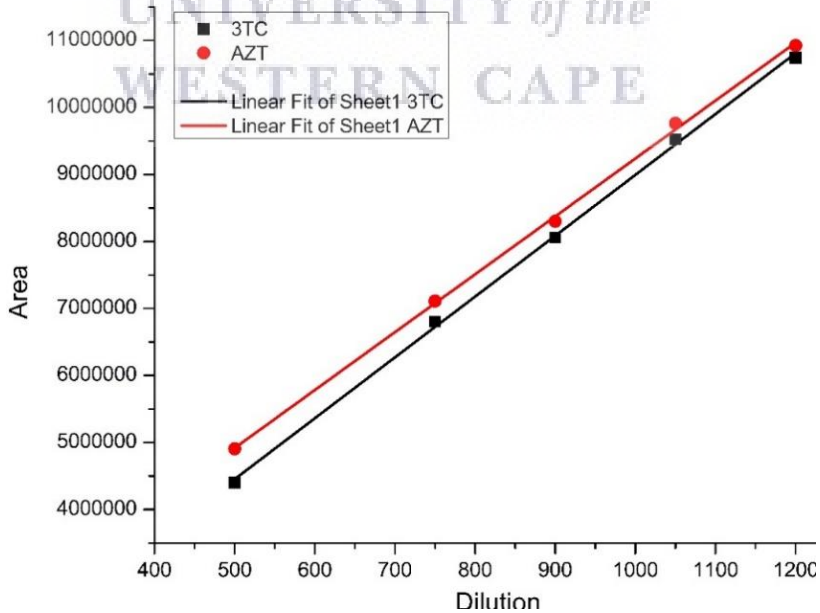

Figure 4.38: The standard curves for AZT and 3TC at 254 wavelengths

Based on the solubility measurements, the statistical data presented in **Figure 4.39** show that both APIs' solubility has increased in the binary eutectic LMZT. As expected, both APIs were more soluble in the surfactant (SDS) than in the buffer media at various pH. Moreover, the result indicated that the co-crystallisation enhanced more 3TC solubility in all buffer media compared to the impact it had on the solubility of AZT. 3TC showed solubility increase by 2-fold in buffer solutions at both 1.2 and 7.4 pH values, 1.8-fold at pH=6.8 and 1.3-fold in the surfactant (SDS).

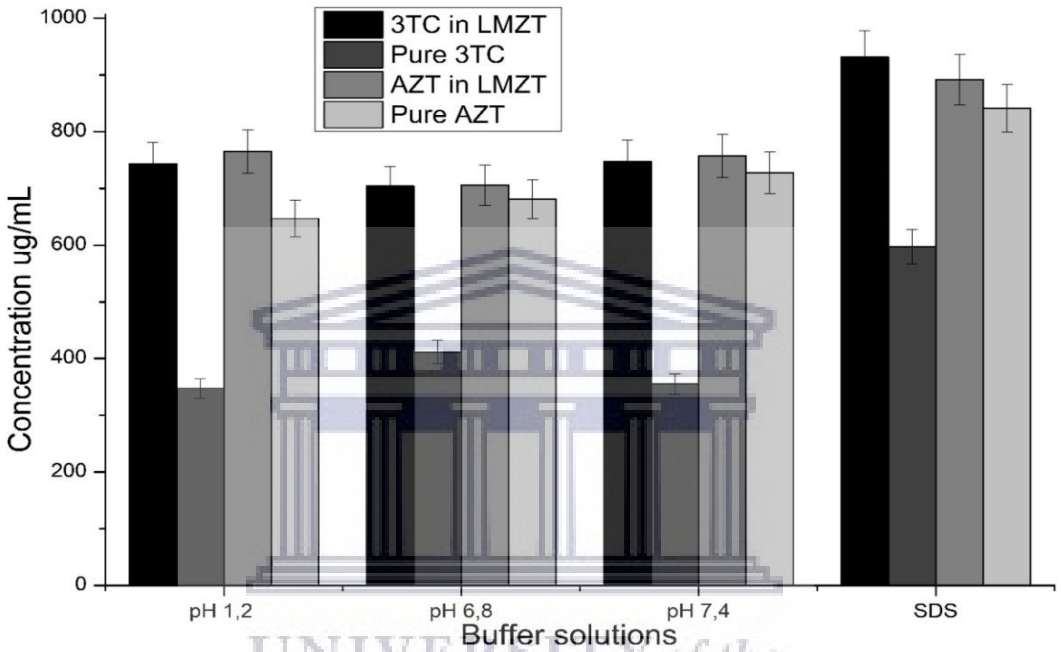

.

Figure 4.39: A solubility histogram comparing LMZT solubility to pure AZT and 3TC in buffer solutions at pH=1.2, 6.8 and 7.4 and SDS solution

To conclude, there was no co-crystal formed between AZT and 3TC after a co-crystallisation attempt using solid-state co-grinding methods. Instead, a binary eutectic LMZT was successfully produced. The thermal analysis confirmed a lower melting point of the eutectic LMZT while SEM analysis confirmed the morphology of its particles and the impact of co-grinding exercise, which resulted in a reduction of LMZT particle sizes. Reduced particle size leads to an increase of contact surfaces, therefore increasing solubility but can also result in the sample instability.

FTIR explored the possible interactions between 3TC and AZT and PXRD confirmed the solid dispersion (binary eutectic mixture). Furthermore, the *in-vitro* solubility carried out over a wide range of pH (1.2-7.4) revealed an enhanced solubility of both

APIs in the eutectic LMZT. This further suggests the possible enhanced bioavailability on both drugs.

4.3.4 Nevirapine-Zidovudine solid forms and co-crystals (NVZA)

4.3.4.1 Thermal analyses

Analyses by the DSC were conducted under nitrogen gas flowing at 20 mL per minute, with samples cramped in aluminium pans and lids (section 3.4.2). The DSC curves for all NVZA solid forms are shown in **Figure 4.40**.

NVZA1; the samples produced by solid-state grinding of the starting materials in 1:1 and 2:1 molar ratios were characterised by unique melting endotherms in the same temperature range (T_{onset}= 110°C, T_{peak}= 116°C), and decomposition at a very high temperature with onset at 215°C. Having obtained melting points of pure drugs, NVP and AZT at 245°C and 122.7°C respectively, **NVZA1** melted earlier than both APIs. This was the initial proof that a possible binary eutectic mixture has resulted.

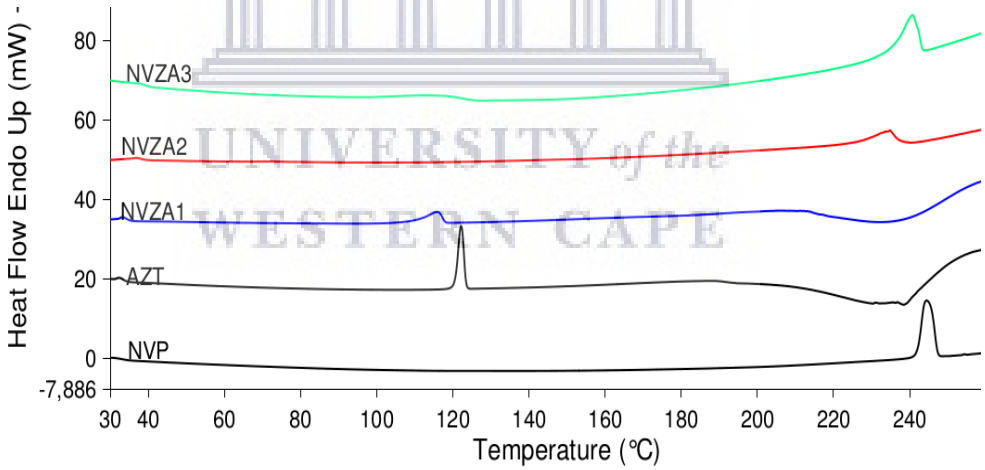

Figure 4.40: The DSC curves of pure AZT and NVP, NVZA1, NVZA2 and NVZA3 derivative solid forms.

Based on the DSC analyses as an advanced tool to rapidly detect the co-crystal/eutectic mixture formation, **NVZA2** sample exhibited a new melting point, with a DSC curve showing a melting endotherm at 234°C (onset at 224°). The DSC analysis of **NVZA3** sample also produced a curve showing a single melting endotherm at 238°C with an

onset at 235°C, confirming new dual-API solid forms **NVZA2** and **NVZA3** as potential co-crystals.

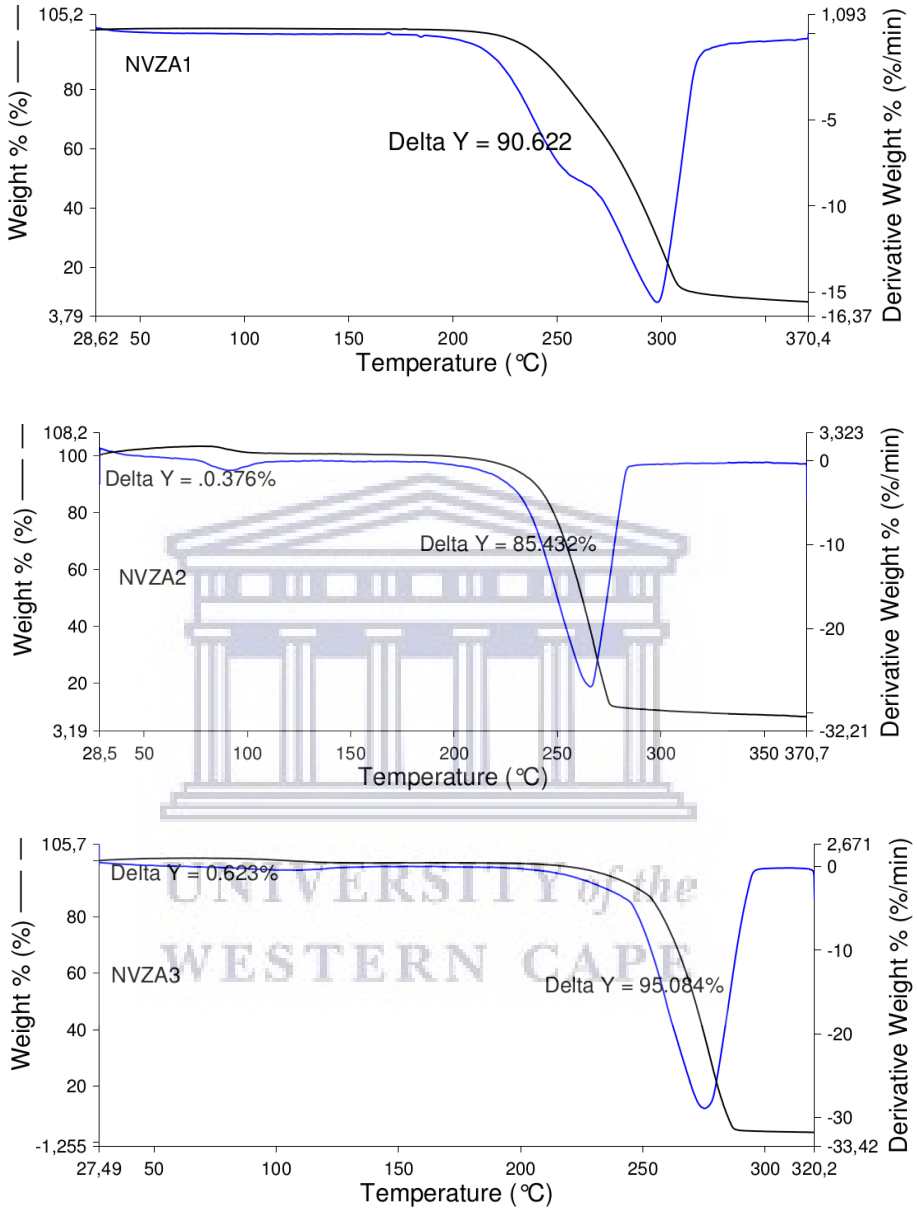

Figure 4.41: The TGA/DTA curves of NVZA1 with a total decomposition mass loss of 90.6%, co-crystal NVZA2 showing a total decomposition mass loss of 85.4% and the co-crystal form NVZA3 with a total decomposition mass loss of 95%

The TGA/TDA curves of all **NVZA** solid forms are shown in **Figure 4.41**. The TGA/DTA curves of **NVZA1** are characterised by a single step of mass loss (90.62%) at 200°C, attributed to the decomposition of the sample. According to the TGA measurements done between room temperature and the melting onset, no significant

loss of weight was revealed (0.0 % loss). Thus, confirming the absence of any inclusion molecules in the NVZA1 sample. The TGA/DTA curves for the **NVZA2** samples also showed no significant mass loss in the temperature ranging below melting onset (0.37 % loss). Therefore, confirming that **NVZA2** samples are purely anhydrous. A total mass loss equal to 85.4% of the initial sample mass, was identified in the temperature range (220-270°C) corresponding to the melting and decomposition. Similarly, there was no indication of significant mass loss in **NVZA3** sample prior to melting range (0.62% loss). The sample decomposed at a high temperature (over 200°C) with a total mass loss of about 95%.

4.3.4.2 Analysis of the structure by Fourier transform infrared spectroscopy

The structural investigation by FTIR was initiated by obtaining individual drugs spectra, then compare to the spectra of the **NVZA** solid forms (**Figure 4.42**). Peaks assignment was only done for characteristic bands in functional groups region of the spectra.

Pure AZT exhibited N−H and O−H bands at 3460 cm^{-1} and 3150 cm^{-1} respectively in the spectrum. Peaks at 3024 cm^{-1} and 2817 cm^{-1} were attributed to stretching C−H respectively, while the peak at 2084 cm^{-1} was assigned to asymmetric N_3 stretching of azido group vibration and the peak at 1669 cm^{-1} was due to the pyrimidine carbonyl C=O stretching (Bansal et al., 2013; De O. Porfírio et al., 2015).

NVP spectrum exhibited bands peak at 3186 cm^{-1} assigned to N–H stretching, band at 3062 cm^{-1} assigned to C–H, 1643 cm^{-1} band assigned stretching carbonyl C=O, associated with N–H.

Both NVP and AZT characteristic bands are present in **NVZA1**. Band positions such as AZT stretching C=O shifted to 1639 cm^{-1} and the N-H stretching subsided. NVP stretching N-H at 3186 cm^{-1} slightly shifted to 3183 cm^{-1} while its stretching C=O shifted to 1685 cm^{-1}, confirming weak bonding interactions between AZT and NVP.

The **NVZA2** spectrum inherited NVP stretching N–H band at 3195 $cm^{-1}$and the stretching C–H shifted to 3068 cm^{-1}. The AZT stretching N–H downshifted to 3451 cm^{-1} while =C-H and C–H peaks shifted to 3068 cm^{-1} and 2830 cm^{-1}, respectively. Its carbonyl C=O stretching also shifted to 1651 cm^{-1}. These band shifting suggested

bonding interactions between NVP and AZT. Furthermore, there was a significant shifting of AZT azido to 2105 cm^{-1} due to bonding interactions between the two APIs.

NVZA3 exhibited NVP stretching N–H band at 3188 cm^{-1}, AZT azido stretching at 2100 cm^{-1} while AZT stretching C-H appeared at 2827 cm^{-1} and stretching C=O band at 1644 cm^{-1}. AZT stretching O-H also subsided in the spectrum of NVZA3 sample. These spectral displacements authenticated the presence of interactions between N-H/O-H and C=O/C-H of both APIs. All identified shifts in IR band positions summarised in **Table 4.6** proved a successful formation of new NVP and AZT derivatives **NVZA1**, **NVZA2** and **NVZA3**.

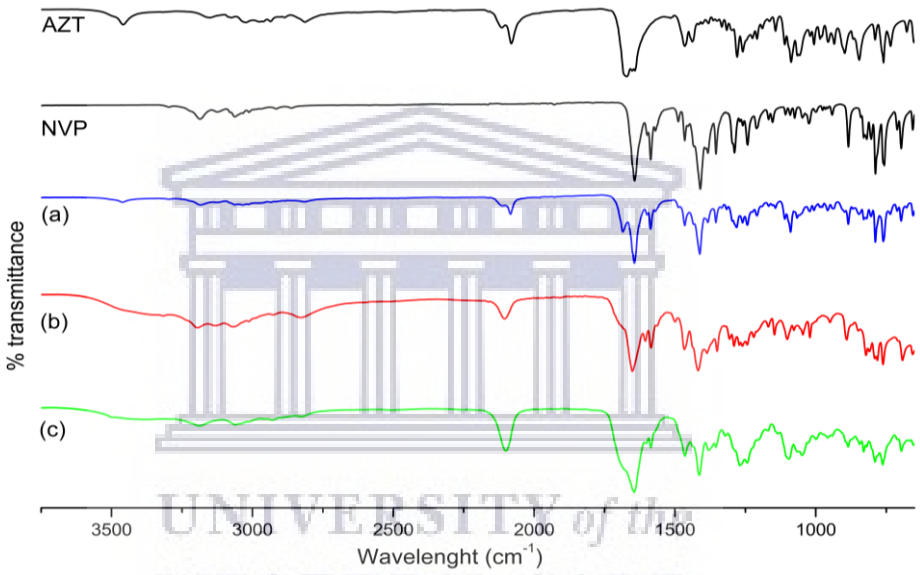

Figure 4.42: FTIR spectra of commercial NVP, AZT and their dual-drug derivative solid forms; (a) NVZA1, (b) NVZA2 and (c) NVZA3

Table 4.6: Summary of IR shifts found in different NVZA co-crystals and the eutectic mixture

	Functional group				
Sample	O–H	H–N	C–H	C=N	C=O
NVP		3186 cm^{-1}	3062 cm^{-1}		1643 cm^{-1}
			3024 cm^{-1}	2081 cm^{-1}	
AZT	3460 cm^{-1}	3150 cm^{-1}	2813 cm^{-1}	2115 cm^{-1}	1669 cm^{-1}
			3063 cm^{-1}		
		3183 cm^{-1}	3034 cm^{-1}	2084 cm^{-1}	1685 cm^{-1}
NVZA1	3461 cm^{-1}		2815 cm^{-1}	2113 cm^{-1}	1639 cm^{-1}
			3068 cm^{-1}		
NVZA2	3451 cm^{-1}	3195 cm^{-1}	2830 cm^{-1}	2105 cm^{-1}	1651 cm^{-1}
			3062 cm^{-1}		
NVZA3	Subside	3188 cm^{-1}	2827 cm^{-1}	2100 cm^{-1}	1645 cm^{-1}

4.3.4.3 Analysis of the NVZA derivative solid forms by Powder X-Rays diffraction

The PXRD patterns of **NVZA1**, **NVZA2**, **NVZA3**, physical mixtures and individual drugs AZT and NVP are presented in

Figure 4.43. Due to the absence of good quality crystals suitable for single X-rays diffraction, there was no elucidation of the structures. However, PXRD data provided enough information to categorize **NVZA** derivative solid forms.

The PXRD pattern of **NVZA1 (**

Figure 4.43a) inherited the characteristic diffraction peaks from individual drugs with minor changes in shapes and size of the peaks. The absence of new diffraction peaks resulted from a failed co-crystallisation and confirmed that **NVZA1** form is a binary eutectic mixture rather than the desired co-crystal.

In comparison to diffraction patterns of individual APIs, the PXRD pattern of **NVZA2** (**Error! Reference source not found.**b) exhibited new diffraction peaks at 2theta 10.5°, 11.6°, 14.21° and 16.2°; confirming it as a new dual-API co-crystal form. **NVZA3** was also confirmed as a new dual-API co-crystal with a PXRD pattern exhibiting the same diffraction peaks at 2theta 10.5°, 11.6°, 14.21°, 16.2° and additional peaks at 2theta 13.6° and 27.8° differing it from **NVZA2** co-crystal form.

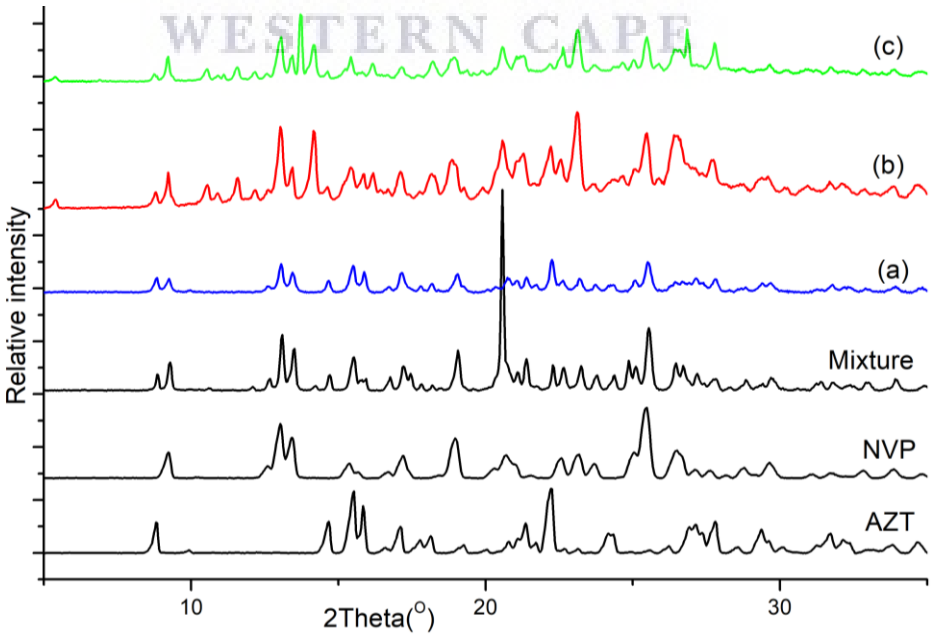

Figure 4.43: The experimental PXRD patterns for pure AZT and NVP, their physical mixture, and their solid derivative forms (a) NVZA1, (b) NVZA2, (c) NVZA3

4.3.4.4 In-vitro solubility evaluation of NVZA dual-APIs solid forms

Excess amounts of the individual drugs NVP, AZT, and their co-crystal were added to USP aqueous buffer solutions at pH 1.2, acetate buffer at pH 4.5 and phosphate buffer solution at pH 5.8, 6.8, and 7.4 and deionised water. The mixtures were continuously shaken in an incubator shaker at 37 °C (± 0.5) and 100 rpm for 48 hours. Samples were filtered using 0.20 μm PVDF syringe filters and analysed using an HPLC. The quantification was performed using a Perkin Elmer HPLC system set with FXB Pump (Flexar Binary Pump), an automated injector equipped with a UV detector (LC 200a Series PDA Detector), and a Flexar autosampler. Isocratic elution, at a flow rate of 10 mL/min was applied. A reversed-phase Supelco Discovery HS C_{18} HPLC column 15 cm x 4 mm, 5μm was utilised. Injection volume was 10 µL and absorbance of elution was recorded at 265 nm following suitable dilutions. The mobile phase used contained 50:50 acetonitrile (aq.).

For the standard/calibration curves, regression equations given by calibration data are as follows: For AZT, the regression equation,

$$Y = 13880x - 4423 \qquad \textit{Equation 4.1}$$

The regression equation for NVP

$$Y = 14384x + 41118 \qquad \textit{Equation 4.2}$$

Squared R deducted are 0.999 and 0.9998 respectively for AZT and NVP

Saturation solubility data for **NVZA1** are presented in **Figure 4.44.** AZT showed increased solubility in the eutectic **NVZA1** sample by 2.3, 2.4, 1.9, 1.6, and 2.3-fold respectively at pH=4.5 (ammonium acetate), pH=5.8, 6.8, 7.4 (0.1M potassium phosphate) and deionised water (H_2O). NVP also showed enhanced solubility by 2.3, 2.6, 2.0, 2.2, and 2.3 at the same pH values. The solubility of NVP in its pure form and the binary eutectic with AZT was inversely proportional to pH. This finding also agreed with the previous publication by Kuminek *et al.*, 2016. A lower melting transition of the binary eutectic **NVZA1** also justified its solubility increase.

The apparent solubility of both AZT and NVP has remarkably enhanced in the co-crystal form **NVZA2**. AZT was more soluble in **NVZA2** with a significant increase by 4.3-fold, 5-fold, and 4.3 at pH =6.8, 7.4 and deionized water. On the contrary, there was a decrease in AZT solubility at pH=1.2 (0.1 N HCl). This tendency is familiar in cases where two co-crystallised drugs have large solubility differences; the solubility increase of a less soluble drug leads to a decrease in solubility of a more soluble drug.

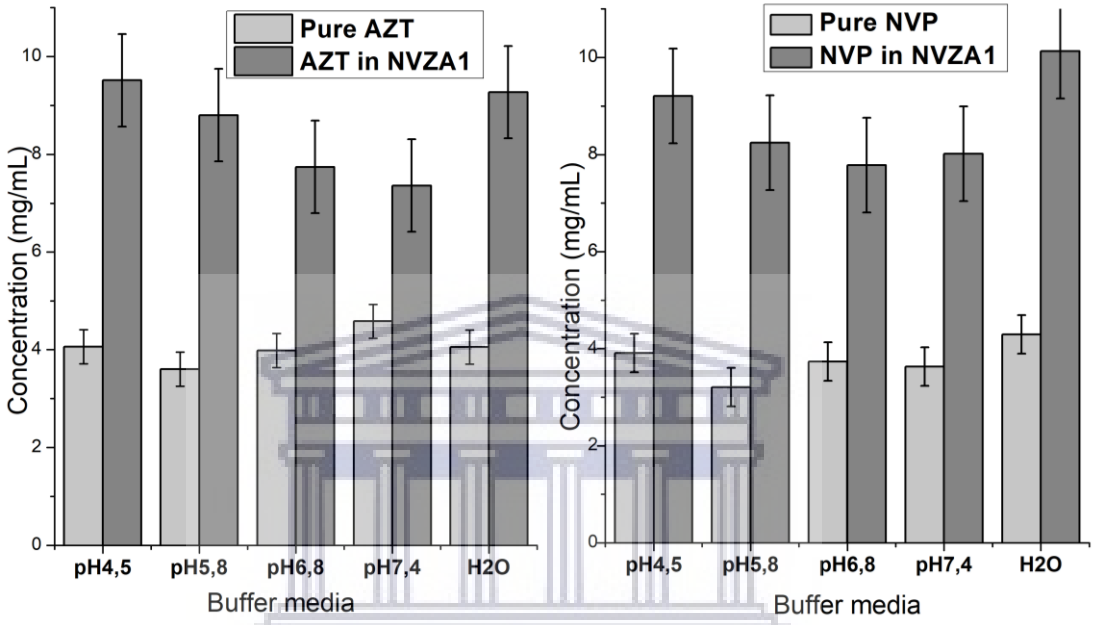

Figure 4.44: Histogram illustrating the dual co-crystallization-related solubility changes for NVP, AZT in the binary eutectic NVZA1 over a wide range of buffered media and unbuffered deionised water

Nonetheless, AZT solubility (in pure form and **NVZA2** co-crystal) was higher at pH=1.2 compared to the rest of the buffer media used and unbuffered deionised water. Compared to pure NVP, the solubility measurements revealed an increase of NVP solubility by ~2-fold in **NVZA2** at all pH environments (1.2-7.4) and unbuffered deionised water (**Figure 4.45**).

NVZA3 co-crystal sample **(Figure 4.46**) generally exhibited enhanced solubility for both AZT and NVP. Solubility measurements also indicated that AZT is less soluble by 0.3 times at pH=1.2 while solubility increase by 4.2, 4.3 and 3-times was recorded at pH=6.8, 7.4 and the aqueous solution respectively. On the other hand, NVP was more soluble by 1.1, 1.6, 1.6 and 1.7-fold respectively at pH=1.2, 6.8, 7.4 and deionized water.

These *in vitro* solubility measurements indicated a clear pH-dependent solubility for the pure form of NVP and all three derivative multicomponent crystal forms, with the maximum at pH=1.2. This attitude is not unusual among weakly basic drugs such as nevirapine (Kuminek et al., 2016), (Jean B. Ngilirabanga et al., 2020). Furthermore, the enhanced apparent solubility in the co-crystals is attributed to an increase in lattice energy by co-crystallisation (Ranjit & Sarma, 2018) of AZT with NVP in this instance.

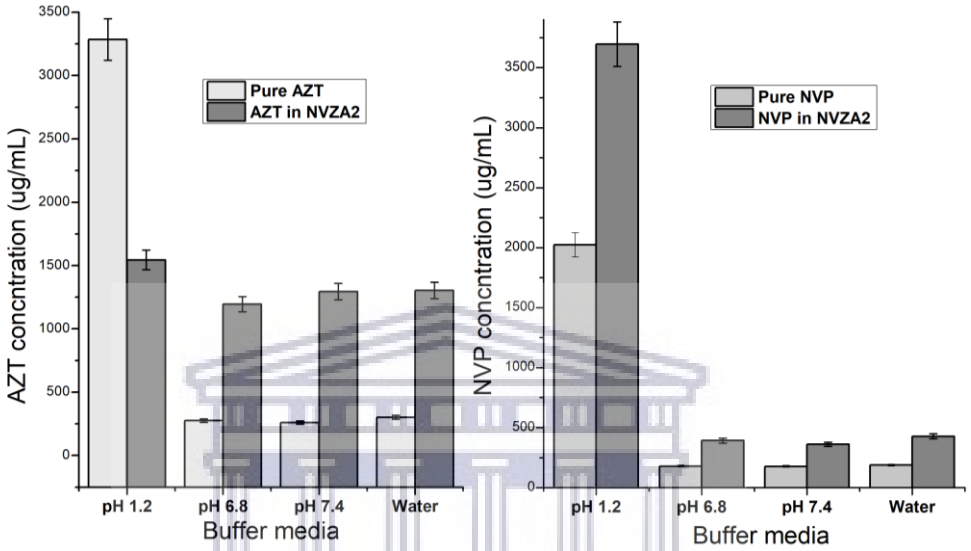

Figure 4.45: Histograms comparing solubility of pure AZT and NVP to NVZA2 co-crystal forms at pH=1.2, 6.8, 7.4 and aqueous media

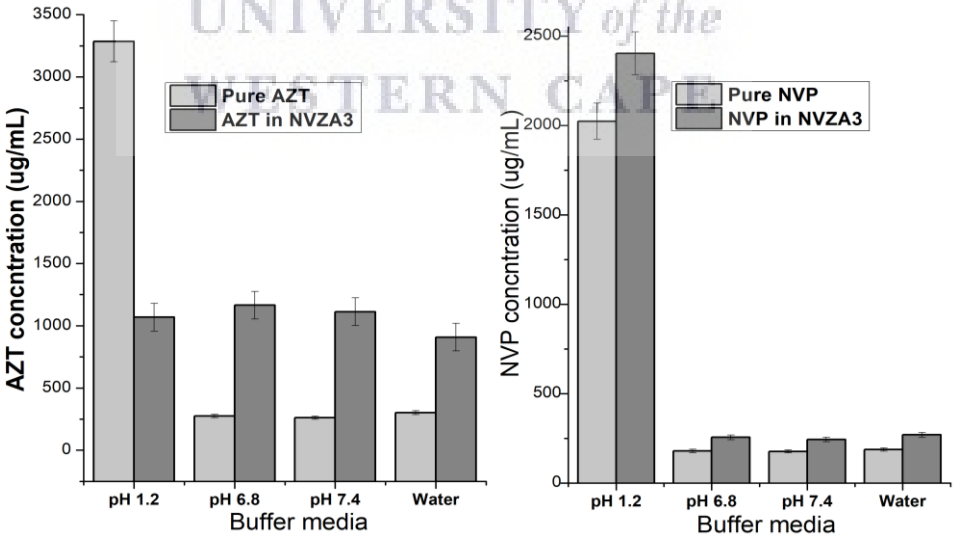

Figure 4.46: Histograms comparing solubility of pure AZT and NVP to NVZA3 co-crystal form in aqueous medium and buffer solutions at pH=1.2, 6.8 and 7.4

In conclusion, the co-crystal formation between nevirapine and zidovudine was successfully investigated using solid-state and solution co-crystallization methods. It

was found that two drugs form a dual-APIs co-crystal via solution crystallization methods while solid-state grinding generated eutectic mixture rather than the desired co-crystal. Thermal analyses, FTIR and PXRD, confirmed the NVZA derivative solid forms produced.

Based on *in vitro* solubility measurements, binary eutectic mixture **NVZA1** and dual-API co-crystal forms **NVZA2** and **NVZA3** are highly soluble compared commercial/starting materials. Combining these two APIs in a single dosage form either a tablet or capsule or any other formulations would significantly reduce the amount of excipients required during the manufacturing process. This is beneficial not only in terms of product cost but also in reducing the volume of the final dosage form; necessary for increased patient compliance to the treatment. Pharmaceutical formulators would, however, look at possible adjustment on the required amount of APIs per dose.

4.3.5 Efavirenz-Lamivudine multicomponent solid forms (EL)

The antiretroviral drugs EFV and 3TC both inhibit the HIV reverse transcriptase but belong to different classes, namely non-nucleoside and nucleoside transcriptase inhibitors, respectively, as discussed in section **3.2.** Despite the potential to interfere with the reserve transcriptase; the enzyme responsible for the multiplication of HIV, EFV is known to its aqueous solubility limitations which in turn affects its bioavailability. In this section, co-crystal formation between EFV and 3TC was attempted using different preparative methods.

4.3.5.1 Thermal analysis of EL solid forms by DSC and TGA

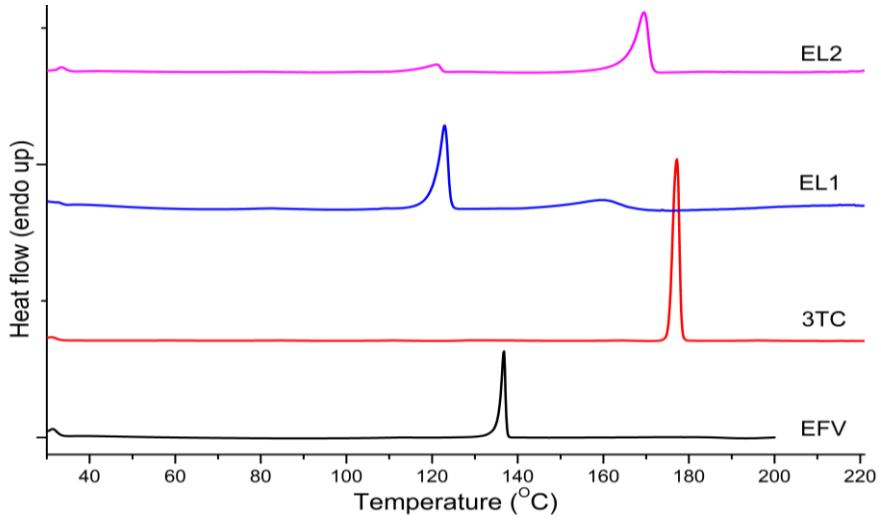

Figure 4.47: The DSC curves of pure EFV, 3TC, eutectic EL1 and the co-crystal EL2 samples

Using DSC analysis as a tool for quick detection of co-crystal formation, it was found that samples produced using a co-grinding method in a 1:1 and 3:2 named **EL1** exhibit the same melting point with a DSC endotherm peak at 119.53°C and onset at 115.40°C. The DSC curves of **EL2** samples prepared using a co-grinding method of APIs in a 1:2, 1:3 and 1:4 molar ratios (**Figure 4.47**) were characterised by two endotherms. The first transition endotherm was small with the maxima at 119.53°C and onset at 115.40°C and second intense endotherm corresponding to samples melt at 167.67°C and an onset at 164.77°C.

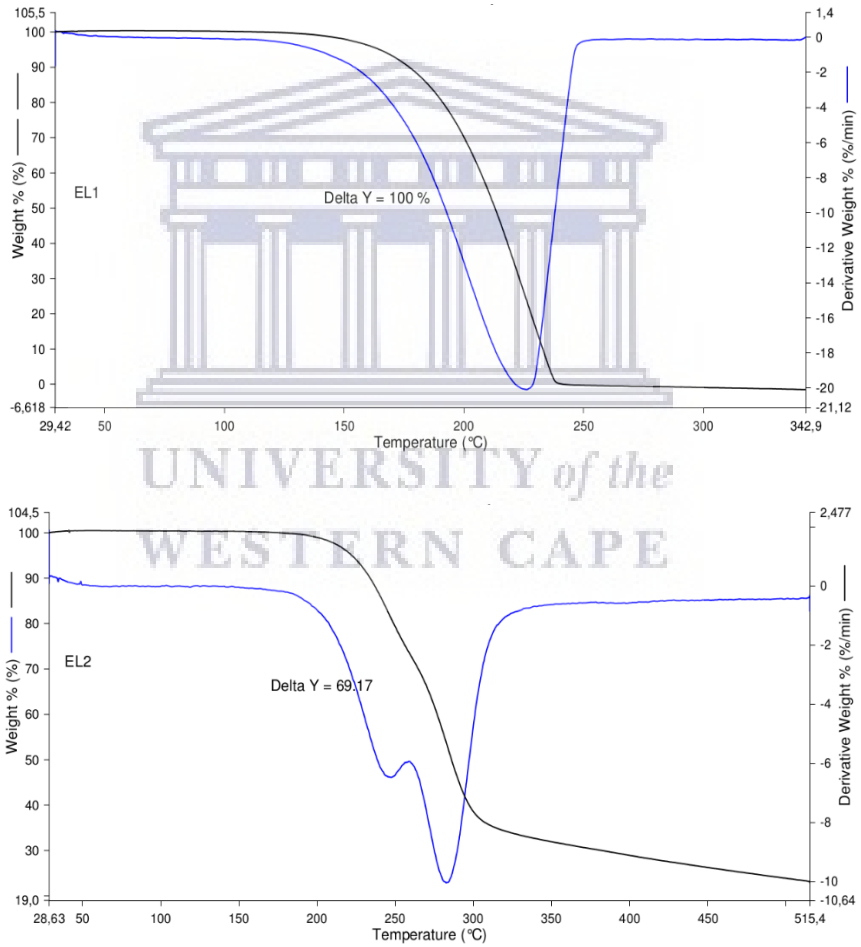

Figure 4.48: TGA/DTA curves of the binary eutectic EL1 showing a decomposition mass loss of ~100% and the co-crystal EL2 showing a total decomposition mass loss of 85%.

The analysis by TGA was carried out to understand the thermal behaviours of the sample further. The TGA/DTA curves of EFV, 3TC and **EL1 and EL2** co-crystalline

samples are shown in **Figure 4.48**. Both samples showed no indication of mass loss until the onset of decomposition upon which a significant loss occurs.

For the eutectic **EL1,** 100% mass loss occurred upon decomposition, whereas only 69.1% mass loss was observed upon the co-crystal **EL2** degradation. The TGA graph of the co-crystal sample **EL2** showed that the weight of the sample remained unchanged until 175°C and start decreasing over melting and degradation. Furthermore, the TGA analysis for the co-crystal **EL2** does not indicate any mass loss around 120°C, therefore, supporting the DSC finding that a small endotherm was due to physical transition of the sample rather than a desolvation or release of any guest molecule.

4.3.5.2 FTIR spectroscopic analysis of EL1 and EL2 co-crystal samples

FTIR spectroscopy as a popular analytical method used for studying hydrogen bond formation in materials was carried out. The FTIR spectra of both individual drugs EFV and 3TC, and the EL1 and EL2 samples are presented in **Figure 4.49**. FTIR analysis was initiated by exploring the structures of pure drugs as references. Characteristic bands for both EFV and 3TC matched the previous reports (N. P. Reddy et al., 2015) (Pandey et al., 2016). EFV spectrum has two absorption bands peaks at 3314 cm^{-1} and 1742 cm^{-1} respectively assigned to the carboxamide N−H and C=O stretch. The peak at 3095 cm^{-1} was due to the aromatic C−H stretch while the band at 2250 cm^{-1} was assigned to stretching C≡C. The FTIR spectrum for 3TC showed characteristic peaks at 3324 cm^{-1} and 3196 cm^{-1} respectively assigned to amino N−H and hydroxyl O−H stretching. The peaks at 3075 cm^{-1} and 2833 cm^{-1} were respectively assigned to sp^2 and sp^3 C−H stretch.

The absorption peak at 3199 cm^{-1} in the **EL1** spectrum had shifted from 3TC peak at 3196 cm^{-1}. EFV carboxamide stretching C=O at 1742 cm^{-1} slightly shifted to 1740 cm^{-1} in the **EL1** spectrum, suggesting weak interactions with 3TC pyrimidine N−H.

In the FTIR spectra generated by **EL2** sample, the 3TC stretching N-H peak at 3324 cm^{-1} has shifted to 3330 cm^{-1}, and the stretching O-H peak at 3196 cm^{-1} has also shifted to 3207 cm^{-1}. Further, 3TC aromatic stretching =C-H peak at 3075 cm^{-1} has shifted to 3080 cm^{-1}. On the other hand, EFV pyrimidine N-H stretching at 3313 cm^{-1} and C-H stretching at 3095 cm^{-1} were significantly displaced to 3330 cm^{-1} and 3030 cm^{-1} respectively (**Figure 4.49**, **Table 4.7**) as a result of possible N-H···O-H/C-H···N-H or

N-H···C=O bonding. Due to these spectral shifting, FTIR studies identified the powder sample **EL2** as a potential dual-API co-crystal form of EFV and 3TC. The possibilities of halogen (Cl or F) bonding interaction were ruled out by the absence of relatively large shifting in spectra of both **EL1** and **EL2** samples. This further indicated that not only did halogens Cl and F have no influence on the complexation process but also expressed very weak or no bonding between **EL** precursors. Different functional groups and assignments in both eutectic mixture **EL1**, co-crystal **EL2** and pure drug spectra were summarised in **Table 4.7**. **Figure 4.50** also illustrates suggested interactions based on FTIR findings.

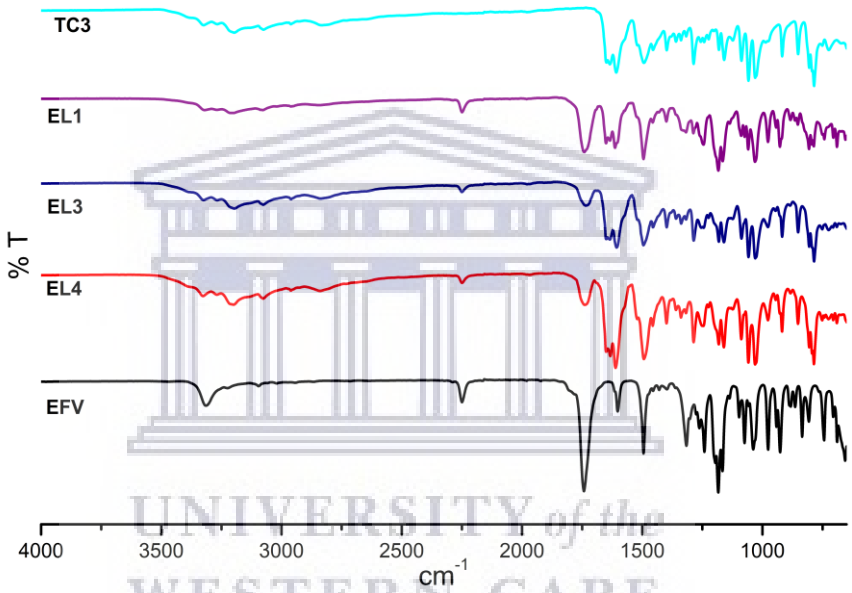

Figure 4.49: FTIR spectra of EFV, 3TC and EL solid forms compared

Table 4.7: Summary of characteristic peaks in the FTIR spectra of EFV, 3TC, the eutectic EL1 and the co-crystal EL2 and their assignments

Assignments	EFV	3TC	EL1	EL2
Pyrimidine N-H	3313 cm^{-1}	3324 cm^{-1}	3463 cm^{-1}	3330 cm^{-1}
Hydroxyl O-H	-	3196 cm^{-1}	3196 cm^{-1}	3207 cm^{-1}
Aromatic =C-H	3095 cm^{-1}	3075 cm^{-1}	3095 cm^{-1}	3080 cm^{-1}
Aliphatic C-H	-	2833 cm^{-1}	2833 cm^{-1}	Subsides
-C=N	2250 cm^{-1}	-	2250 cm^{-1}	Subsides
C=O stretch	1742 cm^{-1}	-	1740 cm^{-1}	1744 cm^{-1}
	-	1649 cm^{-1}	1643 cm^{-1}	1650 cm^{-1}

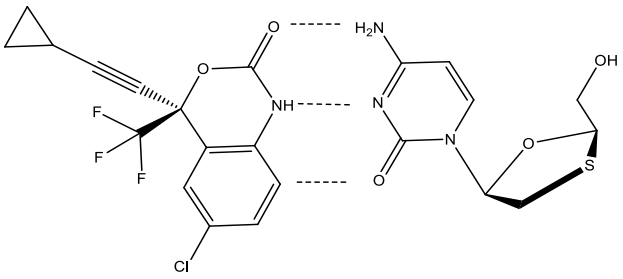

Figure 4.50: Suggested interactions based on the FTIR results

4.3.5.3 Morphology of EL sample particles

Representative SEM micrographs presented in **Figure 4.51**, highlight morphologic differences of **EL** samples to raw materials. Morphology of the sample particles individually also shows different habits among themselves. While EFV exhibited polyhedral rod-shaped particles and lamivudine showed very large, irregularly-shaped particles with smooth surfaces, **EL1** sample is made long fibre-like particles. **EL2** co-crystal sample exhibited a mixture of irregular and fibre-shaped particles, suggesting new crystal habits and a successful formation of new chemical entities.

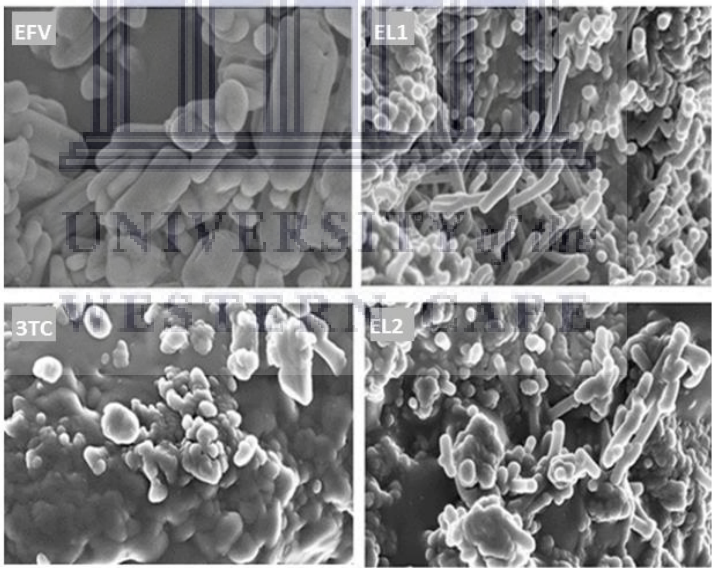

Figure 4.51: SEM images comparing the particle morphology of EFV, eutectic EL1, the co-crystal EL2 and 3TC particles analysed with the magnification of 10.00kX and 1 μm and EHT = 5 kV.

4.3.5.4 Powder X-Rays diffraction discussion of EL solid forms

The Powder XRD analysis was carried out on the starting materials and the powder samples to confirm whether a co-crystal was produced. PXRD patterns are shown in **Figure 4.52**. While the PXRD pattern generated from EFV is characterised by very

sharp, intense characteristic diffraction peaks at 2θ 6.00°, 10.3°, 10.83°, 12.16°, 13.1°, 14.12°, 15.15°, 16.83°, 21.10°, and 24.86°, 19°, 21.84°, 23.00°, 27.1°, 27,9°, 29°, the 3TC pattern exhibited diffraction peaks at 2θ=13.23°, 17.38°, 20.50°, 21.29°, 24.79°, 26.33°. PXRD pattern from **EL1** inherited all diffraction peaks from both EFV and 3TC which confirmed **EL1** as eutectics/solid dispersions rather than a co-crystal desired. On the other hand, the **EL2** pattern exhibited new diffraction peaks at 2θ=11.2°, 11.72°, 13.4°, 17.52° and 21.43° confirming **EL2** as a dual-APIs co-crystal.

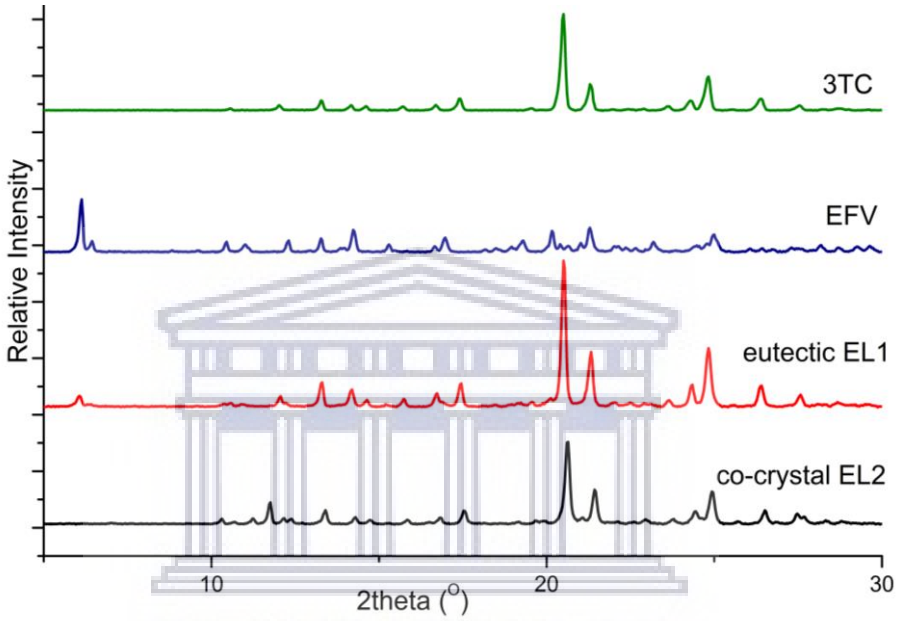

Figure 4.52: The experimental PXRD patterns of pure 3TC, EFV, the binary eutectic EL1 and the co-crystal EL2

4.3.5.5 Solubility evaluation

Evaluating the physicochemical properties of a new active substance such as solubility is an important step in the pharmaceutical development process due to its influence on drug formulation, bioavailability, storage and dosage form itself (Verma & Mishra, 2016). *In vitro* solubility evaluation was carried out by dissolving an excess amount of individual drugs and the co-crystal sample in different buffer solutions at pH 1.2, 6.8 and 7.4 prepared with 0.1% Tween (a surfactant). The mixtures were continuously shaken for 48 hours at a predetermined 100 rpm and 37°C and filtered (0.45 um). Azula HPLC was subsequently used to quantify both pure APIs vs their amount released by eutectic **EL1** and the co-crystal **EL2**.

Azula HPLC system setting

The FXBPump (Flexar Binary Pump), an automated injector equipped with a UV detector (LC 200a Series PDA Detector), and a Flexar autosampler. Isocratic elution, using a flow rate of 1 mL/min with acetonitrile: deionized water (70:30). A reversed-phase Supelco Discovery HS C18 HPLC column 15 cm x 4 mm, 5µm was used. Injection volume was 10 µL, and absorbance of elution was recorded at the necessary wavelength. Standard calibration was performed. Calibration curves are presented in **Figure 4.53**.

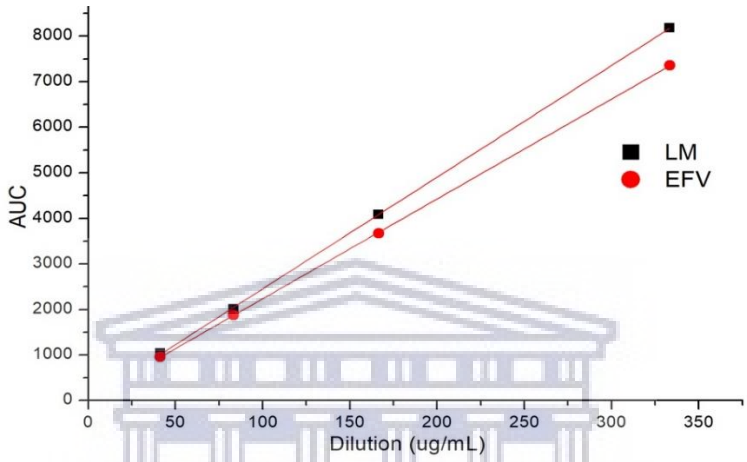

Equation	y = a + b*x	
Adj. R-Square	0,99993	0,99995
		Value
LM	Intercept	5,77328
	Slope	24,50019
EFV	Intercept	47,74053
	Slope	21,90453

Figure 4.53: EFV and 3TC calibration curves

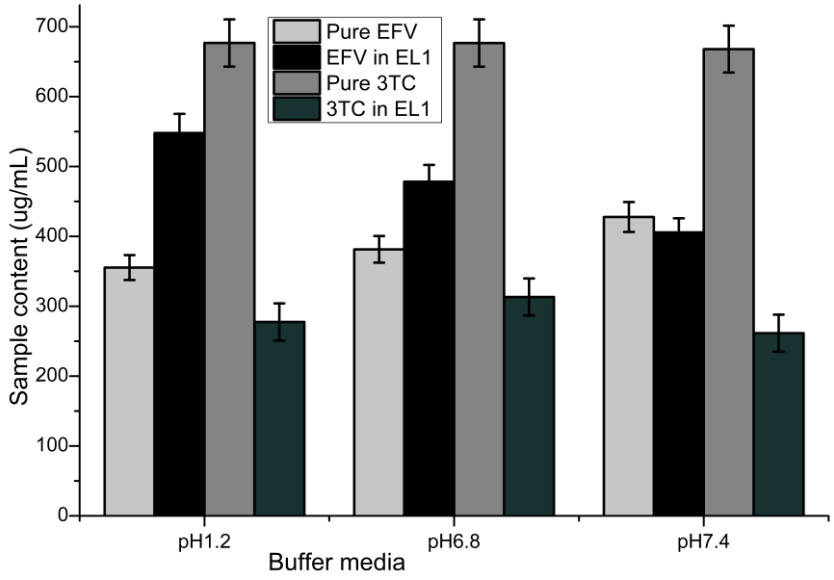

Figure 4.54: Solubility histograms comparing pure EFV and 3TC to their amount released by eutectic EL1 in buffer solution at pH 1.2, 6.8 and 7.4

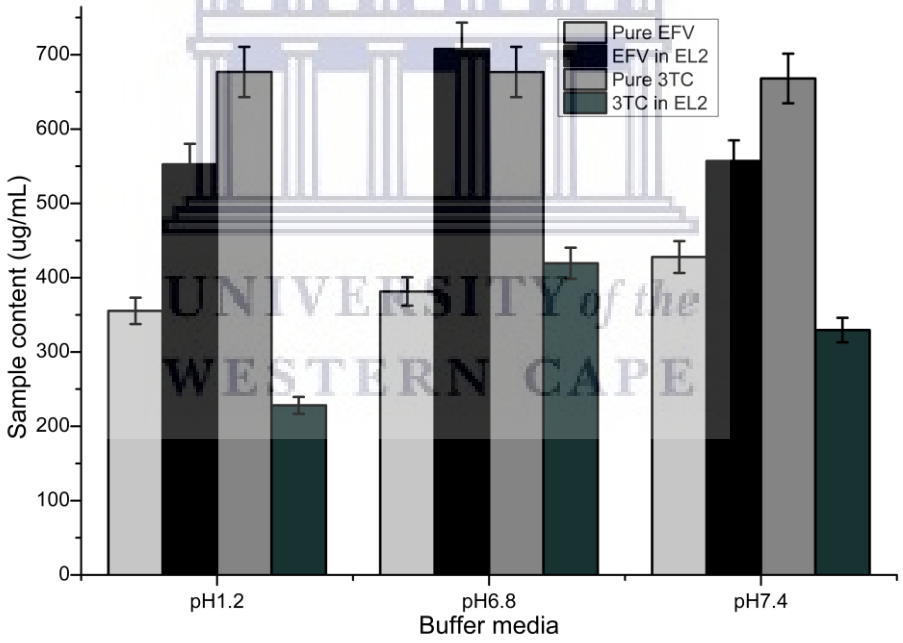

Figure 4.55: Solubility histograms comparing pure EFV and 3TC to their amount released by co-crystal EL2 in 0.1 N HCl buffer solution at pH 1.2, PBS pH 6.8 and 7.4

Solubility measurements suggested that EFV is more soluble in the eutectic **EL1** by 1.5 and 1.3-fold than pure API at acidic pH (1.2 and 6.8). On the contrary, there was no solubility increase at pH 7.4. 3TC exhibited a reduced solubility in buffer solutions used by 2.4, 2.2, and 2.5-fold at pH 1.2, 6.8 and 7.4 respectively.

Unlike its pure form which solubility appears to have increased with pH, EFV solubility in **EL1** is inversely proportional to the pH of the used buffer solutions (pH dependant), with more solubility at pH=1.2 (**Figure 4.54**).

The solubility of the co-crystal sample **EL2** was evaluated under the same pH and analysed against pure EFV and 3TC (**Figure 4.55**). **EL2** solubility histograms are presented in **Figure 4.55**. EFV solubility increase by 1.5, 1.8, 1.3 was respectively observed at pH=1.2, 6.8 and 7.4. Simultaneously, 3TC solubility decreased by 2.9, 1.6 and 2 under the same pH values.

4.3.6 Nevirapine-Lamivudine solid forms (NL)

Antiretroviral drugs nevirapine and lamivudine are used in combination for the treatment of HIV infection. Knowing that NVP suffers from poor aqueous solubility, the study aims at exploring the co-crystal formation between the two APIs for a better pharmacological response.

4.3.6.1 The binary eutectic NL thermal analyses

The DSC analysis was carried out following the method described in section 4.2.3.2 and obtained thermal information was compared to the HSM images to better understand the sample's behaviours and interpretations.

The binary eutectic **NL** sample melted between 170-173°C temperature range and decomposed towards 250°C as indicated by discolouration the sample of the glass slide of the HSM. There was no thermal change observed prior to the melting point, which is consistent with the DSC outcomes presented in **Figure 4.56.** A single endothermic peak at 173°C (an onset at 170°C) marked the melting point of eutectic **NL** sample. Basic DSC parameters of both NVP and 3TC and the binary eutectic NL are summarised in **Table 4.8**.

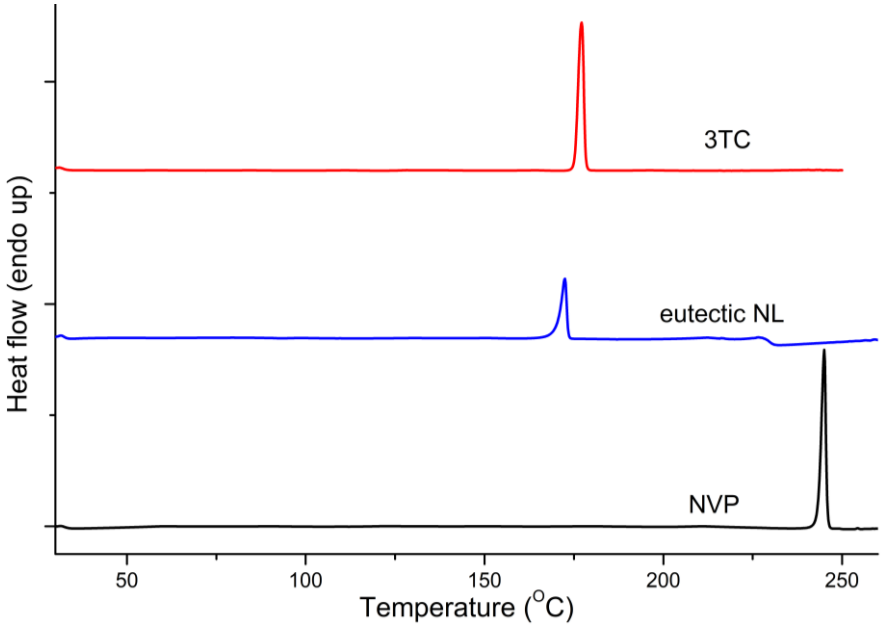

Figure 4.56: DSC graph of pure NVP, 3TC and a lower melting DSC curve of the binary eutectic NL produced

Table 4.8: The summary of essential DSC data of NVP, 3TC and eutectic NL

Material	Melting onset	Melting point	Delta H (jg^{-1})	Peak area (mJ)
NVP	245.49°C	246.87°C	113.909	193.645
3TC	175.32°C	177.17°C	119.987	299.967
Eutectic NL	170.5°C	172.67°C	2.3223	69.669

TG analysis was also carried out using a method outlined in section **4.2.3.3.** The TGA/DTA curves calculated from the eutectic NL sample and presented in **Figure 4.57**, are characterised by a single mass loss deviation due to the decomposition (190°C-350°C) with a total loss of 75% approximately. There was no indication of any mass loss over the temperature ranging below the melting onset, which ultimately suggested the absence of volatile substances in the sample molecular structure.

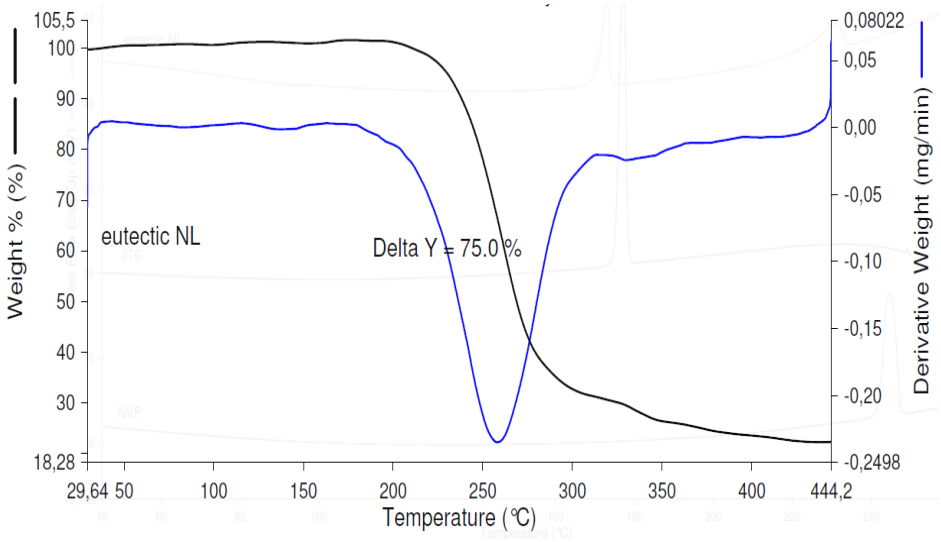

Figure 4.57: The TGA/DTA curves of the binary eutectic sample (NL) with a total decomposition mass loss of 75%

4.3.6.2 FT-IR studies of the binary eutectic NL

The FTIR analysis was carried out to obtained structural information. Spectra of individual APIs were plotted against the newly prepared solid form as presented in **Figure 4.58**

In the FTIR spectrum of 3TC, the amino N–H and hydroxyl O–H stretching peaked at 3324 cm^{-1} and 3196 cm^{-1} respectively, while peaks at 3075 cm^{-1} and 2883 cm^{-1} appeared due to the C–H stretching of cytidine. The spectral peaks at 1648 cm^{-1} and 1635 cm^{-1} belong to C=O and C=C stretching, respectively. This is consistent with the previous work by Pandey, Yadav and Mishra, (2016). Minor differences observed could be due to different instrumentation, sensibility, and purity of samples.

NVP spectral peaks were assigned according to studies found in (Chadha et al., 2010b; Samsodien et al., 2017; Sarkar et al., 2008). Pure NVP spectrum exhibited absorption band peaks at 3185 cm^{-1} and 1641 cm^{-1}, respectively corresponding to N–H and C=O stretch of the carboxamide moiety. The characteristic band at 3062 cm^{-1} was assigned to C–H stretching vibrations.

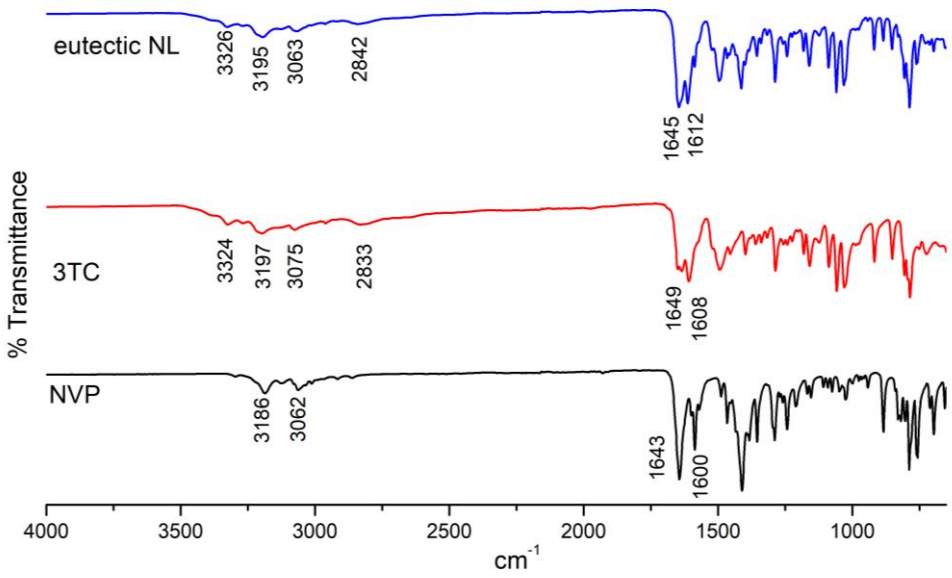

Figure 4.58: The FTIR spectra of NVP, 3TC and the prepared binary eutectic NL compared

The binary eutectic NL inherited both starting materials spectral band peaks with only minor shifting attributed to weak interactions between NVP and 3TC. Given a lower melting transition than pure NVP and 3TC, **NL** was confirmed as a binary eutectic.

4.3.6.3 Powder X-Ray Diffraction analysis of NL sample

The powder X-ray diffraction was used to confirm FTIR findings. The PXRD patterns of pure APIs and NL were presented in **Figure 4.59**. PXRD patterns generated from **NL** sample exhibited characteristic diffraction peaks at 2theta positions 9.3°, 13°, 13.3°, 19°, 20.4°, 21.2°, 24.9°, 25.5° and 26.4°. These positions are similar to those found in patterns generated from pure NVP and 3TC, confirming NL as a binary eutectic and also prove that the co-crystal preparation between these two APIs using solid-state co-grinding was unsuccessful.

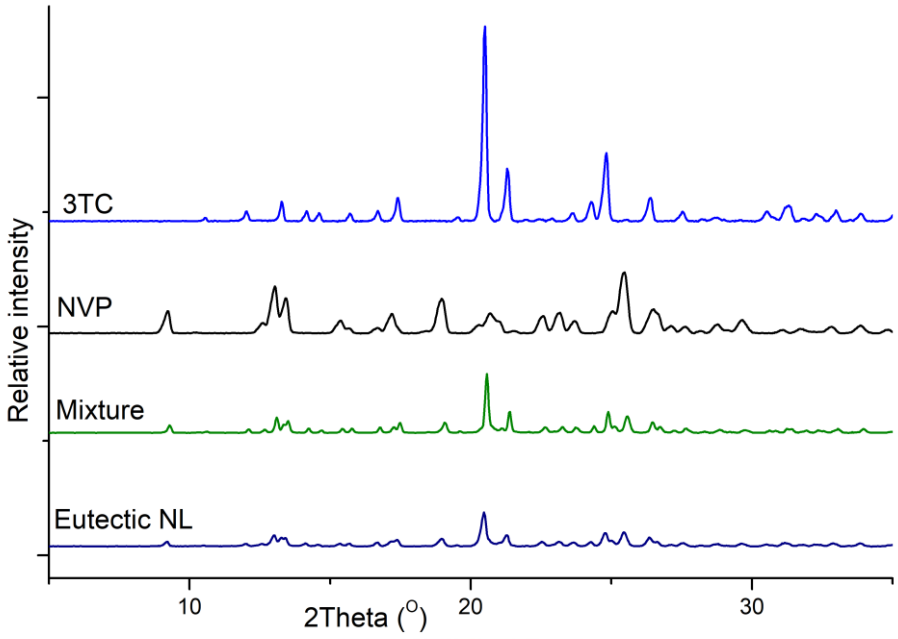

Figure 4.59: The experimental powder X-ray diffraction patterns for NVP, 3TC, NVP-3TC physical mixture and the binary eutectic NL

4.3.6.4 *In vitro* solubility evaluation of the binary eutectic NL

Regardless of this unsuccessful co-crystallisation, solubility evaluation was performed on the binary eutectic formed. Gradient elution, at a flow rate of 10 mL/min was applied as follows: Solvent A = Methanol 85% (aq.) and solvent B: phosphate buffer solution (pH=3.6); equilibration = 5 min (55:45), 3 min (55:45), 1 min (10:90), 5 min (10:90), 1 min (55:45), and 5 min (55:45). A reversed-phase Supelco Discovery HS C18 HPLC column 15 cm x 4 mm, 5µm was used. The injection volume was 10 µL, and absorbance of elution was recorded at the necessary wavelength following suitable dilutions. Squared R was found to be 0.99905 for 3TC and 0.9998 for NVP. Calibration curves are presented in **Figure 4.60**.

The HPLC data presented in **Figure 4.61** and **Figure 4.62** suggested a remarkable solubility increase of both APIs in the binary eutectic **NL**. Compared to untreated 3TC, the amount of 3TC in the **NL** sample increased by 2-fold, 2-fold, 2.6-fold, 2.5-fold, and 2.6-fold respectively at pH = 1.2 (0.1N HCl), pH = 4.5 (Ammonium acetate), 0.1 M potassium phosphate pH = 5.8, 6.8, 7.4 and aqueous (H_2O) medium. The amount of NVP in the **NL** sample was increased by 2.3-fold, 2.2-fold, 2.3-fold, 2.1-fold, and 2-fold respectively at same pH values (pH =1.2, 4.5, 5.8, 6.8, 7.4, and H_2O).

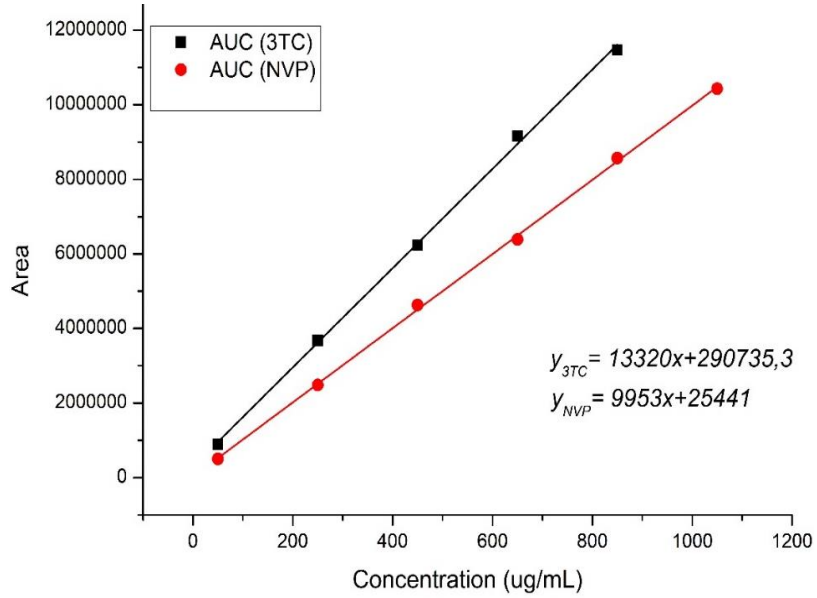

Figure 4.60: Calibration curves for both NVP and 3TC

As a lipophilic drug, NVP is known for its poor aqueous solubility which significantly affects its bioavailability. Just like other weakly basic drugs, NVP has the pH-dependant solubility profile. Pure NVP solubility and its binary eutectic with 3TC were inversely proportional to pH, exhibiting higher solubility at ≤ pH 2. This is consistent with the previous publication (Kuminek et al., 2016). Furthermore, binary eutectic NL showed a lower melting point compared to both 3TC and NVP. This may have contributed to its improved solubility profile.

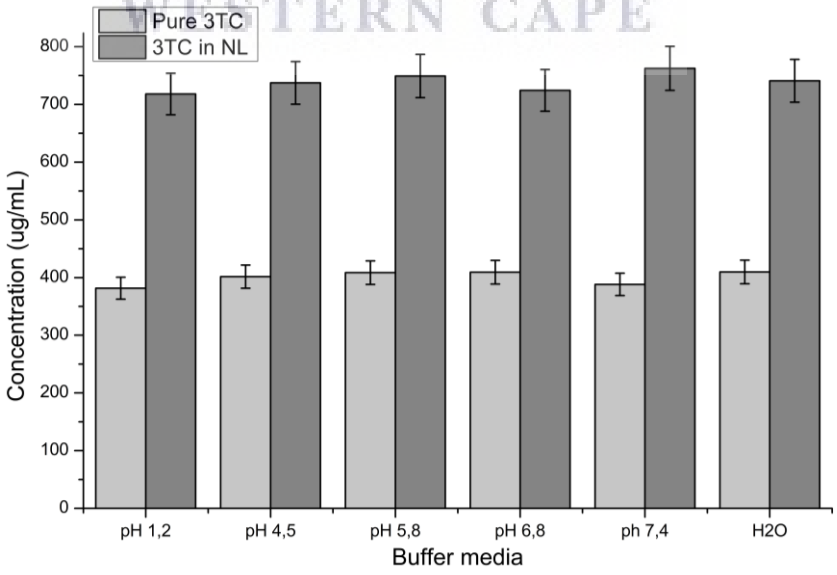

Figure 4.61: Solubility histogram comparing 3TC in the binary eutectic NL to the pure 3TC in different buffer solutions and deionised water

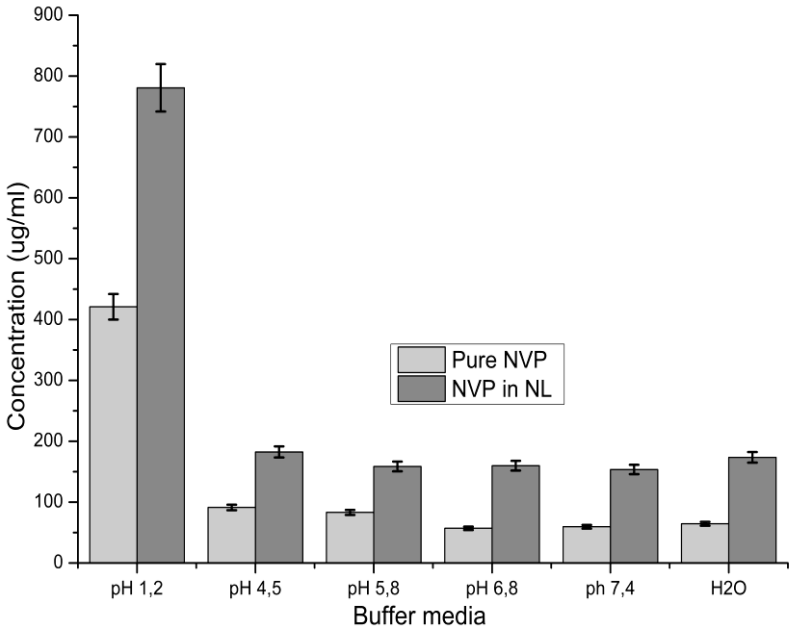

Figure 4.62: Solubility histogram comparing pure NVP to the binary eutectic NL in buffered solutions (different pH) and deionised water

4.4 Conclusion

In total, 5 daul-API co-crystals namely; efavirenz-zidovudine (EFZA), nevirapine-efavirenz (NEF), nevirapine-zidovudine (NVZA2 & NVZA3) efavirenz-lamivudine (EL2) and 4 eutectic binary mixtures including lamivudine-zidovudine (LMZT), nevirapine-zidovudine (NVZA1), efavirenz-lamivudine (EL1), and NL have been successfully produced. All hydrids were characterised for their thermal behaviours using HSM, DSC and TGA/DTA. Spectral studies using FTIR provided information of molecular interactions of the combination systems, whereas SEM and PXRD respectively provided morphology assessment and confirmation of samples chemical identities. Furthermore, the *in-vitro* solubility evaluation of all dual-APIs solid forms suggested enhanced solubility at different pH buffer solutions and water.

Chapter 5 Dual-drug co-crystals/eutectics of selected antiretroviral and anti-tubercular drugs: Non-covalent synthesis and characterisation

In this chapter, the description of co-crystallisation experiments of selected APIs and the discussion of results are presented. The conclusion on the physicochemical properties and the type of solid derivative form produced is also given accordingly.

5.1 Introduction

The current treatment strategies of HIV/TB co-infected patients which involve taking a combination of different doses, present different challenges (Bell & Noursadeghi, 2018; Narendran & Swaminathan, 2016; Pawlowski et al., 2012a). Apart from an increased chance of drug resistance development due to regimen compliance, there are other factors based on the diagnosis itself such as lower sensitivity for smear microscopy, atypical chest radiographic appearances, and frequent extra-pulmonary localisation. Other challenges include a high load of pills and risks of drug interactions, adverse effects and toxicity to patient' internal organs such as live and kidneys, etc. (Efsen AM, Schultze A, Post FA, Panteleev A, Furrer H, Miller RF, Losso MH, Toibaro J, Skrahin A, Miro JM, 2015).

To find a solution to above issues, combination strategies such as fixed-dose combinations have been developed and somehow eased problems such as drug interactions, irregularities in doses but still present additional challenges (Paul, 2019) and does not solve poor physicochemical properties such as poor solubility and stability known among current anti-HIV/TB drugs. Therefore, alternative therapeutic strategies of treatment that are more efficient, cost-effective, and safer are highly in demand.

For the past few years, engineering crystals of pharmaceutical solids has proven to be a fruitful approach to manage different properties of active pharmaceutical ingredients (API); properties such as solubility and dissolution that are strongly dependant on the physical state of the API. Given that fact, there is a fuelled desire to discover and

manipulate different crystal forms of APIs. One type of interesting crystal forms are co-crystals (Ancheria et al., 2019; Couillaud et al., 2019; Vishweshwar et al., 2006). As previously discussed, co-crystals are multicomponent crystal forms in which two or more molecules that are solids under ambient temperature coexist through non-covalent interactions such as hydrogen bonds, halogen bonds, p–p stacking and/or van der Waals interactions (Steed, 2013b).

5.2 Experimentation materials and methodologies

5.2.1 Materials

In this chapter, Efavirenz (EFV) and zidovudine (AZT) obtained as a generous donation from ASPEN Pharmacare (Port Elisabeth, South Africa), 1-adamantylamine (ADT), isoniazid (purity ≥ 99.6%) and pyrazinamide (purity ≥ 98.6%) purchased from Sigma-Aldrich Chemie GmbH (Steinheim, Germany), were used for the co-crystal screening. Synthesis and full characterization of different antiretroviral-antituberculosis dual drug co-crystals and other multicomponent hybrids of selected APIs have been demonstrated.

5.2.2 Preparatory methods

5.2.2.1 Efavirenz-isoniazid co-crystal screening

Mechanochemical reactions were created by physically grinding the mixture of both APIs in an agate mortar and a pestle (**Figure 5.1**) for thirty minutes to produce a dual co-crystal of EFV and INH. Mixtures in different ratios (1:1; 1:2, 1:3) were prepared during the co-crystal screening process. The whole screening data are presented in Appendix A.

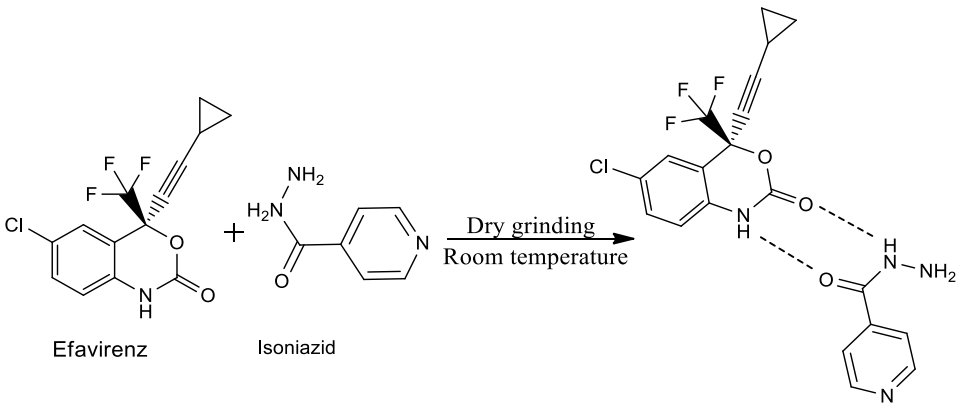

Figure 5.1: Molecular mechanistic for the preparation of EFINH co-crystal

5.2.2.1 Preparation of EFAD sample

The EFAD sample was prepared by the physical co-grinding method, using a mortar and a pestle **(Figure 5.2)**. Pure drugs; efavirenz (EFV) and 1-adamantylamine (ADT) in their 1:1 stoichiometric molar ratio [EFV (0.02 mg) and ADT (0.0096 mg)] were subjected to physical milling for at least thirty minutes. An unstable and hygroscopic sample (EFAD) was obtained and was subsequently analysed. Screening for the co-crystal between EFV and ADT was also attempted using a 2:1 stoichiometric ratio where double the amount of EFV was used while maintaining the weight of ADT. Results are included in experiment summary (Appendix A).

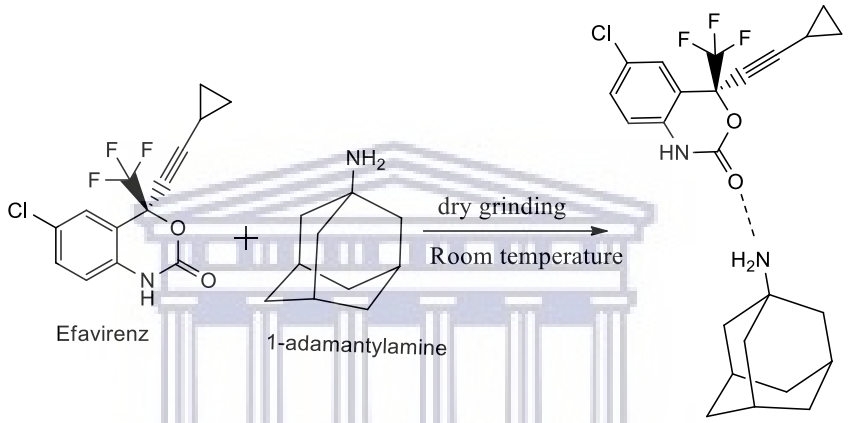

Figure 5.2: Molecular mechanistic for the preparation of EFAD amorphous solid dispersion

5.2.2.2 Synthesis of INHZA

For the preparation of INHZA, AZT and INH were taken in their equimolar ratio (AZT; 10mg, and INH; 20mg) and subjected to solid-state grinding in a mortar-pestle for at least thirty minutes. Powder sample produced was sealed in the polytop vials and was subsequently characterized by a series of analytical instruments. **Error! Reference source not found.** demonstrates the molecular mechanistic for the formation of INHZA solid dispersion.

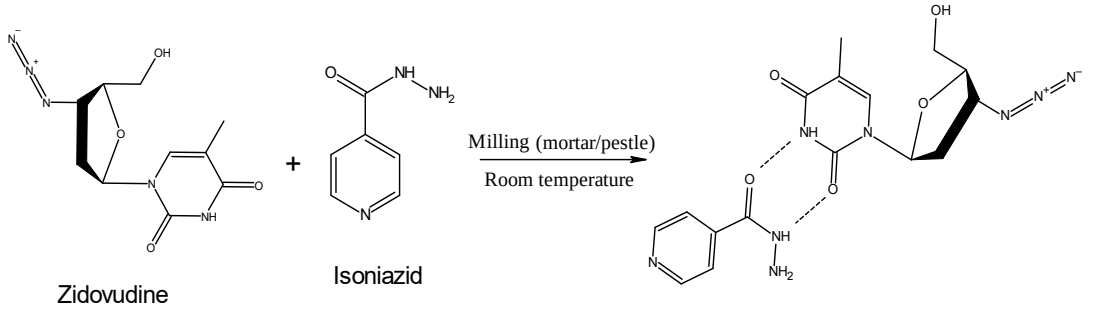

Figure 5.3: The molecular mechanistic for the preparation of INHZA

5.2.2.3 Preparation of AZTPZA sample

A mixture of pure drugs Zidovudine (AZT) and pyrazinamide (PZA) in 1:1 stoichiometric ratio, was prepared in a mortar and physically milled for thirty minutes using a pestle (**Figure 5.4**). A solid crystalline sample obtained was stored in a sealed vial for further analyses and characterisation. The co-crystal formation was also attempted using solvent evaporation. All experimental outcomes are summarised in Appendix A.

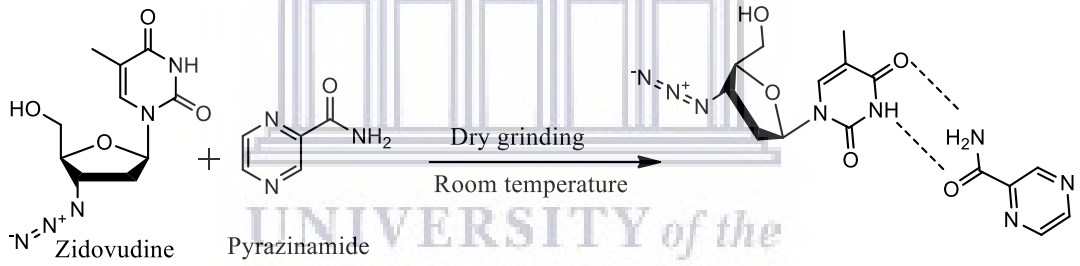

Figure 5.4: The molecular mehcanistics for the preparation of AZTPZA eutectic mixture

5.2.2.4 LMISO preparation

Screening for a co-crystal between 3TC and INH was carried out using the solid-state co-grinding technique. The physical mixtures in a 1:1, 1:2, 2:1 stoichiometric ratio were prepared first. Each mixture was introduced into an agate mortar and co-milled using a pestle for at least thirty minutes (**Figure 5.5**). The resultant powder; LMISO was analysed immediately. The preparation experiments were carried out in triplicate to ensure reproducibility of the samples. There was no need for temperature adjustment as grinding was carried out at room temperature. The co-crystal formation was also attempted using solvent evaporation. All experimental outcomes are summarised in Appendix A.

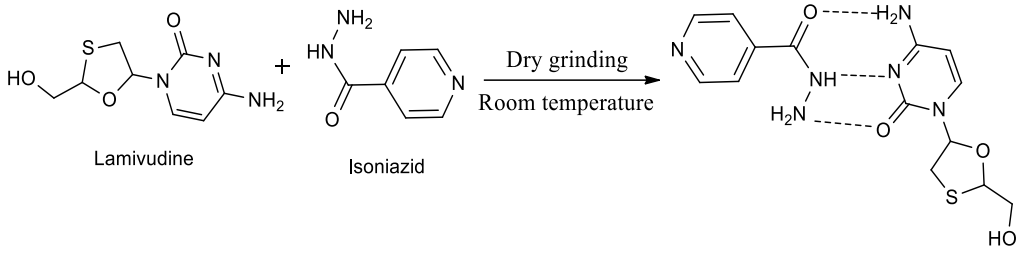

Figure 5.5: The molecular structures of co-formers lamivudine and isoniazid

All samples were prepared in triplicate to ensure that they were reproducible.

5.2.3 Characterization of the samples

A full characterization was carried out for obtained samples vs their starting materials. Thermal analysis using the Hot Stage Microscopy, Differential scanning calorimetry, and thermogravimetric analyses. Sample morphologies were evaluated using Scanning electron Microscopy, while structural information and molecular identities of samples were obtained from Fourier infrared spectroscopy and the powder X-ray diffraction. In vitro solubility of samples was measured using PHLC.

5.2.3.1 Analysis by Hot Stage Microscopy (HSM)

Thermo-microscopic analyses were performed with an optical microscope Olympus (SZX-ILLB200) equipped with a Linkam temperature-controlled stage (THMS600/720), connected to a T95-PE system controller (Linkam Scientific Instruments Ltd., Tadworth, Surrey, UK). Images were recorded with an Olympus UC30 camera attached to the specified microscope (Olympus Optical, Japan) using Stream Essentials software. Samples were heated over a temperature range of 30 C - 350°C at a constant heating rate of 10°C/min, with samples submerged in silicon oil. The hot-stage was calibrated using USP melting point standards.

5.2.3.2 Analysis by Differential Scanning Calorimetry (DSC)

DSC analyses were performed using a DSC 8000 Perkin Elmer instrument (Waltham, USA), incorporating a cooling system. Samples (2.5 - 5 mg) were crimped in the aluminium pans sealed with pierced lids. The instrument was calibrated by measuring the onset temperatures of the melting of indium (m.p. 156.6 ^{o}C) and zinc (m.p. 419.5 ^{o}C) while the heat flow was calibrated from the enthalpy of melting of indium (28.62 J/g). The samples were heated to 20-30 °C above the melting range of the most thermally stable, at a heating rate of 10°C/min. All analyses were performed under

continuous pure (99.8%) dry nitrogen purging with a flow rate of 20 mL/min) and were reproducible.

5.2.3.3 Analysis by Thermogravimetry (TGA)

A Perkin-Elmer 4000 PC thermal system (Waltham, USA) was used. Calibration of the instrument was performed using three different references; Alumel (m.p. = 154.2 °C), Perk alloy (m.p. = 596.00 °C) and iron (m.p. = 780 °C) at 1 and 2°C/min. The samples analysis was carried out over a temperature range between 30 °C – 400 °C at a predetermined heating rate of 10°C/min. Samples were continuously purged by a stream of dry (99.8%) nitrogen gas (20 mL/min) and solvent stoichiometry of the compounds was determined from the percentage mass loss.

5.2.3.4 Morphology evaluation by Scanning Electron Microscopy (SEM)

The morphology of individual pure drugs and co-crystal samples were conducted using an AURIGA Field Emission High-Resolution Scanning Electron Microscope (HRSEM), Zeiss (Germany). Powder samples were mounted onto aluminium stubs using carbon tape. Energy (kV) used for images was 5 kV and 20 kV for EDS. The lament current was set at 2,359 amps. Carbon tabs were placed on the aluminium stubs to hold samples. Working distance (WD) for images is displayed on each image. SmartSEM 90 and AZTEC software were used for imaging and EDS, respectively.

5.2.3.5 Analysis by Fourier Transform Infrared Spectrophotometry (FT-IR)

Infra-red spectra of the individual drugs and the co-crystal samples were obtained using a Perkin-Elmer 100 FTIR instrument (Waltham, USA) fitted with UATR and controlled ® with Spectrum software version 6.3.5.0176 for the analysis. Analyses of powder or crystalline samples were done over the range of 650-4000 cm^{-1} at a spectral resolution of 2 cm^{-1}.

5.2.3.6 Analysis by Powder X-Ray Diffraction (PXRD)

PXRD data were recorded on a D8 Advance powder X-ray diffractometer (Bruker AXS GmbH, Germany) with CuKα radiation (Cu-Kα_1= 1.54056 Å). The tube voltage and current applied were 35 kV and 40 mA, respectively. A V20 variable slit was used. Samples were placed on the sample holder which has 1 mm thickness and 1.5 cm in diameter. With a scan rate of 2° per min, the sample scan was performed in a continuous

scan in locked coupled mode, within a range of 2θ5° to 50°. Origin Pro 8.5. was used to plot PXRD patterns.

5.2.3.7 *In vitro* solubility studies

Excess amounts of the individual drugs zidovudine and lamivudine and their respective co-crystals were added to USP aqueous buffer solutions at pH 1.2 (0.1M hydrochloric acid), 0.2M potassium phosphate buffer (pH 6.8 and pH 7.4, and 0.1% SDS. The mixtures were continuously shaken in an incubator shaker at 37 °C (± 0.5 °C) and 100 rpm for 24/48 hours. Samples were filtered using 0.20 μm PVDF syringe filters and analysed using an HPLC. Both APIs and solid forms were quantified using an Agilent HPLC system setting with FXBPump (Flexar Binary Pump), an automated injector equipped with a UV detector (LC 200a Series PDA Detector), and a Flexar autosampler. NB: HPLC methods were provided separately for each analysis.

All the analyses were carried out in triplicate to ensure the accuracy and reproducibility of the samples.

5.3 Results and discussions of co-crystals/eutectic mixtures

5.3.1 Efavirenz-isoniazid co-crystal (EFINH)

A co-crystal EFINH was formed between EFV and INH. EFV is one of very potent non-nucleoside reverse transcriptase inhibitors and a member of highly active antiretroviral therapy (HAART) drugs used to treat human immunodeficiency virus (HIV). Isoniazid (INH) is an essential drug member of the first-line TB treatment regimens. Both drugs are co-administered in the cases of HIV/TB co-infection. This experiment's objective was to assess the co-crystal forming ability between these two APIs and characterise the resulting co-crystal using analytical methods described in section 5.2.3 of the methodology chapter.

5.3.1.1 Thermal analysis of EFINH co-crystal

Thermal analysis of the EFINH sample was initiated by visual observation of thermal behaviours using the HSM. With samples submerged in silicon, a relatively new transition was observed around 120°C, corresponding to melt of EFINH. Further, the absence of moisture in the EFINH sample was ensured by the absence of air bubbles before the sample melt. Furthermore, decomposition characterized by discolouration

and explosive bubbling was observed from 222°C. The HSM photographs of EFINH complex were shown in **Figure 5.6**.

Thermal analyses were also conducted on DSC to support HSM observed changes with more accuracy. The experiment was performed using a method described in section 5.2.3.2. The DSC curves of pure EFV, INH, and EFINH samples are shown in **Figure 5.7**. First, the melting points of parent drugs EFV and INH were obtained receptively at 137°C (C. Fandaruff et al., 2014) and 172°C (Freire et al., 2009).

The DSC curve of EFINH characterised by a single melting endotherm with an onset at 116°C and the maxima at 120°C; confirmed the HSM findings. This new melting transition was an indication of interactions existing between EFV and INH and the initial confirmation that a new chemical entity was formed.

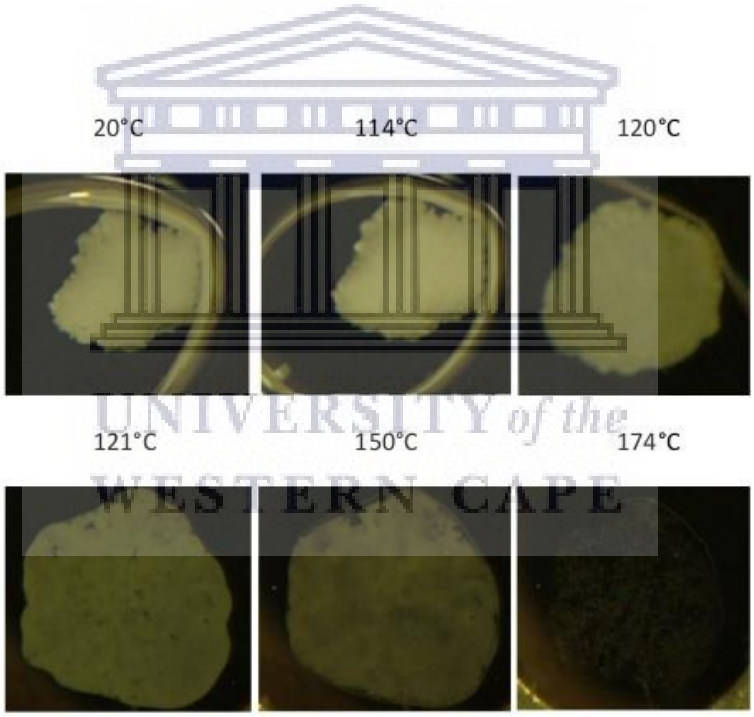

Figure 5.6: HSM photographs of EFINH recorded at room temperature (20°C), Onset of melting (114°C), melting temperature (120°C) and the onset of decomposition (174°C)

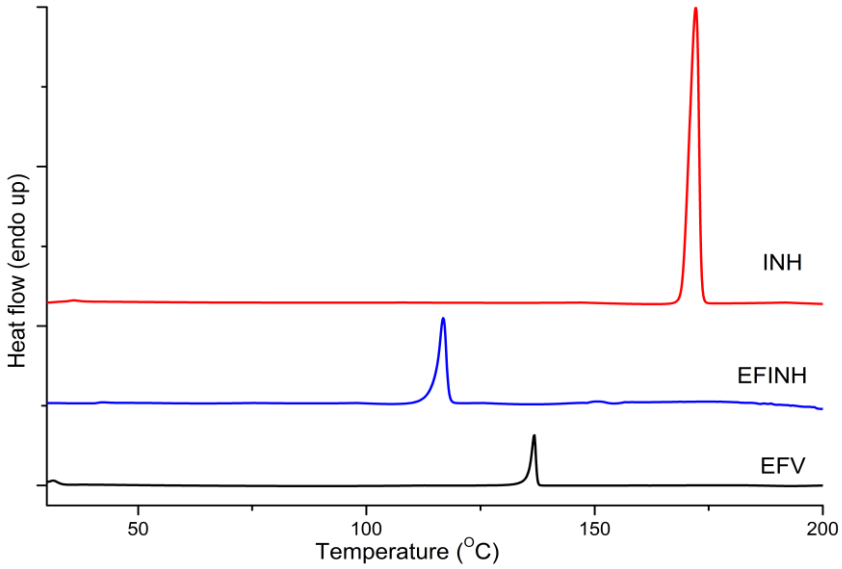

Figure 5.7: DSC curves of pure EFV, INH and the co-crystal EFINH sample showing an earlier melting transition in comparison to melting temperature of pure EFV and INH

Thermal behaviour assessment of EFINH by TGA revealed the absence of any volatile substances in the structure of the sample. **Figure 5.8** presents the TGA/DTA thermograms of EFINH co-crystal sample based on which an undetectable change in mass (0.01 %) was calculated before melting, and a decomposition mass loss (79.45%) was seen at a temperature higher than melting points of both individual APIs (185°C).

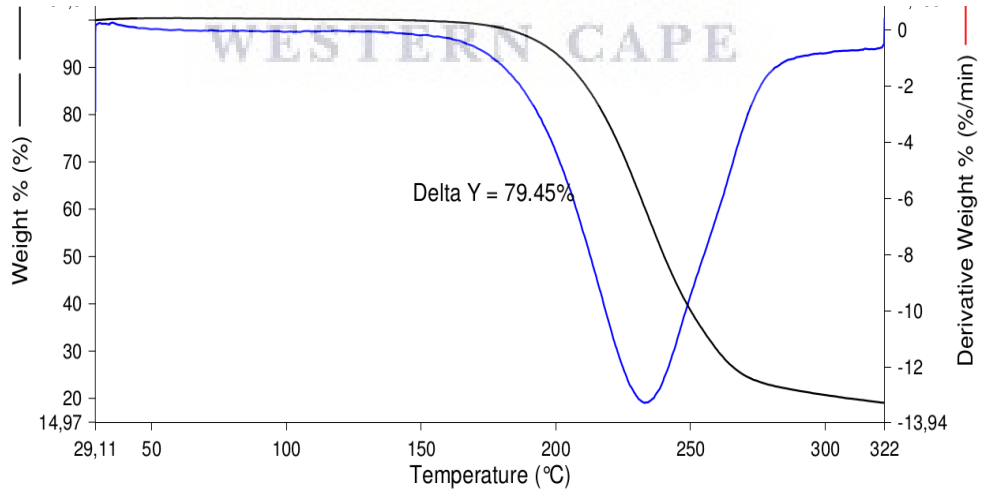

Figure 5.8: The TGA/DTA curves of the EFINH co-crystal showing a single step of mass loss corresponding to its decomposition.

5.3.1.2 FTIR results of EFINH co-crystal

FTIR spectra for EFV, INH, and EFINH are shown in **Figure 5.9.** Analysis of pure drugs was carried out first, and all characteristic peaks were in agreement with literature. The FTIR analysis of EFINH produced a different spectrum that, compared to parent drugs spectra, showed different shifting of bands positions and changes of intensity to various peak across the spectrum. All these changes proved intermolecular interactions between EFV and INH; components of the co-crystal sample. INH spectrum was found to be in a good agreement with previous work (Gunasekaran et al., 2009).

The FTIR spectrum of EFV agrees with Reddy *et al.* (2015). The absorption bands with the maxima at 3314 cm^{-1} and 1742 cm^{-1}, were respectively assigned to stretching vibration of carboxamide N–H and C=O, peak at 3095 cm^{-1} assigned to C-H stretching and 2250 cm^{-1} ascribed to stretching vibration of the alkyl (C–C). The absorption band peaking at 3106 cm^{-1} has been assigned to C–H stretch as well.

The spectrum for INH showed absorption band peaks at 3303 cm^{-1}, 3106 $cm^{-1,}$ and 1663 cm^{-1}. Two formers were assigned to stretch N–H and the latter to C=O of INH carbohydrazide in agreement with (Gunasekaran et al., 2009; Ravikumar et al., 2013).

EFV stretching amine N-H at 3303 cm^{-1} subsides in the FTIR spectrum of the EFINH co-crystal sample. The carbonyl C=O at 1742 cm^{-1} has downshifted to 1738 cm^{-1}. The EFV stretching C-H at 3095 cm^{-1} is also missing in the EFINH spectrum. Spectral bands at 2250 cm^{-1} ascribed to EFV alkyl (C–C) has slightly shifted to 2253 cm^{-1}. On the other hand, the INH spectral band at 3106 cm^{-1} slightly shifted to 3109 cm^{-1}. Further, INH stretching C=O at 1663 cm^{-1} has shifted to 1665 cm^{-1} in the spectrum of the co-crystal EFINH. These changes suggested the possible bonding between N–H and C=O groups of two APIs. All spectral changes described are summarised in **Table 5.1** and constituted a milestone fact that EFINH co-crystal formation was successful.

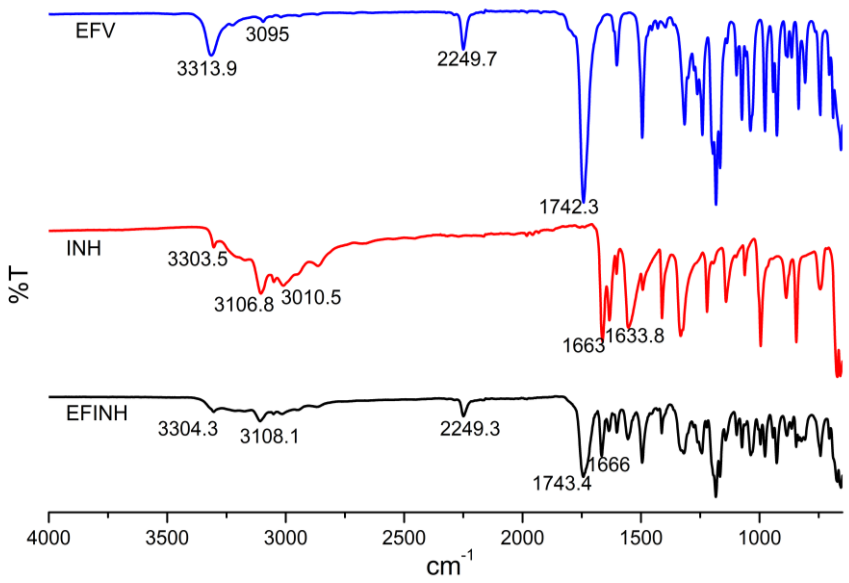

Figure 5.9: The FTIR spectra of efavirenz (EFV), isoniazid (INH) and EFINH

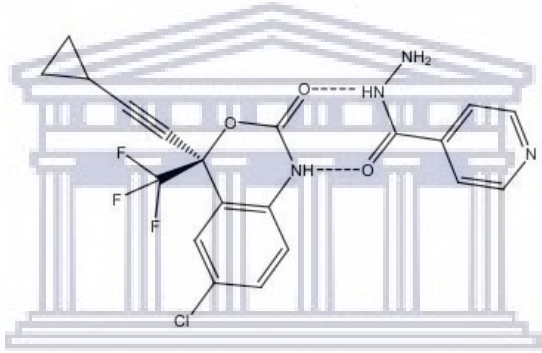

Figure 5.10: EFINH most plausible intermolecular interactions according to the FTIR analyses

Table 5.1: Summary of the main spectral band shifting detected in the EFINH spectrum vs their original band positions

Compounds	Peak positions	Peaks assignments
EFV	3313 cm^{-1}	Stretch pyrimidinic N–H
	3095 cm^{-1}	=C–H stretch
	2250 cm^{-1}	C–C
	1742 cm^{-1}	C=O
INH	3303 cm^{-1}	primary amine N–H
	3107 cm^{-1}	amine N–H stretch
	1663 cm^{-1}	carbonyl C=O stretch
	1554 cm^{-1}	N–C stretch
EFINH	3313 cm^{-1}	missing pyrimidinic N–H stretch

2250 cm^{-1}	alicyclic C–H stretch
2248 cm^{-1}	C=C stretch
1738 cm^{-1}	carbonyl C=O stretch
1665 cm^{-1}	carbonyl C=O stretch
1556 cm^{-1}	N–C stretch

Based on this spectral shifting discussed, the most plausible interactions were suggested (**Figure 5.10**).

5.3.1.3 Scanning electron Microscopic analysis for EFINH adduct

SEM micrographs of the EFINH sample, pure INH and EFV are presented in **Figure 5.11**. EFV sample exhibited block-like particles while irregularly-shaped large particles are characteristic for INH. The physical mixture inherits both APIs' particle morphologies, whereas the co-crystal EFINH sample exhibited needle-like shaped particles, suggesting new crystal habits and formation of a new supramolecular entity.

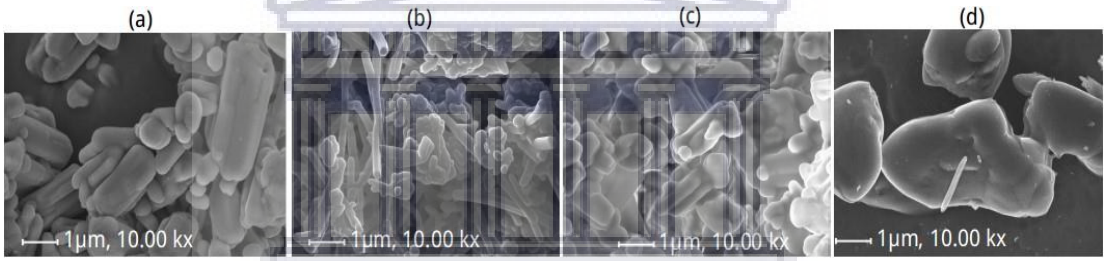

Figure 5.11: Scanning electron microscopy (SEM) images of efavirenz (a), EFINH co-crystal sample (b), EFV-INH 1:1 physical mixture (c) and isoniazid

5.3.1.4 Powder X-Ray diffraction results of EFINH co-crystal sample

The PXRD patterns pure EFV, INH and EFINH co-crystal samples are presented in **Figure 5.12**. INH pattern has diffraction peaks at 2θ = 11.9°, 14.3°, 15.6°, 16.73° 19.65°, 25.3°, 26.95° and 27.3°.

The EFINH diffraction pattern exhibited peaks other than those inherited from parent drugs at 2θ = 12.3°, 16.5°, 25°, 27.2°, thus confirming the EFINH sample as a new co-crystal. PXRD data are consistent with FTIR results and supported the previous thermal analyses results.

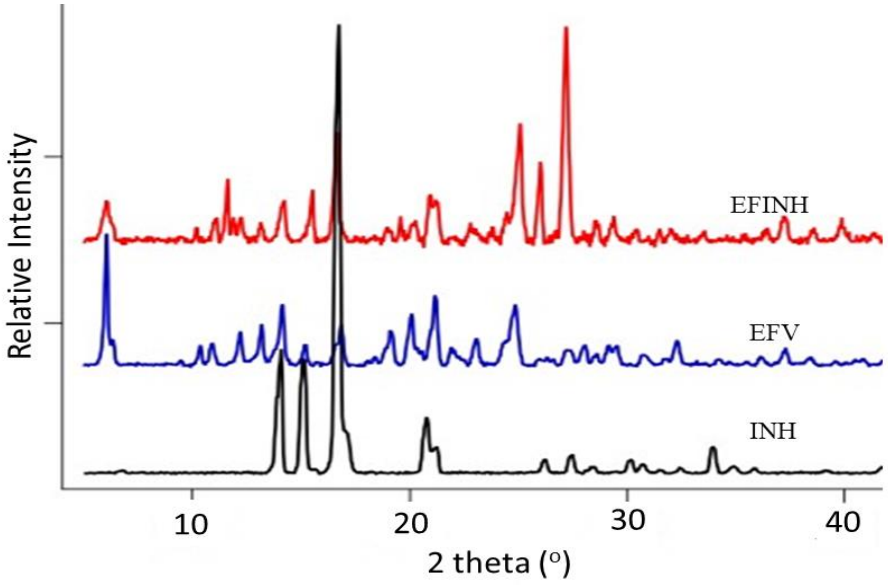

Figure 5.12: The experimental PXRD patterns of pure INH (1), EFV (2) and the co-crystal EFINH (3)

5.3.1.5 Solid-state NMR results for EFINH co-crystals

The bond formation was further confirmed by solid-state CP/MAS ^{13}C-NMR spectra presented in **Figure 5.13**. ^{13}C CP/MAS SSNMR of INH did not exhibit any significant peaks due to possible decomposition of the sample before analysis. However, the co-crystal formation was justified by the presence of new peaks, and other chemical shifting and splitting identified in the spectrum of the co-crystal EFINH. The chemical splitting at 129 ppm was assigned to C–H, while peaks at ppm = 140 and 166 ppm appeared due to the H···N bonding between EFV and INH in the co-crystal. The two peaks are usually assigned to C–H and N–H, respectively. Hence, the bonding took place between EFV pyridinic N–H and C–H.

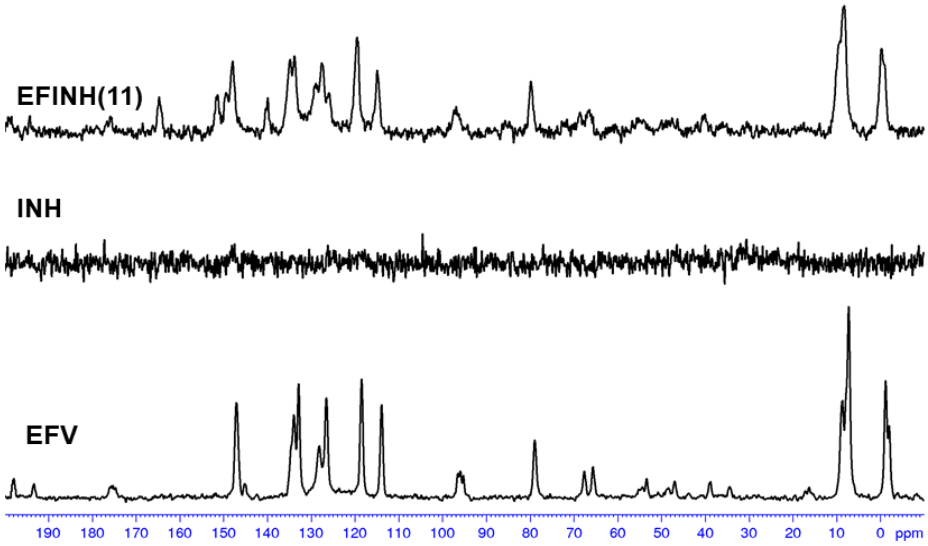

Figure 5.13: EFV, INH, and EFINH co-crystal solid-state CP/MAS 13C-NMR spectra compared

5.3.1.6 In vitro solubility evaluation of pure EFV and INH vs EFINH co-crystal

Solubility evaluation of pure EFV, INH and EFINH co-crystal was carried out by dissolving an excess amount in buffered solutions including 0.1N HCl (pH=1.2), ammonium acetate (pH=4.5) and potassium phosphate buffer at the pH = 7.4, deionized water. Mixtures were agitated continuously for 48 hours at the speed of 100 rpm. Resulting solutions were filtered (0.45 um).

Sample measurements were carried out on a Perkin Elmer HPLC (section 3.4.8 gives the instrument specifications). Gradient elution at a flow rate of 10 mL/min was applied as follows: Solvent A = Methanol 85% (aq.) and solvent B: phosphate buffer solution (pH=3.6); equilibration = 5 min (55:45), 3 min (55:45), 1 min (10:90), 5 min (10:90), 1 min (55:45), and 5 min (55:45). A reversed-phase Supelco Discovery HS C18 HPLC column 15 cm x 4 mm, 5µm was used. Injection volume was 10 µL and absorbance of elution was recorded at 260 wavelengths following suitable dilutions.

R^2 = 0.9997 was calculated for EFV and R^2 = 0.9998 for INH based on the following regression equations;

$$Y_{\mathbf{EFV}} = \mathbf{13226}x - \mathbf{1964.6} \qquad \textbf{Equation 5.1}$$

$$Y_{\mathbf{INH}} = \mathbf{10715}x + \mathbf{44076} \qquad \textbf{Equation 5.2}$$

From solubility measurements, it is clear that EFV solubility was significantly increased by this co-crystallisation with INH. Compared to pure EFV, a solubility increase by 8-times was measured at pH=1.2 (0.1N HCl) while a 7.2-times increase was

reported at pH=4.5 (ammonium acetate). A 2.7-times solubility increase was measured in aqueous media, while a negative solubility outcome was recorded at pH=7.4 (**Figure 5.14**). Its higher dissociation further explains EFV solubility increase in the EFINH co-crystal in a highly acidic environment such as the stomach.

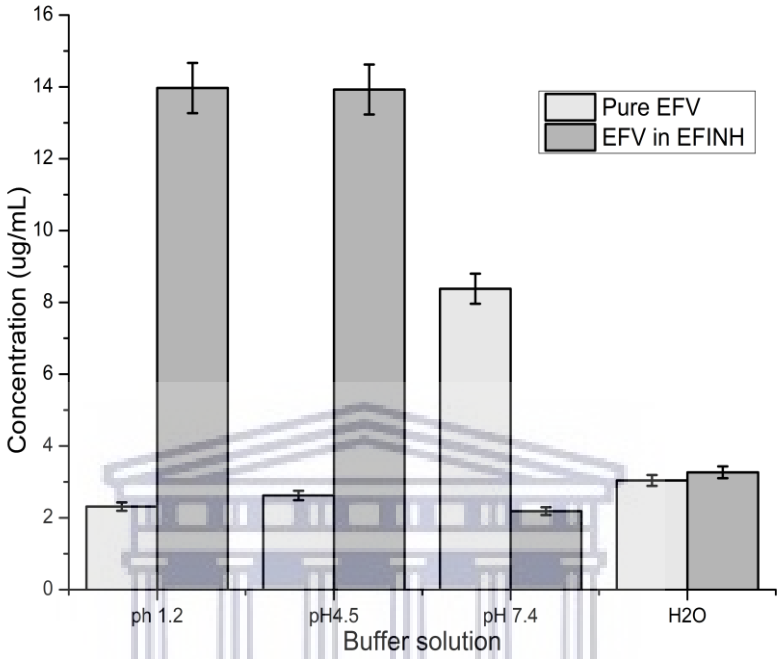

Figure 5.14: Solubility histogram of the commercial EFV and the co-crystal EFINH at acidic pH=1.2, (0.1N HCl), 4.5 (ammonium acetate), at pH= 7.4 (phosphate buffer solution) and deionised water

The solubility measurements also showed a higher INH concentration in the co-crystal than pure INH, at pH=4.5, 7.4 and aqueous solution. Solubility histograms of pure INH and the co-crystal EFINH in different buffer solutions and deionised water are shown in **Figure 5.15**. While an increase in INH solubility by 1.2-fold was observed in unbuffered deionised water and acidic buffer solution at pH=4.5., there was no significant solubility increase at pH=7.4. Furthermore, the co-crystal EFINH showed a negative solubility outcome in acidic media at pH 1.2 (0.1N HCl). It is worth noting that sometimes, solubility increase of one co-former may reduce the solubility of the other co-former, especially when their solubility difference is very large.

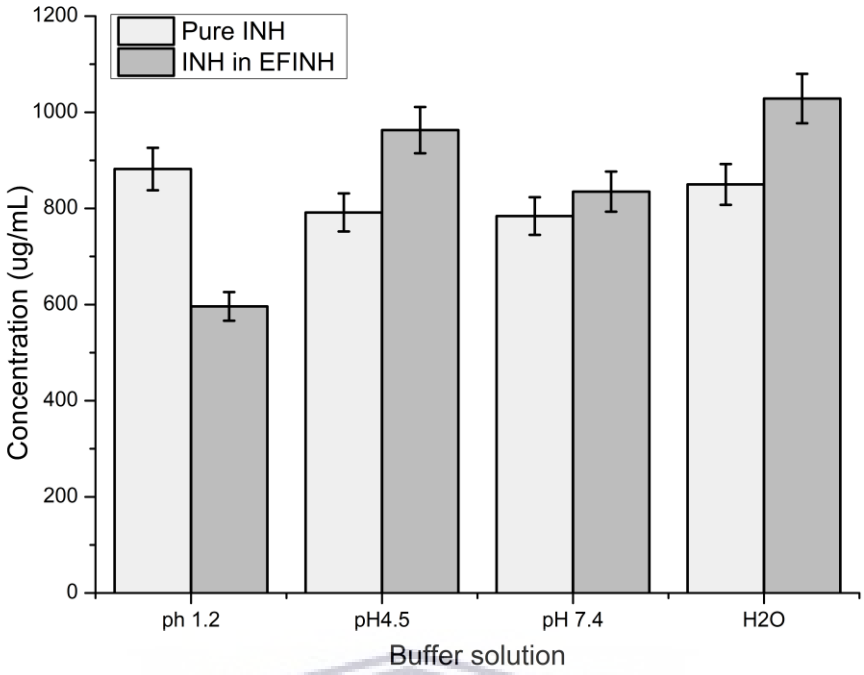

Figure 5.15: Solubility histogram comparing the commercial INH and INH in the co-crystal EFINH at acidic pH=1.2, (0.1N HCl), 4.5 (ammonium acetate), at pH= 7.4 (phosphate buffer solution) and deionised water

In conclusion, a dual-API co-crystal between EFV and INH was successfully produced using solid-state grinding in a 1:1 molar ratio. The co-crystal was characterised for its physicochemical properties. In vitro solubility assessment indicated that EFV is more soluble at acidic environment while INH did not show such behaviour. This solubility-dependence behaviour is common among weakly basic/hygroscopic drugs as previously discussed. Unfortunately, EFINH co-crystal is unstable and decomposes within days of exposure to light. Stability analysis should provide data regarding this INH inherited instability.

5.3.2 Efavirenz-1-adamantylamine hybrid (EFAD)

Combining two APIs in a co-crystal or other supramolecular assemblies is relatively a new drug combination strategy used to enhance the physicochemical properties and increase synergistic effects of drugs. In this section, two antiviral APIs EFV and ADT were combined in the attempt to assess their co-crystal forming ability and establish whether such a combination can offer an improvement on poor physicochemical properties of EFV or both APIs in general.

5.3.2.1 Thermal analysis of EFAD solid form

The HSM photographs of the EFAD sample are presented in **Figure 5.16**. Using microscopic observation on the HSM, the EFAD sample showed a melt-like transition over 45-90°C; a much lower temperature than the melting temperatures of both ADT and EFV. The absence of air bubbles ensured the purity of the sample. To better understand the HSM observed changes, DSC analysis was carried out on the same sample and the starting materials for comparison purpose. DSC curves of EFV, ADT and EFAD solid form are presented in **Figure 5.17**. ADT exhibited a single melting endotherm at 206°C (with an onset at 202°C) immediately followed by an exothermic peak corresponding to its decomposition. EFV generated a DSC curve showing a sharp melting endotherm with the maxima at 138°C and onset at 136°C, consistent with the literature (C. Fandaruff et al., 2014).

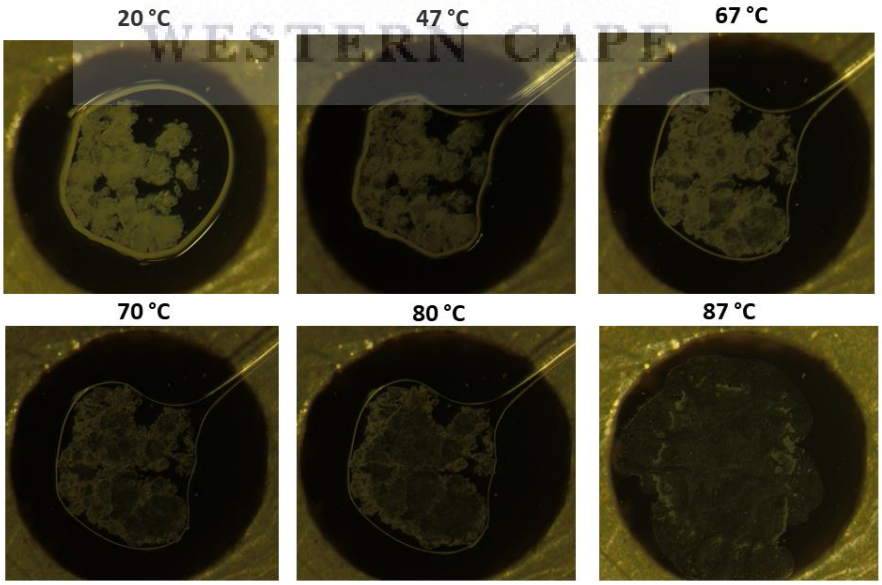

Figure 5.16: The HSM images of EFAD sample recorded based on thermal changes observed at indicated temperatures.

On the other hand, the DSC curve generated from EFAD sample showed a glass transition that initiated at 45°C rather than a melting endotherm. The absence of endotherm or exotherm throughout the curve suggested that the sample EFAD is co-amorphous later confirmed by the PXRD analysis.

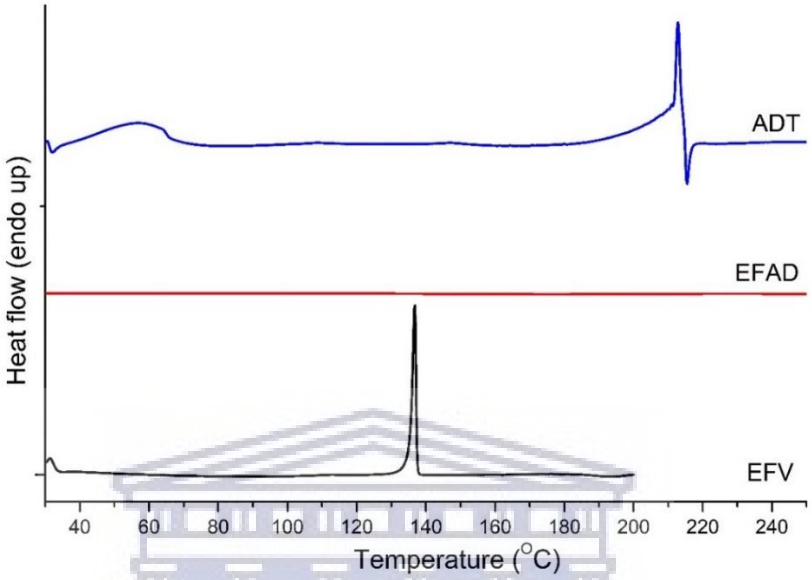

Figure 5.17: Figure Illustration of DSC thermograms of EFV, ADT and EFAD solid form

Figure 5.18 displays EFAD TGA/DTA curves showing initial 0.08% mass loss over glass transition followed by two consecutive decomposition mass losses (37%) and (56.4%) over a wide temperature range 100-200°C. These measurements supported the HSM observations and proved the absence of any volatile molecules in the binary eutectic EFAD sample

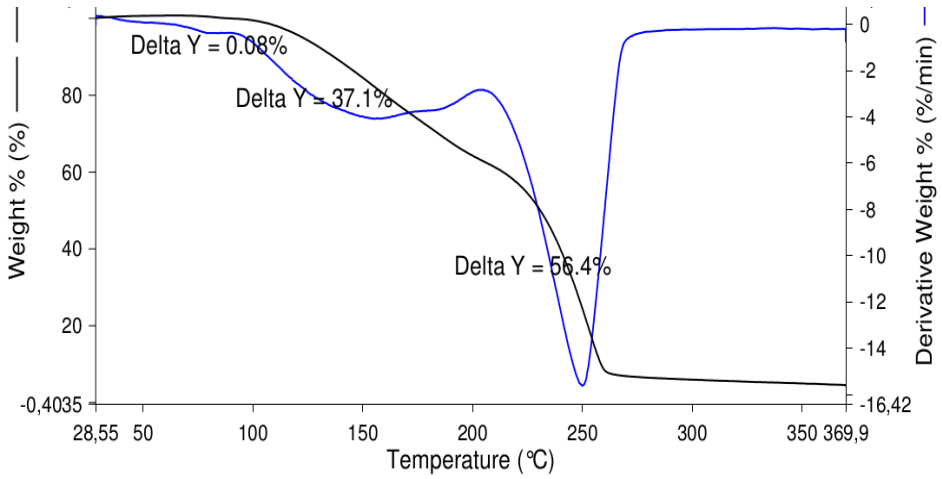

Figure 5.18: The TGA/DTA thermograms of EFAD sample

5.3.2.2 Structure studies of EFAD by FTIR

FTIR spectra of EFV, ADT, and EFAD hybrid are represented in **Figure 5.19**. Pure drugs ADT and EFV were analysed and were refereed to for EFAD analysis. The EFV characteristic bands are in agreement with literature (Cinira Fandaruff et al., 2014).

The FTIR spectrum of ADT displayed a characteristic peak at 3340 cm^{-1} assigned to the amine N−H stretching and double peaks at 2899 cm^{-1} and 2847 cm^{-1} corresponding to C−H of the amantadane cage. This is consistent with the infrared spectrum reported by Lemmon, McLinden and Friend, (2017). EFV exhibited characteristic infrared peaks at 3313cm^{-1} and 3095 cm^{-1} respectively assigned to N−H and =C−H stretching, and the absorption peak at 1742 cm^{-1} corresponding to carboxamide C=O stretch.

The carboxamide N−H stretching vibration of EFV subsides while the carbonyl C=O stretch slightly shifted to the lower frequency at 1740 cm^{-1} in the spectrum of EFAD. This suggested the possible N-H···C=O bond formation between ADT and EFV complementary functional groups. Reduced-intensity of ADT double peaks at 2899 and 2847 cm^{-1}assigned to C−H stretch and their shifting to the higher frequencies (2914 cm^{-1} and 2858 cm^{-1} respectively), further their contributions in EFV-ADT interactions and formation of the hybrid.

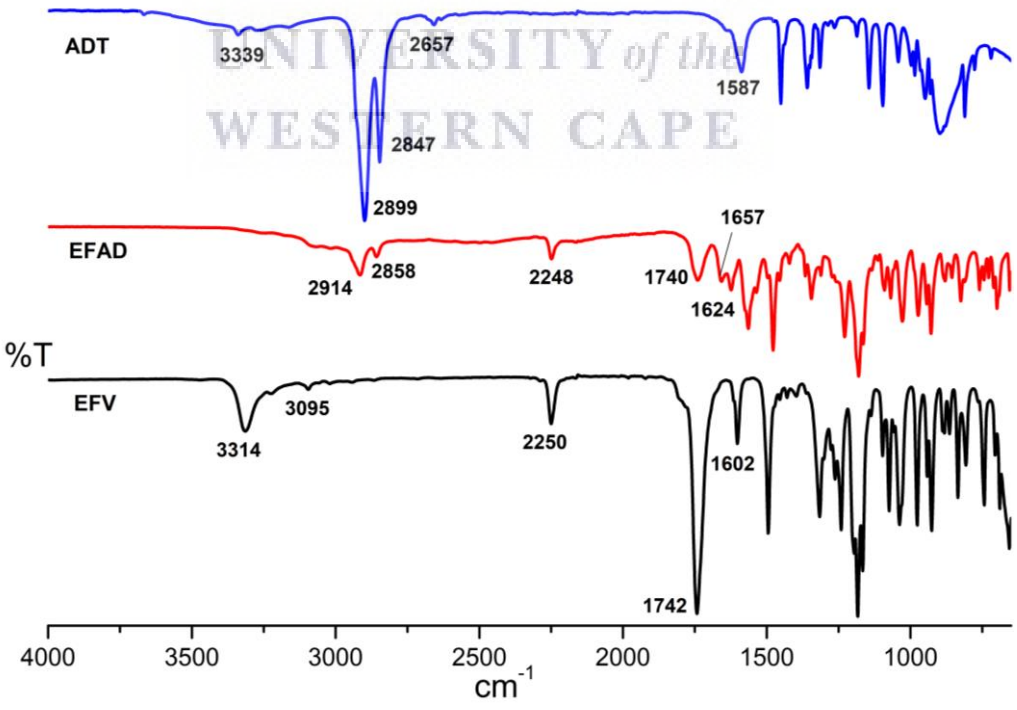

Figure 5.19: FTIR spectra of pure EFV and ADT compared to EFAD solid form

The aryl C-H stretching at 3095 cm^{-1} in EFV spectrum also subsided in the EFAD spectrum while two new peaks at 1657 cm^{-1} and 1624 cm^{-1} in the EFAD spectrum were associated with possible intermolecular bonding between EFV and ADT. All these spectral changes confirmed that a new entity EFAD was successfully attained. Summary of main FTIR peaks of EFV, ADT, and EFAD is shown in **Table 5.2**.

Additionally, the presence of halogens; F and Cl and pyrimidine (NH) in EFV molecular structure may result in different types of interactions such as strong H-bonding or halogen bonding. Therefore, it is important to note that further analyses using more powerful analytical tools such as PXRD and SSNMR would disclose information concerning the identity of EFAD solid form.

Table 5.2: Shifts of the main bands identified in the spectrum of EFAD vs pure EFV and ADT

Assignments	EFV	ADT	EFAD
Pyrimidine N-H	3313 cm^{-1}	3339 cm^{-1}	3313 cm^{-1}
Aromatic =C-H	3095 cm^{-1}		
Aliphatic C-H		2869 cm^{-1}	2914 cm^{-1}
-C=N	2250 cm^{-1}	2847 cm^{-1}	2248 cm^{-1}
		2656 cm^{-1}	
C=O stretch	1742 cm^{-1}		1740 cm^{-1}
C-N		1643 cm^{-1}	1657 cm^{-1}

5.3.2.3 Morphology evaluation of EFAD particles by Scanning electron microscopic

SEM images of pure EFV and ADT were compared to the solid form EFAD as presented in **Figure 5.20**. While EFV crystalline powder showed smooth surfaces rod-shaped particles with different fractions, pure ADT had irregularly-shaped particles of different size and rough surfaces. Compared to pure commercial drugs, the solid form EFAD particles are made of mixtures of long filament-like and irregularly shaped amassed particles. The difference in particle morphology implies a different habit which in this case confirmed that a newly phased solid material was indeed formed.

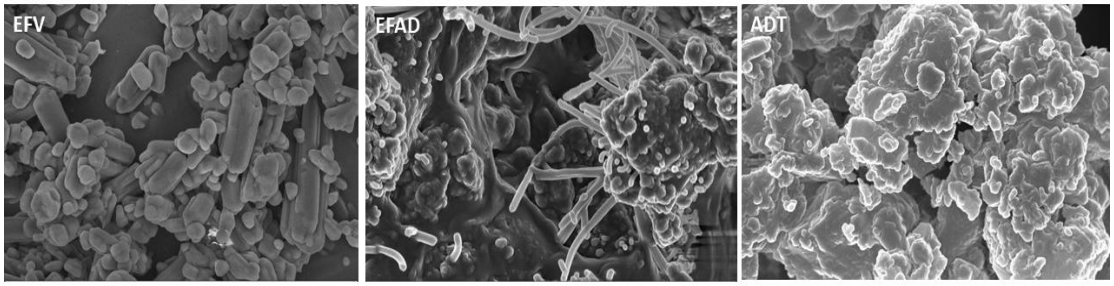

Figure 5.20: SEM images for EFV, EFAD, and ADT recorded at *μ*m, 5.00 K.X and EHT = 5.00 kV

5.3.2.4 Powder X-Rays diffraction analysis of EFAD solid form

The diffraction patterns of pure drugs EFV, ADT and the solid form produced are presented in **Figure 5.21**. The powder X-Ray diffraction pattern generated from EFV exhibited very sharp and intense diffraction peaks at 2θ = 6°, 14.12°, 21.1°and 24.86°, medium peaks at 2θ = 12.16°, 13.1°, 16.83°, 19°and small peaks at 2θ = 10.3°, 10.83°, 15.15°, 21.84°, 23, 27.1°, 27.9°, 29°, 32.27°and 37.27°. The ADT PXRD pattern is characterised by a very sharp peak at 2θ = 17°, two medium peaks at 2θ = 14°, 15°, and smaller double peaks at 2θ = 20.7°and 33.8°. On the contrary, the PXRD pattern of the EFAD sample exhibited no significant diffraction peaks. Such absences of peaks indicated that EFAD is co-amorphous solid form. Only two small diffraction peaks at 2θ = 15.83° and 20.73° were present in the pattern.

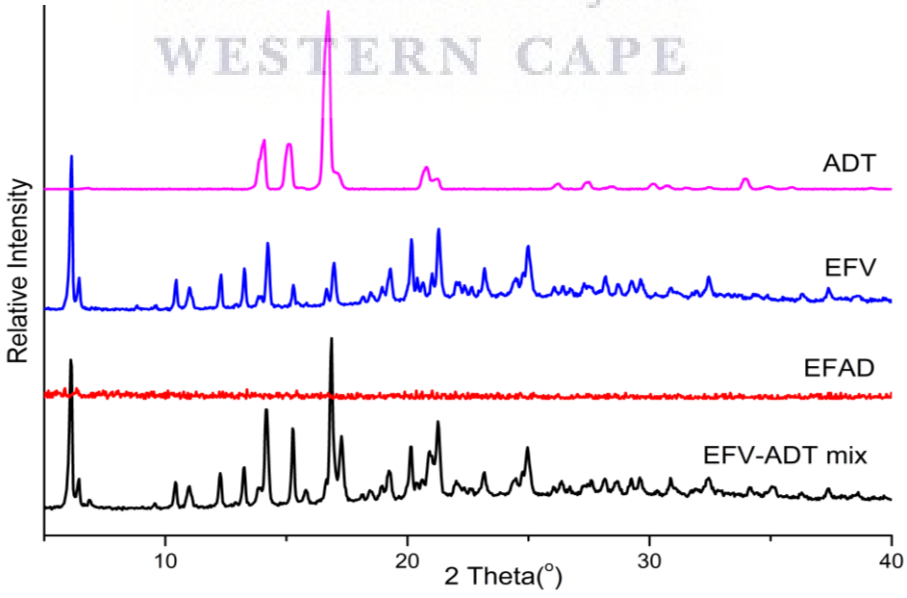

Figure 5.21: The experimental powder X-ray diffraction patterns of ADT, EFV, EFAD co-amorphous and the physical mixture

5.3.2.5 In vitro solubility evaluation of the co-amorphous solid form EFAD

Change in solubility was assessed by dissolving an excess amount of EFAD in potassium phosphate buffer solution at pH = 7.4, deionized water, and acidic buffer solution at pH = 1.2 (0.1N HCl). Mixtures were continuously shaken at 37°C for 48 hours at the speed of 100 rpm. Resulting solutions were filtered (0.45 um) and analysed.

The sample measurements were carried out on a Perkin Elmer HPLC whose specifications can be found in section 3.4.8. A gradient elution, at a flow rate of 1 mL/min was applied as follows: Solvent A = Methanol 85% (aq.) and solvent B: phosphate buffer solution (pH=3.6); equilibration = 5 min (55:45), 3 min (55:45), 1 min (10:90), 5 min (10:90), 1 min (55:45), and 5 min (55:45). A reversed-phase Supelco Discovery HS C18 HPLC column 15 cm x 4 mm, 5µm was used. Injection volume was set to 10 µL, and absorbance of elution was recorded at 255 nm following suitable dilutions.

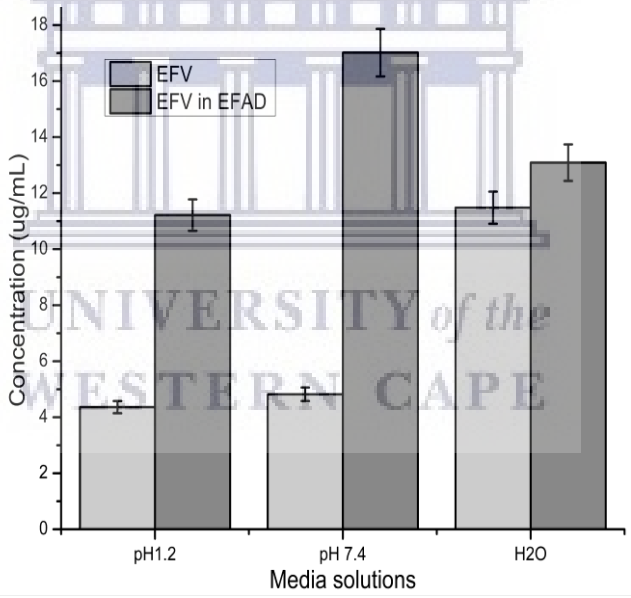

Figure 5.22: Solubility histogram of the commercial EFV vs the co-amorphous solid form EFAD in acidic pH1.2 (0.1N HCl), pH 7.4 buffer solutions and deionised water

Based on quantified data, it was apparent that the solubility of co-amorphous EFAD was much higher than that of EFV in all three buffer media used (**Figure 5.22**). An increase by 3.5-fold was observed in phosphate buffer media at pH = 7.4, a 1.3-fold increase in EFV solubility was measured in aqueous solution. Furthermore, A 2.6-fold solubility increase was recorded in acidic media at pH=1.2 (0.1N HCl). The increase in solubility of EFV in the co-amorphous solid form can be explained by high

solubilisation behaviours of EFAD co-amorphous solid form. Further, it is very clear that EFV exhibited pH-dependence solubility in its pure form and as a co-amorphous with ADT. As previously discussed, this behaviour is not uncommon among weakly basic drugs such as EFV.

5.3.3 Isoniazid-zidovudine binary eutectic (INHZA)

5.3.3.1 Thermal analyses of INHZA sample

Using the HSM, it was observed that the INHZA sample melted over 98-106°C range of temperature. Different photographs recorded based on sample behaviours over the heating experiment are presented in **Figure 5.23**. Decomposition was characterized by sample discolouration and explosive bubbling observed over 210-245°C temperature range. Additionally, the DSC experiment was performed under an inert atmosphere with a 20mL/min flow of N_2 gas to confirm HSM observation with precision. DSC thermograms are presented in **Figure 5.24**. The accurate weight of the sample was prepared in an aluminium pan covered with a pierced lid to allow the escape of volatiles. Following the method described in section **5.2.3.2**, the heat was applied at a rate of 10°C per minute.

In comparison to both APIs INH and AZT melting temperatures, respectively found at 172°C and 121°C respectively, a DSC curve of INHZA exhibited a melting transition at 100°C with an onset at 96°C. This melting transition also differs from API's physical mixture which melted over 105-122°C temperature range.

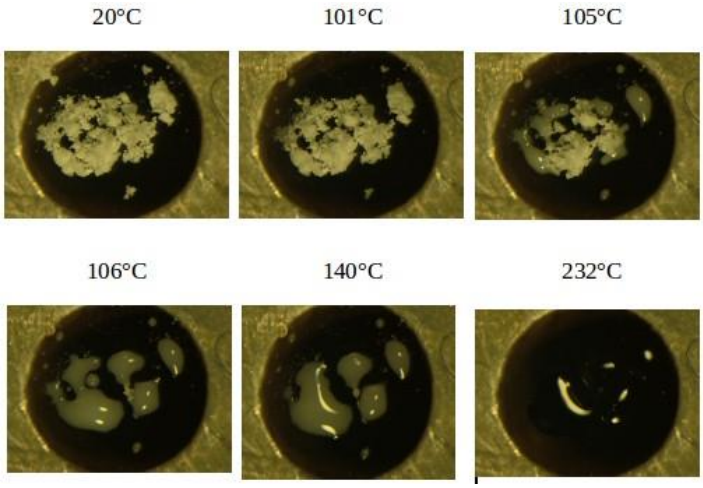

Figure 5.23: The HSM photographs of INHZA sample recorded at room temperature (20°C), the beginning of a melting transition (101°C), a complete melting (106°C) and over decomposition at 232°C

Thermal measurements from DSC and the HSM findings are very consistent and both confirmed the INHZA new melting transition as proof of interaction/bonding between INH and AZT and the possible formation of a binary eutectic solid form.

The TGA was used to support visually observed thermal behaviours by the HSM analysis. The TGA thermograph generated INHZA sample, is depicted in The TGA/DTA curves presented in **Figure 5.25** revealed that INHZA sample remains intact over melting with only a negligible mass loss of approximately 0.001% until decomposition onset (185°C); the temperature at which the weight of the sample started diminishing. Approximated weight loss over decomposition (185-325°C) was ~ 80% of the entire amount of the INHZA sample. TGA also confirmed the absence of any volatile substances in the structure of the INHZA sample.

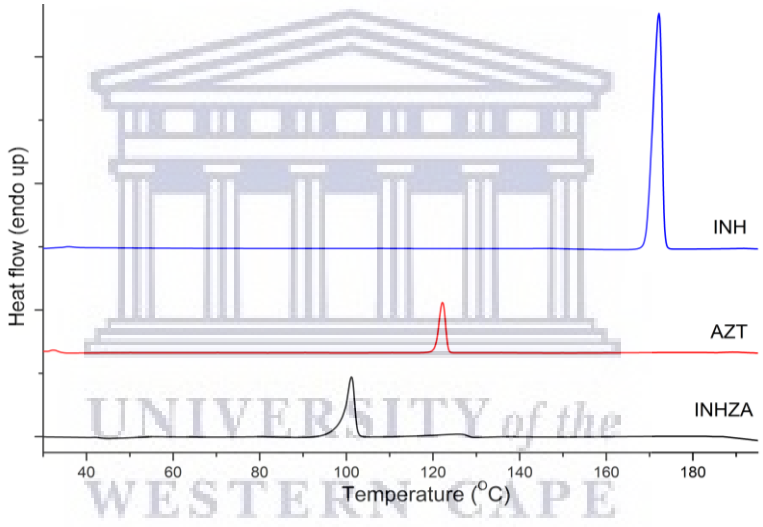

Figure 5.24: The DSC curve of the binary eutectic INHZA showing a melting transition at a lower temperature compared to pure INH, AZT and their physical mixture

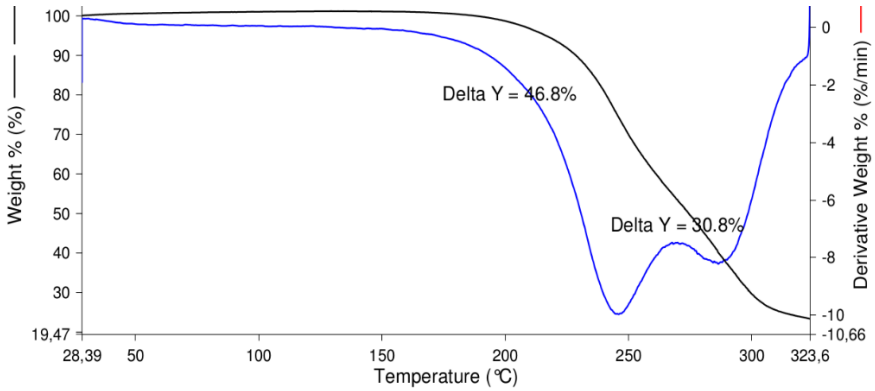

Figure 5.25: The TGA/DTA curves of the INHZA sample with two consecutive decomposition mass losses from 185 to 325°C.

5.3.3.2 Scanning Electron Microscopy analysis of INHZA

Analysis by SEM was carried out to investigate changes in the morphology of particles induced by milling exercise. Micrographs are presented in **Figure 5.26**. Large block-shaped particles characterized the AZT sample (**Figure 5.26**a) while INH exhibited large particles with irregular shapes and smooth surfaces (**Figure 5.26**c). The INHZA sample particles are different from INH and AZT with irregularly shaped aggregates, very smaller in size than both individual drugs as a result of the milling process (**Figure 5.26**b). Such a particles size decrease of INHZA sample is thought to have contributed to enhanced solubility due to the increased surface exposure.

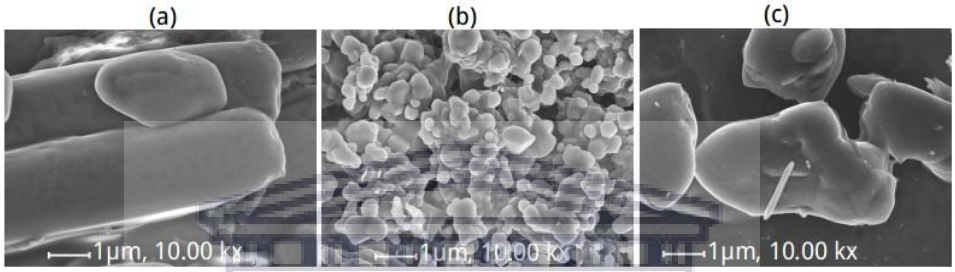

Figure 5.26: Scanning electron microscopic images of (a) pure AZT, (b) INHZA and (c) INH particles recorded at 1 µm, 10.00 k.x.

5.3.3.3 Structure evaluation of INHZA eutectic by FTIR

FTIR spectra generated from INH, ZT, and INHZA are depicted in **Figure 5.27**. Spectra from both pure drugs matched the ones reported in the literature (Gunasekaran et al., 2009) and (Jain et al., 2013). INH spectrum displayed characteristic bands at 3303 cm^{-1} and 3106 cm^{-1} corresponding to the asymmetric and symmetric carbohydrazide N–H stretch. The absorption band at 3010 cm^{-1} rose due to the aliphatic C–H stretch. Absorption bands at 1663.13 cm^{-1} and 1634 cm^{-1} were attributed to stretch carbohydrazide C=O and C–N respectively. FTIR spectrum of AZT exhibited characteristic band at 3458 cm^{-1} assigned to O–H stretching whereas peaks at 3150 cm^{-1} and 3024 cm^{-1} were respectively assigned to N-H and aromatic C–H stretch. Bands positioned at 2814 cm^{-1} were attributed to C-H stretch vibration. The IR peak at 2081 cm^{-1} was due to azido group C=N=N while carbonyl asymmetric stretch C=O double-peaked at 1671 and 1678 cm^{-1}.

From INHZT spectrum, the INH characteristic bands at 3303 cm^{-1} and 3106 cm^{-1} assigned to N–H stretching subsided. The FTIR band at 3462 cm^{-1} slightly shifted

from 3459 cm^{-1} (O–H stretch vibration of AZT) while 3033 cm^{-1} (C–H) is missing in the INHZA spectrum. The AZT azido group at 2083 cm^{-1} was also slightly down-shifted to 2081 cm^{-1}. This shifting in wavelength and changes in peaks intensities happened as a result of interacting components and formation of INHZA. It is also confirmed that the INHZA sample is not a salt due to the absence of any significant lower shifting (Childs et al., 2007).

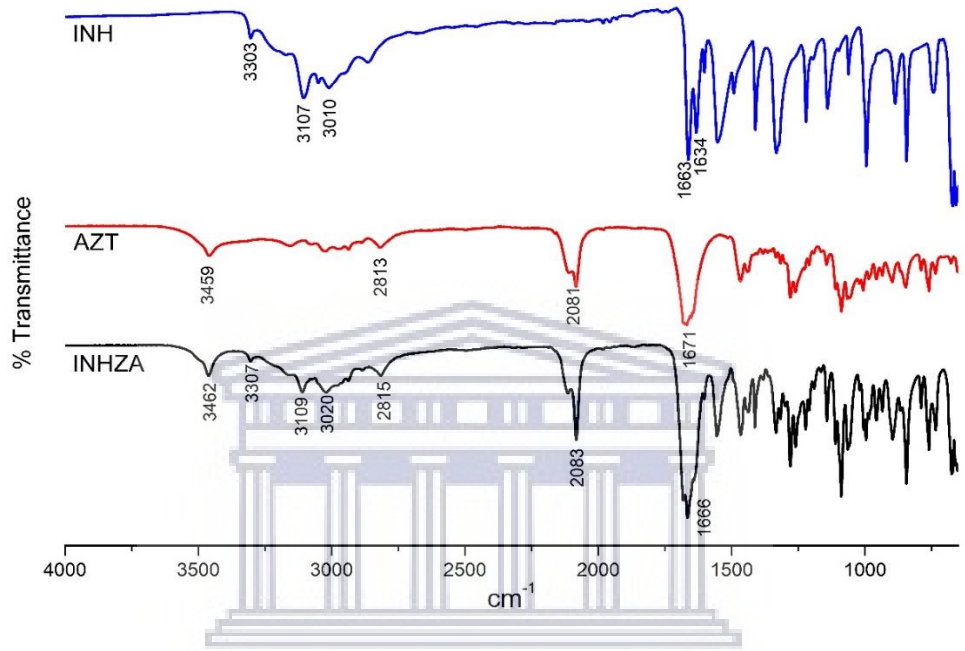

Figure 5.27: The FTIR spectra of INHZA, pure INH and pure AZT compared.

Table 5.3: Summary of spectral changes detected in INHZA spectrum as a result of weak interactions between INH and AZT

Compounds	Band	INHZA	Peaks assignments
AZT	3459 cm^{-1}	3462 cm^{-1}	Stretch pyrimidinic N–H
	3150 cm^{-1}		Hydroxyl O–H
	3024 cm^{-1}	3024 cm^{-1}	C– H stretch
	2813 cm^{-1}	2815 cm^{-1}	C–H
	2081 cm^{-1}	2083 cm^{-1}	AZT azole -N=N+=N-
	1671 cm^{-1}	1666 cm^{-1}	C=O
INH	3304 cm^{-1}	3307 cm^{-1}	Primary amine N–H
	3107 cm^{-1}	3109 cm^{-1}	Amine N–H stretch
	3010 cm^{-1}	3020 cm^{-1}	asymmetric C-H stretch
	1663 cm^{-1}	1666 cm^{-1}	Carbonyl C=O stretch
	1634 cm^{-1}	miss	N-C stretch
	1666 cm^{-1}		Carbonyl C=O stretch

A summary of shifts in wavelengths of the characteristic spectral bands is given in **Table 5.3.**

Based on IR changes discussed herein**, Figure 5.28** suggests some of the plausible weak interactions that may have occurred between carbonyls C=O, O–H and N–H.

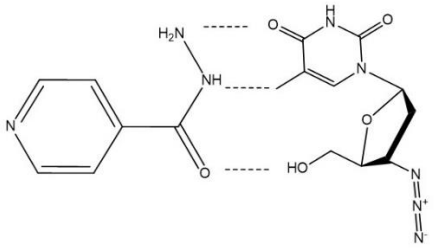

Figure 5.28: Suggested INHZA structures with possible intermolecular interactions.

5.3.3.4 Powder X-ray diffraction analysis of INHZA sample

The diffraction patterns of AZT, INH, their simulated patterns, INHZA solid form and the physical mixtures are presented in **Figure 5.29**. The INHZA powder sample generated a pattern exhibiting the summation of characteristic diffraction peaks of individual components AZT and INH. Same 2theta angles but a major difference that some of the peaks such as 2theta 12.3°, 14.6°, 19.4° subsided. This confirmed that the INHZA sample is a binary eutectic mixture rather than the desired co-crystal. The physical mixture also inherited all characteristic diffraction peaks from both APIs.

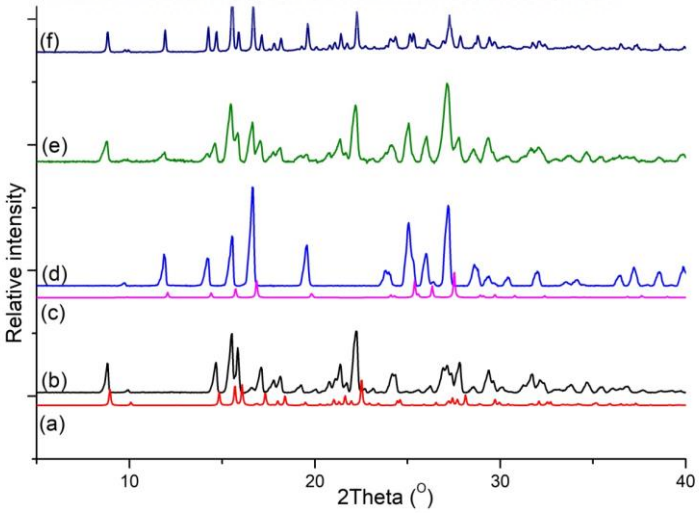

Figure 5.29: AZT calculated (a) and experimental (b) PXRD patterns, INH calculated (c) and experimental (d) PXRD patterns, (e) the binary eutectic INHZA and (f) INH-AZT physical mixture

5.3.3.5 Solubility evaluation of INHZA vs its components AZT and INH

Excess amounts of the individual drugs INH, AZT and their binary eutectic were added to USP aqueous buffer solutions at pH 1.2 (0.1M hydrochloric acid), 0.2M potassium phosphate buffer at pH 6.8 and pH 7.4, and deionized water (18. sMΩ). The suspensions were continuously shaken in an incubator shaker at 37 °C (± 0.5 °C) and 100 rpm for 24 hours, filtered using 0.20 μm PVDF syringe filters and analysed using an HPLC. INH and AZT in the eutectic preparation were quantified using an Agilent HPLC system setting with FXBPump (Flexar Binary Pump), an automated injector equipped with a UV detector (LC 200a Series PDA Detector), and a Flexar autosampler. Isocratic elution using acetonitrile solution (30:70) was applied at a 10 mL/min flow rate. A reversed-phase Luna C_{18} HPLC column 250 mm x 4.6 mm, 5μm was used. Injection volume was set at 10 µL and absorbance of elution was recorded at 262 and 270 nm following suitable dilutions. The calibration curves for two individual drugs INH and AZT were reported.

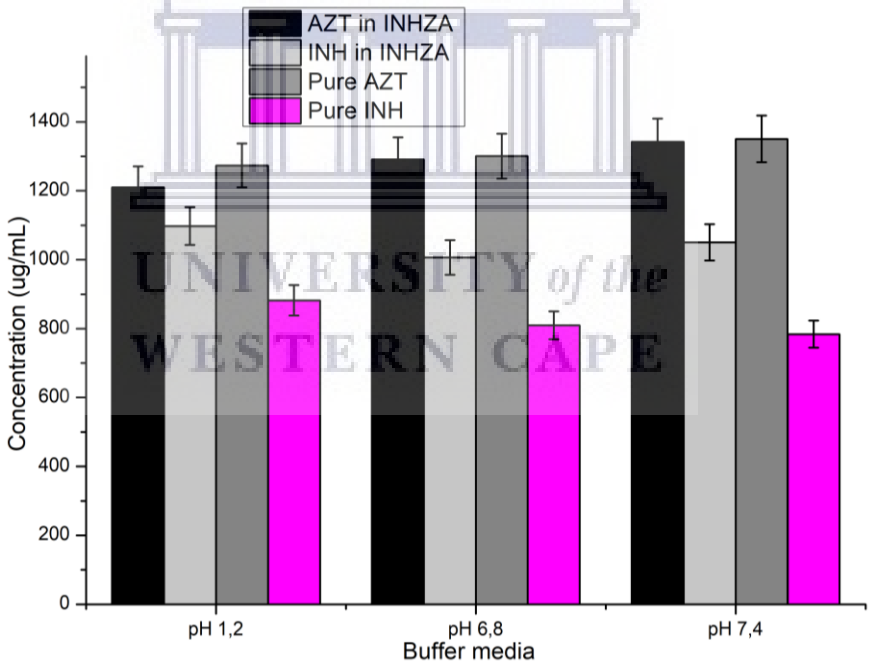

Figure 5.30: The solubility histograms comparing pure INH and AZT to their enhanced solubility in the binary eutectic INHZA in acidic buffer solution at pH 1.2 (0.1N HCl) and PBS at pH 6.8 and 7.4

In vitro solubility evaluation results are shown in **Figure 5.30** indicated a better solubility profile for INH in the INHZA sample; the concentration of INH in three simulated physiological environments (HCl, pH=1.2), potassium phosphate (PBS)

pH=6.8 and pH=7.4, has significantly increased. AZT concentration, on the other hand, did not significantly change in all three environmental conditions.

5.3.4 Zidovudine-pyrazinamide binary eutectic (AZTPZA)

Zidovudine is a well-known antiviral drug used to treat HIV/AIDS, and pyrazinamide is an anti-tubercular drug. This exercise aimed to explore the co-crystal forming ability of these two since both drugs are part of some HIV/TB co-infection treatment regimens.

5.3.4.1 Thermal analyses of AZTPZA sample

The HSM analysis of the AZTPZA sample showed a melt over 101-110°C temperature range and immediately followed by explosive bubbling characteristic of the sample decomposition. Different HSM photographs recorded are presented in **Figure 5.31**.

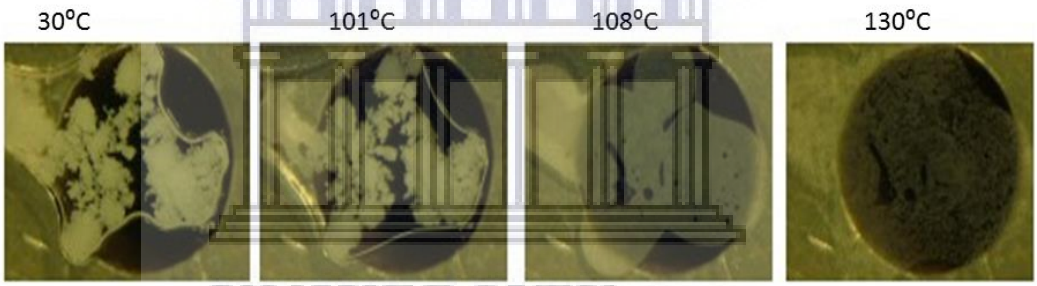

Figure 5.31: HSM photographs of the AZTPZA sample recorded at the beginning of the experiment (room temperature), the beginning of melting 101°C, a complete melting at 108°C and onset of decomposition at 130°C

DSC analysis further confirmed the melting transition of the sample reported by HSM with more accuracy. Initially, melting points of pure drugs AZT and PZA were obtained at 121°C and 190°C respectively. The physical mixture also generated a DSC thermogram with unique broad endotherm peaking at 109.7°C and an onset at 105°C. On the other hand, the AZTPZA melting endotherm peaked at 104.8°C (onset at 102.8°C). This melting transition lower than both APIs and the physical mixture melting points (**Figure 5.32**) was the first evidence of interactions between AZT and PZA and correlated with the HSM observations. Basic DSC data of APIs, physical mixture and the eutectic AZTPZA have been summarised in **Table 5.4**

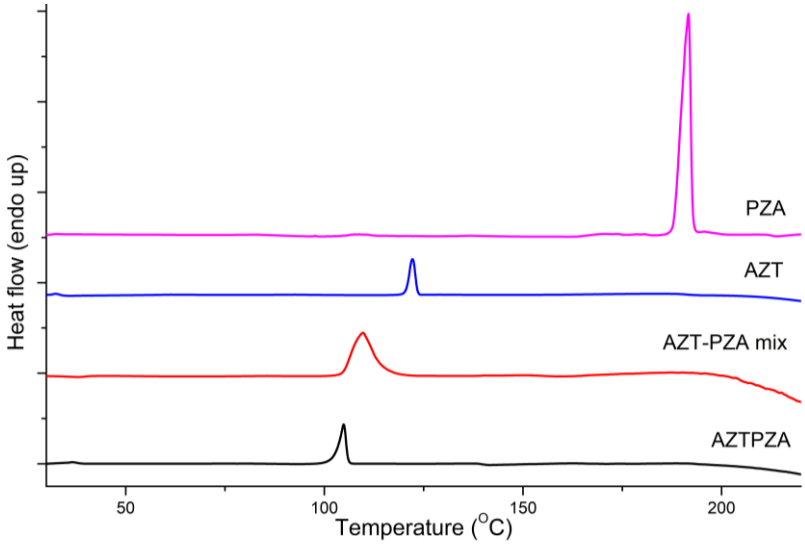

Figure 5.32: DSC thermograms of pure AZT, PZA and AZT-PZA physical mixture compared to the binary eutectic AZTPZA sample

Table 5.4: DSC thermal data of the individual drugs AZT, PZA, and the AZTPZA and AZT-PZA mixture (physical mixture)

Material	Onset (°C)	Melting point (°C)	Delta H (jg^{-1})
PZA	187.67	190.17	216.44
AZT	117	121	146.21
AZT-PZA Mixture	104.7	109.67	12.87
AZTPZA	102.77	104.83	70.42

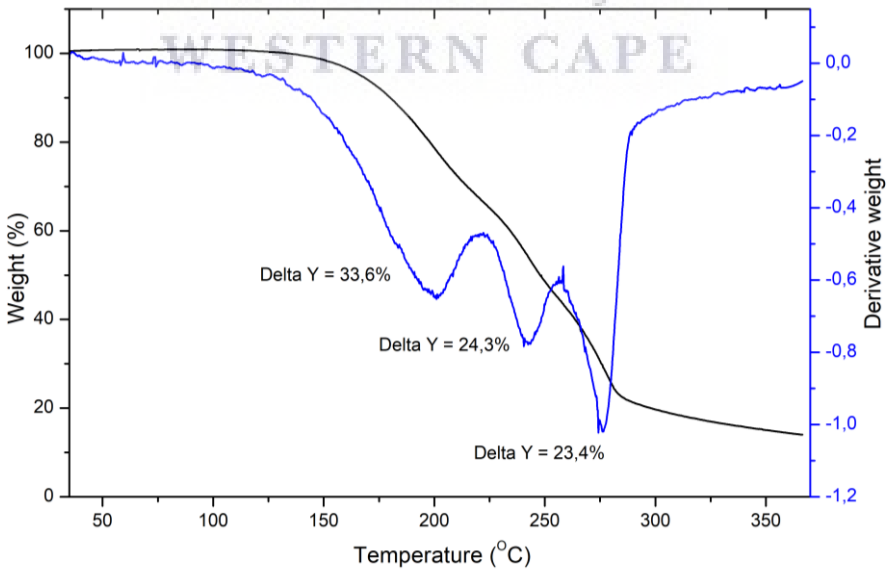

Figure 5.33: The TGA/DTA thermograms generated from the AZTPZA sample characterised by 81% decomposition mass loss in three consecutive steps

The TGA/DTA thermograms of the AZTPZA sample are depicted in **Figure 5.33.** Based on TGA/DTA measurements, there was no mass loss prior to the melting temperature (0.01 % mass loss), suggesting the absence of any volatile substances.

A stepwise decomposition mass loss is evident in the DTA curve; the first mass loss occurred over 130-200°C temperature range (33.6%), the second mass loss (25.3%) over 200-240°C and the third decomposition mass loss (23.4%) between 250°C and 300°C).

5.3.4.2 FTIR analysis of AZTPZA solid form sample

The FTIR spectra of AZT, PZA and the binary eutectic AZTPZA are shown in **Figure 5.34**. AZT spectrum showed absorption bands at 3458 cm^{-1}, assigned to N–H stretch, band at 3150 cm^{-1} representing O–H stretch and bands at 3024 cm^{-1} and C–H stretching peaked at 2813 cm^{-1}. The characteristic absorption band at 2081 cm^{-1} was due to azido group C=N=N while carbonyl asymmetric stretch C=O double-peaked at 1671 cm^{-1} and 1678 cm^{-1}.

The IR spectrum of pure PZA exhibited symmetry and asymmetry N–H stretch vibrations at 3409 cm^{-1} and 3288 cm^{-1} respectively, the C=O stretching band at 1709 cm^{-1} and the stretching pyrimidine N–C peaking at 1602 cm^{-1}. Experimental FTIR characteristic bands of both AZT and PZA agree with literature (Jain, Prabhakar, and Singh, 2013) (Gunasekaran and Sailatha, 2009).

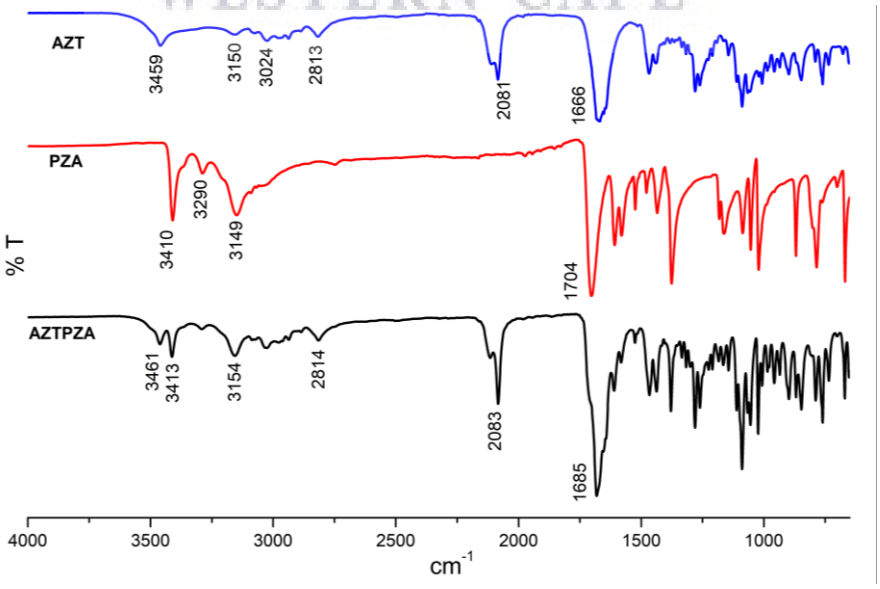

Figure 5.34: The FTIR spectrum from AZTPZA sample compared to pure AZT and PZA spectra

An in-depth analysis of the AZTPZA spectrum has indicated that the AZT absorption band at 3458 cm^{-1} (O–H) had shifted to 3461, while 3150 cm^{-1} (N–H) up-shifted to 3154 cm^{-1} in the AZTPZA FTIR spectrum. The intensity of the AZT absorption band at 3024 cm^{-1} (=C–H stretch) reduces whereas C–H stretch at 2813 $cm^{-1,}$ and azido $^{-}N=N=N^{+}$ at 2081 cm^{-1} showed very slightly shifting in the AZTPZA FTIR spectrum. The C=O stretching band of both APIs overlapped within a new band peaking at 1685 cm^{-1}, suggesting the possible weak bonding interactions with N–H/C–H stretch on both drugs. On the other hand, the PZA amide stretching N-H at 3409 cm^{-1} N−H also shifted to 3413 cm^{-1} due to possible bonding interactions with AZT stretching C=O.

Spectral changes in wavelength observed in the AZTPZA spectrum are compared to the starting materials' FTIR spectra in **Table 5.5**. Various changes and shifts calculated across the AZTPZA spectrum confirmed weak intermolecular interactions between AZT and PZA. **Figure 5.35** shows the suggested interactions based on FTIR spectral reports.

Table 5.5: Summary of different FTIR band shifting in AZTPZA spectrum vs original band positions in AZT and PZA spectra

Compound	Peak position	AZTPZA peaks	Band assignment
AZT	3459	3461.5	Strong to weak N–H
	3150	3154	Overlapped N–H of PZA
	3024	weak	Asy C–H
	2081	2083	N=N=N
	1671	1685	C=O
PZA	3410	3413	Asymmetric N-H stretch
	3149	3154	Symmetric N–H
	1704	1685	Overlapped AZT C=O

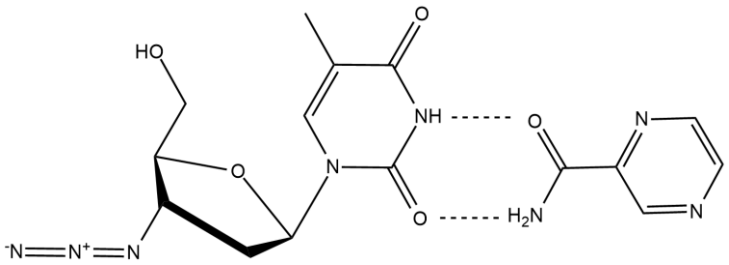

Figure 5.35: Suggested structure based on FTIR band shifting in AZTZA spectrum

5.3.4.3 Powder X-ray diffraction results of the AZTPZA multicomponent sample

The experimental and simulated PXRD patterns of AZT, PZA, AZTPZA sample and the physical mixtures are shown in **Figure 5.36**. The PXRD pattern generated from untreated AZT has sharp characteristic diffraction peaks at 2θ =15.49°, 15.83°, 22.18°and medium peaks at 2θ = 8.84°, 14.67°, 17.1°, 21.39°, 27.12°, 27.77°, 29.35° and small peaks at 2theta 18.13°, 24.2°, 31.68°. The PXRD pattern from PZA, on the other hand, shows two sharp diffraction peaks at 2θ = 14.4° and 27.19°, medium diffraction peaks at 2θ= 7.6°, double 15.06°, 15.25°, 26°and 35.5°, small diffraction peaked at 2theta 13.4°, 20.19°, 23.35°, 24.15°, 28.83°and 39.57°.

The PXRD pattern of the AZTPZA sample exhibited intense diffraction peaks at 2θ = 15.42°, 15.8°, 17.52°, 22.1°, 27.22° and 27.67°, medium diffraction peaks (above 1000 units) at 2θ = 8.7°, 14.6°, 17°, 18.1°, 21.3°, 24.17°, 26.19°, 29.35° and smaller diffraction peaks (below 1000 units) at 2θ = 7.67°, 61.65°, 32.2°, 33.8°, 34.6°, 35.5°, 36.83°and 39.71°. These diffraction data clearly show that AZTPZA sample inherits all diffraction peaks from pure AZT and PZA with minor differences in peak positions, intensities and shapes. Therefore, confirming that the present solid form is not a co-crystal as expected but a solid dispersion (binary eutectic mixture).

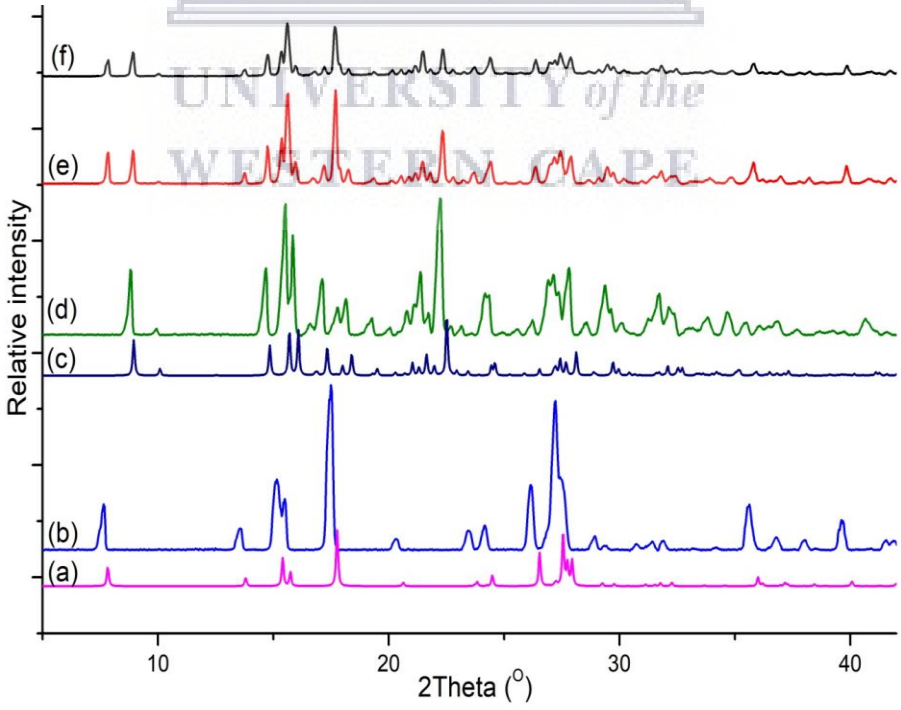

Figure 5.36: The experimental and simulated PXRD patterns of pure PZA (a and b) and AZT (c and d), AZTPZA binary eutectic (e) and the physical mixture AZT-PZA (f).

5.3.4.4 *In vitro* solubility evaluation of AZTPZA

Equilibrium solubility was carried out following the same method described in section 5.3.3.5. Compared to untreated APIs, solubility measurements indicated a significant increase in solubility of both APIs in the AZTPZA solid dispersion (**Figure 5.37**). AZT solubility increase by 1.13, 1.2, 1.15 and 1.14-times was recorded in a simulated gastric fluid (0.1N HCl, pH=1.2) and acetate buffer solution pH 4.5, potassium phosphate buffer solution (PBS) at pH=5.8 and pH=6.8 whereas a slight solubility decrease (0.1) was recorded at pH = 7.4 and deionised water.

Compared to its pure form, PZA exhibited an improved solubility 2.4-fold at pH=1.2 (0.1N HCl), 3.5-fold at pH=4.5 (acetate buffer), 3.5-fold and 2.5-fold respectively at pH=5.8 and pH=6.8. Furthermore, a 2.8-fold and 2.9-fold solubility increase was recorded at pH=7.4 and deionised water, respectively.

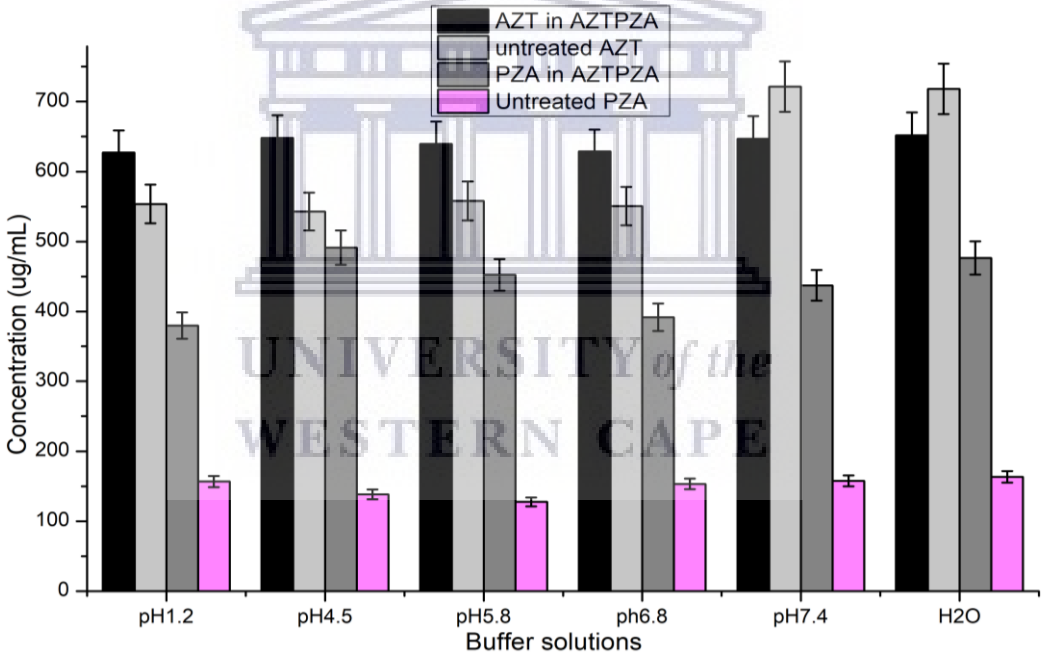

Figure 5.37: Solubility diagrams comparing the concentration of untreated AZT and PZA to their concentration in AZTPZA sample at different pH environment

5.3.5 Lamivudine-isoniazid binary eutectic LMISO

Solid-state, liquid assisted co-milling and solvent evaporation methods were utilised in the attempt to produce a binary co-crystal between two APIs lamivudine (3TC) and isoniazid (INH). A binary eutectic mixture LMISO was produced following an unsuccessful co-crystal formation between two APIs.

5.3.5.1 Binary eutectic LMISO thermal analyses

LMISO characterisation followed the analytical methods described in section 3.4. Thermal analyses by DSC and TGA were carried out to understand the thermal behaviours of the sample. DSC thermograms for pure APIs, the physical mixture and LMISO are shown in **Figure 5.38**. 3TC melted at 177°C and INH at 172°C. LMISO generated a DSC thermogram with a single melting endotherm at 134.3°C (onset at 132.4°C). This new melting transition is lower than both APIs' melting points, suggesting LMISO as a possible eutectic mixture rather than a desired dual-API co-crystal. The physical mixture also exhibited a DSC curve showing a very broad endotherm at 138°C.

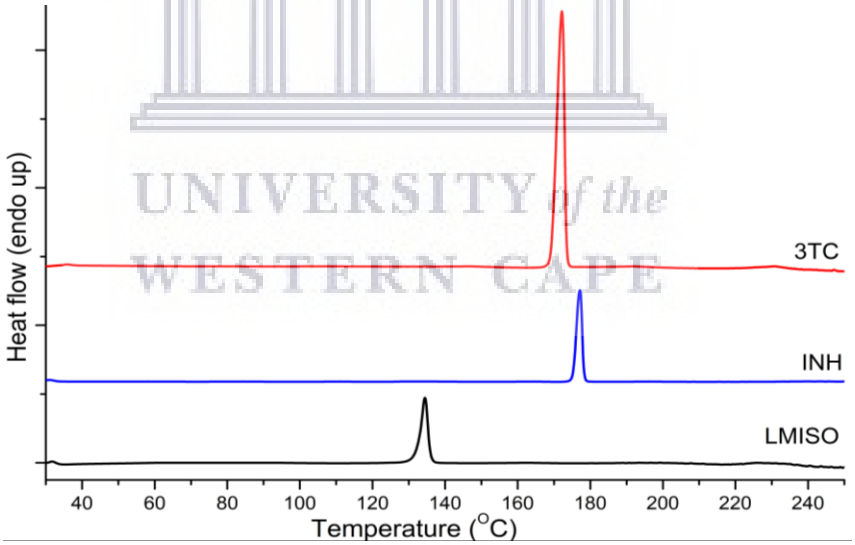

Figure 5.38: The DSC curves of pure 3TC, INH, their physical mixture and the binary eutectic LMISO showing a new melting transition at a lower temperature than both starting materials and their physical mixture

The TGA/DTA curves of LMISO are presented in **Figure 5.39.** TGA/DTA thermograms of both pure drugs are included in Appendix C. The TGA curve generated from LMISO sample is characterised by a decomposition mass loss at elevated temperature with an onset at 155.8°C, an inflection point = 260.0°C and a total mass

loss of 67%. There was no significant mass loss before melting onset, which indicated the absence of any volatile substances (moisture) in the sample.

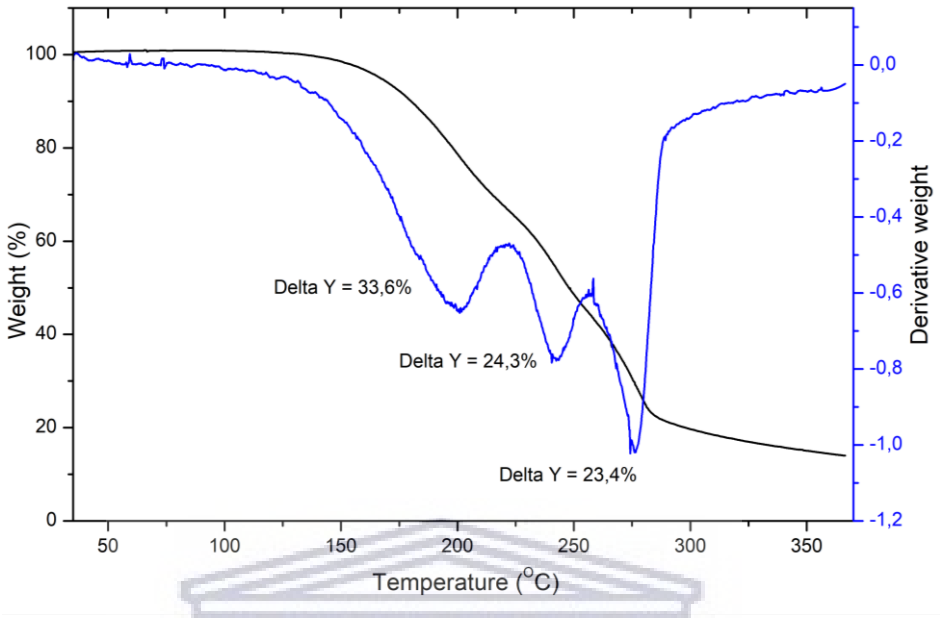

Figure 5.39: TGA/DTA curves of the binary eutectic LMISO showing decomposition mass loss in three steps.

5.3.5.2 LMISO characterisation by FTIR

Structural analysis by FTIR spectroscopy was conducted to examine the formation of intermolecular interactions between INH and 3TC. FTIR spectra for pure APIs and LMISO sample are shown in **Figure 5.40**.

There was a displacement of INH asymmetric N-H stretching band from 3292 cm^{-1} to 3305 cm^{-1} and the stretching C-H from 3094 cm^{-1} to 3108 cm^{-1} (**Figure 5.40a**) in the LMISO spectrum. 3TC hydroxyl O-H stretching at 3324 cm^{-1} subsides while its symmetric N-H at 3197 cm^{-1} intensified and shifted to 3267 cm^{-1} in the spectrum of LMISO (**Figure 5.40c**). There were also minor changes in 3TC characteristic band positions of C=O stretching, suggesting less influence by this complexation. These shifts were strong evidence on intermolecular bonding between INH and 3TC.

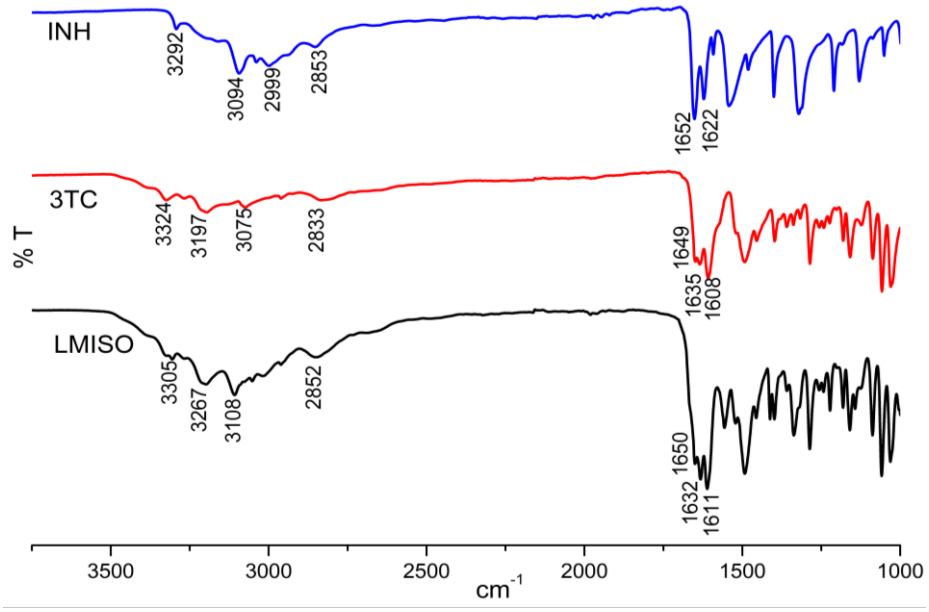

Figure 5.40: FTIR spectra of pure INH, 3TC the binary eutectic LMISO compared

5.3.5.3 Analysis of LMISO by the powder X-ray diffraction

The powder X-ray diffraction was used to identify the powder sample obtained. Experimental and calculated PXRD patterns of pure INH and 3TC were compared to that of solid crystalline form produced LMISO in **Figure 5.41**.

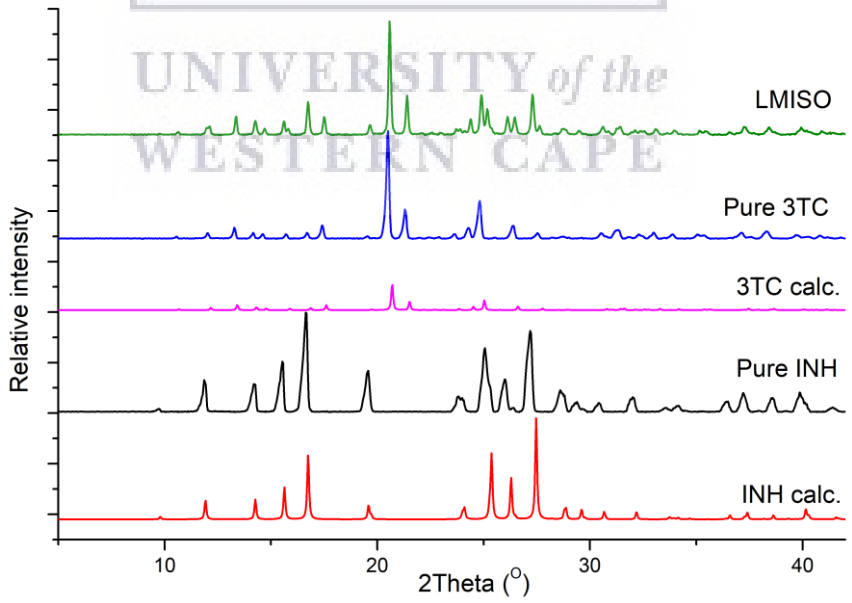

Figure 5.41: Experimental and simulated PXRD patterns of pure 3TC and INH compared to the eutectic LMISO

The characteristic diffraction peaks appear at 2θ=13.23°, 17.38°, 20.50°, 21.29°, 24.79°, 26.33° in the 3TC pattern while INH pattern exhibited diffraction peaks at 2θ=

11.9°, 14.3°, 15.6°, 16.73°, 19.65°, 25.3°, 26.95°, and 27.3°. LMISO pattern inherited all diffraction peaks from 3TC and INH with only minor intensity changes; confirming that the sample LMISO is a binary eutectic solid form.

5.3.5.4 In vitro solubility of LMISO

Excess amounts of pure 3TC and INH and binary eutectic mixture LMISO were added to USP aqueous buffer solutions at pH 1.2 (0.1M hydrochloric acid), 0.2M potassium phosphate buffer pH 6.8 and deionized water (18.s MΩ). Mixtures were continuously shaken in an incubator shaker at 37 °C (± 0.5 °C) at 150 rpm speed for 24 hours. Samples were filtered using 0.45 μm PVDF syringe filters and analysed using an HPLC.

An Azula HPLC system setting with FXBPump (Flexar Binary Pump), an automated injector equipped with a UV detector (LC 200a Series PDA Detector), and a Flexar autosampler was used to measure INH and 3TC in the samples. Isocratic elution using a mobile phase made of 10:90 method 85%: PBS (with pH adjusted to 3.6), at a flow rate of 1.0 mL/min. A reversed-phase supelco C_{18} column 150 mm x 4.6 mm, 5μm was used. Injection volume was 10 µL, and absorbance of elution was recorded at 260 nm following a suitable dilution.

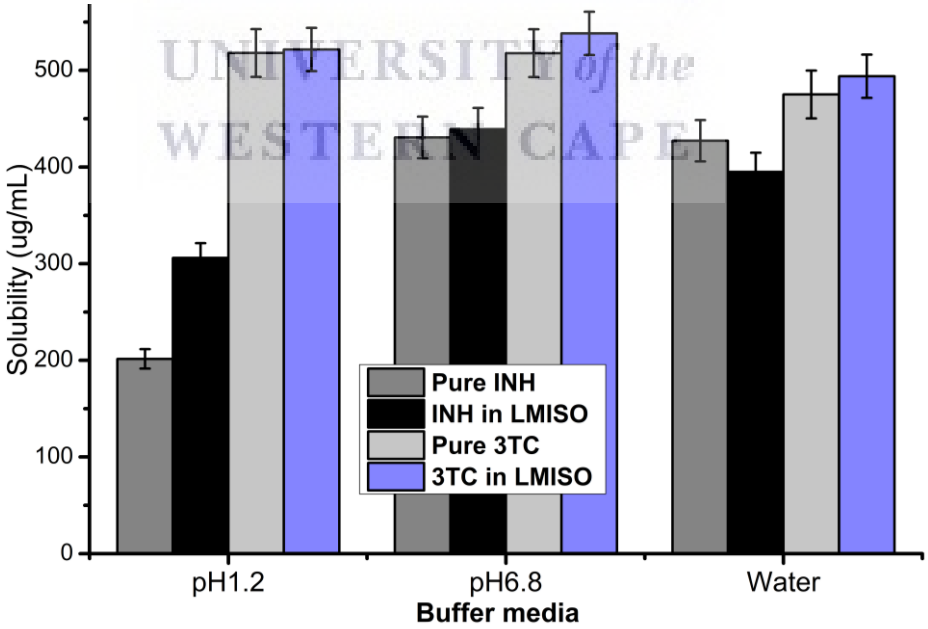

Figure 5.42: Solubility histograms comparing in vitro solubility of pure INH, 3TC to the binary eutectic mixture LMISO at pH 1.2 (0.1 N HCl), phosphate buffer solution at pH 6.8 and unbuffered deionised water

An increase in INH solubility by 1.3-fold was measured at acidic pH=1.2 while no significant increase was achieved in PBS at pH=6.8. On the contrary, a decrease of INH apparent solubility in LMISO was detected in deionised water, suggesting a possible INH decomposition in deionised water. 3TC did not show a significant increase in apparent solubility by this complexation in buffered solutions at pH=1.2, 6.8 and deionised water.

It is worth noting that based on the data presented in **Figure 5.42**, the solubility profile of pure INH as well as in LMISO showed a typical pH-dependence, with lower solubility at pH=1.2 and higher solubility at pH=6.8. However, this may have occurred due to possible decomposition at acidic pH environment.

5.4 Conclusion

A co-crystal EFINH between efavirenz and isoniazid was successfully prepared using solid-state grinding. A co-amorphous EFAD between efavirenz and 1-adamantylamine, and three dual-API solid dispersions (binary eutectic mixtures) INHZA and AZTPZA respectively between isoniazid-zidovudine, zidovudine-pyrazinamide and lamivudine-isoniazid LMISO, were successfully produced. Thermal behaviours of the samples were ensured using HSM, DSC and TGA/DTA. Spectral studies using FTIR provided information of molecular interactions between co-formers, whereas SEM and PXRD respectively provided morphology assessment and confirmation of samples chemical identities. Furthermore, solubility evaluation of all four dual-APIs solid forms carried out on the HPLC showed enhanced solubility in different pH buffer solutions and water.

Chapter 6 Non-covalent synthesis and characterisation of multicomponent hybrids of selected anti-tubercular drugs

This chapter describes the co-crystallisation experiments of the selected anti-tubercular drugs and discusses results for each successful multi-component derivative solid form obtained.

6.1 Introduction

Tuberculosis (TB) remains a great threat to humankind. TB is an infection caused by a bacillus known as *Mycobacterium tuberculosis*. TB is transmitted through air droplets containing the bacillus from an infected person. Compared to 2012-2013 WHO report, an approximation of 8.6 million TB infections and 1.3 million deaths associated with TB, 10 million new cases, and 1.5 million deaths were reported in 2018 (Baddeley, A; Dean, A; Monica-Dias, H; Falzon, D; Floyd, K; Garcia, 2013). The latent *Mycobacterium tuberculosis* (Mtb) estimated to have infected one-fourth of the population worldwide serves as a reservoir for the active and deadly form of the infection, making it even harder to control the infection. The threat is further aggravated by the appearance of drug resistance making treatment very complicated and in some cases resulting in treatment failure (N. C. Howard et al., 2018; Y. Hu et al., 2017; Somoskovi et al., 2001), and co-infection with HIV/AIDS (Bell & Noursadeghi, 2018; Duarte et al., 2018; Letang et al., 2020; Mesfin et al., 2014; Pawlowski et al., 2012b). The recent increase of drug resistance to available anti-tubercular treatment regimens (first-line and second-line) raised even greater concern about the future management of the infection, thus, the high pressure of finding alternative medicines.

Among anti-tubercular drugs used, isoniazid, chemically known as isonicotinic acid hydrazide (INH) and pyrazinamide known pyrazinecarboxamide (PZA) are two key drugs in the first-line treatment of TB. Both drugs are used in a single combined dose concomitant with rifampicin (RIF) and ethambutol (ETB) or streptomycin. INH and

PZA are prodrugs in nature; both activated after administration, the process triggered by the bacterial enzymes. The mechanisms of action were thoroughly explained by Unissa et al. (2016). INH is the most used drug in TB treatment. Its potential is well understood not only by its activity but also through the meaning of multidrug-resistance TB (MDR-TB).

However, despite its remarkable activity which seems to relate to molecular targets of the prokaryotic cells, toxicity and different side effects (dryness of the mouth, flu-like syndrome, allergic reactions, peripheral neuritis, mental abnormalities, methemoglobinemia, and hepatotoxicity), have been linked to the use of INH (Sarceviča et al., 2016).

PZA is also a very effective antimycobacterial agent that offers to the combinations (regimens) its unique sterilizing activity against persistent tubercle bacilli during the initial intensive phase of treatment. The use of PZA is also associated with shortening the duration of TB treatment, from 9 to 6 months (Chiș et al., 2005; Somoskovi et al., 2001). PZA shows prodigious but pH-dependent *in-vivo* activity. It is effective against *M. tuberculosis* only under acidic conditions. However, like many other drugs, different side effects have been attributed to the prolonged use of PZA (Schaberg et al., 1996).

Different co-crystals containing isoniazid and pyrazinamide have been reported with different carboxylic acids (Cherukuvada & Nangia, 2012; Grobelny et al., 2011; B. Yadav et al., 2019). This shows undoubtedly the complementary potential of these two for co-crystal formation driven by the presence of N–H, C=O and O–H moieties.

The work presented in this chapter encompasses screening, preparation and characterization of multicomponent hybrids based on two key anti-tubercular drugs isoniazid and pyrazinamide. Screening for co-crystals is initially carried out. Then, the thermal analysis of each co-crystal/hybrid using various thermal analytical instruments such as DSC, HSM, and TGA is presented. The chapter further explores the utility and ability of SEM, FTIR, and PXRD to study the morphologies and possible interactions and confirm the identity of the prepared samples. The results of *in-vitro* solubility evaluation conducted at body temperature, under different buffered solutions are demonstrated and discussed. Lastly, the initial evaluation of the biological activity is discussed.

6.2 Material and experimentation

6.2.1 Materials

For this part of research, two anti-tubercular drugs, i.e isoniazid and pyrazinamide were selected due to their potential inhibitory activity on the mycobacterium tuberculosis. These active substances were purchased from Sigma-Aldrich Chimie GmbH (Steinheim, Germany) and were used as received.

6.2.2 Preparatory methods

Grinding methods (solid-state and liquid-assisted grinding) were used first. An amount of APIs in their stoichiometric ratios, were consistently and vigorously ground in the mortar using a pestle for about half an hour (30 min). The screening was further carried out using solution crystallisation methods (solvent evaporation). All experiments were conducted in triplicate to ensure the samples reproducibility.

6.2.2.1 Dual-APIs isoniazid –pyrazinamide (INHPZA) solid forms

The solid-state grinding method was used in the attempt to produce INHPZA dual co-crystal. The INH-PZA mixtures in molar ratios (1:1; 2:1; 1:2) were subjected to the grinding exercise using an agate mortar and a pestle. The same grinding process assisted by a few drops of the solvent (ethanol 96%) added to the mixtures throughout the grinding process, was carried out.

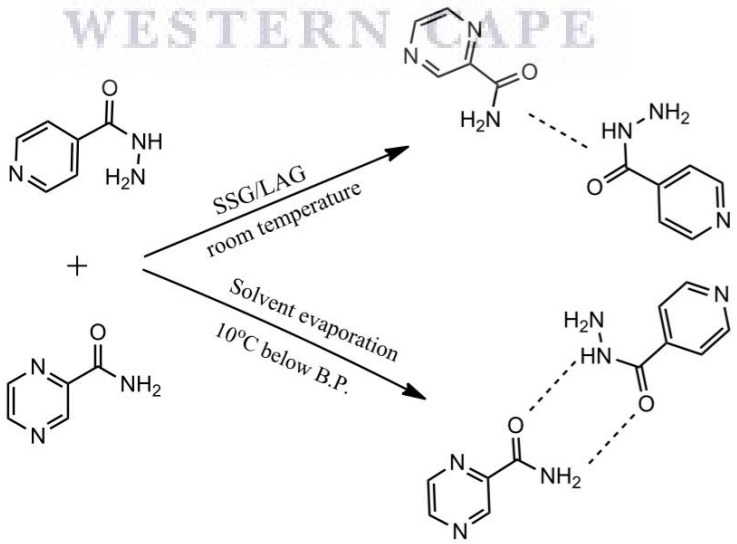

Figure 6.1: The proposed molecular mechanistic for the preparation of INHPZA solid forms

The molecular mechanistic of this preparation is shown in Error! Reference source not found.. Powder samples, namely INHPZA1, were obtained and kept in airtight polytops and subsequently analysed.

The screening was further carried out using the solvent evaporation method. A 1:1 stoichiometric amount of individual drugs was accurately weighed and transferred into vials and separately dissolved in 2mL of ethanol, methanol, and 2-propanol at elevated temperature (10°C below the boiling point of ethanol, methanol and/or 2-propanol). The resultant solutions were then mixed in a single vial and stirred for an additional 10 minutes, filtered (0.45 *u*m) and stored in clean vial sealed with a perforated parafilm and evaporated at ambient environmental conditions. Needle-like crystals (INHPZA2) were produced, dried on the filter paper and analysed.

6.2.2.2 Preparation of the co-crystal between isoniazid and pentanedioic acid (INHGA) (2:1)

The co-crystal preparation was carried out using solid-state grinding (SSG) and the solvent assisted grinding (LAG) method, as presented in **Figure 6.2**. For solid-state grinding, mixtures of INH: GA in different molar ratios (1:1; 2:1; 1:2) were subjected to physical milling using a mortar and a pestle. The same grinding procedure assisted by a few drops of the solvent (ethanol 96%) added to the mixtures throughout the grinding experiment was also utilised. Resultant powder samples were kept in airtight polytops for further characterization.

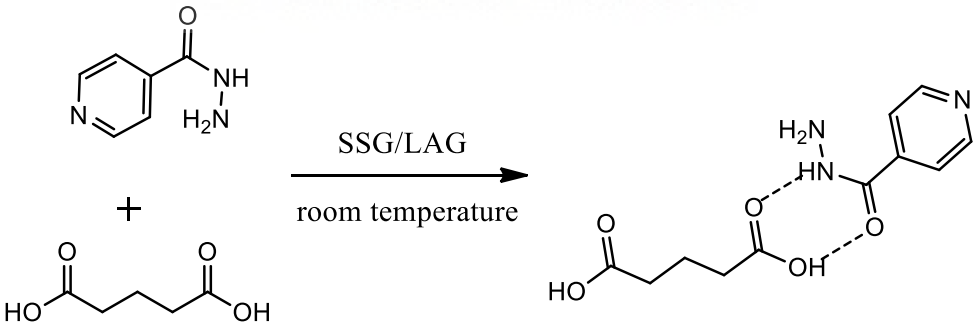

Figure 6.2: The molecular mechanistic for the preparation of INHGA (2:1) co-crystal

6.2.2.3 Pyrazinamide-glutaric acid co-crystal PGA (2:1) preparation

Pure pyrazinamide (PZA), and the co-former, glutaric acid (GA) were taken in their stoichiometric amount (2:1) to agate mortar and were physically milled for 30 minutes

using a pestle. The powder co-crystal sample was obtained and subsequently analysed. The co-crystallization was further attempted using solvent-assisted grinding, also known as liquid assisted grinding (LAG). PZA-GA mixture in the same molar ratio (2:1) was subjected to physical grinding, but this time, the mixture was wetted by a continuous introduction of ethanol (96%) drops throughout the grinding exercise. Resulted powder sample was kept in an airtight vial till analysed. The reproducibility of samples was ensured by repeating experiments in triplicate. The molecular procedure is presented in **Figure 6.3.**

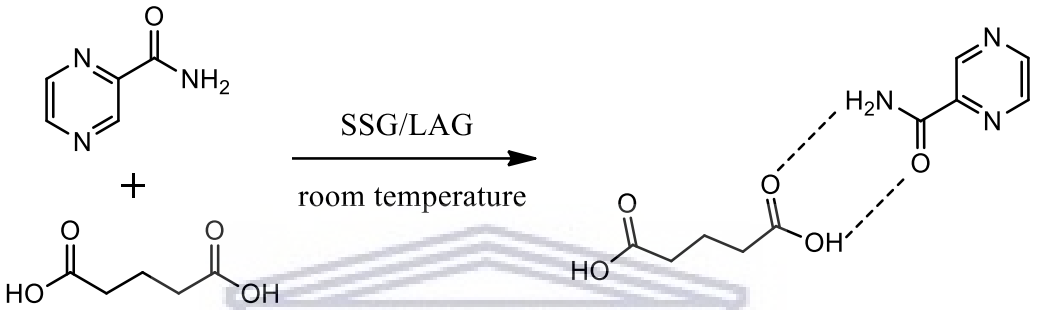

Figure 6.3: The molecular mechanistic for the preparation of the propose PGA (2:1) co-crystal

6.2.3 Characterisation

A full characterisation was carried out for the obtained samples vs their starting materials. Thermal analysis using the Hot Stage Microscopy, Differential scanning calorimetry, and thermogravimetric analyses. Sample morphologies were evaluated using Scanning electron Microscopy, while structural information and molecular identities of samples were obtained from Fourier infrared spectroscopy and the powder X-ray diffraction. In vitro solubility of samples was measured using PHLC.

6.2.3.1 Analysis by Hot Stage Microscopy (HSM)

Thermo-microscopic analyses were performed with an optical microscope Olympus (SZX-ILLB200) equipped with a Linkam temperature-controlled stage (THMS600/720), connected to a T95-PE system controller (Linkam Scientific Instruments Ltd., Tadworth, Surrey, UK). Images were recorded with an Olympus UC30 camera attached to the specified microscope (Olympus Optical, Japan) using Stream Essentials software. Samples were heated over a temperature range of 30 °C – 350 °C at a constant heating rate of 10°C/min, with samples submerged in silicon oil. The hot-stage was calibrated using USP melting point standards.

6.2.3.2 Analysis by Differential Scanning Calorimetry (DSC)

DSC analyses were performed using a DSC 8000 Perkin Elmer instrument (Waltham, USA), incorporating a cooling system. Samples (2.5 - 5 mg) were crimped in the aluminium pans sealed with pierced lids. The instrument was calibrated by measuring the onset temperatures of the melting of indium (m.p. 156.6 ^{o}C) and zinc (m.p. 419.5 ^{o}C) while the heat flow was calibrated from the enthalpy of melting of indium (28.62 J/g). The samples were heated to 20-30 °C above the melting range of the most thermally stable, at a heating rate of 10°C/min. All analyses were performed in triplicate under continuous pure (99.8%) dry nitrogen purging with a flow rate of 20 mL/min) and were reproducible.

6.2.3.3 Analysis by Thermogravimetry (TGA)

A Perkin-Elmer 4000 PC thermal system (Waltham, USA) was used. Calibration of the instrument was performed using three different references; Alumel (m.p. = 154.2 °C), Perk alloy (m.p. = 596.00 °C) and iron (m.p. = 780 °C) at 1 and 2°C/min. The samples analysis was carried out over a temperature range between 30 °C – 400 °C at a predetermined heating rate of 10°C/min. Samples were continuously purged by a stream of dry (99.8%) nitrogen gas (20 mL/min) and solvent stoichiometry of the compounds was determined from the percentage mass loss.

6.2.3.4 Morphology evaluation by Scanning Electron Microscopy (SEM)

The morphology of individual pure drugs and co-crystal samples were conducted using an AURIGA Field Emission High-Resolution Scanning Electron Microscope (HRSEM), Zeiss (Germany). Powder samples were mounted onto aluminium stubs using carbon tape. Energy (kV) used for images was 5 kV and 20 kV for EDS. The lament current was set at 2,359 amps. Carbon tabs were placed on the aluminium stubs to hold samples. Working distance (WD) for images is displayed on each image. SmartSEM 90 and AZTEC software were used for imaging and EDS, respectively.

6.2.3.5 Analysis by Fourier Transform Infrared Spectrophotometry (FT-IR)

Infra-red spectra of the individual drugs and the co-crystal samples were obtained using a Perkin-Elmer 100 FTIR instrument (Waltham, USA) fitted with UATR and controlled ® with Spectrum software version 6.3.5.0176 for the analysis. Analyses of powder or

crystalline samples were done over the range of 650-4000 cm^{-1} at a spectral resolution of 2 cm^{-1}.

6.2.3.6 Analysis by Powder X-Ray Diffraction (PXRD)

PXRD data were recorded on a D8 Advance powder X-ray diffractometer (Bruker AXS GmbH, Germany) with CuKαradiation (Cu-$K\alpha_1$= 1.54056 Å). The tube voltage and current applied were 35 kV and 40 mA, respectively. A V20 variable slit was used. Samples were placed on the sample holder which has 1 mm thickness and 1.5 cm in diameter. With a scan rate of 2°per min, the sample scan was performed in a continuous scan in locked coupled mode, within a range of 2θ5°to 50°. Origin Pro 8.5. was used to plot PXRD patterns.

6.2.3.7 *In vitro* solubility studies

Excess amounts of the individual drugs isoniazid and pyrazinamide, and their respective co-crystals (or eutectic mixtures) were added to USP aqueous buffer solutions at pH 1.2 (0.1M hydrochloric acid), 0.2M potassium phosphate buffer (pH 6.8 and pH 7.4, and 0.1% SDS. The mixtures were continuously shaken in an incubator shaker at 37 °C (± 0.5 °C) and 100 rpm for 24/48 hours. Samples were filtered using 0.20 μm PVDF syringe filters and analysed using an HPLC. AZT, 3TC, and both co-crystals were quantified using an Agilent HPLC system setting with FXBPump (Flexar Binary Pump), an automated injector equipped with a UV detector (LC 200a Series PDA Detector), and a Flexar autosampler. Isocratic elution using acetonitrile: water solution (30:70) was applied at a flow rate of 10 mL/min. A reversed-phase Luna C_{18}HPLC column 250 mm x 4.6 mm, 5μm was used. Injection volume was 10 µL and absorbance of elution was recorded at 262 and 270 nm following suitable dilutions.

6.3 Co-crystallisation results and discussion

The co-crystallisation results of all solid derivative forms produced between INH and PZA are presented and discussed in this section.

6.3.1 Dual-APIs isoniazid –pyrazinamide (INHPZA) solid forms

6.3.1.1 Thermal analysis of INHPZA1&2 solid forms

The HSM analysis was carried out by submerging the INHPZA1 powder and INHPZA2 crystals in the silicon oil and observed thermal changes under the

microscope. As shown in **Figure 6.4**, HSM images of the INHPZA1 sample were recorded over the temperature range 25-150°C. No thermal changes occurred in the sample prior to the melting point observed at about 147°C. INHPZA2 images showed air bubbles from 140°C due to crystal breaking and a possible solvent release. The melting of INHPZA2 crystals started at 168°C.

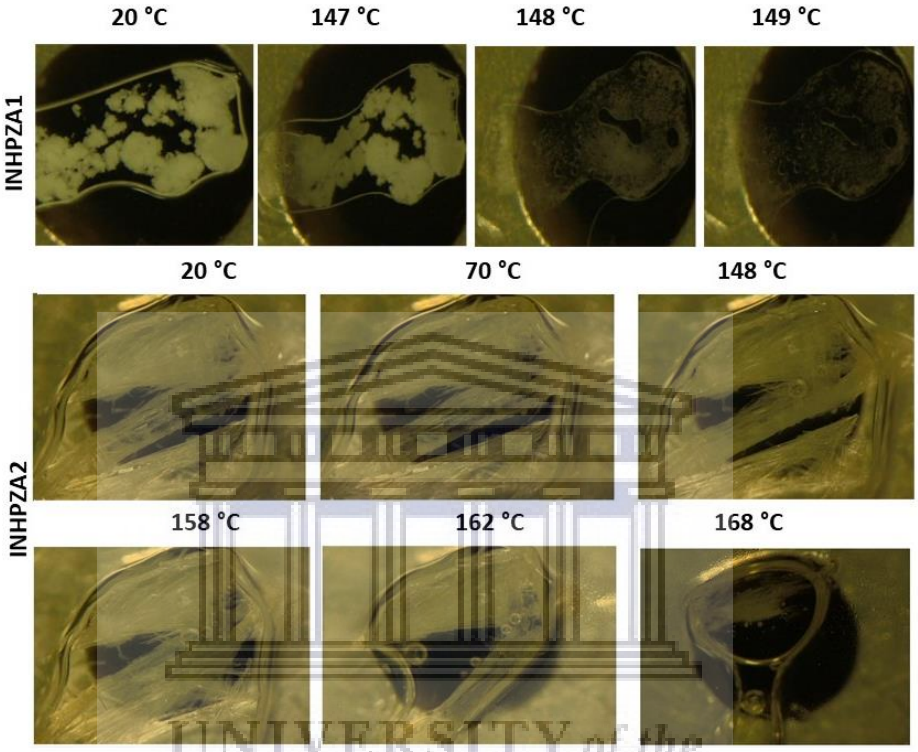

Figure 6.4: The HSM images for INHPZA1 and INHPZA2 samples showing different thermal behaviours.

Thermal behaviours of individual APIs were obtained using DSC and agreed with literature. INH sample exhibited a melt at 173°C and PZA at 190°C. Thermal analysis of the sample INHPZA1 revealed a lower melting endotherm at 142°C and an onset at 140.4°C (**Figure 6.5**). A DSC curve of INHPZA2 crystal showed two endotherms. The small bump at 140°C attributed to crystal breaking and/or desolvation and a melting transition between input materials at 184°C with an onset at 178.6°C, suggesting that INHPZA2 is a possible solvate co-crystal. This is consistent with HSM observations.

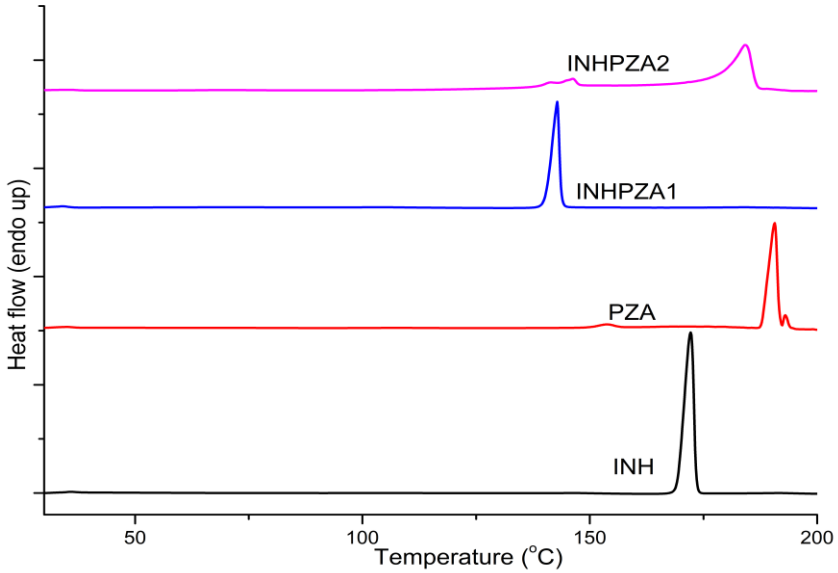

Figure 6.5: A diagram comparing DSC curves obtained from INHPZA1 and INHPZA2 solid forms and input drugs, INH and PZA

Thermal behaviour of INHPZA1 and INHPZA2 samples were further investigated using the TGA. The TGA/DTA curves are presented in **Figure 6.6**. The TGA curve generated from the INHPZA1 sample is characterized by two steps of mass loss, respectively over the sample melting (mass loss = 57%) and decomposition (loss =43%). The sample remained intact prior to the melting point.

The TGA analysis was utilised to investigate further the presence of solvent molecules in the crystal sample INHPZA2, as previously indicated by air bubbles release at 140°C during the HSM experiment and a small bump in the DSC curve.

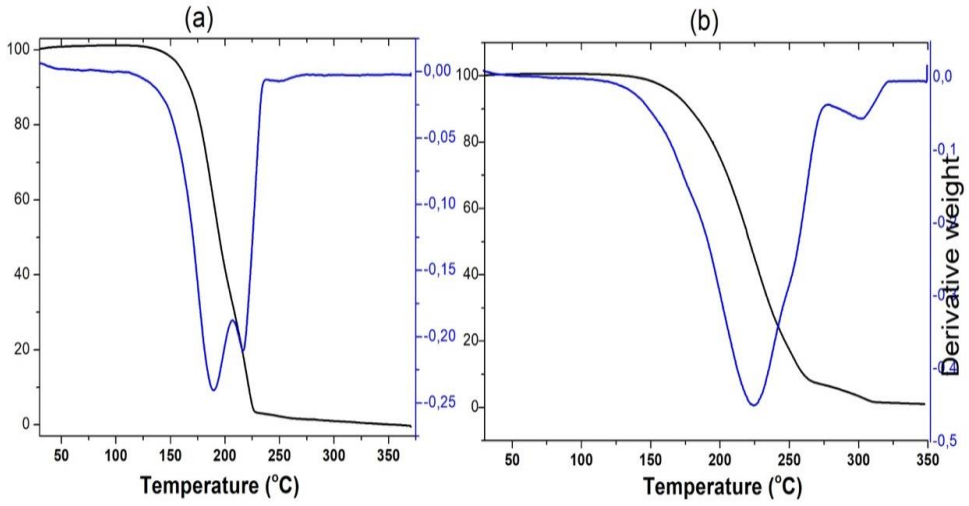

Figure 6.6: TGA and DTA curves of INH-PZA dual-API solid forms; (a) INHPZA1 and (b) INHPZA2

Based on the TGA thermogram measured from INHPZA2 crystals, there was a continuous mass loss starting before melting range of the sample with 12.4% calculated mass loss (inflection point at 184.5°C) and continued over melting and decomposition temperatures with a total mass loss of approximately 88.33% **Figure 6.6**b. This correlated well with HSM finding and confirmed that INHPZA2 crystal sample is indeed a solvated co-crystal.

6.3.1.2 Particle morphology analysis by scanning electron microscopy

SEM analysis offers a rapid way to characterise particle morphology of powder and crystal habits of the samples. Not only this powerful tool offers high-quality images of the particles, but it also provides atomic details of the sample being analysed.

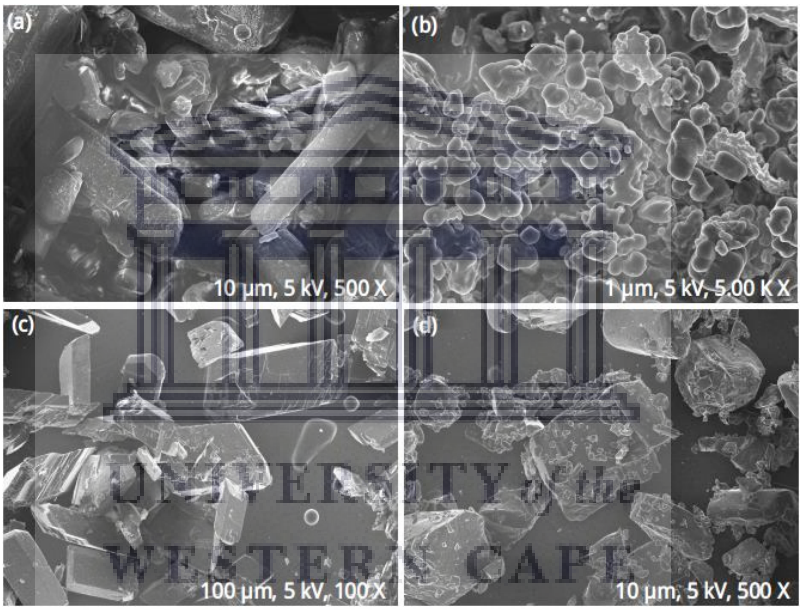

Figure 6.7: SEM images for (a) PZA, (b) INHPZA1, (c) INHPZA2 and (d) INH intact

Morphology analysis by SEM was carried out on pure INH, PZA, and the dual-APIs hybrids INHPZA1 and INHPZA2 samples. SEM micrographs are shown in **Figure 6.7**. The difference in morphology; specifically the shape and size of particles, was thoroughly examined. While pure PZA exhibited block-like particles with a smooth surface, INH particles were irregularly shaped and broken in pieces with sharp edges (**Figure 6.7**d). INHPZA1 exhibited round particles of different sizes, smaller than both APIs due to co-grinding **Figure 6.7**b. INHPZA2 obtained from solution crystallisation exhibited triclinic-shaped particles crystals **Figure 6.7**c.

6.3.1.3 Structural evaluation by FT-IR of IHNPZA solid forms

Structural evaluation by FTIR was carried out to confirm intermolecular interaction between two APIs in the co-crystalline samples produced. Pure INH and PZA spectra were assigned first and were used as references to analyse the samples.

As shown in **Figure 6.8** the FTIR spectrum of PZA exhibited an intense and sharp band at 3409.46 cm^{-1} and a weak band at assigned to asymmetric and symmetric υ(N–H) vibration modes respectively. The band at 3148 cm^{-1} was attributed to cyclic υ(C–H) stretching vibration modes. Further, the PZA carbonyl stretching υ(C=O) appears at 1704 cm^{-1} which agrees with literature according to Gunasekaran & Sailatha, (2009).

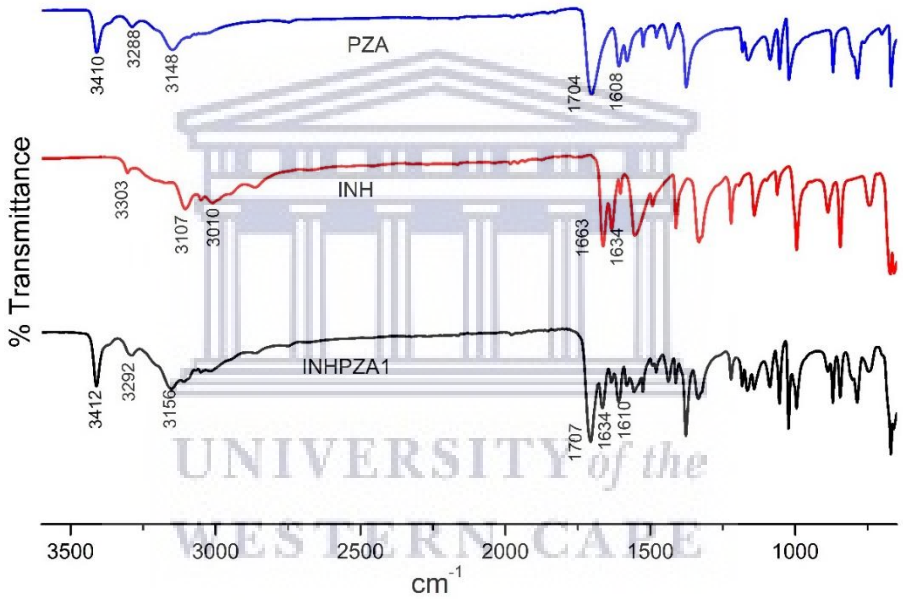

Figure 6.8: FTIR spectra of INH, PZA and INHPZA1 powder sample

The spectrum of pure INH has υ(N–H) stretching band at 3303.46 cm^{-1}, asymmetric υ(C–H) stretching at 3010 cm^{-1} and the carbonyl υ(C=O) at 1663 cm^{-1} (Gunasekaran et al., 2009; Ravikumar et al., 2013).

Respectively, INH stretching primary amine ν(N–H) has shifted to 3292 cm^{-1} while N-H at 3148 cm^{-1} has shifted to 3155 cm^{-1} in the spectrum of the INHPZA1 sample. The intensity of the υ(C–H) stretching band at 3010 cm^{-1} has significantly reduced. The PZA band at 1704 cm^{-1} and INH band at 1634 cm^{-1}, both assigned to carbonyl moieties, υ(C=O) have shifted to 1707 cm^{-1} and 1665 cm^{-1} respectively in the

INHPZA1 spectrum. These spectral changes confirmed interactions between INH and PZA.

FTIR spectra of the starting material of INH, PZA and INHPZA2 are shown in **Figure 6.9**Figure 6.8**.** INH spectrum exhibited two characteristic bands at 3303 cm^{-1}, 3107 cm^{-1} corresponding to stretching amine ν(N–H), stretching vibrations, ν(C–H) bands at 3010 cm^{-1} and 1663 cm^{-1} corresponding to the carbonyl ν(C=O) group. PZA spectrum also has two characteristic bands at 3410 cm^{-1} and 3288 cm^{-1} attributed to stretching amine ν(N–H) (asymmetric and symmetric N-H stretching, respectively), bands at 3148 cm^{-1} presenting stretching ν(C–H) and 1704 cm^{-1} corresponding to carbonyl ν(C=O) stretching vibration.

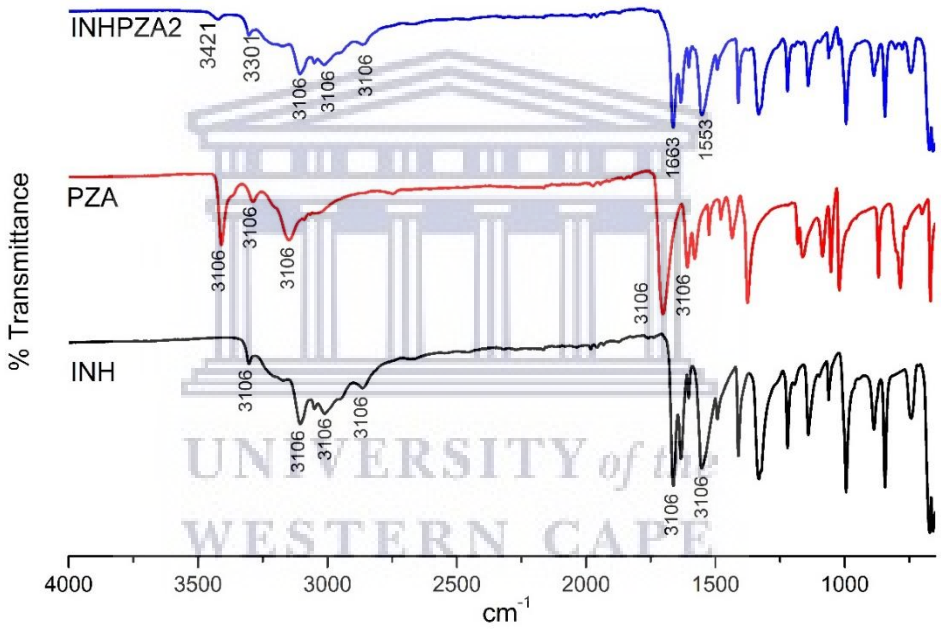

Figure 6.9: Diagram comparing FTIR spectra of pure INH and PZA to solvated co-crystal INHPZA2

The FTIR spectrum of INHPZA2 shows band position shifts as an indication of interactions between the co-formers. PZA asymmetric N-H stretching band at 3410 cm^{-1} has shifted to 3421 cm^{-1} while its stretching amine N-H at 3288 cm^{-1} subsided. There was a slight shifting in INH FTIR band peaks, suggesting that both APIs are held together by guest molecules in the structure of INHPZA2 via N-H and C=O interactions.

Table 6.1: The prominent IR spectral band positions in pure INH and PZA spectra and their respective positions in the spectra of the multi-component solid forms INHPZA1 and INHPZA2

Bands	INH	PZA	INHPZA1	INHPZA2	Comments
N–H		3410	3412	3421	asymmetric stretching
N-H		3288	3292	Disappears	symmetric stretching
N-H	3303		3292	3301	H–N shifting
C–H	3010		Disappears		Aromatic stretching
		3148	3155	Disappears	Aromatic stretching
C=O		1704	1707	Disappears	carbonyl stretching
C=O	1663		1667	1663	carbonyl stretching

6.3.1.4 Analysis by Powder X-ray diffraction

In the absence of good quality crystals suitable for single X-ray diffraction, PXRD provides an opportunity to understand the nature of the sample or even solve its structure. Diffraction patterns of individual drugs and co-crystalline samples are shown in **Figure 6.10**.

The difference in PXRD patterns is an indication that a new crystalline phase was attained. INH pattern exhibited diffraction peaks at 2θ = 11.9°, 14.3°, 15.6°, 16.73° 19.65°, 25.3°, 26.95° and 27.3°. PZA exhibited peaks at 2θ = 7.7°, 15.56° with a shoulder on the right, 17.58°, 27° and 27.29°. INHPZA1 generated a pattern exhibiting a summation of characteristic diffraction peaks of individual APIs with significantly reduced intensities. This suggested that the sample INHPZA1 is not a co-crystal, but a solid dispersion confirmed as a eutectic mixture. Reduced intensities also imply that the sample is less crystalline than entreated APIs, probably due to the grinding method used. Characteristic peaks are positioned at 2θ = 16.76°, 17.69°, 26°, 27°, 27.36°. On the other hand, INHPZA2 pattern exhibited new peaks at 2θ = 9°, 16.25°, 18.3° and 27.7° confirming INHPZA2 as a new phase and a successful co-crystal proven to be a solvate by thermal analyses.

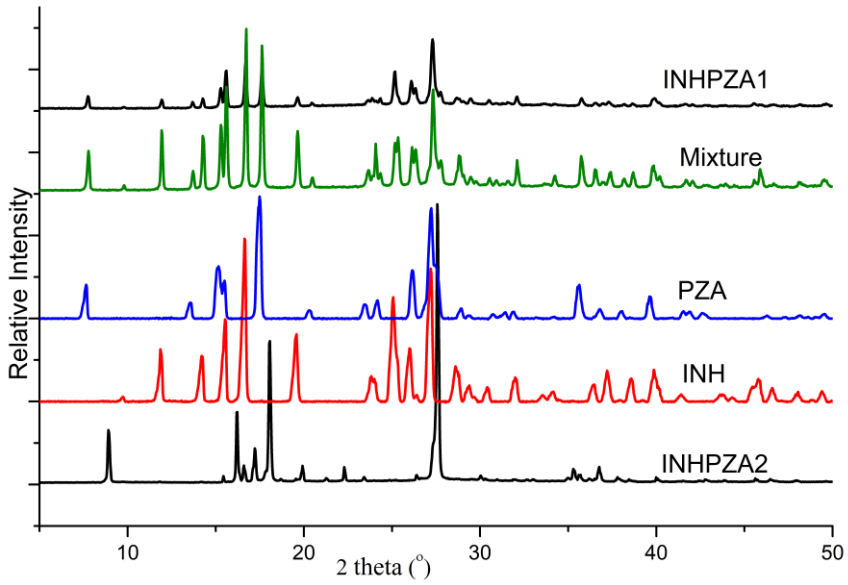

Figure 6.10: The PXRD patterns for pure INH, PZA, their physical mixture, and two derivative hybrids INHPZA1 and INHPZA2

6.3.1.5 *In vitro* solubility evaluation of the produced materials

Excess amounts of the individual drugs INH, PZA, and their respective co-crystals were added to USP buffer solutions at pH=1.2 (0.1M hydrochloric acid), 0.2M potassium phosphate buffer at pH=6.8 and pH 7.4, and deionized water (18.s MΩ). The mixtures were continuously shaken in an incubator shaker at 37°C (± 0.5°C) and 100 rpm for 24 hours. Samples were filtered using 0.20 μm PVDF syringe filters and analysed using an HPLC. In both preparations, INH and PZA were quantified using an Agilent HPLC system setting with FXBPump (Flexar Binary Pump), an automated injector equipped with a UV detector (LC 200a Series PDA Detector), and a Flexar autosampler. Isocratic elution using 30 % acetonitrile solution (30:70) was applied at a 10 mL/min flow rate. A reversed-phase Luna C_{18} HPLC column 250 mm x 4.6 mm, 5μm was used. Injection volume was 10 µL and absorbance of elution was recorded at 262 and 270 nm following suitable dilutions. The standard calibration curves for two individual drugs INH and PZA were reported in **Figure 6.11**.

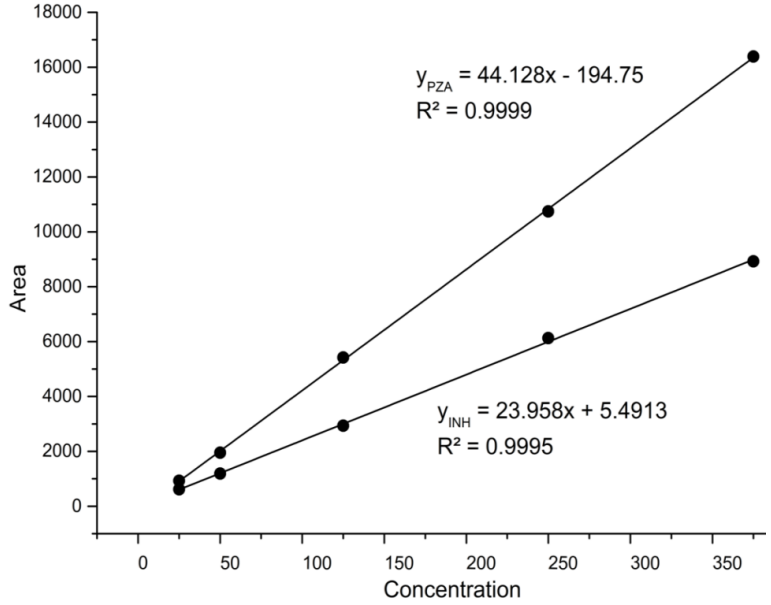

Figure 6.11: INH and PZA standard calibration curves with regression equations used to measure the solubility of both APIs at different pH

Solubility measurements presented in **Figure 6.12** suggests an enhanced solubility for both actives in the binary eutectic INHPZA1. A solubility increase of 1.7-fold and 1.35-fold was measured for INH at acidic pH=1.2 (0.1N HCl) and potassium phosphate pH=6.8. There was no significant increase of INH solubility in aqueous and buffer solution at pH=7.4.

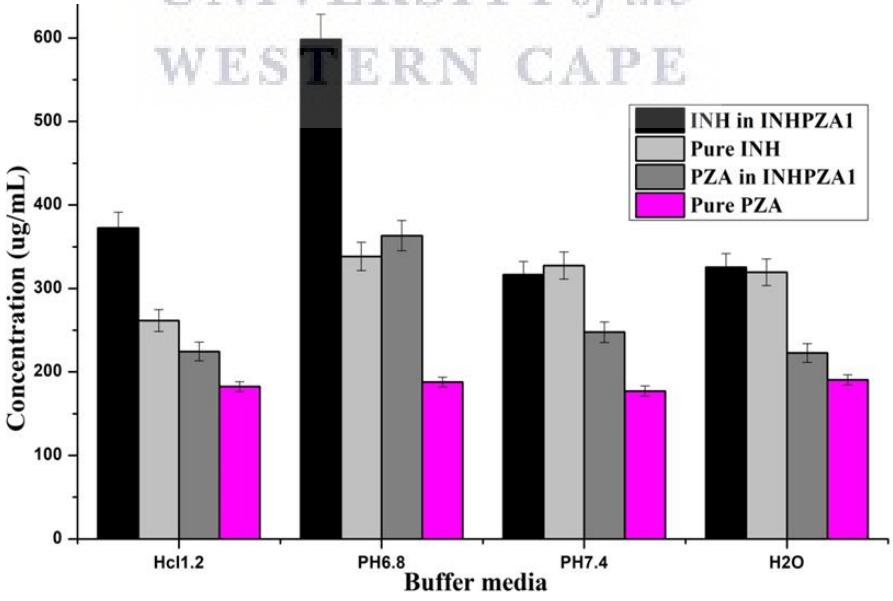

Figure 6.12: Solubility histogram of pure INH and PZA vs their binary eutectic

PZA has shown a significant solubility increase by 1.3-fold at pH=1.2 (0.1N HCl), 2-fold at pH=6.8, 1.5-fold at pH=7.4 and 1.23-fold in an unbuffered aqueous medium.

6.3.1.6 Minimal Inhibitory Concentration (MIC) Testing

The MGIT 960 with Epicentre software and the TB eXiST (TB Extended Susceptibility Testing) module was used to determine the MIC of 2 compounds against a H37Rv and a pan-susceptible *Mycobacterium tuberculosis* clinical isolate. Both strains were exposed to the compounds at final concentrations of 100, 10 and 1.0 µg/mL. MIC results were interpreted according to the 1% proportion method, which is defined as the lowest drug concentration that inhibits ≥99.0% of the bacterial population.

Table 6.2: MICs of INH and PZA (controls) and INHZA solid forms against M tuberculosis stains

Compound	**Minimum Inhibitory Concentration (MIC) µg/ml**	
	H37Rv (ATCC27294)	***M tuberculosis* Clinical Strain**
INH (Control)	<1.0	<1.0
PZA (Control)	<100	<100
INHPZA1	<1.0	<1.0
INHPZA2	<1.0	<1.0

Interestingly, based on results presented in **Table 6.2**, both solid forms inhibited the same anti-tubercular activity as the control INH, which is susceptible at 1.0 µg/mL, and far better than PZA. Determining the exact MICs must be carried out at a lower concentration range.

6.3.2 Isoniazid- pentanedioic acid co-crystal (INHGA) (2:1)

In this section, results from the co-crystal screening conducted on INH and the co-crystal former (pentanedioic acid or glutaric acid) using mechanochemical reactions, are discussed.

6.3.2.1 Thermal analysis of INHGA (2:1) co-crystal

Initially, thermal analysis by DSC confirmed the melting points of the pure INH and the co-former GA at 177°C (onset at 175.3°C), and 96.1-100.3°C respectively. The GA curve showed an additional broad peak at 74.0 °C, corresponding to the polymorphic transition (polymorph-β to α) (Bruni et al., 2013). The co-crystal INHGA (2:1)

exhibited a melting endotherm at 109.1°C and an onset at 107.0°C **Figure 6.14**. This new melting transition falls in the range between INH and GA melting points, thus indicating the complexation or interactions between INH and GA.

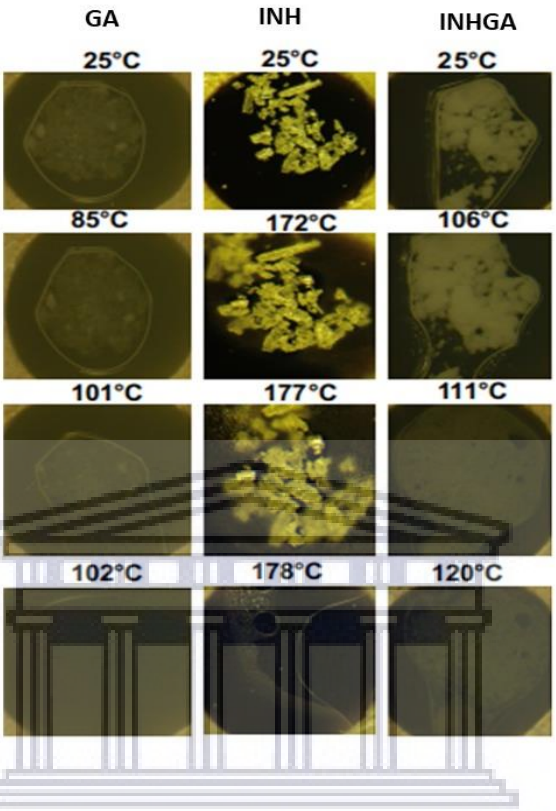

Figure 6.13: HSM images for INH, GA and the co-crystal INHGA (2:1) recorded over the range 25-200°C

HSM and TGA were conducted, and the results were matched with DSC results. In both experiments, the co-crystal sample remains stable until the melting point is reached. There was no indication of desolvation observed prior to the melting range during both HSM (no air bubbles) and TGA analyses. Based on the HSM analysis, the melting point of GA occurs over 98-101°C temperature range. The melting transition of the co-crystal sample INHGA (2:1) was observed over 106-111°C temperature range and INH exhibited a melt over 177-178°C range (**Figure 6.13**). Both DSC (**Figure 6.14**) and HSM results showed a very good correlation. The decomposition of the sample was characterised by explosive bubbling and discolouration (images not shown here).

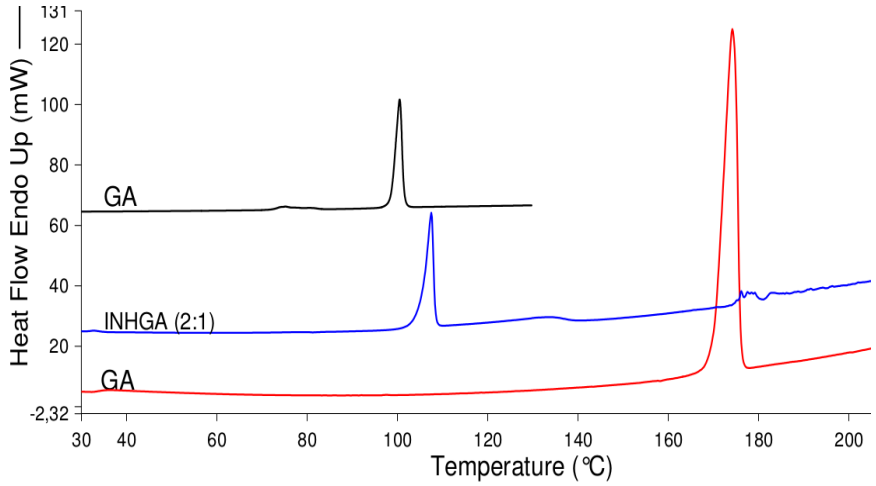

Figure 6.14: The DSC curves of pure INH, the co-crystal former GA, and the co-crystal INHGA (2:1)

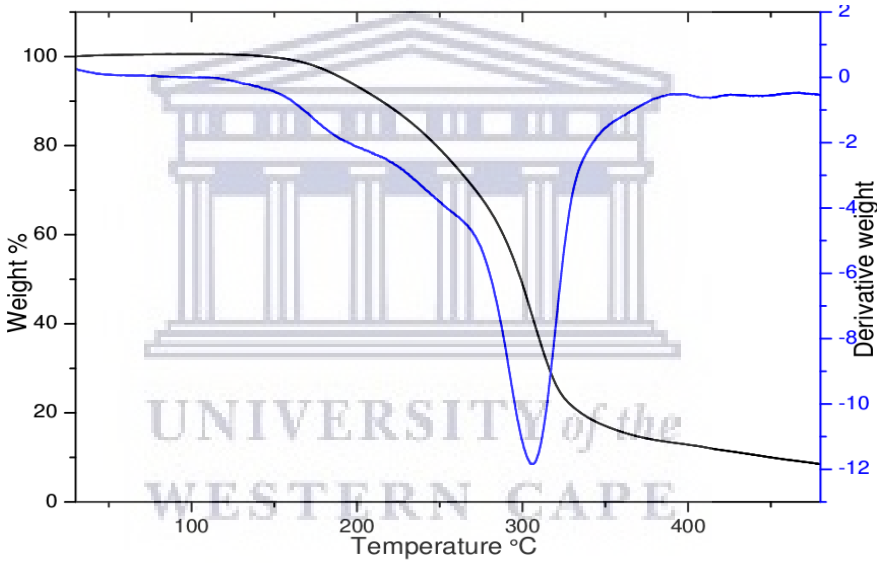

Figure 6.15:TGA/DTA thermograms of INHGA (2:1) co-crystal

TGA and DTA curves generated by INHGA (2:1) sample are characterised by a wide range of mass loss occurred upon a slow decomposition at high temperature, with an onset of sample decomposition at 180°C (**Figure 6.15**). The mass loss measured prior to the melting range of INHGA (2:1) samples was (0.02%), confirming that the present co-crystal is anhydrous. TGA/DTA curves of the starting materials INH and GA are available in **Appendix C** (**Supporting figure 4**)

6.3.2.2 Structural studies of INHGA (2:1) co-crystal by Infrared spectroscopy

Structural studies by FT-IR were conducted to confirm the formation of the co-crystal by monitoring spectral changes of band positions in the INHGA (2:1) spectrum in

comparison to pure INH and co-crystal former GA, changes that occur as a result of intermolecular interaction between INH and GA (Ali et al., 2012; S. Kumar, 2017). **Figure 6.16** illustrates spectral details of INH, GA, and INHGA (2:1) co-crystal samples.

FTIR spectra of the individual drug INH and the co-former GA were obtained first and were used as reference spectra for the co-crystal. IR spectrum of pure INH exhibits two stretching amine bands at 3303 cm^{-1} and 3107 cm^{-1}, stretch υ(C-H) at 3010 cm^{-1} and stretching carbonyl at 1663 cm^{-1} in agreement with the literature (Gunasekaran et al., 2009; Ravikumar et al., 2013).

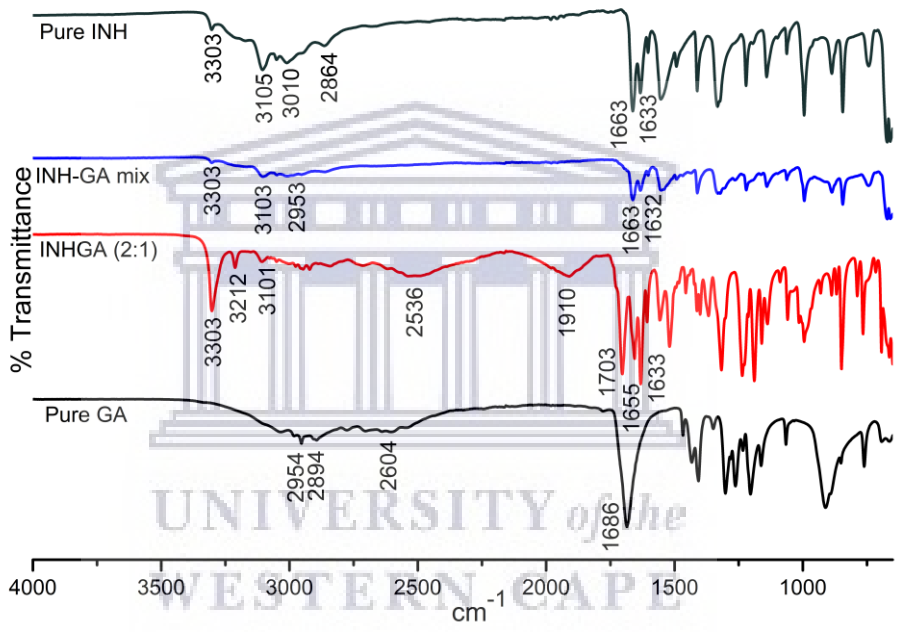

Figure 6.16: The FT-IR spectra of isoniazid (INH), the physical mixture, INHGA (2:1) co-crystal and pentanedioic acid (GA)

FTIR spectrum obtained from INHGA (2:1) exhibited carbonyl υ(C=O) stretch band at 1656 cm^{-1} (shift from 1663 cm^{-1} of INH), while GA stretching carboxylic carbonyl υ(C=O) at 1686 cm^{-1} shifted to 1704 cm^{-1}as a result of possible C=O···N–H formation, the GA carboxylic υ(O–H) overlaps with υ(C-H) vibration at 2954 cm^{-1} as a result of H-bonding with C=O of INH. A new broad peak at 1910 cm^{-1} in the INHGA (2:1) spectrum was attributed to H-bonding effect. **Table 6.3** summarises the main spectral band shifting in INHGA (2:1) vs its components.

Table 6.3: The FTIR shifts detected in the spectra of INH, GA and their co-crystal INHGA (2:1)

Assignment	INH	INHGA(2:1)	GA	Comments
Stretching N−H	3303 cm-^{1}	3303 cm-^{1}	3398 cm-^{1}	Intensified in INHGA (2:1)
Asymmetric C−H	3107 cm-^{1}	3101 cm-^{1}		Shifting in INHGA (2:1)
Stretching O−H			2954 cm-^{1}	O–H subsided in INHGA (2:1)
C−H	3010 cm-^{1}			Disbanded in INHGA (2:1)
C−H			2894 cm-^{1}	Disbanded
C−H		2536 cm-^{1}	2604 cm-^{1}	downshifting & less intensified
H-bonded C=O		1910 cm-^{1}		New in INHGA (2:1) spectrum
Carbonyl C=O	1663 cm-^{1}	1704 cm-^{1}	1683 cm-^{1}	shifting in INHGA (2:1)
Stretching C=N		1633 cm-^{1}	1632 cm-^{1}	intensified in INHGA (2:1)

Figure 6.17 suggests the possible bonding in the co-crystal between INH and GA, where the latter acts like a bridge binding two INH molecules.

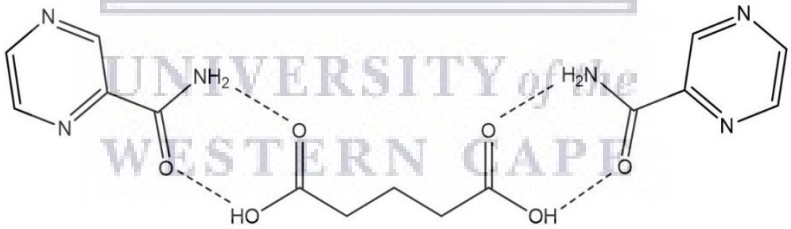

Figure 6.17: Suggested bonding interactions between isoniazid amide and carboxylic moieties of glutaric acid suggested based on the FTIR spectral results

6.3.2.3 Morphology results of INHGA (2:1) co-crystal by SEM

SEM analysis was carried out to evaluate changes in the morphology of the co-crystal sample vs its untreated components. SEM micrographs are shown in (**Figure 6.18**).

INH exhibited dusty irregularly shaped particles with sharp edges (**Figure 6.18a**), and GA is made of particles with round shapes and smooth surfaces (**Figure 6.18c**). INHGA (2:1) co-crystal exhibited irregularly shaped particles with sharp surfaces and dusty aggregates due to the grinding exercise (**Figure 6.18b**).

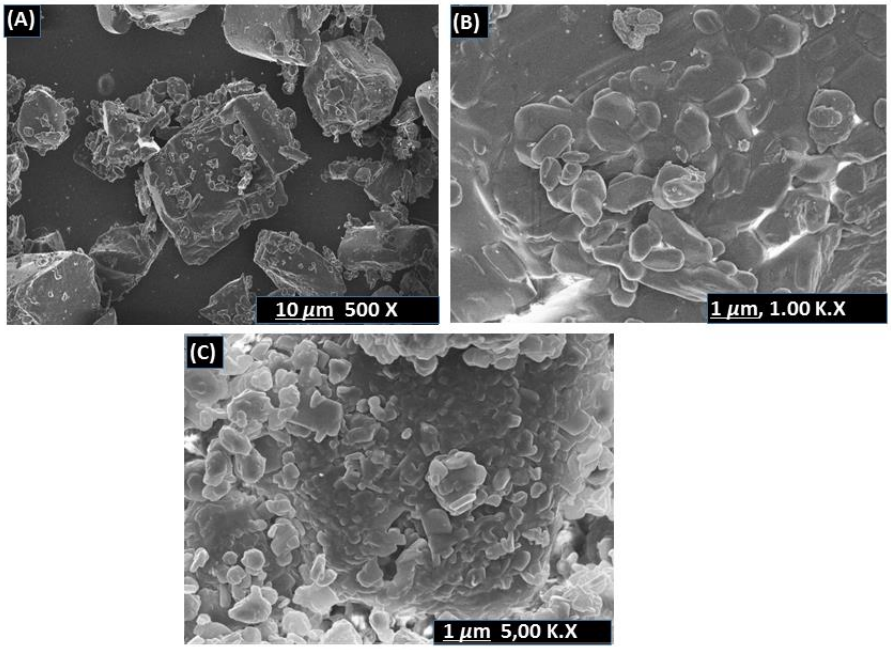

Figure 6.18: SEM micrographs for (a) pure INH, (b) the co-former GA and (c) the co-crystal INHGA (2:1)

6.3.2.4 Crystallographic results of INHGA (2:1) co-crystal sample

PXRD authenticated the successful co-crystallization as previously confirmed by FTIR and other thermal analyses used. The PXRD patterns from individual drugs and the co-crystalline sample are depicted in **Figure 6.19**.

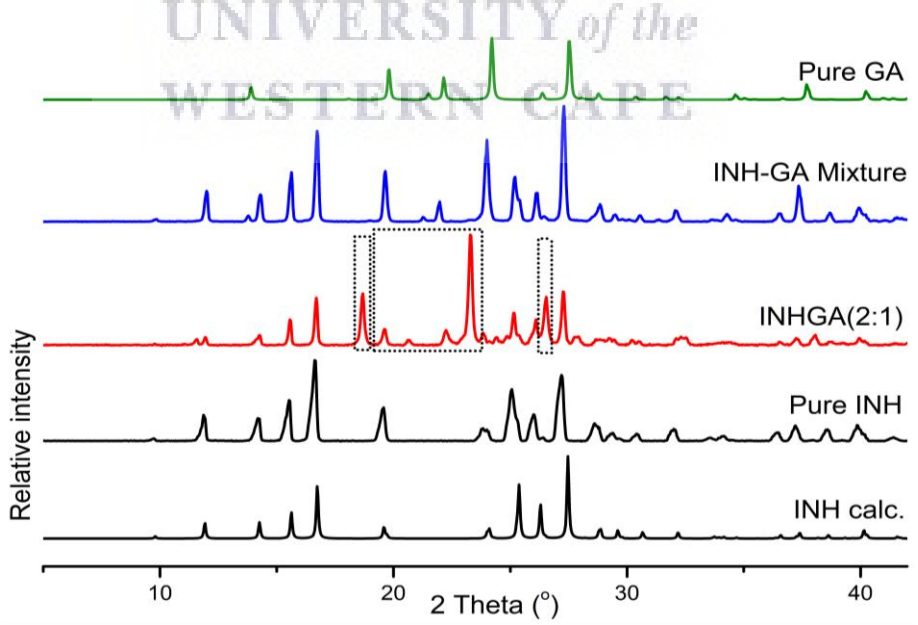

Figure 6.19: Experimental and simulated PXRD patterns of pure isoniazid and pentanedioic acid compared to the INHGA (2:1) co-crystal and INH-GA physical mixture

Differences in positions of diffraction peaks are a clear indication of the successful co-crystal formation. While INH PXRD pattern exhibited diffraction peaks at 2θ= 11.9°, 14.3°, 15.6°, 16.73°, 19.65°, 25.3°, 26.95°, and 27.3°, the main diffraction peaks in GA pattern appeared at 2θ= 13.88°, 19.7°, 22.24°, and 28°. The PXRD pattern from INHGA (2:1) exhibited new diffraction peaks at 2θ= 18.7°, 24°, and 27.4°, thus confirming that the co-crystal INHGA (2:1) was successfully produced.

6.3.2.5 Solid-state NMR (SS-NMR) analysis of the local chemical environment

Solid-state nuclear magnetic resonance (SS-NMR) as well as solution NMR, exhibit changes such as splitting and shifting in the local electronic environment as a result of molecular interactions. These changes are conclusive evidence on alteration in the molecular structure of a compound. Co-crystallisation, due to the formation of intermolecular H-bonds leads to such changes.

We used C^{13}CPMAS SS-NMR to detect isotropic chemical shifts as a way to further confirm the co-crystal produced. The assignment of the INHGA (2:1) co-crystal was based on pure API and the co-former (GA, glutaric acid). While INH was assigned using ChemDraw Ultra 12.0 software, GA was assigned based on previous experiments by Vigilante & Mehta, 2017. Isotropic chemical shifts were detected in the comparative spectral representation (**Figure 6.20),** and details are presented in **Table 6.4**.

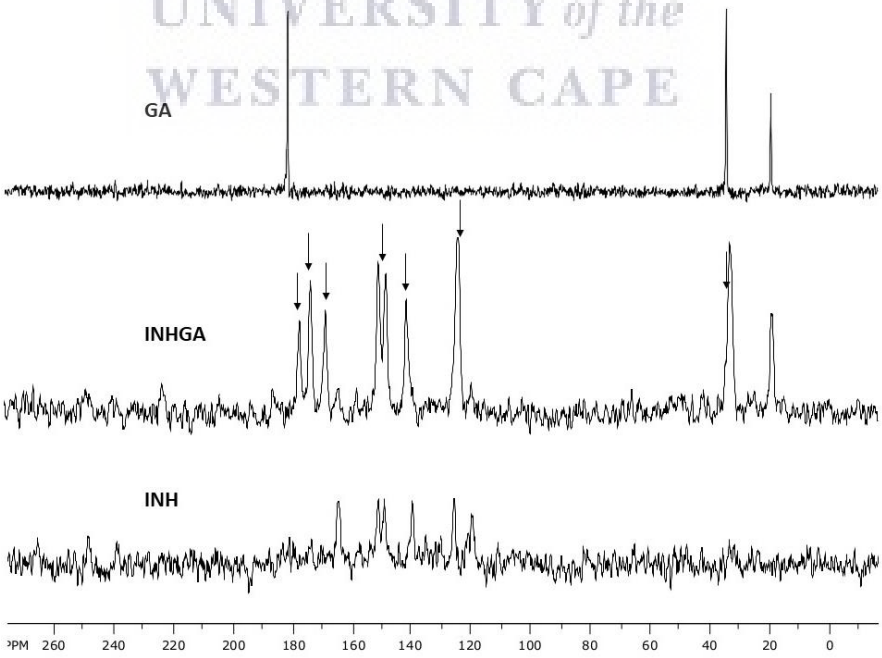

Figure 6.20: SS-NMR spectra for INH, GA and INHGA (2:1) co-crystal

Table 6.4: Isotropic chemical shifting due to the INHGA (2:1) **co-crystal**

GA	INHGA(2:1)	INH	Assignment
18.693	18.228; 18.510		Central methylene C
33.744	32.687; 34.045		Carbonyl C–C=O
		119.459; 119.875	pyridine C–C–N
	123.972; 124.295	125.543	pyridine C=C
	141.549	139.621; 139.874	Pyridine C=C–O
	148.433	149.220; 149.849	pyridine C=N
	149.963; 150.989	151.156; 151.497	Pyridine C=N
	168.751; 169.404	164.679	Amide C–N
181.451	173.802; 177.462		Carboxyl C=O (O–H)

6.3.2.6 INHGA (2:1) co-crystal solubility evaluation

Excess amounts of untreated INH and INHGA (2:1) co-crystal were added to USP aqueous buffer solutions at pH 1.2 (0.1M hydrochloric acid), 0.2M potassium phosphate buffer pH 6.8 and pH 7.4, and deionized water (18.s MΩ). The mixtures were continuously shaken in an incubator shaker at 37 °C (± 0.5 °C) and 100 rpm for 24 hours. Samples were filtered using 0.20 μm PVDF syringe filters and analysed using an HPLC.

An Agilent HPLC system setting with FXBPump (Flexar Binary Pump), an automated injector equipped with a UV detector (LC 200a Series PDA Detector), and a Flexar autosampler was used to quantify INH in the original INH and INHGA (2:1) co-crystal solutions. Isocratic elution using acetonitrile solution (30:70) was applied at a 10 mL/min flow rate. A reversed-phase Luna C_{18} HPLC column 250 mm x 4.6 mm, 5μm was used. Injection volume was 10 µL, and absorbance of elution was recorded at 262 and 270 nm following suitable dilutions. After the necessary dilutions, samples were analysed using HPLC. INH calibration data indicated a squared regression value was 0.999.

Solubility quantification suggested an enhanced solubility of INH in the co-crystal INHGA (2:1). An increase of 1.7-fold and 1.35-fold were measured at acidic pH values 1.2 (HCl) and 6.8 (PBS) for INH in the INHGA (2:1) co-crystal. Results indicated no significant increase in INH solubility in the aqueous and neutral pH = 7.4 **Figure 6.21**.

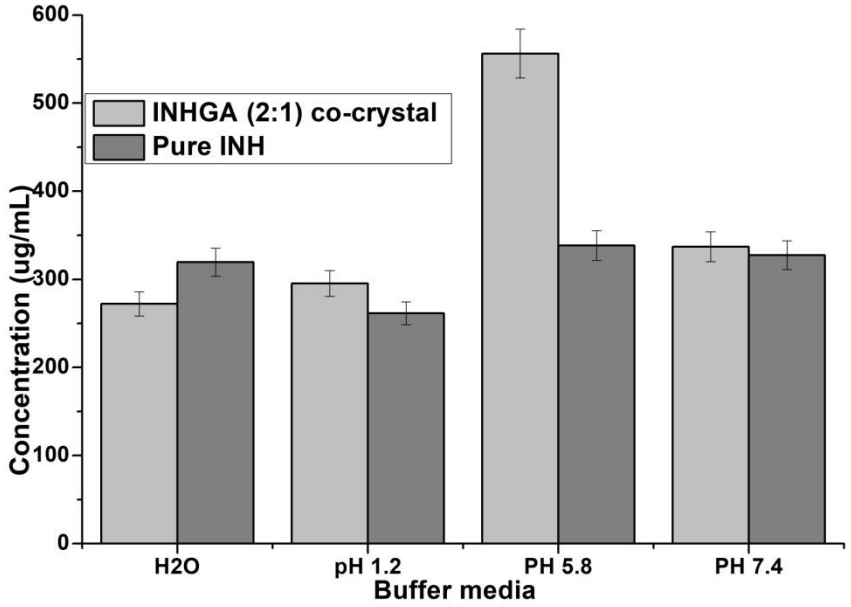

Figure 6.21: Histogram comparing the solubility of untreated INH to INHGA (2:1) co-crystal

6.3.2.7 *In vitro* antimicrobial evaluation

Minimal Inhibitory Concentration (MIC) testing of the co-crystal INHGA (2:1) was carried out. The MGIT 960 with Epicentre software and the TB eXiST (TB Extended Susceptibility Testing) module was used to determine the co-crystal MIC against H37Rv and a pan-susceptible *Mycobacterium tuberculosis* clinical isolate. Both strains were exposed to the compound at final concentrations of 100, 10 and 1.0 µg/mL. MIC results were interpreted according to the 1% proportion method.

Table 6.5: MICs of INH (control) and INHGA (2:1) against M tuberculosis stains

Compound	**Minimum Inhibitory Concentration (MIC) µg/ml**	
	H37Rv (ATCC27294)	***M tuberculosis* Clinical Strain**
INH (Control)	<1.0	<1.0
INHGA (2:1)	<1.0	<1.0

Based on the results presented in **Table 6.5**, co-crystal INHGA (2:1) shows anti-tubercular activity. INH was included as controls and should be susceptible at 1.0 µg/ml.

This is very interesting because as expected the co-crystal INHGA (2:1) even though containing less amount of INH than the control, exhibited the same activity. Therefore,

it is safe to say that co-crystallising INH with GA not only increased the solubility but also may result into the bioavailability enhancement of the drug.

6.3.3 Pyrazinamide-pentanedioic acid co-crystal

Like isoniazid, co-crystals of pyrazinamide (PZA) and different carboxylic acids including amino and hydroxybenzoic acids (Abourahma et al., 2011), different carboxylic acids including pentanedioic acid (Cherukuvada & Nangia, 2012) and other co-formers (Évora et al., 2011) have been previously reported. Basic information on the crystal such as unit cell parameters, space group have been presented, but neither full characterisation was presented or structure uploaded to the Cambridge structure database (CSD).

In this section, results from mechanochemistry; a green, simple and cost-effective method used to screen for the co-crystal between PZA and GA, are presented. While a full screening for the co-crystal can be found in Appendix A, here we present a full discussion of results, and recommendations for further uses.

6.3.3.1 Thermal analysis of PGA co-crystal sample

Thermal analysis of the sample was initiated by observation of thermal behaviour on the HSM. Images recorded at various temperatures over the experiment are presented in **Figure 6.22**. Based on the HSM analysis, melting was observed over 98-101°C temperature range for GA and 190-195°C for PZA. PGA (2:1) sample remains stable until the melting point between 106-108°C. There was no desolvation as indicated by the absence of air bubbles during HSM experiment.

Thermal analysis by DSC was carried out to establish PGA (2:1) melting temperature with more accuracy. PZA exhibited a broad polymorphic transition (Polymorph I to II) endotherm between 152-157°C and its melting point was confirmed 192.2°C (onset at 189.7°C) (Lavor et al., 2012). A DSC curve of the co-former GA also showed a broad peak at 74.0°C, corresponding to its polymorphic transition (polymorph-β to α) and a melting endotherm at 100.3°C (onset at 96.1 °C) (Bruni et al., 2013).

The 2:1 co-crystal of pyrazinamide-glutaric acid PGA (2:1) exhibited a single sharp endothermic melt at 105.3°C (**Figure 6.23**). This melting temperature falls between PZA and GA melting points.

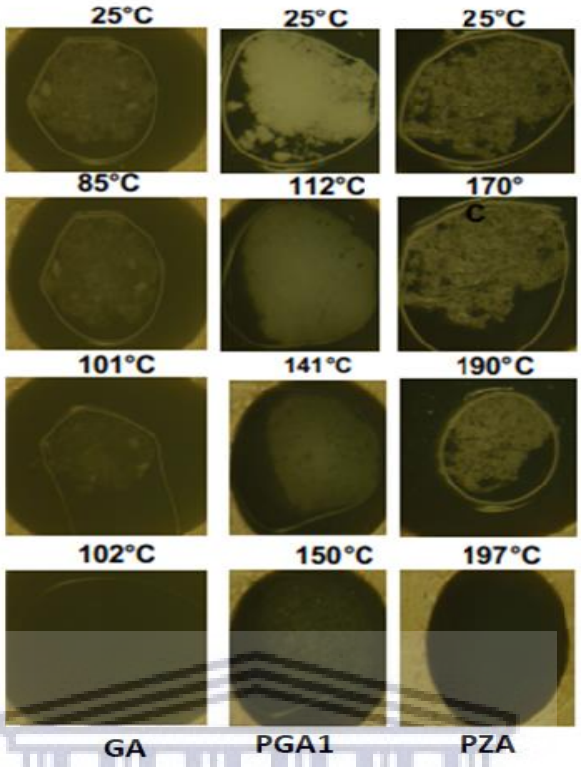

Figure 6.22: HSM images of PZA, GA and PGA (2:1) co-crystal sample

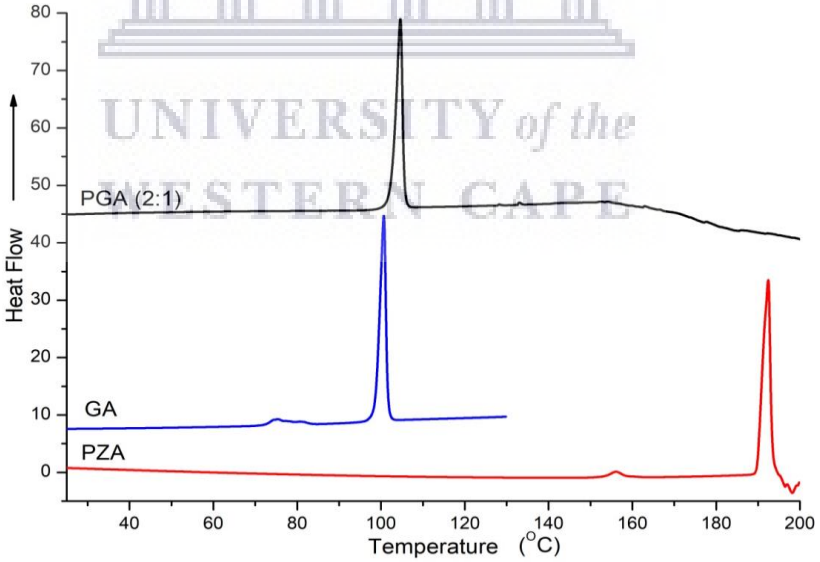

Figure 6.23: The DSC curves of PZA, the co-crystal former GA, and the co-crystal PGA (2:1).

The co-crystal did not inherit any polymorphic transition. The new melting transition was the first indication of a successful co-crystallization experiment, although further confirmation by other analytical techniques is warranted since the change in melting

points among multicomponent solid forms may occur either due to formation of non-covalent bonding interaction between API and co-formers, alteration in packing arrangements, or change in crystallinity. The fact that a single peak was established during DSC analysis certainly identifies interaction between the two parent compounds. **Table 6.6** summarises the essential thermal properties of the samples.

Table 6.6: Thermal properties for pure PZA, GA, and the co-crystal PGA (2:1) from DSC.

Sample	Melting onset temperature (°C)	Melting peak temperature (°C)	Δ H (J/g)	Peak area (mJ)	Peak Height (mW)
GA	98.6	100.5	96.7118	386.869	35.7522
PGA (2:1)	102.4	105.3	99.8891	289.678	24.5016
PZA	189.7	192.3	227.915	501.413	35.1694

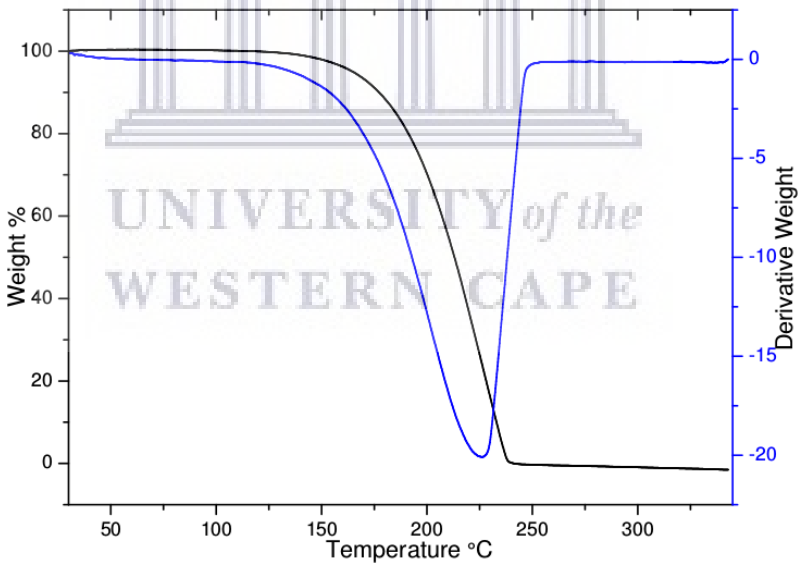

Figure 6.24: TGA and DTA thermograms of PGA (2:1) co-crystal

The thermal analysis further carried out on the TGA indicated that the PGA (2:1) sample remains stable until melting point temperatures are reached. Further, the TGA/DTA curves (**Figure 6.24**) are similarly characterised by a step of weight loss upon decomposition, which took place at a high temperature (decomposition onset at ~180°C)**Error! Reference source not found.**. Calculated mass loss before melting

range was (0.02%), thus confirming that the produced co-crystal PGA (2:1) is anhydrous (solvent-free).

6.3.3.2 Structural evaluation by infrared spectroscopy

The FTIR spectra of PZA, PGA (2:1) co-crystal, 2:1 physical mixture, and GA are shown in **Figure 6.25**. PZA spectrum exhibited characteristic bands at 3410 cm^{-1} and 3149 cm^{-1}, which correspond to the asymmetric and symmetric amide υ(N–H) stretching as well as 1704 cm^{-1} of carbonyl υ(C=O) stretch. GA spectrum exhibited characteristic bands at 2954 and 2603 cm^{-1} respectively attributed to stretching υ(C–H) and carboxylic υ(O–H). The carbonyl υ(C=O) stretching band appeared at 1686cm^{-1}.

PZA characteristic absorption bands have respectively shifted to 3397 cm^{-1}, 3164 $cm^{-1,}$ and 1694 cm^{-1} in the spectrum of the PGA(2:1) co-crystal whereas both GA C-Hand O-H bands shifted to 2931 cm^{-1} and 2543 cm^{-1} in PGA (2:1) spectrum. The GA carbonyl υ(C=O) stretch band at 1686 cm^{-1} significantly shifted to 1694 cm^{-1} in PGA (2:1), inferring the participation of these in H-bonding with N–H of PZA (C=O···N–H). The intensity of υ(O–H) which overlapped with υ(C–H) subsided in the co-crystal spectra accordingly. New characteristic bands at 2543 cm^{-1} and 1853 cm^{-1} were attributed to H-bonded carboxyl υ(C=O) and υ(O–H) in a possible (C=O···O–H) vibrational interactions.

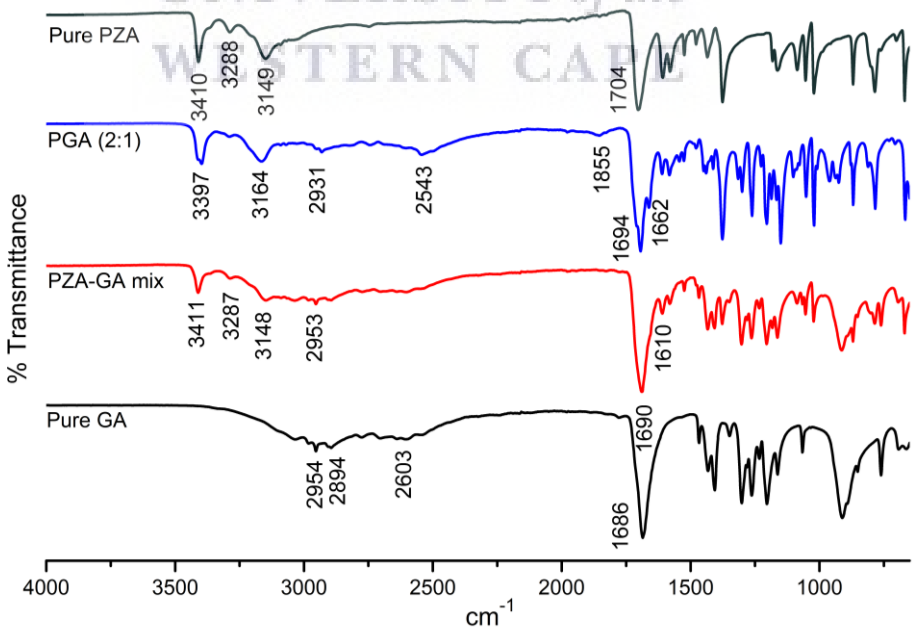

Figure 6.25: FTIR spectra of pure pyrazinamide (PZA), PGA (2:1) co-crystal, 2:1 physical mixture, and pure pentanedioic acid (GA)

Based on these data, it is safe to say that PZA is in intermolecular contact with GA. It is also worth mentioning that both GA carboxylic acid moieties are equally prone to intermolecular interactions with PZA, as suggested in **Figure 6.26.**

Table 6.7: Summary of all shifts in wavelength in both PGA (2:1) sample

F(x) groups	**PZA**	**PGA** (2:1)	**GA**	**Comments**
N−H	3409 cm^{-1}	3398 cm^{-1}		Broad & shifted
Sym-N-H	3288 cm^{-1}			Subsided
Stretching C−H	3148 cm^{-1}	3159 cm^{-1}		Bands shifted in PGA(2:1)
Carboxylic		2931 cm^{-1}	2954 cm^{-1}	shifted significantly
O−H		2543 cm^{-1}	2604 cm^{-1}	
Carbonyl C=O	1704 cm^{-1}	1694 cm^{-1}		Significant band shifting
Carbonyl C=O		1662 cm^{-1}	1686 cm^{-1}	Significant band shifting

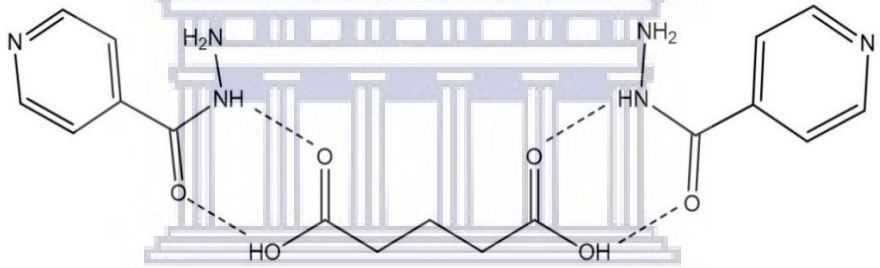

Figure 6.26: Suggested structure of PGA (2:1) co-crystal

6.3.3.3 Particle morphology by scanning electron microscope

SEM analysis of the powder samples was carried out to understand the morphology of PGA co-crystalline samples. SEM micrograms for PGA (2:1), PZA, and GA are presented in **Figure 6.27**.

The SEM images of untreated PZA, GA, and PGA (2:1) are presented in **Figure 6.27**. Pure PZA powder consists of large and differently shaped crystals (**Figure 6.27a**), whereas GA powder has small amassed aggregates of round shapes (**Figure 6.27b**). Rod-like particles mixed with round irregularly shaped aggregates with smooth edges were observed for the PGA (2:1) co-crystal (**Figure 6.27).**

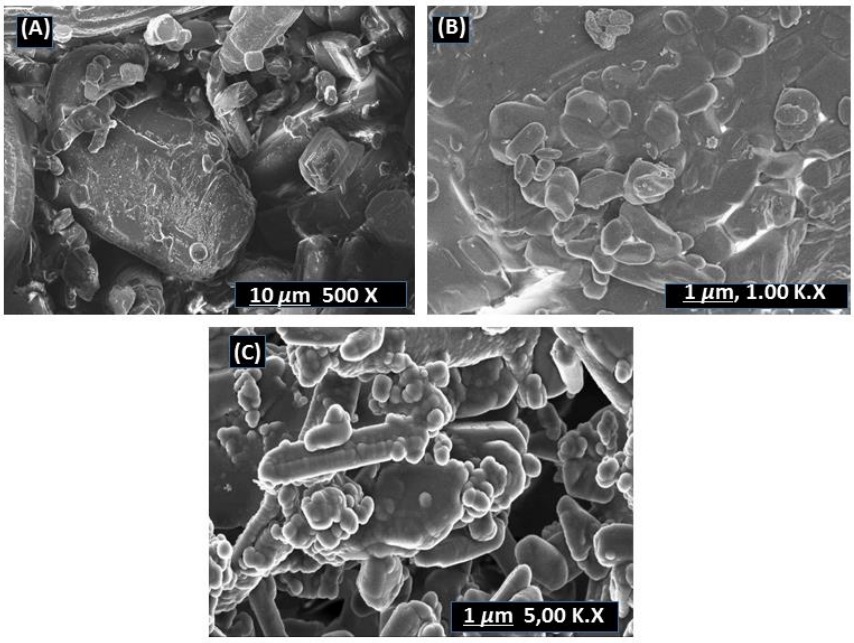

Figure 6.27: SEM micrographs comparing the morphology of (A) pure PZA, (B) GA and (C) PGA (2:1) co-crystal

6.3.3.4 Analysis of PGA sample by the powder diffraction

PXRD analysis was carried out for both starting material and the co-crystal sample. Experimental and calculated XRD patterns of Pure PZA, GA, and XRD pattern of PGA (2:1) co-crystal are shown in **Figure 6.28**. PXRD authenticated the successful co-crystallization as previously confirmed by FTIR and other thermal analyses used. Experimental samples of pure PZA and GA compare to calculated patterns.

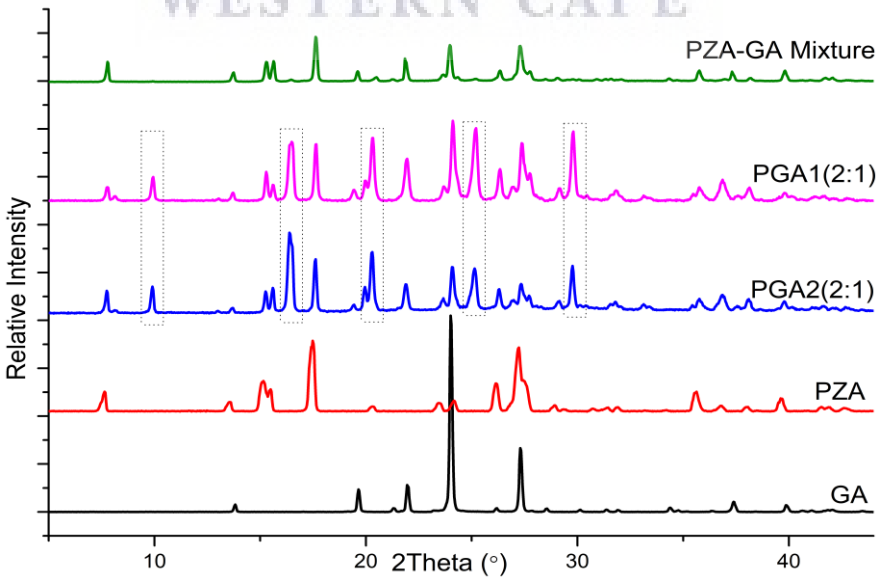

Figure 6.28: Experimental and calculated PXRD patterns of pure pyrazinamide and pentanedioic acid, PZA-GA physical mixture and PGA (2:1) co-crystal.

While GA XRD pattern presents diffraction peaks at 2θ= 13.88°, 19.7°, 22.24°, and 28°, PZA pattern displayed various diffraction peaks at 2θ= 7.7°, 15.56°, 17.58°, 27°, and 27.29°. The new phase was confirmed by new peaks found in PGA (2:1) patterns in which the most intense are positioned at 2θ= 10°, 16.55°, 20.36°, 25.23°and 29.83°, thus confirming the co-crystal **PGA (2:1)**. The PXRD pattern generated from PZA-GA physical mixture is characterised by a summation of diffraction peaks from individual co-formers (**Figure 6.28**).

6.3.3.5 PGA Samples characterisation by solid-state NMR

In solid-state nuclear magnetic resonance (SS-NMR) as well as solution NMR, changes such as splitting and shifting in the local electronic environment are conclusive evidence on change in the molecular structure of a compound. Co-crystallisation, due to the formation of intermolecular H-bonds leads to such changes. To identify changes in local chemical environment Cross Polarizing (CP) Magic Angle Spin (MAS) ^{13}C SS-NMR experiments were carried. Shifting or splitting detected was seen as an indication of a successful complexation/co-crystallisation. Pure PZA and GA were referred to in order to assign PGA (2:1) co-crystal. GA was assigned based on previous experiments (Vigilante & Mehta, 2017). Isotropic chemical shifts were detected in the comparative spectral representation (**Figure 6.29**)

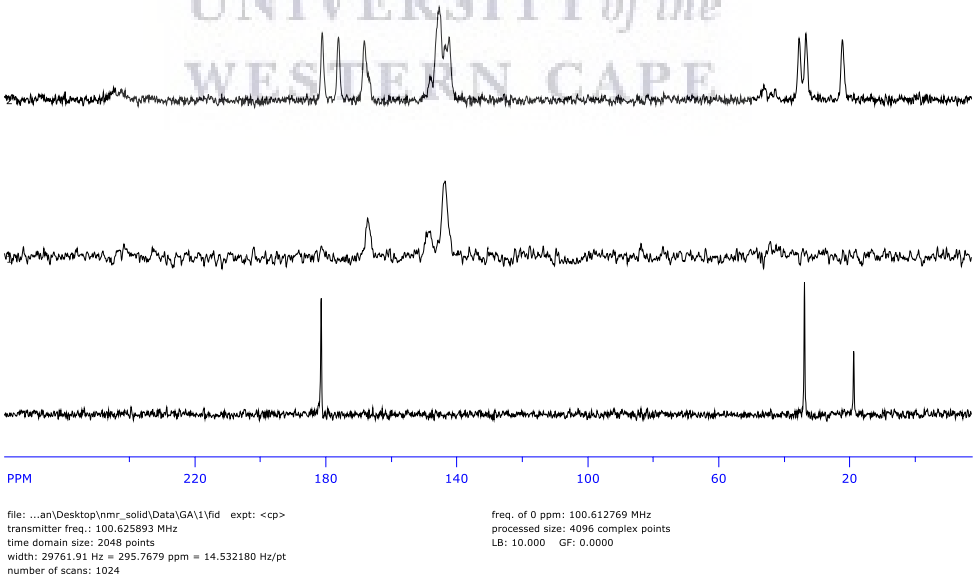

Figure 6.29: 13C CP MAS SSNMR chemical shifting of GA (bottom), PZA (middle) vs PGA (2:1) co-crystal (top)

6.3.3.6 Solubility evaluation of PGA co-crystal

Excess amounts of untreated PZA and PGA (2:1) co-crystal were added to USP aqueous buffer solutions at pH 1.2 (0.1M hydrochloric acid), 0.2M potassium phosphate buffer pH 6.8 and pH 7.4, and deionized water (18.s MΩ). The mixtures were continuously shaken in an incubator shaker at 37 °C (± 0.5°C) and 100 rpm for 24 hours. Samples were filtered using 0.20 μm PVDF syringe filters and analysed using an HPLC.

An Agilent HPLC system setting with FXBPump (Flexar Binary Pump), an automated injector equipped with a UV detector (LC 200a Series PDA Detector), and a Flexar autosampler was used to quantify PZA in the samples. Isocratic elution using acetonitrile solution (30:70) was applied at a 10 mL/min flow rate. A reversed-phase Luna C_{18} HPLC column 250 mm x 4.6 mm, 5μm was used. Injection volume was 10 µL, and absorbance of elution was recorded at 262 and 270 nm following suitable dilutions.

PZA indicated a significant increase in solubility by 1.3-fold at acidic pH=1.2 (0.1 M Hydrochloric acid), 2-fold at pH=5.8 and 1.5-fold at pH=7.4 (potassium phosphate buffer) and 1.23-fold in unbuffered aqueous solution (deionised) (**Figure 6.30**). Despite an increase in PGA (2:1) co-crystal solubility in aqueous solution, the co-crystal showed a slight decrease in solubility at acidic medium pH 1.2 (0.1M HCl).

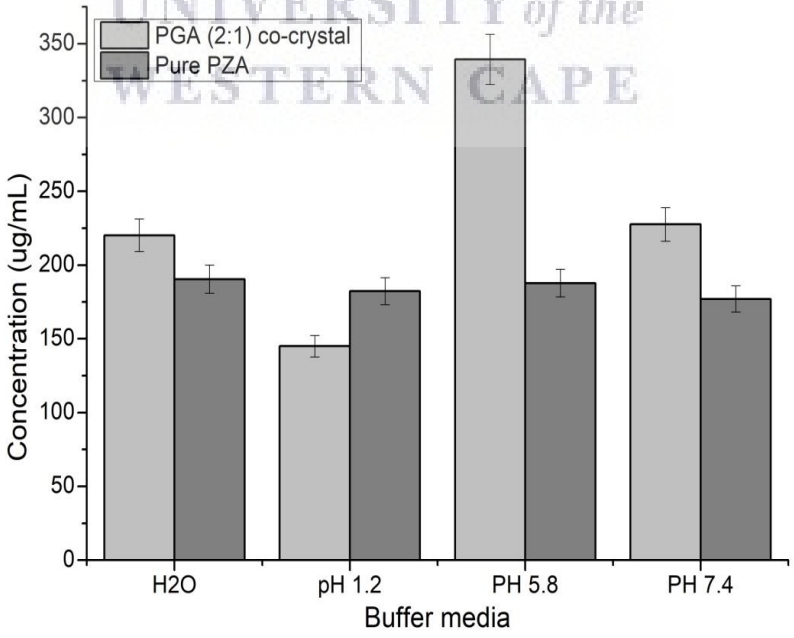

Figure 6.30: Solubility histogram comparing untreated PZA to the co-crystal PGA (2:1) in different buffered solution and deionised water

6.3.3.7 In *vitro* antimicrobial evaluation for PGA (2:1) co-crystal

The *in vitro* antibacterial activity of the co-crystal was assessed by the tube dilution method against both *Mycobacterium tuberculosis* (Mtb) H37Rv (ATCC 27294) and pan-susceptible clinical isolate strains. Pyrazinamide was used as a standard antimycobacterial drug.

The MGIT 960 with Epicentre software and the TB eXiST (TB Extended Susceptibility Testing) module was used to determine the MIC of PGA (2:1) co-crystal against a H37Rv and a pan-susceptible *Mycobacterium tuberculosis* clinical isolate. Both strains were exposed to the compound at final concentrations of 100, 10 and 1.0 µg/mL. MIC results were interpreted according to the 1% proportion method known as the lowest drug concentration that inhibits ≥99.0% of the bacterial population.

Based on the results presented in **Table 6.8**, the co-crystal PGA (2:1) showed no anti-TB activity against all strains. PZA was included as controls and should be susceptible at 100µg/mL.

It is worth noting that the same amount of standard and the co-crystal was used and the co-crystal PGA (2:1) contains equilibrium of PZA and the co-former GA. Therefore, it is safe to say that less amount of PZA was used which may have contributed to negative MIC results obtained. Addition tests are to be conducted at smaller different concentration range to verify the exact MICs.

Table 6.8: MIC of PGA (2:1) co-crystal against M tuberculosis

Compound	**Minimum Inhibitory Concentration (MIC) µg/ml**	
	H37Rv (ATCC27294)	***M tuberculosis* Clinical Strain**
PZA (Control) PGA (2:1) co-crystal	<100 >100	<100 >100

6.4 Conclusion

In total, four multi-component solid forms were produced; of which, three of them were confirmed co-crystals. These are INHPZA2; a dual API solvated co-crystal between INH and PZA, INHGA (2:1); a co-crystal of INH with glutaric acid (GA) and PGA (2:1); a co-crystal of PZA with GA. INHPZA1 was confirmed as a binary eutectic mixture similarly to early work by Cherukuvada and Nangia, 2012. While INHPZA2 was produced from solvent evaporation, using ethanol or isopropanol as solvents, co-crystals INHGA (2:1) and PGA (2:1) were successfully prepared using co-grinding; a

simple, safe and cost-effective method. Characterisation established different properties of each novel supramolecular adduct produced.

Solubility studies conducted divulged an enhanced solubility of both drugs in their respective co-crystals, at different pH environments. INH is known to be highly soluble in water and also known for its instability when exposed to light or other compounds. The drug interaction is a known phenomenon between INH and RIF in the dose and other APIs, resulting in serious adverse effects (Cherukuvada & Nangia, 2012). The co-crystal formation is known to stabilize unstable drugs. Therefore, a reduced solubility of the co-crystal INHGA (2:1) in aqueous medium has been remarked and was likely caused by increased stability by hydrogen bonding with GA or possible degradation of INH during solubility experiments. Solubility studies also suggested enhanced solubility of PZA in the PGA (2:1) sample and both INH and PZA in INHPZA1 at different pH environments.

Solid forms INHPZA1, INHPZA2, INHGA (2:1) showed inhibitory activity comparable to that of INH. It is worth noting that the initial amount of APIs in these solid forms is less than that of the control. This suggested the contribution of enhanced solubility to the bioavailability of these solid forms. PGA (2:1) showed no activity at the used dilution. It is, however; worth noting that the PZA content in the co-crystal is less than the amount of the control use. Therefore, further testing at lower concentration is recommended in order to understand the exact MIC for each co-crystal sample.

Chapter 7 Conclusions and future works

This chapter provides the concluding remarks on the work presented in this thesis and provides recommendations on future work.

7.1 Concluding remarks

HIV/AIDS and TB infections are still threatening the global population. Even though so much improvement has been achieved over the years, the battle is far from over. The appearance of drug-resistant strains affects standard treatment strategies, rendering addition complications such as longer treatment courses and hospitalisation. The study was undertaken to investigate the possible combinations of selected antiretroviral and anti-tubercular drugs for enhanced physicochemical properties, biological activity, pharmacokinetics, and drug resistance management by developing more efficient, cost-effective and patient-friendly treatment courses. To do so, selected APIs were subjected to the co-crystal screening process using different methods under various environmental conditions.

The co-crystal formation provides a great opportunity to fine-tune properties of active pharmaceutical ingredients (APIs), therefore offering products with better therapeutic effects. However, a successful co-crystal formation requires a proper choice of the right co-crystal former compatible with an API, usually selected from Generally Regarded as Safe drugs list of the US-FDA. Even with the current advances in technology for predicting interaction in self-assembly supramolecular systems, a tactless approach involving different trials remains the only strategy used to ensure a triumph.

The formation of dual drug co-crystals enhances the physicochemical properties of either one or both drug components in question and provides synergistic effects. The development of such hybrids would reduce the amount of bulk material used during the manufacturing process (cost-effect) and would increase the patient's compliance with the cure and reduced appearance of drug resistance accordingly.

A failed co-crystal formation does not necessarily define the end of research but opens the door to other interesting discoveries. As discussed in section 2.5.1, co-crystallisation does not always lead to the desired co-crystal. Solid forms such as amorphous, solid dispersions, hydrates are among essential by-products of the co-crystallisation that can sometimes offer as many benefits as the co-crystal counterpart.

7.1.1 Remarks on non-covalent synthetic methods used for multicomponent solid forms preparation

Generally, the synthetic methods used in this work were conventional mechanochemistry during which solid-state grinding (SSG) and liquid assisted grinding (LAG) techniques were applied. Slurry, as well as solvent evaporation techniques, were also used in the attempt to produce desired co-crystals of selected APIs.

Several drug-drug combinations have been non-covalently prepared, of which, some have been confirmed as dual-API co-crystals, others eutectic binary mixtures or solid dispersions of selected antiretroviral, anti-TB drugs, 1-adamantylamine that was included due to its antiviral activity and glutaric acid used as a co-crystal former in a variety of available co-crystals.

Even though different methods were used to screen for co-crystals, most of the multicomponent adducts resulted from mechanochemical reactions by solid-state or liquid assisted co-grinding techniques. This is because, due to the type of APIs being co-crystallised and large solubility differences of APIs combined during this study, the solution crystallization approach failed to produce the desired co-crystals in most of the cases. Instead, the experiments resulted in either one API, a mixture of both or nothing at all.

Compared to other solution co-crystallisation methods such as solvent evaporation, vapour diffusion, etc., mechanochemistry has proven to be the cost-effective, rapid and promising preparative method of multicomponent systems. Unfortunately, the method suffers from its inability to produce crystals for single X-ray diffraction, making structure elucidation difficult or even impossible in many cases.

7.1.2 Physicochemical characterisation remarks

Each co-crystallisation outcome was subjected to a full characterization using a series of the analytical techniques such DSC, HSM, TGA, FTIR, and PXRD, and (in some cases) with solid-state NMR and confirmed a successful formation of the co-crystals as well as eutectic mixtures (in cases of a failed co-crystallisation).

Thermal analytical techniques such as HSM, DSC, and TGA were quite useful in confirming the samples' thermal behaviours such as glass/polymorphic transitions, crystallisation, recrystallisation, melting, decomposition and assessing the possibility of any entrapped molecular substances. Compared to the starting materials, the new

chemical hybrids behaved thermodynamically differently. Accordingly, DSC was quite useful in the early detection of co-crystallisation outcomes.

Structural information and intermolecular interaction in the multicomponent hybrids were generated by FTIR/FT-Near spectroscopy. On the other hand, the powder X-ray diffraction and solid-state NMR (in some cases) revealed the successful formation of intermolecular interactions and helped decide and draw the conclusion on the type of multicomponent prepared. Scanning electron microscope enabled a complete evaluation of the samples morphological properties, identifying differences in terms of shapes and sizes across the range of adducts formed and suggest the reason for altered properties accordingly.

In vitro solubility evaluation compared the concentrations of untreated APIs to the formed supramolecular complexes. An enhanced solubility was suggested according to the data collected.

Besides enhancing aqueous solubilities, cocrystals have the ability to fine-tune solubility advantage over drug, supersaturation index, and bioavailability. This study presents a few of the important facts about cocrystals that sets them apart from other solid-state forms of drugs. It is well known that a quantitative set of rules for the selection of additives and solution/formulation conditions that predict cocrystal solubility, supersaturation index, and transition points exist. Cocrystal eutectic constants are shown to be the most important cocrystal property that can be measured once a cocrystal is discovered. Simple relationships can be presented that allow for the prediction of cocrystal behavior as a function of pH and drug solubilizing agents. Cocrystal eutectic constants is a stability or supersatuation index that reflects how close or far from equilibrium a cocrystal is, it establishes transition points, and it can provide a quantitative scale of cocrystal true solubility changes over the drug. The benefit of this strategy is that a single measurement, that requires little material and time, provides a principled basis to tailor cocrystal supersaturation index by the rational selection of cocrystal formulation, dissolution, and processing conditions. Given the multitude of co-crystals and possible eutectic mixtures formed, the scope of this study did not explore all of these relationships simultaneously, however subsequent publications are exploring each of the behaviours in relation to the drug.

7.1.3 Chapters overview

Chapter 1 gives a brief history of discovery and progress made in finding better treatment of HIV and TB. The chapter also identified issues encountered with the current treatment strategies and suggest alternative, more effective methods. The aims and objectives of this work are also described towards the end of the chapter.

Chapter 2 gives a literature review on co-crystallization; the proposed method of the alternative drug combination. In this chapter, the co-crystal design, development, and preparatory methods are briefly explained. A complete process from co-crystal former selection to the manufacturing of the co-crystal is given through the co-crystal development pathway suggested by Duggirala *et al.*, (2016). Furthermore, the chapter introduces dual-API co-crystals, their impact and benefits of their introduction in the pharmaceutical industry as a way of combining APIs in a single dose while improving their physicochemical properties, alternatively to fixed-dose combinations and old drug combinations known as a "cocktail". The chapter also gives a few examples of such hybrids currently available in the literature.

Chapter 3 introduces selected APIs. The chapter describes properties of the APIs including their scientific (IUPAC) names, known biological/pharmacological activity against either HIV/AIDS or tuberculosis, mechanisms of action, the co-crystal forming ability from previous literature. The chapter also explores different synthetic methods used in the production of the co-crystals and various analytical methods/instruments used to characterise co-crystals from thermal analyses using the HSM, DSC, TGA, morphology studies using SEM and the structural investigation using FTIR to sample identification using PXRD and, in some cases, the solid-state NMR. The quantification method by the HPLC through *in vitro* solubility evaluations is also presented in this chapter.

Due to pharmacological uses of selected API candidates, the results and discussion party of this thesis was divided into three chapters. Each of these chapters explores the screening/preparation procedures for the co-crystals and other solid hybrids, preparatory methods and full physicochemical characterisation of the sample produced. Results from different API-API/co-former combinations and their discussions as well as conclusions are presented.

Chapter 4 encompasses different solid crystalline hybrids produced from different combinations of HIV reverse transcriptase inhibitors (RTIs). Preparation procedures

and all characterization analyses have been reported with details. The discussion of results from each sample was given accordingly.

Overall, eight multicomponent hybrids were non-covalently synthesised. Of which five were confirmed co-crystals successfully produced by solid-state and liquid assisted grinding and solvent evaporation techniques. These include efavirenz-zidovudine co-crystal (**EFZA**), nevirapine-efavirenz co-crystal (**NEF**), two co-crystal forms of nevirapine-zidovudine (**NVZA2** and **NVZA3**), and a co-crystal form of efavirenz-lamivudine (**EL2**). Binary eutectic mixtures; lamivudine-zidovudine (**LMZT**), nevirapine-zidovudine (**NVZA1**), efavirenz-lamivudine (**EL1**), nevirapine-lamivudine (**NL**) were also confirmed.

Chapter 5 covers the preparation and characterisation of different multicomponent solid forms produced from a selected number of antiretroviral and anti-TB drugs and 1-adamantylamine. These include efavirenz-isoniazid co-crystal (**EFINH**), a co-amorphous solid form of EFV and amantadine (**EFAD**), binary eutectics isoniazid-zidovudine (**INHZA**), zidovudine-pyrazinamide (**AZTPZA**) and lamivudine-isoniazid (**LMISO**).

Chapter 6 reports the preparation, characterisation, results and discussion of four multicomponent hybrids of selected drug members of first-line anti-tubercular drugs isoniazid and pyrazinamide. Three of these solid derivative forms, were confirmed co-crystals namely **INHPZA2**; a dual-API solvated co-crystal between INH and PZA, **INHGA (2:1);** a co-crystal of INH with glutaric acid (GA) and **PGA (2:1)** a co-crystal of PZA with GA. **INHPZA1** was confirmed as a eutectic binary mixture. While **INHPZA2** co-crystal solvate was produced from solvent evaporation, using ethanol or isopropanol as solvents, co-crystals **INHGA (2:1)** and **PGA (2:1)** were successfully prepared using co-grinding; a simple, safe and cost-effective method.

All derivative multicomponent solid forms outlined herein were confirmed thermally by the hot stage microscopy (HSM), differential scanning calorimetry (DSC) and thermogravimetric analysis (TGA), and structurally by the Fourier transform infrared spectroscopy (FTIR) and the powder X-ray diffraction (PXRD) and in some cases by solid-state NMR. Physically, new particle morphologies were confirmed by the scanning electron microscope (SEM). Lastly, all multicomponent supramolecular adducts produced, have demonstrated a significant increase in solubility in different buffered solutions.

7.2 Future works

Regrettably, due to limited resources and other inconveniences, including the current pandemic, some of the objectives set at the beginning of the project, were not achieved, and some experiments were interrupted. Therefore, studies such as biological activity and dissolution studies are recommended. It is also important to point out that regardless of the known activity of the APIs used, cytotoxicity, permeability studies should be carried out before formulation decision. Furthermore, stability (physical or chemical) studies are also recommended for all multicomponent hybrids produced.

References

Aakeröy, C. B., & Salmon, D. J. (2005). Building co-crystals with molecular sense and supramolecular sensibility. *CrystEngComm*, *7*, 439–448. https://doi.org/10.1039/b505883j

Aakeröy, C. B., & Sinha, A. S. (2018). Co-crystals: Introduction and Scope. In C. B. Aakeröy & A. S. Sinha (Eds.), *Co-crystals: Preparation, Characterization and Applications* (pp. 1–32). Royal Society of Chemistry.

Abd-Elghany, M., & Klapötke, T. M. (2018). A review on differential scanning calorimetry technique and its importance in the field of energetic materials. *Physical Sciences Reviews*, *3*(4). https://doi.org/10.1515/psr-2017-0103

Abdul, S., & Poddar, S. S. (2004). A flexible technology for modified release of drugs: multi layered tablets. *Journal of Controlled Release*, *97*(3), 393–405. https://doi.org/10.1016/j.jconrel.2004.03.034

Abidi, S. S. A., Azim, Y., Gupta, A. K., & Pradeep, C. P. (2017). Mechanochemical synthesis and structural characterization of three novel cocrystals of dimethylglyoxime with N-heterocyclic aromatic compounds and acetamide. *Journal of Molecular Structure*, *1150*, 103–111. https://doi.org/10.1016/j.molstruc.2017.08.080

Abourahma, H., Cocuzza, D. S., Melendez, J., & Urban, J. M. (2011). Pyrazinamide cocrystals and the search for polymorphs. *CrystEngComm*, *13*(21), 6442–6450. https://doi.org/10.1039/c1ce05598d

Aher, S., Dhumal, R., Mahadik, K., Ketolainen, J., & Paradkar, A. (2013). Effect of cocrystallization techniques on compressional properties of caffeine/oxalic acid 2: 1 cocrystal. *Pharmaceutical Development and Technology*, *18*(1), 55–60. https://doi.org/10.3109/10837450.2011.618950

Aitipamula, S., Chow, P. S., & Tan, R. B. H. (2009). Trimorphs of a pharmaceutical cocrystal involving two active pharmaceutical ingredients: potential relevance to combination drugs. *CrystEngComm*, *11*(9), 1823–1827. https://doi.org/10.1039/b904616j

References

Aitipamula, S., Chow, P. S., & Tan, R. B. H. (2014). Polymorphism in cocrystals: A review and assessment of its significance. *CrystEngComm*, *16*(17), 3451–3465. https://doi.org/10.1039/c3ce42008f

Aitipamula, S., Wong, A. B. H., Chow, P. S., & Tan, R. B. H. (2013). Novel solid forms of the anti-tuberculosis drug, Isoniazid: Ternary and polymorphic cocrystals. *CrystEngComm*, *15*(29), 5877–5887. https://doi.org/10.1039/c3ce40729b

Al-Zakwani, I., Zubaid, M., Panduranga, P., Rashed, W., Sulaiman, K., Almahmeed, W., Al-Motarreb, A., Al Suwaidi, J., & Amin, H. (2011). Medication use pattern and predictors of optimal therapy at discharge in 8176 patients with acute coronary syndrome from 6 Middle Eastern countries: data from the gulf registry of acute coronary events. *Angiology*, *62*(6), 447–454. https://doi.org/10.1177/0003319710394163

Albrecht, M. (2007). Supramolecular chemistry—general principles and selected examples from anion recognition and metallosupramolecular chemistry. *Naturwissenschaften*, *94*, 951–966. https://doi.org/10.1007/s00114-007-0282-7

Alhalaweh, A., Kaialy, W., Buckton, G., Gill, H., Nokhodchi, A., & Velaga, S. P. (2013). Theophylline cocrystals prepared by spray drying: Physicochemical properties and aerosolization performance. *AAPS PharmSciTech*, *14*(1), 265–276. https://doi.org/10.1208/s12249-012-9883-3

Alhalaweh, A., & Velaga, S. P. (2010). Formation of cocrystals from stoichiometric solutions of incongruently saturating systems by spray drying. *Crystal Growth and Design*, *10*(8), 3302–3305. https://doi.org/10.1021/cg100451q

Ali, H. R. H., Alhalaweh, A., Mendes, N. F. C., Ribeiro-Claro, P., & Velaga, S. P. (2012). Solid-state vibrational spectroscopic investigation of cocrystals and salt of indomethacin. *CrystEngComm*, *14*(20), 6665–6674. https://doi.org/10.1039/c2ce25801c

Am Ende, D. J., Anderson, S. R., & Salan, J. S. (2014). Development and scale-up of cocrystals using resonant acoustic mixing. *Organic Process Research and Development*, *18*(2), 331–341. https://doi.org/10.1021/op4003399

References

Ammaranond, P., & Sanguansittianan, S. (2012). Mechanism of HIV antiretroviral drugs progress toward drug resistance. *Fundamental & Clinical Pharmacology*, *26*(1), 146–161. https://doi.org/10.1111/j.1472-8206.2011.01009.x

Ancheria, R. K., Jain, S., Kumar, D., Soni, S. L., & Sharma, M. (2019). An Overview of Pharmaceutical Co-Crystal. *Asian Journal of Pharmaceutical Research and Development*, *7*(2), 39–46. https://doi.org/10.22270/ajprd.v7i2.483

Andrade, C. H., de Freitas, L. M., & de Oliveira, V. (2011). Twenty-six years of HIV science: An overview of anti-HIV drugs metabolism. *Brazilian Journal of Pharmaceutical Sciences*, *47*(209–230). https://doi.org/10.1590/S1984-82502011000200003

Andree, S. N. L., Sinha, A. S., & Aaker y, C. B. (2018). Structural examination of halogen-bonded co-crystals of tritopic acceptors. *Molecules*, *23*(1), 163. https://doi.org/10.3390/molecules23010163

Anil Kumar Kruthiventi, Saikat Roy, Rajesh Goud, Iqbal Javed, Ashwini Nangia, J. S. R. (2009). *Synergistic pharmaceutical cocrystals* (Patent No. WO 2009/136408 Al).

Araújo, A. A. S., Bezerra, M. dos S., Storpirtis, S., & Matos, J. do R. (2010). Determination of the melting temperature, heat of fusion, and purity analysis of different samples of zidovudine (AZT) using DSC. *Brazilian Journal of Pharmaceutical Sciences*, *46*(1), 37–43. https://doi.org/10.1590/S1984-82502010000100005

Arnold, E., Das, K., Ding, J., Yadav, P. N., Hsiou, Y., Boyer, P. L., & Hughes, S. H. (1996). Targeting HIV reverse transcriptase for anti-AIDS drug design: structural and biological considerations for chemotherapeutic strategies. *Drug Design and Discovery*, *13*(3–4), 29–47.

Arunan, E., Desiraju, G. R., Klein, R. A., Sadlej, J., Scheiner, S., Alkorta, I., Clary, D. C., Crabtree, R. H., Dannenber, J. J., Hobza, P., Kjaergaard, H. G., Legon, A. C., Mennucci, B., & Nesbitt, D. J. (2011). Definition of the hydrogen bond (IUPAC Recommendations 2011). *Pure and Applied Chemistry*, *83*(8), 1637–1941. https://doi.org/10.1351/PAC-REC-10-01-02

References

Asija, R., Sharma, R., & Gupta, A. (2013). Emulgel: A novel approach to topical drug delivery. *Journal of Biomedical and Pharmaceutical Research*, *2*(6), 91–94. http://localhost:80/xmlui/handle/123456789/168

Atta, M. G., De Seigneux, S., & Lucas, G. M. (2019). Clinical pharmacology in HIV therapy. *Clinical Journal of the American Society of Nephrology*, *14*(3), 435–444. https://doi.org/10.2215/CJN.02240218

Babu, N. J., & Nangia, A. (2011). Solubility advantage of amorphous drugs and pharmaceutical cocrystals. *Crystal Growth & Design*, *11*(7), 2662–2679. https://doi.org/10.1021/cg200492w

Babu, N. J., Reddy, L. S., Aitipamula, S., & Nangia, A. (2008). Polymorphs and polymorphic cocrystals of temozolomide. *Chemistry - An Asian Journal*, *3*(7), 1122–1133. https://doi.org/10.1002/asia.200800070

Baddeley, A; Dean, A; Monica-Dias, H; Falzon, D; Floyd, K; Garcia, I. et al. (2013). Global Tuberculosis Report 2013. *World Health Organization*. https://doi.org/10.3917/spub.092.0139

Balkenhohl, F., von dem Bussche-Hünnefeld, C., Lansky, A., & Zechel, C. (1996). Combinatorial synthesis of small organic molecules. *Angewandte Chemie International Edition in English*, *35*(20), 2288–2337. https://doi.org/10.1002/anie.199622881

Bangalore, S., Kamalakkannan, G., Parkar, S., & Messerli, F. H. (2007). Fixed-dose combinations improve medication compliance: a meta-analysis. *The American Journal of Medicine*, *120*(8), 713–719. https://doi.org/10.1016/j.amjmed.2006.08.033

Bannister, W. P., Cozzi-Lepri, A., Clotet, B., Mocroft, A., Kjær, J., Reiss, P., von Wyl, V., Lazzarin, A., Katlama, C., Phillips, A. N., & others. (2008). Transmitted drug resistant HIV-1 and association with virologic and CD4 cell count response to combination antiretroviral therapy in the EuroSIDA Study. *JAIDS Journal of Acquired Immune Deficiency Syndromes*, *48*(3), 324–333. https://doi.org/10.1097/QAI.0b013e31817ae5c0

Bansal, R., Guleria, A., & Acharya, P. C. (2013). FT-IR method development and

validation for quantitative estimation of zidovudine in bulk and tablet dosage form. *Drug Research*, *63*(04), 165–170. https://doi.org/10.1055/s-0032-1333297

Barré-Sinoussi, F., Chermann, J.-C., Rey, F., Nugeyre, M. T., Chamaret, S., Gruest, J., Dauguet, C., Axler-Blin, C., Vézinet-Brun, F., Rouzioux, C., & others. (1983). Isolation of a T-lymphotropic retrovirus from a patient at risk for acquired immune deficiency syndrome (AIDS). *Science*, *220*(4599), 868–871. issn: 00348376

Bavishi, D. D., & Borkhataria, C. H. (2016). Spring and parachute: How cocrystals enhance solubility. *Progress in Crystal Growth and Characterization of Materials*. https://doi.org/10.1016/j.pcrysgrow.2016.07.001

Bell, L. C. K., & Noursadeghi, M. (2018). Pathogenesis of HIV-1 and mycobacterium tuberculosis co-infection. *Nature Reviews Microbiology*, *16*(2), 80–90. https://doi.org/10.1038/nrmicro.2017.128

Bethune, S. J., Huang, N., Jayasankar, A., & Rodríguez-Hornedo, N. (2009). Understanding and predicting the effect of cocrystal components and pH on cocrystal solubility. *Crystal Growth and Design*, *9*(9), 3976–3988. https://doi.org/10.1021/cg9001187

Bethune, S. J., Schultheiss, N., & Henck, J.-O. (2011). Improving the poor aqueous solubility of nutraceutical compound pterostilbene through cocrystal formation. *Crystal Growth & Design*, *11*(7), 2817–2823. https://doi.org/10.1021/cg1016092

Bhatt, P. M., Azim, Y., Thakur, T. S., & Desiraju, G. R. (2008). Co-crystals of the anti-HIV drugs lamivudine and zidovudine. *Crystal Growth and Design*, *9*(2), 951–957. https://doi.org/10.1021/cg1016092

Bhatt, P. M., Azim, Y., Thakur, T. S., & Desiraju, G. R. (2009a). Co-crystals of the anti-HIV drugs lamivudine and zidovudine. *Crystal Growth and Design*, *9*(2), 951–957. https://doi.org/10.1021/cg8007359

Bhatt, P. M., Azim, Y., Thakur, T. S., & Desiraju, G. R. (2009b). Co-crystals of the anti-HIV drugs lamivudine and zidovudine. *Crystal Growth and Design*, *9*(2), 951–957. https://doi.org/10.1021/cg8007359

Bhatt, P. M., Azim, Y., Thakur, T. S., & Desiraju, G. R. (2009c). Co-crystals of the anti-HIV drugs lamivudine and zidovudine. *Crystal Growth and Design*, *9*(2), 951–957. https://doi.org/10.1021/cg1016092

Bhattacharya, S., Peraka, K. S., & Zaworotko, M. J. (2018). Chapter 2: The Role of Hydrogen Bonding in Co-crystals. In *Monographs in Supramolecular Chemistry* (Vols. 2018-January, Issue 24, pp. 33–79). Royal Society of Chemistry. https://doi.org/10.1039/9781788012874-00033

Bhutani, H., Singh, S., Jindal, K. C., & Chakraborti, A. K. (2005). Mechanistic explanation to the catalysis by pyrazinamide and ethambutol of reaction between rifampicin and isoniazid in anti-TB FDCs. *Journal of Pharmaceutical and Biomedical Analysis*, *39*(5), 892–899. https://doi.org/10.1016/j.jpba.2005.05.015

Bisht, R., Katiyar, A., Singh, R., & Mittal, P. (2009). Antibiotic resistance-A global issue of concern. *Asian Journal of Pharmaceutical and Clinical Research*, *2*(2), 34–39. issn: 09742441

Blázquez, A. B., Martín-Acebes, M. A., & Saiz, J. C. (2016). Inhibition of West Nile virus multiplication in cell culture by anti-parkinsonian drugs. *Frontiers in Microbiology*, *7*, 296. https://doi.org/10.3389/fmicb.2016.00296

Blomberg, B., Spinaci, S., Fourie, B., & Laing, R. (2001). The rationale for recommending fixed-dose combination tablets for treatment of tuberculosis. *Bulletin of the World Health Organization*, *79*(1), 61–68. https://doi.org/10.1590/S0042-96862001000100012

Bobat, R., & Archary, M. (2017). HIV infection. In *Viral Infections in Children* (Vol. 1, pp. 69–100). Springer International Publishing. https://doi.org/10.1007/978-3-319-54033-7_3

Bolla, G., Sanphui, P., & Nangia, A. (2013). Solubility advantage of tenoxicam phenolic cocrystals compared to salts. *Crystal Growth & Design*, *13*(5), 1988–2003. https://doi.org/10.1021/cg4000457

Booth, C. L., & Geretti, A. M. (2007). Prevalence and determinants of transmitted antiretroviral drug resistance in HIV-1 infection. *Journal of Antimicrobial Chemotherapy*, *59*(6), 1047–1056. https://doi.org/10.1021/cg4000457

References

Boothroyd, S., Kerridge, A., Broo, A., Buttar, D., & Anwar, J. (2018). Why Do Some Molecules Form Hydrates or Solvates? *Crystal Growth and Design*, *18*(3), 1903–1908. https://doi.org/10.1021/acs.cgd.8b00160

Boyer, P. L., Das, K., Arnold, E., & Hughes, S. H. (2015). *Analysis of the Zidovudine Resistance Mutations T215Y, M41L, and L210W in HIV-1 Reverse Transcriptase*. *59*(12), 7184–7196. https://doi.org/10.1128/AAC.05069-14

Braga, D., Grepioni, F., & Maini, L. (2010). The growing world of crystal forms. In *Chemical Communications* (Vol. 46, Issue 34, pp. 6232–6242). Royal Society of Chemistry. https://doi.org/10.1039/c0cc01195a

Braga, D., Maini, L., & Grepioni, F. (2013). Mechanochemical preparation of co-crystals. *Chemical Society Reviews*, *42*(18), 7638–7648. https://doi.org/10.1039/c3cs60014a

Brittain, H. G., & Felice, P. V. (n.d.). Intravenous formulation with water-soluble co-crystals of acetylsalicylic acid and theanine. 2010. In *United States Patent Application US/2010-0286099*.

Bruni, G., Maietta, M., Maggi, L., Mustarelli, P., Ferrara, C., Berbenni, V., Milanese, C., Girella, A., & Marini, A. (2013). Preparation and physicochemical characterization of acyclovir cocrystals with improved dissolution properties. *Journal of Pharmaceutical Sciences*, *102*(11), 4079–4086. https://doi.org/10.1002/jps.23721

Bucar, D.-K., Henry, R. F., Zhang, G. G. Z., & MacGillivray, L. R. (2014). Synthon hierarchies in crystal forms composed of theophylline and hydroxybenzoic acids: cocrystal screening via solution-mediated phase transformation. *Crystal Growth & Design*, *14*(10), 5318–5328. https://doi.org/10.1021/cg501204k

Buchacz, K., Baker, R. K., Palella Jr, F. J., Chmiel, J. S., Lichtenstein, K. A., Novak, R. M., Wood, K. C., Brooks, J. T., Investigators, H., & others. (2010). AIDS-defining opportunistic illnesses in US patients, 1994--2007: a cohort study. *Aids*, *24*(10), 1549–1559. https://doi.org/10.1097/QAD.0b013e32833a3967

Byrn, S. R., Zografi, G., & Chen, X. S. (2017). Solvates and Hydrates. In *Solid State Properties of Pharmaceutical Materials* (pp. 38–47). John Wiley &

Sons, Inc. https://doi.org/10.1002/9781119264408.ch3

Caira, M. R., Bourne, S. A., Samsodien, H., Engel, E., Liebenberg, W., Stieger, N., & Aucamp, M. (2012). Co-crystals of the antiretroviral nevirapine: crystal structures, thermal analysis and dissolution behaviour. *CrystEngComm*, *14*(7), 2541–2551. https://doi.org/10.1039/c2ce06507j

Calzolari, D., Bruschi, S., Coquin, L., Schofield, J., Feala, J. D., Reed, J. C., McCulloch, A. D., & Paternostro, G. (2008). Search algorithms as a framework for the optimization of drug combinations. *PLoS Comput Biol*, *4*(12), e1000249. https://doi.org/10.1371/journal.pcbi.1000249

Capriotti, T. (2018). HIV/AIDS. *Home Healthcare Now*, *36*(6), 348–355. https://doi.org/10.1097/NHH.0000000000000706

CDC. (2003). Morbidity and Mortality Weekly Report Treatment of Tuberculosis American Thoracic Society , CDC , and Infectious Diseases Society of America Centers for Disease Control and Prevention. *CDC*, *52*. https://www.cdc.gov/mmwr/preview/mmwrhtml/rr5211a1.htm

Chadha, R., Arora, P., & Bhandari, S. (2012). Polymorphic forms of lamivudine: characterization, estimation of transition temperature, and stability studies by thermodynamic and spectroscopic studies. *ISRN Thermodynamics*, *2012*(ID 671027), 8 pages. https://doi.org/10.5402/2012/671027

Chadha, R., Arora, P., Saini, A., & Jain, D. S. (2010a). Solvated crystalline forms of nevirapine: thermoanalytical and spectroscopic studies. *AAPS PharmSciTech*, *11*(3), 1328–1339. https://doi.org/10.1208/s12249-010-9511-z

Chadha, R., Arora, P., Saini, A., & Jain, D. S. (2010b). Solvated crystalline forms of nevirapine: Thermoanalytical and spectroscopic studies. *AAPS PharmSciTech*, *11*(3), 1328–1339. https://doi.org/10.1208/s12249-010-9511-z

Chadha, R., Saini, A., Arora, P., & Bhandari, S. (2012). Crystal Forms of Anti-HIV Drugs: Role of Recrystallization. In *Recrystallization* (pp. 448–463). INTECH Open Access Publisher. https://doi.org/10.5772/33777

Chavan, R. B., Thipparaboina, R., Yadav, B., & Shastri, N. R. (2018). Continuous

manufacturing of co-crystals: challenges and prospects. *Drug Delivery and Translational Research*, *8*(6), 1726–1739. https://doi.org/10.1007/s13346-018-0479-7

Cheney, M. L., Weyna, D. R., Shan, N., Hanna, M., Wojtas, L., & Zaworotko, M. J. (2011). Coformer selection in pharmaceutical cocrystal development: a case study of a meloxicam aspirin cocrystal that exhibits enhanced solubility and pharmacokinetics. *Journal of Pharmaceutical Sciences*, *100*(6), 2172–2181. https://doi.org/10.1002/jps.22434

Cherukuvada, S., Kaur, R., & Guru Row, T. N. (2016). Co-crystallization and small molecule crystal form diversity: From pharmaceutical to materials applications. *CrystEngComm*, *18*(44), 8528–8555. https://doi.org/10.1039/c6ce01835a

Cherukuvada, S., & Nangia, A. (2012). Fast dissolving eutectic compositions of two anti-tubercular drugs. *CrystEngComm*, *14*(7), 2579–2588. https://doi.org/10.1039/c2ce06391c

Cherukuvada, S., & Nangia, A. (2014). Eutectics as improved pharmaceutical materials: Design, properties and characterization. *Chemical Communications*, *50*(8), 906–923. https://doi.org/10.1039/c3cc47521b

Childs, S. L., Stahly, G. P., & Park, A. (2007). The salt- cocrystal continuum: the influence of crystal structure on ionization state. *Molecular Pharmaceutics*, *4*(3), 323–338. https://doi.org/10.1021/mp0601345

Chiş, V., Pîrnău, A., Jurcă, T., Vasilescu, M., Simon, S., Cozar, O., & David, L. (2005). Experimental and DFT study of pyrazinamide. *Chemical Physics*, *316*(1–3), 153–163. https://doi.org/10.1016/j.chemphys.2005.05.004

Chorghade, M. S. (2006). *Drug Discovery and Development*, *Drug Discovery* (Vol. 1). John Wiley & Sons.

Coffin, J. M. (1995). HIV population dynamics in vivo: implications for genetic variation, pathogenesis, and therapy. *Science*, *267*(5197), 483–489. https://doi.org/10.1126/science.7824947

Cohen, M. S., Chen, Y. Q., McCauley, M., Gamble, T., Hosseinipour, M. C.,

Kumarasamy, N., Hakim, J. G., Kumwenda, J., Grinsztejn, B., Pilotto, J. H. S., Godbole, S. V., Mehendale, S., Chariyalertsak, S., Santos, B. R., Mayer, K. H., Hoffman, I. F., Eshleman, S. H., Piwowar-Manning, E., Wang, L., … Fleming, T. R. (2011). Prevention of HIV-1 infection with early antiretroviral therapy. *New England Journal of Medicine*, *365*(6), 493–505. https://doi.org/10.1056/NEJMoa1105243

Cohen, M. S., Chen, Y. Q., McCauley, M., Gamble, T., Hosseinipour, M. C., Kumarasamy, N., Hakim, J. G., Kumwenda, J., Grinsztejn, B., Pilotto, J. H. S., & others. (2016). Antiretroviral therapy for the prevention of HIV-1 transmission. *New England Journal of Medicine*, *375*(9), 830–839. https://doi.org/10.1056/nejmoa1600693

Couillaud, B. M., Espeau, P., Mignet, N., & Corvis, Y. (2019). State of the Art of Pharmaceutical Solid Forms: from Crystal Property Issues to Nanocrystals Formulation. In *ChemMedChem*. https://doi.org/10.1002/cmdc.201800612

Currie, C. S. M., Williams, B. G., Cheng, R. C. H., & Dye, C. (2003). Tuberculosis epidemics driven by HIV: is prevention better than cure? *Aids*, *17*(17), 2501–2508. https://doi.org/10.1097/00002030-200311210-00013

da Costa, M. A., Seiceira, R. C., Rodrigues, C. R., Hoffmeister, C. R. D., Cabral, L. M., & Rocha, H. V. A. (2012). Efavirenz dissolution enhancement I: co-micronization. *Pharmaceutics*, *5*(1), 1–22. https://doi.org/10.3390/pharmaceutics5010001

Daingade, C. S., Jain, B. U., & Kondawar, M. (2019). Pharmaceutical Co-Crystalization: A Review. *Research Journal of Pharmaceutical Dosage Forms and Technology*, *11*(2), 143. https://doi.org/10.5958/0975-4377.2019.00024.7

Das, K., Clark, A. D., Lewi, P. J., Heeres, J., De Jonge, M. R., Koymans, L. M. H., Vinkers, H. M., Daeyaert, F., Ludovici, D. W., Kukla, M. J., & others. (2004). Roles of conformational and positional adaptability in structure-based design of TMC125-R165335 (etravirine) and related non-nucleoside reverse transcriptase inhibitors that are highly potent and effective against wild-type and drug-resistant HIV-1 varian. *Journal of Medicinal Chemistry*, *47*(10), 2550–2560. https://doi.org/10.1021/jm030558s.

References

Davies, W. L., Grunert, R. R., Haff, R. F., Mcgahen, J. W., Neumayer, E. M., Paulshock, M., Watts, J. C., Wood, T. R., Hermann, E. C., & Hoffmann, C. E. (1964). Antiviral activity of 1-adamantanamine (amantadine). *Science*, *144*(3620), 862–863. https://doi.org/10.1126/science.144.3620.862

De Clercq, E. (1995). Antiviral therapy for human immunodeficiency virus infections. *Clinical Microbiology Reviews*, *8*(2), 200–239. https://doi.org/10.1128/cmr.8.2.200

De Gomes, E. C. L., Mussel, W. N., Resende, J. M., Fialho, S. L., Barbosa, J., & Yoshida, M. I. (2013). Chemical interactions study of antiretroviral drugs efavirenz and lamivudine concerning the development of stable fixed-dose combination formulations for AIDS treatment. *Journal of the Brazilian Chemical Society*, *24*(4), 573–579. https://doi.org/10.5935/0103-5053.20130071

De O. Porfírio, L., Costa, A. A., Conceição, R. R., De O. Matos, T., Almeida, E. D. P., Sarmento, V. H. V., Araújo, A. A. S., De S. Nunes, R., & Lira, A. A. M. (2015). Compatibility study of hydroxypropylmethylcellulose films containing zidovudine and lamivudine using thermal analysis and infrared spectroscopy. *Journal of Thermal Analysis and Calorimetry*, *120*(1), 817–828. https://doi.org/10.1007/s10973-014-3938-5

Desai, D., Wang, J., Wen, H., Li, X., & Timmins, P. (2013). Formulation design, challenges, and development considerations for fixed dose combination (FDC) of oral solid dosage forms. *Pharmaceutical Development and Technology*, *18*(6), 1265–1276. https://doi.org/10.3109/10837450.2012.660699

Desiraju, G. R. (1995). Supramolecular synthons in crystal engineering—a new organic synthesis. *Angewandte Chemie International Edition in English*, *34*(21), 2311–2327. https://doi.org/10.1002/anie.199523111

Desiraju, G. R., & others. (2001). Crystal engineering: outlook and prospects. *CURRENT SCIENCE-BANGALORE-*, *81*(8), 1038–1042. https://www.jstor.org/stable/i24102498

Desiraju, G. R., Shing Ho, P., Kloo, L., Legon, A. C., Marquardt, R., Metrangolo, P., Politzer, P., Resnati, G., & Rissanen, K. (2013). Definition of the halogen bond

(IUPAC recommendations 2013). *Pure and Applied Chemistry*, *85*(8), 1711–1713. https://doi.org/10.1351/PAC-REC-12-05-10

Dever, L. A., & Dermody, T. S. (1991). Mechanisms of bacterial resistance to antibiotics. *Archives of Internal Medicine*, *151*(5), 886–895. https://doi.org/10.1001/archinte.1991.00400050040010

Ding, J, Das, K., Tantillo, C., Zhang, W., Clark Jr, A. D., Jessen, S., Lu, X., Hsiou, Y., Jacobo-Molina, A., Andries, K., & others. (1995). Structure of HIV-1 reverse transcriptase in a complex with the non-nucleoside inhibitor $α$-APA R 95845 at 2.8 Åresolution. *Structure*, *3*(4), 365–379. https://doi.org/10.1016/S0969-2126(01)00168-X

Ding Jianping, Kalyan Das, Yu Hsiou, Wanyi Zhang, Edward Arnold, Prem NS Yadav, and S. H. H. (2018). Structural studies of HIV-1 reverse transcriptase and implications for drug design. In P. Veerapandian (Ed.), *Structure-Based Drug Design* (pp. 41–82). https://doi.org/10.1201/9780203738023-2

Ding, Jianping, Das, K., Hsiou, Y., Sarafianos, S. G., Clark, A. D., Jacobo-Molina, A., Tantillo, C., Hughes, S. H., & Arnold, E. (1998). Structure and functional implications of the polymerase active site region in a complex of HIV-1 RT with a double-stranded DNA template-primer and an antibody Fab fragment at 2.8 Åresolution. *Journal of Molecular Biology*, *284*(4), 1095–1111. https://doi.org/10.1006/jmbi.1998.2208

Domingo, E., & Holland, J. J. (1997). RNA virus mutations and fitness for survival. *Annual Reviews in Microbiology*, *51*(1), 151–178. https://doi.org/10.1146/annurev.micro.51.1.151

Dooner, H., Mundin, G., Mersmann, S., Bennett, C., Lorch, U., Encabo, M., Escriche, M., Encina, G., & Smith, K. (2019). Pharmacokinetics of Tramadol and Celecoxib in Japanese and Caucasian Subjects Following Administration of Co-Crystal of Tramadol-Celecoxib (CTC): A Randomised, Open-Label Study. *European Journal of Drug Metabolism and Pharmacokinetics*, *44*(1), 63–75. https://doi.org/10.1007/s13318-018-0491-9

Douroumis, D., Ross, S. A., & Nokhodchi, A. (2017). Advanced methodologies for

cocrystal synthesis. *Advanced Drug Delivery Reviews*, *117*, 178–195. https://doi.org/10.1016/j.addr.2017.07.008

Drozd, K. V, Manin, A. N., Churakov, A. V, & Perlovich, G. L. (2017). Novel drug-drug cocrystals of carbamazepine with para-aminosalicylic acid: screening, crystal structures and comparative study of carbamazepine cocrystal formation thermodynamics. *CrystEngComm*, *19*(30), 4273–4286. https://doi.org/10.1039/c7ce00831g

Du, B., & Shim, J. S. (2016). Targeting epithelial-mesenchymal transition (EMT) to overcome drug resistance in cancer. *Molecules*, *21*(7), 965. https://doi.org/10.3390/molecules21070965

Duarte, R., Lönnroth, K., Carvalho, C., Lima, F., Carvalho, A. C. C., Muñoz-Torrico, M., & Centis, R. (2018). Tuberculosis, social determinants and co-morbidities (including HIV). *Pulmonology*, *24*(2), 115–119. https://doi.org/10.1016/j.rppnen.2017.11.003

Duggirala, N. K., Perry, M. L., Almarsson, Ö., & Zaworotko, M. J. (2016). Pharmaceutical cocrystals: along the path to improved medicines. *Chemical Communications*, *52*(4), 640–655. https://doi.org/10.1039/c5cc08216a

Dunitz, J. D., & Gavezzotti, A. (2009). How molecules stick together in organic crystals: Weak intermolecular interactions. *Chemical Society Reviews*, *38*(9), 2622–2633. https://doi.org/10.1039/b822963p

Efsen AM, Schultze A, Post FA, Panteleev A, Furrer H, Miller RF, Losso MH, Toibaro J, Skrahin A, Miro JM, C. J. (2015). Major challenges in clinical management of TB/HIV coinfected patients in Eastern Europe compared with Western Europe and Latin America. *PLoS One*, *10*(12), e0145380. https://doi.org/10.1371/journal.pone.0145380

Eggink, D., Berkhout, B., & W Sanders, R. (2010). Inhibition of HIV-1 by fusion inhibitors. *Current Pharmaceutical Design*, *16*(33), 3716–3728. https://doi.org/10.2174/138161210794079218

Epand, R. M., Walker, C., Epand, R. F., & Magarvey, N. A. (2016). Molecular mechanisms of membrane targeting antibiotics. *Biochimica et Biophysica Acta* -

Biomembranes, *1858*(5), 980–987. https://doi.org/10.1016/j.bbamem.2015.10.018

Évora, A. O. L., Castro, R. A. E., Maria, T. M. R., Rosado, M. T. S., Silva, M. R., Beja, A. M., Canotilho, J., & Eusébio, M. E. S. (2011). Pyrazinamide-diflunisal: A new dual-drug Co-crystal. *Crystal Growth and Design*, *11*(11), 4780–4788. https://doi.org/10.1021/cg200288b

Fábián, L. (2009). Cambridge structural database analysis of molecular complementarity in cocrystals. *Crystal Growth and Design*, *9*(3), 1436–1443. https://doi.org/10.1021/cg800861m

Fandaruff, C., Araya-Sibaja, A. M., Pereira, R. N., Hoffmeister, C. R. D., Rocha, H. V. A., & Silva, M. A. S. (2014). Thermal behavior and decomposition kinetics of efavirenz under isothermal and non-isothermal conditions. *Journal of Thermal Analysis and Calorimetry*, *115*(3), 2351–2356. https://doi.org/10.1007/s10973-013-3306-x

Fandaruff, Cinira, Rauber, G. S., Araya-Sibaja, A. M., Pereira, R. N., De Campos, C. E. M., Rocha, H. V. A., Monti, G. A., Malaspina, T., Silva, M. A. S., & Cuffini, S. L. (2014). Polymorphism of anti-HIV drug efavirenz: Investigations on thermodynamic and dissolution properties. *Crystal Growth and Design*, *14*(10), 4968–4975. https://doi.org/10.1021/cg500509c

Ferguson, M. R., Rojo, D. R., Von Lindern, J. J., & O'Brien, W. A. (2002). HIV-1 replication cycle. *Clinics in Laboratory Medicine*, *22*(3), 611–635. https://doi.org/10.1016/S0272-2712(02)00015-X

Fernandes, J. A., Sardo, M., Mafra, L., Choquesillo-Lazarte, D., & Masciocchi, N. (2015). X-ray and NMR crystallography studies of novel theophylline cocrystals prepared by liquid assisted grinding. *Crystal Growth & Design*, *15*(8), 3674–3683. https://doi.org/10.1021/acs.cgd.5b00279

Freire, F. D., Aragão, C. F. S., De Lima E Moura, T. F. A., & Raffin, F. N. (2009). Thermal studies of isoniazid and mixtures with rifampicin. *Journal of Thermal Analysis and Calorimetry*, *97*(1), 333–336. https://doi.org/10.1007/s10973-009-0084-6

References

Frestedt, J. L. (2018). Foods, Food Additives, and Generally Regarded as Safe (GRAS) Food Assessments. In *Food Control and Biosecurity* (Vol. 16, pp. 543–565). Elsevier Inc. https://doi.org/10.1016/B978-0-12-811445-2.00016-7

Friić, T. (2010). New opportunities for materials synthesis using mechanochemistry. *Journal of Materials Chemistry*, *20*(36), 7599–7605. https://doi.org/10.1039/c0jm00872a

Friscic, T., & Jones, W. (2009). Recent advances in understanding the mechanism of cocrystal formation via grinding. *Crystal Growth and Design*, *9*(3), 1621–1637. https://doi.org/10.1021/cg800764n

Friščić, T., & Jones, W. (2010). Benefits of cocrystallisation in pharmaceutical materials science: an update. *Journal of Pharmacy and Pharmacology*, *62*(11), 1547–1559. https://doi.org/10.1111/j.2042-7158.2010.01133.x

Fukte, S. R., Wagh, M. P., & Rawat, S. (2014). Coformer selection: An important tool in cocrystal formation review article. *Int J Pharm Pharm Sci*, *6*, 9–14. https://innovareacademics.in/journals/index.php/ijpps/article/view/1733.

Gagnière, E., Mangin, D., Veesler, S., & Puel, F. (2011). Chapter 9. Co-crystallization in Solution and Scale-up Issues. In *Pharmaceutical Salts and Co-crystals* (pp. 188–211). https://doi.org/10.1039/9781849733502-00188

Gajda, M., Nartowski, K. P., Pluta, J., & Karolewicz, B. (2019). Continuous, one-step synthesis of pharmaceutical cocrystals via hot melt extrusion from neat to matrix-assisted processing – State of the art. *International Journal of Pharmaceutics*, *558*, 426–440. https://doi.org/10.1016/j.ijpharm.2019.01.016

Gandhi, N. R., Moll, A., Sturm, A. W., Pawinski, R., Govender, T., Lalloo, U., Zeller, K., Andrews, J., & Friedland, G. (2006). Extensively drug-resistant tuberculosis as a cause of death in patients co-infected with tuberculosis and HIV in a rural area of South Africa. *The Lancet*, *368*(9547), 1575–1580. https://doi.org/10.1016/S0140-6736(06)69573-1

Gao, F., Bailes, E., Robertson, D. L., Chen, Y., Rodenburg, C. M., Michael, S. F., Cummins, L. B., Arthur, L. O., Peeters, M., Shaw, G. M., & others. (1999). Origin of HIV-1 in the chimpanzee Pan troglodytes troglodytes. *Nature*,

397(6718), 436. https://doi.org/10.1038/17130

Garnero, C., Zoppi, A., Aloisio, C., & Longhi, M. R. (2017). Technological delivery systems to improve biopharmaceutical properties. In *Nanoscale Fabrication, Optimization, Scale-up and Biological Aspects of Pharmaceutical Nanotechnology* (pp. 253–299). Elsevier. https://doi.org/10.1016/B978-0-12-813629-4.00007-3

Gatch, M. B., Kozlenkov, A., Huang, R.-Q., Yang, W., Nguyen, J. D., González-Maeso, J., Rice, K. C., France, C. P., Dillon, G. H., Forster, M. J., & others. (2013). The HIV antiretroviral drug efavirenz has LSD-like properties. *Neuropsychopharmacology*, *38*(12), 2373–2384. https://doi.org/10.1038/npp.2013.135

Ghadi, R. (2014). CO-CRYSTALS: EMERGING APPROACH IN PHARMACEUTICAL DESIGN. *Indo American Journal of Pharmaceutical Research*, *4*(9), 3881–3893.

Goldstein, J. I., Newbury, D. E., Michael, J. R., Ritchie, N. W. M., Scott, J. H. J., & Joy, D. C. (2017). Scanning electron microscopy and x-ray microanalysis. In *Scanning Electron Microscopy and X-ray Microanalysis*. https://doi.org/10.1007/978-1-4939-6676-9

González-Bello, C. (2017a). Antibiotic adjuvants--A strategy to unlock bacterial resistance to antibiotics. *Bioorganic & Medicinal Chemistry Letters*, *27*(18), 4221–4228. https://doi.org/10.1016/j.bmcl.2017.08.027

González-Bello, C. (2017b). Antibiotic adjuvants – A strategy to unlock bacterial resistance to antibiotics. *Bioorganic and Medicinal Chemistry Letters*, *27*(18), 4221–4228. https://doi.org/10.1016/j.bmcl.2017.08.027

Gonzalez, A. L. (2015). BACTERIAL RESISTANCE DEVELOPS THROUGH MULTIPLE MECHANISMS. *Cataract & Refractive Surgery Today*, 40–43. https://crstoday.com/articles/2015-feb/bacterial-resistance-develops-through-multiple-mechanisms/#

Good, D. J., & Rodriguez-Hornedo, N. (2009). Solubility advantage of pharmaceutical cocrystals. *Crystal Growth and Design*, *9*(5), 2252–2264.

https://doi.org/10.1021/cg801039j

Gottesman, M. M. (2002). Mechanisms of cancer drug resistance. *Annual Review of Medicine*, *53*(1), 615–627. https://doi.org/10.1146/annurev.med.53.082901.103929

Goud, N. R., Gangavaram, S., Suresh, K., Pal, S., Manjunatha, S. G., Nambiar, S., & Nangia, A. (2012). Novel furosemide cocrystals and selection of high solubility drug forms. *Journal of Pharmaceutical Sciences*, *101*(2), 664–680. https://doi.org/10.1002/jps.22805

Greco, W. R., Bravo, G., & Parsons, J. C. (1995). The search for synergy: a critical review from a response surface perspective. *Pharmacological Reviews*, *47*(2), 331–385.

Grobelny, P., Mukherjee, A., & Desiraju, G. R. (2011). Drug-drug co-crystals: Temperature-dependent proton mobility in the molecular complex of isoniazid with 4-aminosalicylic acid. *CrystEngComm*, *13*(13), 4358–4364. https://doi.org/10.1039/c0ce00842g

Groom, C. R., Bruno, I. J., Lightfoot, M. P., & Ward, S. C. (2016). The Cambridge structural database. *Acta Crystallographica Section B: Structural Science, Crystal Engineering and Materials*. https://doi.org/10.1107/S2052520616003954

Gunasekaran, S., & Sailatha, E. (2009). Vibrational analysis of pyrazinamide. *Indian Journal of Pure and Applied Physics*, *47*(4), 259–264.

Gunasekaran, S., Sailatha, E., Seshadri, S., & Kumaresan, S. (2009). FTIR, FT Raman spectra and molecular structural confirmation of isoniazid. *Indian Journal of Pure and Applied Physics*, *47*(1), 12–18.

Günthard, H. F., Aberg, J. A., Eron, J. J., Hoy, J. F., Telenti, A., Benson, C. A., Burger, D. M., Cahn, P., Gallant, J. E., Glesby, M. J., Reiss, P., Saag, M. S., Thomas, D. L., Jacobsen, D. M., & Volberding, P. A. (2014). Antiretroviral treatment of adult HIV infection: 2014 Recommendations of the International Antiviral Society-USA panel. *JAMA - Journal of the American Medical Association*, *312*(4), 410–425. https://doi.org/10.1001/jama.2014.8722

Hamed, R., Awadallah, A., Sunoqrot, S., Tarawneh, O., Nazzal, S., AlBaraghthi, T., Al Sayyad, J., & Abbas, A. (2016). pH-Dependent Solubility and Dissolution Behavior of Carvedilol—Case Example of a Weakly Basic BCS Class II Drug. *AAPS PharmSciTech*, *17*(2), 418–426. https://doi.org/10.1208/s12249-015-0365-2

Harris, R., Yeung, R., áBrian Lamont, R., Lancaster, R., Lynn, S., & Staniforth, S. (1997). 'Polymorphism'in a novel anti-viral agent: Lamivudine. *Journal of the Chemical Society, Perkin Transactions 2*, *12*, 2653–2660. https://doi.org/10.1039/a704709f

Hasa, D., Schneider, G., Voinovich, D., & Jones, W. (2015). Cocrystal Formation through Mechanochemistry: From Neat and Liquid-Assisted Grinding to Polymer-Assisted Grinding. *Angewandte Chemie - International Edition*. https://doi.org/10.1002/anie.201501638

Hay, A. J. (1989). The Mechanism of Action of Amantadine and Rimantadine Against Influenza Viruses. In *Concepts in Viral Pathogenesis III*. https://doi.org/10.1007/978-1-4613-8890-6_42

Healy, A. M., Worku, Z. A., Kumar, D., & Madi, A. M. (2017). Pharmaceutical solvates, hydrates and amorphous forms: A special emphasis on cocrystals. In *Advanced Drug Delivery Reviews* (Vol. 117, pp. 25–46). Elsevier B.V. https://doi.org/10.1016/j.addr.2017.03.002

Herrick, T. M., & Million, R. P. (2007). Tapping the potential of fixed-dose combinations. *Nature Reviews Drug Discovery*, *6*(7), 513–514.

Hickey, M. B., Peterson, M. L., Scoppettuolo, L. A., Morrisette, S. L., Vetter, A., Guzmán, H., Remenar, J. F., Zhang, Z., Tawa, M. D., Haley, S., & others. (2007). Performance comparison of a co-crystal of carbamazepine with marketed product. *European Journal of Pharmaceutics and Biopharmaceutics*, *67*(1), 112–119. https://doi.org/10.1016/j.ejpb.2006.12.016

HIV transmission. (2003). In *HIV and AIDS: A Foundation for Nursing and Healthcare Practice* (pp. 32–42). CRC Press. https://doi.org/10.1201/b13504-5

Hollingsworth, T. D., Anderson, R. M., & Fraser, C. (2008). HIV-1 transmission, by

stage of infection. *Journal of Infectious Diseases*, *198*(5), 687–693. https://doi.org/10.1086/590501

Homer, J., Ritchie-Dunham, J., Rabbino, H., Puente, L. M., Jorgensen, J., & Hendricks, K. (2000). Toward a dynamic theory of antibiotic resistance. *System Dynamics Review*, *16*(4), 287–319. https://doi.org/10.1002/sdr.200

Hong, K. C. S. (1989). Acceptability, compliance, and adverse reactions when isoniazid, rifampin, and pyrazinamide are given as a combined formulation or separately during three-times-weekly antituberculosis chemotherapy. *The American Review of Respiratory Disease*, *140*(6), 1618. https://doi.org/10.1164/ajrccm/140.6.1618

Housman, G., Byler, S., Heerboth, S., Lapinska, K., Longacre, M., Snyder, N., & Sarkar, S. (2014). Drug resistance in cancer: an overview. *Cancers*, *6*(3), 1769–1792. https://doi.org/10.3390/cancers6031769

Howard, J. L., Qun, C., & Duncan L., B. (2018). Mechanochemistry as an emerging tool for molecular synthesis: what can it offer?. *Chemical Science*, *9*(12), 3080–3094. https://doi.org/10.1039/c7sc05371a

Howard, N. C., Marin, N. D., Ahmed, M., Rosa, B. A., Martin, J., Bambouskova, M., Sergushichev, A., Loginicheva, E., Kurepina, N., Rangel-Moreno, J., Chen, L., Kreiswirth, B. N., Klein, R. S., Balada-Llasat, J. M., Torrelles, J. B., Amarasinghe, G. K., Mitreva, M., Artyomov, M. N., Hsu, F. F., … Khader, S. A. (2018). Mycobacterium tuberculosis carrying a rifampicin drug resistance mutation reprograms macrophage metabolism through cell wall lipid changes. *Nature Microbiology*, *3*(10), 1099–1108. https://doi.org/10.1038/s41564-018-0245-0

Hu, Y., Xu, L., He, Y. L., Pang, Y., Lu, N., Liu, J., Shen, J., Zhu, D. M., Feng, X., Wang, Y. W., & Yang, C. (2017). Prevalence and Molecular Characterization of Second-Line Drugs Resistance among Multidrug-Resistant Mycobacterium tuberculosis Isolates in Southwest of China. *BioMed Research International*, *2017*(Article ID 4563826), 9 pages. https://doi.org/10.1155/2017/4563826

Hu, Yun, Gniado, K., Erxleben, A., & McArdle, P. (2014). Mechanochemical reaction

of sulfathiazole with carboxylic acids: Formation of a cocrystal, a salt, and coamorphous solids. *Crystal Growth and Design*, *14*(2), 803–813. https://doi.org/10.1021/cg401673z

Hubsher, G., Haider, M., & Okun, M. S. (2012). Amantadine: The journey from fighting flu to treating Parkinson disease. In *Neurology* (Vol. 78, Issue 14, pp. 1096–1099). Lippincott Williams and Wilkins. https://doi.org/10.1212/WNL.0b013e31824e8f0d

Hutchins, K. M. (2018). Functional materials based on molecules with hydrogen-bonding ability: Applications to drug co-crystals and polymer complexes. In *Royal Society Open Science*. https://doi.org/10.1098/rsos.180564

Izutsu, K. I., Koide, T., Takata, N., Ikeda, Y., Ono, M., Inoue, M., Fukami, T., & Yonemochi, E. (2016). Characterization and quality control of pharmaceutical cocrystals. In *Chemical and Pharmaceutical Bulletin* (Vol. 64, Issue 10, pp. 1421–1430). Pharmaceutical Society of Japan. https://doi.org/10.1248/cpb.c16-00233

Jacobson, M. A., & French, M. (1997). Altered natural history of AIDS-related opportunistic infections in the era of potent combination antiretroviral therapy. *AIDS (London, England)*, *12*, S157--63.

Jain, N., Prabhakar, S., & Singh, R. A. (2013). Fourier transform infrared spectra and normal mode analysis of drug molecules: Zidovudine. *Journal of Molecular Structure*, *1036*, 414–421. https://doi.org/10.1016/j.molstruc.2012.10.063

James, S. L., & Friščić, T. (2013a). Mechanochemistry: a web themed issue. *Chemical Communications*, *49*(47), 5349–5350. https://doi.org/10.1039/c3cc90136j

James, S. L., & Friščić, T. (2013b). Mechanochemistry. *Chemical Society Reviews*, *42*(18), 7494–7496. https://doi.org/10.1039/C3CS90058D

Jayasankar, A., Somwangthanaroj, A., Shao, Z. J., & Rodr\'\iguez-Hornedo, N. (2006). Cocrystal formation during cogrinding and storage is mediated by amorphous phase. *Pharmaceutical Research*, *23*(10), 2381–2392. https://doi.org/10.1007/s11095-006-9110-6

Jiang, L., Huang, Y., Zhang, Q., He, H., Xu, Y., & Mei, X. (2014). Preparation and Solid-State Characterization of Dapsone Drug-Drug Co-Crystals. *Crystal Growth & Design*, *14*(9), 4562–4573. https://doi.org/10.1021/cg500668a

Jianping Ding Kalyan Das, Y. H. W. Z. E. A. P. N. S. Y. S. H. H. (1997). *Structure-based drug design*. Marcel Dekker.

Jones, W., & Eddleston, M. D. (2014). Introductory lecture: Mechanochemistry, a versatile synthesis strategy for new materials. In *Faraday Discussions* (pp. 9–34). https://doi.org/10.1039/c4fd00162a

Jones, W., Motherwell, W. D., & Trask, A. V. (2006). Pharmaceutical cocrystals: an emerging approach to physical property enhancement. *MRS Bulletin*, *31*(11), 875–879. https://doi.org/10.1557/mrs2006.206

Jovanović, N., Jovanović, J., Stefan-Mikić, S., Kulauzov, M., Aleksic-Dordević, M., & Cvjetković, D. (2008). Mechanisms of bacterial resistance to antibiotics. *Medicinski Pregled*, *61*, 9–14. https://doi.org/10.1128/9781555819316.part3

Julian Davies and Dorothy Davies. (2010). Origins and evolution of antibiotic resistance. *Microbiology and Molecular Biology Reviews*, *74*(3), 417–433. https://doi.org/10.1128/mmbr.00016-10

Jung, S., Choi, I., & Kim, I. W. (2015). Liquid-assisted grinding to prepare a cocrystal of adefovir dipivoxil thermodynamically less stable than its neat phase. *Crystals*, *5*(4), 583–591. https://doi.org/10.3390/cryst5040583

Kampman, K., Volpicelli, J. R., Alterman, A., Cornish, J., Weinrieb, R., Epperson, L., Sparkman, T., & O'Brien, C. P. (1996). Amantadine in the early treatment of cocaine dependence: A double-blind, placebo-controlled trial. *Drug and Alcohol Dependence*. https://doi.org/10.1016/0376-8716(96)01225-2

Karagianni, A., Malamatari, M., & Kachrimanis, K. (2018a). Pharmaceutical cocrystals: New solid phase modification approaches for the formulation of APIs. In *Pharmaceutics*. https://doi.org/10.3390/pharmaceutics10010018

Karagianni, A., Malamatari, M., & Kachrimanis, K. (2018b). Pharmaceutical Cocrystals: New Solid Phase Modification Approaches for the Formulation of

APIs. *Pharmaceutics*, *10*(1), 18. https://doi.org/10.3390/pharmaceutics10010018

Karimi-Jafari, M., Padrela, L., Walker, G. M., & Croker, D. M. (2018). Creating cocrystals: A review of pharmaceutical cocrystal preparation routes and applications. In *Crystal Growth and Design*. https://doi.org/10.1021/acs.cgd.8b00933

Karki, S., Fábián, L., Friščić, T., & Jones, W. (2007). Powder X-ray diffraction as an emerging method to structurally characterize organic solids. *Organic Letters*, *9*(16), 3133–3136. https://doi.org/10.1021/ol071329t

Kim, H.-R., Hwang, S. S., Kim, H. J., Lee, S. M., Yoo, C.-G., Kim, Y. W., Han, S. K., Shim, Y.-S., & Yim, J.-J. (2007). Impact of extensive drug resistance on treatment outcomes in non-HIV-infected patients with multidrug-resistant tuberculosis. *Clinical Infectious Diseases*, *45*(10), 1290–1295. https://doi.org/10.1086/522537

Koff, W. C., Elm, J. R., & Halstead, S. B. (1980). Inhibition of dengue virus replication by amantadine hydrochloride. *Antimicrobial Agents and Chemotherapy*. https://doi.org/10.1128/AAC.18.1.125

Kohlstaedt, L. A., Wang, J., Friedman, J. M., Rice, P. A., & Steitz, T. A. (1992). Crystal structure at 3.5 A resolution of HIV-1 reverse transcriptase complexed with an inhibitor. *Science*, *256*(5065), 1783–1790. https://doi.org/10.1126/science.1377403

Kornhuber, J., Retz, W., & Riederer, P. (1995). Slow accumulation of psychotropic substances in the human brain. Relationship to therapeutic latency of neuroleptic and antidepressant drugs? *Journal of Neural Transmission, Supplement*. https://pubmed.ncbi.nlm.nih.gov/8821068/

Kumar, A. R., Saloni, J., Deepak, K., Sankar Lal, S., & Mukesh, S. (2019). An Overview of Pharmaceutical Co-Crystal. *Asian Journal of Pharmaceutical Research and Development*, *7*(2), 39–46. https://doi.org/10.22270/ajprd.v7i2.483

Kumar, S. (2017). Pharmaceutical Cocrystals: An Overview. *Indian Journal of Pharmaceutical Sciences*, *79*(6), 858–871. https://doi.org/10.4172/pharmaceutical-sciences.1000302

Kuminek, G., Rodríguez-Hornedo, N., Siedler, S., Rocha, H. V. A., Cuffini, S. L., & Cardoso, S. G. (2016). How cocrystals of weakly basic drugs and acidic coformers might modulate solubility and stability. *Chemical Communications*, *52*(34), 5832–5835. https://doi.org/10.1039/c6cc00898d

Lange, L., & Sadowski, G. (2016). Polymorphs, Hydrates, Cocrystals, and Cocrystal Hydrates: Thermodynamic Modeling of Theophylline Systems. *Crystal Growth and Design*, *16*(8), 4439–4449. https://doi.org/10.1021/acs.cgd.6b00554

Laserson, K., Kenyon, A., Kenyon, T., Layloff, T., Binkin, N., & others. (2001). Substandard tuberculosis drugs on the global market and their simple detection. *The International Journal of Tuberculosis and Lung Disease*, *5*(5), 448–454. https://pubmed.ncbi.nlm.nih.gov/11336276/

Lavor, E. P., Freire, F. D., Aragão, C. F. S., Raffin, F. N., & De Lima E Moura, T. F. A. (2012). Application of thermal analysis to the study of anti-tuberculosis drug compatibility. Part 1. *Journal of Thermal Analysis and Calorimetry*, *108*(1), 207–212. https://doi.org/10.1007/s10973-011-1770-8

Leach, A. R. (2001). *Molecular modelling: principles and applications*. Pearson education.

Lee, H.-G., Zhang, G. G. Z., & Flanagan, D. R. (2011). Cocrystal intrinsic dissolution behavior using a rotating disk. *Journal of Pharmaceutical Sciences*, *100*(5), 1736–1744. https://doi.org/10.1002/jps.22400

Lemey, P., Pybus, O. G., Wang, B., Saksena, N. K., Salemi, M., & Vandamme, A.-M. (2003). Tracing the origin and history of the HIV-2 epidemic. *Proceedings of the National Academy of Sciences*, *100*(11), 6588–6592. https://doi.org/10.1073/pnas.0936469100

Lemmerer, A., Adsmond, D. A., Esterhuysen, C., & Bernstein, J. (2013). Polymorphic co-crystals from polymorphic co-crystal formers: Competition between carboxylic acid···pyridine and phenol···pyridine hydrogen bonds. *Crystal Growth and Design*, *13*(9), 3935–3952. https://doi.org/10.1021/cg4006357

Lemmon, E. W., McLinden, M. O., & Friend, and D. G. (2017). NIST Chemistry WebBook, NIST Standard Reference Database. In W. G. M. P.J. Linstrom (Ed.),

NIST Chemistry WebBook (Issue 69). National Institute of Standards and Technology. https://doi.org/10.18434/T4D303

Letang, E., Ellis, J., Naidoo, K., Casas, E. C., Sánchez, P., Hassan-Moosa, R., Cresswell, F., Miró, J. M., & García-Basteiro, A. L. (2020). Tuberculosis-HIV Co-Infection: Progress and Challenges After Two Decades of Global Antiretroviral Treatment Roll-Out. *Archivos de Bronconeumologia*, *56*(7), 446–454. https://doi.org/10.1016/j.arbres.2019.11.015

Leyssens, T., & Ter Horst, J. H. (2017). Solution co-crystallisation and its applications. In *Multi-Component Crystals: Synthesis, Concepts, Function*. https://doi.org/10.1515/9783110464955-009

Lienhardt, C., Vernon, A., & Raviglione, M. C. (2010). New drugs and new regimens for the treatment of tuberculosis: review of the drug development pipeline and implications for national programmes. *Current Opinion in Pulmonary Medicine*, *16*(3), 186–193. https://doi.org/10.1097/MCP.0b013e328337580c

Lin, C. C., & Chen, W. C. (2016). Treatment effectiveness of amantadine against dengue virus infection. *American Journal of Case Reports*, *17*, 921–924. https://doi.org/10.12659/AJCR.901014

Lloyd, S. B., Kent, S. J., & Winnall, W. R. (2014). The high cost of fidelity. In *AIDS Research and Human Retroviruses* (Vol. 30, Issue 1, pp. 8–16). Mary Ann Liebert Inc. https://doi.org/10.1089/aid.2013.0153

Luo, Y. H., & Sun, B. W. (2013). Pharmaceutical co-crystals of pyrazinecarboxamide (PZA) with various carboxylic acids: Crystallography, hirshfeld surfaces, and dissolution study. *Crystal Growth and Design*, *13*(5), 2098–2106. https://doi.org/10.1021/cg400167w

Maggiolo, F., & Leone, S. (2010). Is HAART modifying the HIV epidemic? *The Lancet*, *376*(9740), 492–493. https://doi.org/10.1016/S0140-6736(10)61057-4

Mahapatra, S., Thakur, T. S., Joseph, S., Varughese, S., & Desiraju, G. R. (2010). New solid state forms of the anti-HIV drug efavirenz. Conformational flexibility and high *Z′* issues. *Crystal Growth and Design*. https://doi.org/10.1021/cg100342k

Maheshwari, C., Jayasankar, A., Khan, N. A., Amidon, G. E., & Rodríguez-Hornedo, N. (2009). Factors that influence the spontaneous formation of pharmaceutical cocrystals by simply mixing solid reactants. *CrystEngComm*, *11*(3), 493–500. https://doi.org/10.1039/b812264d

Maheshwari, R., Kuche, K., Mane, A., Chourasiya, Y., Tekade, M., & Tekade, R. K. (2018). Manipulation of Physiological Processes for Pharmaceutical Product Development. In *Dosage Form Design Considerations: Volume I* (pp. 701–729). Elsevier. https://doi.org/10.1016/B978-0-12-814423-7.00020-4

Malamatari, M., Ross, S. A., Douroumis, D., & Velaga, S. P. (2017). Experimental cocrystal screening and solution based scale-up cocrystallization methods. In *Advanced Drug Delivery Reviews* (Vol. 117, pp. 162–177). Elsevier B.V. https://doi.org/10.1016/j.addr.2017.08.006

Mandal, U., & Pal, T. K. (2008). Formulation and in vitro studies of a fixed-dose combination of a bilayer matrix tablet containing metformin HCl as sustained release and glipizide as immediate release. *Drug Development and Industrial Pharmacy*, *34*(3), 305–313. https://doi.org/10.1080/03639040701657487

Marston, H. D., Dixon, D. M., Knisely, J. M., Palmore, T. N., & Fauci, A. S. (2016). Antimicrobial resistance. *JAMA - Journal of the American Medical Association*, *316*(11), 1193–1204. https://doi.org/10.1001/jama.2016.11764

Martinez-Picado, J., DePasquale, M. P., Kartsonis, N., Hanna, G. J., Wong, J., Finzi, D., Rosenberg, E., Günthard, H. F., Sutton, L., Savara, A., & others. (2000). Antiretroviral resistance during successful therapy of HIV type 1 infection. *Proceedings of the National Academy of Sciences*, *97*(20), 10948–10953. https://doi.org/10.1073/pnas.97.20.10948

Matsuno, T., Fujita, M., Fukunaga, K., Sato, S., & Isobe, H. (2018). Concyclic CH-π arrays for single-axis rotations of a bowl in a tube. *Nature Communications*, *9*(1), 3779. https://doi.org/10.1038/s41467-018-06270-6

Mesfin, Y. M., Hailemariam, D., Biadglign, S., & Kibret, K. T. (2014). Association between HIV/AIDS and multi-drug resistance tuberculosis: A systematic review and meta-analysis. *PLoS ONE*, *9*(1), e82235.

https://doi.org/10.1371/journal.pone.0082235

Michalchuk, A. A. L., Hope, K. S., Kennedy, S. R., Blanco, M. V., Boldyreva, E. V., & Pulham, C. R. (2018). Ball-free mechanochemistry:: In situ real-time monitoring of pharmaceutical co-crystal formation by resonant acoustic mixing. *Chemical Communications*, *54*(32), 4033–4036. https://doi.org/10.1039/c8cc02187b

Migliori, G. B., Centis, R., D'Ambrosio, L., Spanevello, A., Borroni, E., Cirillo, D. M., & Sotgiu, G. (2012). Totally drug-resistant and extremely drug-resistant tuberculosis: the same disease? *Clinical Infectious Diseases*, *54*(9), 1379–1380. https://doi.org/10.1093/cid/cis128

Migliori, G. B., Ortmann, J., Girardi, E., Besozzi, G., Lange, C., Cirillo, D. M., Ferrarese, M., De Iaco, G., Gori, A., Raviglione, M. C., & others. (2007). Extensively drug-resistant tuberculosis, Italy and Germany. *Emerging Infectious Diseases*, *13*(5), 780. https://doi.org/10.3201/eid1305.060200

Miller, S. (2002). Mechanism of action of antiretroviral agent. *Southern African Journal of HIV Medicine*, *3*(2). https://hdl.handle.net/10520/EJC65697

Montaner, J. S. G., Lima, V. D., Barrios, R., Yip, B., Wood, E., Kerr, T., Shannon, K., Harrigan, P. R., Hogg, R. S., Daly, P., & others. (2010). Association of highly active antiretroviral therapy coverage, population viral load, and yearly new HIV diagnoses in British Columbia, Canada: a population-based study. *The Lancet*, *376*(9740), 532–539. https://doi.org/10.1016/S0140-6736(10)60936-1

Morris, K. (2009). Global tuberculosis control amid the world economic crisis. In *The Lancet infectious diseases* (Vol. 9, Issue 3, pp. 144–145). https://doi.org/10.1016/S1473-3099(09)70030-1

Mukherjee, A., Rogers, R. D., & Myerson, A. S. (2018). Cocrystal formation by ionic liquid-assisted grinding: case study with cocrystals of caffeine. *CrystEngComm*, *20*(27). https://doi.org/10.1039/C8CE00859K

Mukherjee, B., & Howard, L. (2011). *Combination therapy in pulmonary arterial hypertension: do we have the right strategy?* https://doi.org/org/10.1586/ers.11.13

References

Munita, J. M., & Arias, C. A. (2016). Mechanisms of antibiotic resistance. *Microbiology Spectrum*, *4*(2). https://doi.org/10.1128/microbiolspec.VMBF-0016-2015

Murphy, E. L., Collier, A. C., Kalish, L. A., Assmann, S. F., Para, M. F., Flanigan, T. P., Kumar, P. N., Mintz, L., Wallach, F. R., & Nemo, G. J. (2001). Highly active antiretroviral therapy decreases mortality and morbidity in patients with advanced HIV disease. *Annals of Internal Medicine, 135*(1), 17–26. https://doi.org/10.7326/0003-4819-135-1-200107030-00005

Naidoo, K. L. (2020). Prevention of mother to child transmission of HIV. In *HIV Infection in Children and Adolescents* (pp. 265–284). Springer International Publishing. https://doi.org/10.1007/978-3-030-35433-6_20

Najar, A. A., & Azim, Y. (2014). Pharmaceutical co-crystals: A new paradigm of crystal engineering. *Journal of the Indian Institute of Science*, *94*(1), 45–68.

Narendran, G., & Swaminathan, S. (2016). TB-HIV co-infection: A catastrophic comradeship. *Oral Diseases*. https://doi.org/10.1111/odi.12389

Nasri, H., Baradaran, A., Shirzad, H., & Kopaei, M. R. (2014). New concepts in nutraceuticals as alternative for pharmaceuticals. *International Journal of Preventive Medicine*, *5*(12), 1487–1499. https://pubmed.ncbi.nlm.nih.gov/25709784/

Nauha, E. (2012). *Crystalline forms of selected agrochemical actives: design and synthesis of cocrystals*. http://urn.fi/URN:ISBN:978-951-39-4493-3

Nayyar, A., & Jain, R. (2005). Recent advances in new structural classes of anti-tuberculosis agents. *Current Medicinal Chemistry*, *12*(16), 1873–1886. https://doi.org/10.2174/0929867054546654

Ngilirabanga, Jean B., Rosa, P. P., Aucamp, M., Kippie, Y., & Samsodien, H. (2020). Dual-drug co-crystal synthesis for synergistic in vitro effect of three key first-line antiretroviral drugs. *Journal of Drug Delivery Science and Technology*, *60*. https://doi.org/10.1016/j.jddst.2020.101958

Ngilirabanga, Jean Baptiste. (2014). *A supramolecular derivatised study of BIS*

(Adamantan-1-Aminium) carbonate [University of the Western Cape]. http://hdl.handle.net/11394/4188

Nutrition, C. for F. S. and A. (2009). Everything added to food in the united states. *U.S. Food and Drug Administration*, 115326. http://www.fda.gov/Food/FoodIngredientsPackaging/ucm115326.htm%5Cninternal-pdf://999/ucm115326.html

Organization, W. H. (2009). *Global tuberculosis control: epidemiology, strategy, financing: WHO report 2009*. World Health Organization.

Organization, W. H., Organization, W. H., & others. (2012). Geneva, Switzerland: WHO; 2013. *Global Tuberculosis Report*.

Organization, W. H., & others. (2014). *Antimicrobial resistance: global report on surveillance*. World Health Organization.

Palella Jr, F. J., Delaney, K. M., Moorman, A. C., Loveless, M. O., Fuhrer, J., Satten, G. A., Aschman, D. J., & Holmberg, S. D. (1998). Declining morbidity and mortality among patients with advanced human immunodeficiency virus infection. *New England Journal of Medicine*, *338*(13), 853–860. https://doi.org/10.1056/nejm199803263381301

Pandey, G., Yadav, S. K., & Mishra, B. (2016). Preparation and characterization of isoniazid and lamivudine co-loaded polymeric microspheres. *Artificial Cells, Nanomedicine and Biotechnology*, *44*(8), 1867–1877. https://doi.org/10.3109/21691401.2015.1111229

Panzade, P., Shendarkar, G., Shaikh, S., & Rathi, P. B. (2017). Pharmaceutical Cocrystal of Piroxicam: Design, formulation and evaluation. *Advanced Pharmaceutical Bulletin*, *7*(3), 399–408. https://doi.org/10.15171/apb.2017.048

Park, T. J., Ko, D. H., Kim, Y. J., & Kim, Y. (2009). Polymorphic characterization of pharmaceutical solids, donepezil hydrochloride, by 13C CP/MAS solid-state nuclear magnetic resonance spectroscopy. *Bulletin of the Korean Chemical Society*. https://doi.org/10.5012/bkcs.2009.30.9.2007

Patel, P., Borkowf, C. B., Brooks, J. T., Lasry, A., Lansky, A., & Mermin, J. (2014).

Estimating per-act HIV transmission risk: A systematic review. *AIDS*, *28*(10), 1509–1519. https://doi.org/10.1097/QAD.0000000000000298

Patrick J. Brennan, Douglas B. Young, B. D. R. (2008). Handbook of Anti-Tuberculosis Agents. *Tuberculosis*, *88*(2), 85–170. https://doi.org/10.1016/S1472-9792(08)70002-7

Paul, A. (2019). Fixed-Dose Combinations. In *Introduction to Basics of Pharmacology and Toxicology: Volume 1: General and Molecular Pharmacology: Principles of Drug Action* (pp. 307–312). Springer Singapore. https://doi.org/10.1007/978-981-32-9779-1_21

Pawlowski, A., Jansson, M., Sköld, M., Rottenberg, M. E., & Källenius, G. (2012a). Tuberculosis and HIV co-infection. In *PLoS Pathogens* (Vol. 8, Issue 2). Public Library of Science. https://doi.org/10.1371/journal.ppat.1002464

Pawlowski, A., Jansson, M., Sköld, M., Rottenberg, M. E., & Källenius, G. (2012b). Tuberculosis and HIV co-infection. *PLoS Pathogens*, *8*(2), e1002464. https://doi.org/10.1371/journal.ppat.1002464

Peterson, M. L., Collier, E. A., Hickey, M. B., Guzman, H., & Almarsson, O. (2010). Multi-component pharmaceutical crystalline phases: engineering for performance. *Organic Crystal Engineering: Frontiers in Crystal Engineering*. https://doi.org/10.1002/9780470681794.ch3

Pillay, D., & Porter, K. (2006). The impact of transmitted drug resistance on the natural history of HIV infection and response to first-line therapy. *AIDS*. https://doi.org/10.1097/01.aids.0000196172.35056.b7

Pindelska, E., Sokal, A., & Kolodziejski, W. (2017). Pharmaceutical cocrystals, salts and polymorphs: Advanced characterization techniques. In *Advanced Drug Delivery Reviews* (Vol. 117, pp. 111–146). Elsevier B.V. https://doi.org/10.1016/j.addr.2017.09.014

Podczeck, F. (2011). Theoretical and experimental investigations into the delamination tendencies of bilayer tablets. *International Journal of Pharmaceutics*, *408*(1), 102–112. https://doi.org/10.1016/j.ijpharm.2011.02.007

Prasad, B., Bhutani, H., & Singh, S. (2006). Study of the interaction between rifapentine and isoniazid under acid conditions. *Journal of Pharmaceutical and Biomedical Analysis*, *41*(4), 1438–1441. https://doi.org/10.1016/j.jpba.2006.03.004

Prime, R. B., Bair, H. E., Vyazovkin, S., Gallagher, P. K., & Riga, A. (2008). Thermogravimetric Analysis (TGA). In *Thermal Analysis of Polymers: Fundamentals and Applications* (pp. 241–317). https://doi.org/10.1002/9780470423837.ch3

Qiao, N., Li, M., Schlindwein, W., Malek, N., Davies, A., & Trappitt, G. (2011). Pharmaceutical cocrystals: an overview. *International Journal of Pharmaceutics*, *419*(1–2), 1–11. https://doi.org/10.1016/j.ijpharm.2011.07.037

Rager, T., & Hilfiker, R. (2010). Cocrystal formation from solvent mixtures. *Crystal Growth and Design*, *10*(7), 3237–3241. https://doi.org/10.1021/cg100361y

Rajbongshi, T., Sarmah, K. K., Sarkar, A., Ganduri, R., Cherukuvada, S., Thakur, T. S., & Thakuria, R. (2018). Preparation of Pyrazinamide Eutectics versus Cocrystals Based on Supramolecular Synthon Variations. *Crystal Growth and Design*. https://doi.org/10.1021/acs.cgd.8b00878

Raju, A., Reddy, A., Satheesh, J., & Jithan, A. V. (2014). Preparation and characterisation of nevirapine oral nanosuspensions. *Indian Journal of Pharmaceutical Sciences*. https://pubmed.ncbi.nlm.nih.gov/24799740/

Ranjit, T., & Sarma, B. (2018). Drug-Drug and Drug-Nutraceutical Cocrystal/Salt as Alternative Medicine for Combination Therapy: A Crystal Engineering Approach. *Crystals*, *8*(2), 101. https://doi.org/10.3390/cryst8020101

Ravikumar, N., Gaddamanugu, G., & Anand Solomon, K. (2013). Structural, spectroscopic (FT-IR, FT-Raman) and theoretical studies of the 1:1 cocrystal of isoniazid with p-coumaric acid. *Journal of Molecular Structure*, *1033*, 272–279. https://doi.org/10.1016/j.molstruc.2012.10.029

Reddy, D. S., Craig, D. C., & Desiraju, G. R. (1996). Supramolecular Synthons in Crystal Engineering. 4. Structure Simplification and Synthon Interchangeability in Some Organic Diamondoid Solids1. *Journal of the American Chemical*

Society, *118*(17), 4090–4093. https://doi.org/10.1021/ja953373m

Reddy, N. P., Padmavathi, Y., Mounika, P., & Anjali, A. (2015). FTIR spectroscopy for estimation of efavirenz in raw material and tablet dosage form. *International Current Pharmaceutical Journal*, *4*(6), 390–395. https://doi.org/10.3329/icpj.v4i6.23290

Reguri, B, & Chakka, R. (2006). *Crystalline forms of nevirapine*. Google Patents. https://www.google.com/patents/US20060183738

Reguri, Buchi, & Chakka, R. (2004). *Novel crystalline forms of 11-cyclopropyl-5, 11-dihydro-4-methyl-6H-dipyrido [3, 2-b: 2', 3'-e][1, 4] diazepin-6-one (nevirapine)*.

Remenar, J. F., Morissette, S. L., Peterson, M. L., Moulton, B., MacPhee, J. M., Guzmán, H. R., & Almarsson, Ö. (2003). Crystal engineering of novel cocrystals of a triazole drug with 1, 4-dicarboxylic acids. *Journal of the American Chemical Society*, *125*(28), 8456–8457. https://doi.org/10.1021/ja035776p

Ren Jingshan, Robert Esnouf, Elspeth Garman, Donald Somers, Carl Ross, Ian Kirby, J. K. et al. (1995). High resolution structures of HIV-1 RT from four RT–inhibitor complexes. *Nature Structural Biology*, *2*(4), 293. https://doi.org/10.1038/nsb0495-293

Saganowska, P., & Wesolowski, M. (2018). DSC as a screening tool for rapid co-crystal detection in binary mixtures of benzodiazepines with co-formers. *Journal of Thermal Analysis and Calorimetry*. https://doi.org/10.1007/s10973-017-6858-3

Samsodien, H., M, B., Tl, D., Z, H., AS, L., IC, S., AB, S., & B, G. (2017). FTIR, Dissolution and Anti-viral Activity of Nevirapine Co-crystals. *Pharmaceutica Analytica Acta*, *8*(9), 1000561. https://doi.org/10.4172/2153-2435.1000561

Sandeep, K., & Arun, N. (2018). Approaches to Design of Pharmaceutical Cocrystals: A Review. *Molecular Crystals and Liquid Crystals*, *667*(1), 54–77. https://doi.org/10.1080/15421406.2019.1577462

Sanphui, P., Goud, N. R., Khandavilli, U. B. R., & Nangia, A. (2011). Fast dissolving

curcumin cocrystals. *Crystal Growth & Design*, *11*(9), 4135–4145. https://doi.org/10.1021/cg200704s

Sarabu, S., Bandari, S., Kallakunta, V. R., Tiwari, R., Patil, H., & Repka, M. A. (2019). An update on the contribution of hot-melt extrusion technology to novel drug delivery in the twenty-first century: part II. In *Expert Opinion on Drug Delivery* (Vol. 16, Issue 6, pp. 567–582). Taylor and Francis Ltd. https://doi.org/10.1080/17425247.2019.1614912

Sarceviča, I., Kons, A., & Orola, L. (2016). Isoniazid cocrystallisation with dicarboxylic acids: Vapochemical, mechanochemical and thermal methods. *CrystEngComm*, *18*(9), 1625–1635. https://doi.org/10.1039/c5ce01774b

Sarkar, M., Perumal, O., & Panchagnula, R. (2008). Solid-state characterization of nevirapine. *Indian Journal of Pharmaceutical Sciences*, *70*(5), 619–630. https://doi.org/10.4103/0250-474X.45401

Sathisaran, I., & Dalvi, S. V. (2018). Engineering cocrystals of poorlywater-soluble drugs to enhance dissolution in aqueous medium. In *Pharmaceutics* (Vol. 10, Issue 3). MDPI AG. https://doi.org/10.3390/pharmaceutics10030108

Sawyer, T. K. (2006). Smart drug discovery leveraging innovative technologies and predictive knowledge. *Nature Chemical Biology*, *2*(12), 646–648. https://doi.org/10.1038/nchembio1206-646

Schaberg, T., Rebhan, K., & Lode, H. (1996). Risk factors for side-effects of isoniazid, rifampin and pyrazinamide in patients hospitalized for pulmonary tuberculosis. *European Respiratory Journal*, *9*(10), 2026–2030. https://doi.org/10.1183/09031936.96.09102026

Schultheiss, N., & Newman, A. (2009a). Pharmaceutical cocrystals and their physicochemical properties. *Crystal Growth and Design*, *9*(6), 2950–2967.

Schultheiss, N., & Newman, A. (2009b). Pharmaceutical cocrystals and their physicochemical properties. *Crystal Growth and Design*, *9*(6), 2950–2967. https://doi.org/10.1021/cg900129f

Sekhon, B. S. (2009). *Pharmaceutical co-crystals-a review*.

https://doi.org/10.3390/iocc_2020-07331

Sekhon, B. S. (2012). Drug-drug co-crystals. *DARU Journal of Pharmaceutical Sciences*, *20*(1), 45. https://doi.org/10.1186/2008-2231-20-45

Shah, N. S., Wright, A., Bai, G.-H., Barrera, L., Boulahbal, F., Mart\'\in-Casabona, N., Drobniewski, F., Gilpin, C., Havelková, M., Lepe, R., & others. (2007). Worldwide emergence of extensively drug-resistant tuberculosis. *Emerging Infectious Diseases*, *13*(3), 380. https://doi.org/10.3201/eid1303.061400

Shan, N., Perry, M., Weyna, D., & Zaworotko, M. (2014). Impact of pharmaceutical cocrystals: the effects on drug pharmacokinetics. *Expert Opinion on Drug Metabolism & Toxicology*, *10*(9), 1255–1271. https://doi.org/10.1517/17425255.2014.942281

Shan, N., & Zaworotko, M. J. (2008). The role of cocrystals in pharmaceutical science. *Drug Discovery Today*, *13*(9–10), 440–446. https://doi.org/10.1016/j.drudis.2008.03.004

Sharp, P. M., & Hahn, B. H. (2011). Origins of HIV and the AIDS pandemic. *Cold Spring Harbor Perspectives in Medicine*, *1*(1), a006841. https://doi.org/10.1101/cshperspect.a006841

Shaw, G. M., & Hunter, E. (2012). HIV transmission. *Cold Spring Harbor Perspectives in Medicine*, *2*(11). https://doi.org/10.1101/cshperspect.a006965

Singh, G. P., S. Dhananjai, M. B. Saini, and P. U. (2007). *A novel crystalline form of lamivudine* (Patent No. 119248 (2007): A1).

Sinha, A. S., Maguire, A. R., & Lawrence, S. E. (2015). Cocrystallization of nutraceuticals. *Crystal Growth & Design*, *15*(2), 984–1009. https://doi.org/10.1021/cg501009c

Sluis-Cremer, N., & Tachedjian, G. (2008). Mechanisms of inhibition of HIV replication by non-nucleoside reverse transcriptase inhibitors. *Virus Research*. https://doi.org/10.1016/j.virusres.2008.01.002

Smerdon, S. J., Jäger, J., Wang, J., Kohlstaedt, L. A., Chirino, A. J., Friedman, J. M., Rice, P. A., & Steitz, T. A. (1994). Structure of the binding site for

nonnucleoside inhibitors of the reverse transcriptase of human immunodeficiency virus type 1. *Proceedings of the National Academy of Sciences*, *91*(9), 3911–3915. https://doi.org/10.1142/9789811215865_0030

Smith, A. J., Kim, S.-H., Duggirala, N. K., Jin, J., Wojtas, L., Ehrhart, J., Giunta, B., Tan, J., Zaworotko, M. J., & Shytle, R. D. (2013). Improving lithium therapeutics by crystal engineering of novel ionic cocrystals. *Molecular Pharmaceutics*, *10*(12), 4728–4738. https://doi.org/10.1021/mp400571a

Smyth, R. P., Davenport, M. P., & Mak, J. (2012). The origin of genetic diversity in HIV-1. *Virus Research*, *169*(2), 415–429. https://doi.org/10.1016/j.virusres.2012.06.015

Somoskovi, A., Parsons, L. M., & Salfinger, M. (2001). The molecular basis of resistance to isoniazid, rifampin, and pyrazinamide in Mycobacterium tuberculosis. *Respiratory Research*, *2*(3), 164. https://doi.org/10.1186/rr54

Sonali R. Devne, Vidya N. Kapse, D. P. L. I. (2019). COCRYSTAL: A REVIEW ON PHARMACEUTICAL CORYSTALS DESIGN AND PREPARATION. *World Journal of Pharmaceutical Research*, *8*(7), 1936–1950.

Staničová, J., Miškovský, P., & Šutiak, V. (2001). Amantadine: An antiviral and antiparkinsonian agent. In *Veterinarni Medicina* (Vol. 46, Issues 9–10, pp. 244–256). https://doi.org/10.17221/7884-vetmed

Steed, J. W. (2013a). The role of co-crystals in pharmaceutical design. *Trends in Pharmacological Sciences*, *34*(3), 185–193. https://doi.org/10.1016/j.tips.2012.12.003

Steed, J. W. (2013b). The role of co-crystals in pharmaceutical design. In *Trends in Pharmacological Sciences* (Vol. 34, Issue 3, pp. 185–193). https://doi.org/10.1016/j.tips.2012.12.003

Stephenson, J. (1997). The art of'HAART': researchers probe the potential and limits of aggressive HIV treatments. *Jama*, *277*(8), 614–616. https://doi.org/10.1001/jama.1997.03540320016008

Stieger, N., Aucamp, M., Zhang, S. W., & De Villiers, M. M. (2012). Hot-stage

optical microscopy as an analytical tool to understand solid-state changes in pharmaceutical materials. *American Pharmaceutical Review*, *15*(2), 32–36.

Stieger, N., Liebenberg, W., Wessels, J. C., Samsodien, H., & Caira, M. R. (2010). Channel inclusion of primary alcohols in isostructural solvates of the antiretroviral nevirapine: An X-ray and thermal analysis study. *Structural Chemistry*. https://doi.org/10.1007/s11224-010-9610-1

Strohl, W. R. (2000). The role of natural products in a modern drug discovery program. *Drug Discovery Today*, *5*(2), 39–41. https://doi.org/10.1016/s1359-6446(99)01443-9

Sun, C. C. (2013). Cocrystallization for successful drug delivery. *Expert Opinion on Drug Delivery*, *10*(2), 201–213. https://doi.org/10.1517/17425247.2013.747508

Surov, A. O., Voronin, A. P., Manin, A. N., Manin, N. G., Kuzmina, L. G., Churakov, A. V, & Perlovich, G. L. (2014). Pharmaceutical cocrystals of diflunisal and diclofenac with theophylline. *Molecular Pharmaceutics*, *11*(10), 3707–3715. https://doi.org/10.1021/mp5004652

Swapna, B., Maddileti, D., & Nangia, A. (2014). Cocrystals of the tuberculosis drug isoniazid: Polymorphism, isostructurality, and stability. *Crystal Growth and Design*. https://doi.org/10.1021/cg501182t

Tantillo, C., Ding, J., Jacobo-Molina, A., Nanni, R. G., Boyer, P. L., Hughes, S. H., Pauwels, R., Andries, K., Janssen, P. A. J., & Arnold, E. (1994). Locations of anti-AIDS drug binding sites and resistance mutations in the three-dimensional structure of HIV-1 reverse transcriptase: implications for mechanisms of drug inhibition and resistance. *Journal of Molecular Biology*, *243*(3), 369–387. https://doi.org/10.1006/jmbi.1994.1665

Tao, Q., Chen, J.-M., Ma, L., & Lu, T.-B. (2012). Phenazopyridine cocrystal and salts that exhibit enhanced solubility and stability. *Crystal Growth & Design*, *12*(6), 3144–3152. https://doi.org/10.1021/cg300327x

Télessy, I. G. (2018). Nutraceuticals. In *The Role of Functional Food Security in Global Health*. https://doi.org/10.1016/B978-0-12-813148-0.00024-4

References

Tenover, F. C. (2006). Mechanisms of antimicrobial resistance in bacteria. *The American Journal of Medicine*, *119*(6), S3–S10. https://doi.org/10.1016/j.amjmed.2006.03.011

Thakur, T. S., Dubey, R., & Desiraju, G. R. (2015). Intermolecular atom-atom bonds in crystals - A chemical perspective. In *IUCrJ*. https://doi.org/10.1107/S205225251500189X

Thakuria, R., Delori, A., Jones, W., Lipert, M. P., Roy, L., & Rodr\'\iguez-Hornedo, N. (2013). Pharmaceutical cocrystals and poorly soluble drugs. *International Journal of Pharmaceutics*, *453*(1), 101–125. https://doi.org/10.1016/j.ijpharm.2012.10.043

Thakuria, R., & Sarma, B. (2018). Drug-Drug and Drug-Nutraceutical Cocrystal/Salt as Alternative Medicine for Combination Therapy: A Crystal Engineering Approach. *Crystals*, *8*(2), 101. https://doi.org/10.3390/cryst8020101

Thipparaboina, R., Kumar, D., Chavan, R. B., & Shastri, N. R. (2016). Multidrug co-crystals: towards the development of effective therapeutic hybrids. *Drug Discovery Today*, *21*(3), 481–490. https://doi.org/10.1016/j.drudis.2016.02.001

Toossi, Z., Mayanja-Kizza, H., Hirsch, C. S., Edmonds, K. L., Spahlinger, T., Hom, D. L., Aung, H., Mugyenyi, P., Ellner, J. J., & Whalen, C. W. (2001). Impact of tuberculosis (TB) on HIV-1 activity in dually infected patients. *Clinical & Experimental Immunology*, *123*(2), 233–238. https://doi.org/10.1046/j.1365-2249.2001.01401.x

Trask, A. V., & Jones, W. (2005). Crystal engineering of organic cocrystals by the solid-state grinding approach. In *Topics in Current Chemistry* (Vol. 254, pp. 41–70). https://doi.org/10.1007/b100995

Trask, A. V, Motherwell, W. D. S., & Jones, W. (2005). Pharmaceutical cocrystallization: engineering a remedy for caffeine hydration. *Crystal Growth & Design*, *5*(3), 1013–1021. https://doi.org/10.1021/cg0496540

Trueba, G. (2014). The origin of human pathogens. In *Confronting Emerging Zoonoses: The One Health Paradigm* (pp. 3–11). Springer Japan. https://doi.org/10.1007/978-4-431-55120-1_1

Udwadia, Z. F., Amale, R. A., Ajbani, K. K., & Rodrigues, C. (2012). Totally drug-resistant tuberculosis in India. *Clinical Infectious Diseases*, *54*(4), 579–581. https://doi.org/10.1093/cid/cir889

UNAIDS. (2019). Global HIV and AIDS statistics 2019 Fact sheet. *Global HIV and AIDs Ststistics, World AIDS Day 2019 Fact Sheet*.

UNAIDS, U. (2013). *AIDS epidemic update: November 2009*.

Unissa, A. N., Subbian, S., Hanna, L. E., & Selvakumar, N. (2016). Overview on mechanisms of isoniazid action and resistance in Mycobacterium tuberculosis. *Infection, Genetics and Evolution*, *45*, 474–492. https://doi.org/10.1016/j.meegid.2016.09.004

Van Hoogevest, P., Liu, X., & Fahr, A. (2011). Drug delivery strategies for poorly water-soluble drugs: The industrial perspective. *Expert Opinion on Drug Delivery*, *8*(11), 1481–1500. https://doi.org/10.1517/17425247.2011.614228

Van Vaerenbergh, K., Harrer, T., Schmit, J.-C., Carbonez, A., Fontaine, E., Kurowski, M., Grünke, M., Löw, P., Rascu, A., Schmidt, B., & others. (2002). Initiation of HAART in drug-naive HIV type 1 patients prevents viral breakthrough for a median period of 35.5 months in 60% of the patients. *AIDS Research and Human Retroviruses*, *18*(6), 419–426. https://doi.org/10.1089/088922202753614182

Vangala, V. R., Chow, P. S., & Tan, R. B. H. (2011). Characterization, physicochemical and photo-stability of a co-crystal involving an antibiotic drug, nitrofurantoin, and 4-hydroxybenzoic acid. *CrystEngComm*, *13*(3), 759–762. https://doi.org/10.1039/c0ce00772b

Vázquez-Laslop, N., & Mankin, A. S. (2018). How macrolide antibiotics work. *Trends in Biochemical Sciences*, *43*(9), 668–684. https://doi.org/10.1016/j.tibs.2018.06.011

Veal, G. J., & Back, D. J. (1995). Metabolism of zidovudine. *General Pharmacology*, *26*(7), 1469–1475. https://doi.org/10.1016/0306-3623(95)00047-X

Velayati, A. A., Masjedi, M. R., Farnia, P., Tabarsi, P., Ghanavi, J., ZiaZarifi, A. H.,

& Hoffner, S. E. (2009). Emergence of new forms of totally drug-resistant tuberculosis bacilli: super extensively drug-resistant tuberculosis or totally drug-resistant strains in Iran. *Chest Journal*, *136*(2), 420–425. https://doi.org/10.1378/chest.08-2427

Vercauteren, J., Wensing, A. M. J., van de Vijver, D. A. M. C., Albert, J., Balotta, C., Hamouda, O., Kücherer, C., Struck, D., Schmit, J.-C., Åsjö, B., & others. (2009). Transmission of drug-resistant HIV-1 is stabilizing in Europe. *Journal of Infectious Diseases*, *200*(10), 1503–1508. https://doi.org/10.1086/644505

Verma, G., & Mishra, M. K. (2016). Pharmaceutical preformulation studies in formulation and development of new drug: A review. *International Journal of Pharmaceutical Sciences and Research*, *7*(6), 2313–2320. https://doi.org/10.13040/IJPSR.0975-8232.7(6).2313-20

Vigilante, N. J., & Mehta, M. A. (2017). A 13C solid-state NMR investigation of four cocrystals of caffeine and theophylline. *Acta Crystallographica Section C: Structural Chemistry*, *73*(3), 234–243. https://doi.org/10.1107/S2053229617000869

Vinesh, V., Sevukarajan, M., Rajalakshmi, R., Chowdary, G. T., & Haritha, K. (2013). Enhancement of solubility of tadalafil by cocrystal approach. *Int. Res. J. Pharm*, *4*, 218–223. https://doi.org/10.7897/2230-8407.04444

Vishweshwar, P., McMahon, J. A., Bis, J. A., & Zaworotko, M. J. (2006). Pharmaceutical co-crystals. *Journal of Pharmaceutical Sciences*, *95*(3), 499–516. https://doi.org/10.1002/jps.20578

Vishweshwar, P., Nangia, A., & Lynch, V. M. (2003). Molecular complexes of homologous alkanedicarboxylic acids with isonicotinamide: X-ray crystal structures, hydrogen bond synthons, and melting point alternation. *Crystal Growth & Design*, *3*(5), 783–790. https://doi.org/10.1021/cg034037h

Vogt, F. G., Clawson, J. S., Strohmeier, M., Edwards, A. J., Pham, T. N., & Watson, S. A. (2009). Solid-state NMR analysis of organic cocrystals and complexes. *Crystal Growth and Design*, *9*(2), 921–937. https://doi.org/10.1021/cg8007014

Walker, B. D., & Burton, D. R. (2008). Toward an AIDS vaccine. *Science*, *320*(5877),

760–764. https://doi.org/10.1126/science.1152622

Wang, T., Stevens, J. S., Vetter, T., Whitehead, G. F. S., Vitorica-Yrezabal, I. J., Hao, H., & Cruz-Cabeza, A. J. (2018). Salts, Cocrystals, and Ionic Cocrystals of a "simple" Tautomeric Compound. *Crystal Growth and Design*, *18*(11), 6973–6983. https://doi.org/10.1021/acs.cgd.8b01159

Wechter, W. J., Johnson, M. A., Hall, C. M., Warner, D. T., Berger, A. E., Wenzel, A. H., Gish, D. T., & Neil, G. L. (1975). Nucleic acids. 14. ara-Cytidine acylates. Use of drug design predictors in structure-activity relation correlation. *Journal of Medicinal Chemistry*, *18*(4), 339–344. https://doi.org/10.1021/jm00238a003

Wheeler, W. H., Ziebell, R. A., Zabina, H., Pieniazek, D., Prejean, J., Bodnar, U. R., Mahle, K. C., Heneine, W., Johnson, J. A., Hall, H. I., & others. (2010). Prevalence of transmitted drug resistance associated mutations and HIV-1 subtypes in new HIV-1 diagnoses, US--2006. *Aids*, *24*(8), 1203–1212. https://doi.org/10.1097/QAD.0b013e3283388742

Who. (2010). Global Tuberculosis Control. WHO 2010. In *Control: Vol. WHO/HTM/TB* (p. 218). https://doi.org/WHO/HTM/TB 2010.7

WHO. (2013). World Health Organization 2013 Global Tuberculosis Report. *Http://Apps.Who.Int/Iris/Bitstream/10665/91355/1/9789241564656_eng.Pdf*.

WHO. (2016). Global Tuberkulosis Report 2016. *European Respiratory Journal*, *44*(1), 23–63. https://doi.org/10.1183/09031936.00188313

Williams, B. G., & Dye, C. (2003). Antiretroviral drugs for tuberculosis control in the era of HIV/AIDS. *Science*, *301*(5639), 1535–1537. https://doi.org/10.1126/science.1086845

Williams, K. J. (2009). The introduction of "chemotherapy" using arsphenamine - The first magic bullet. *Journal of the Royal Society of Medicine*, *102*(8), 343–348. https://doi.org/10.1258/jrsm.2009.09k036

World Health Organization. (2014). Antimicrobial resistance - global report on surveillance. *World Health Organization*, *61*(3), 383–394. https://doi.org/10.1007/s13312-014-0374-3

References

World Health Organization. (2019). *New report calls for urgent action to avert antimicrobial resistance crisis*.

Wright, G. D. (2005). Bacterial resistance to antibiotics: enzymatic degradation and modification. *Advanced Drug Delivery Reviews*, *57*(10), 1451–1470. https://doi.org/10.1016/j.addr.2005.04.002

Wright, G. D. (2016). Antibiotic Adjuvants: Rescuing Antibiotics from Resistance. *Trends in Microbiology*, *24*(11), 928. https://doi.org/10.1016/j.tim.2016.06.009

Wu, Q., Yang, Z., Nie, Y., Shi, Y., & Fan, D. (2014). Multi-drug resistance in cancer chemotherapeutics: mechanisms and lab approaches. *Cancer Letters*, *347*(2), 159–166. https://doi.org/10.1016/j.canlet.2014.03.013

Xu, Y., Southern, S. A., Szell, P. M. J., & Bryce, D. L. (2016). The role of solid-state nuclear magnetic resonance in crystal engineering. *CrystEngComm*. https://doi.org/10.1039/c6ce01206j

Yadav, B., Gunnam, A., Thipparaboina, R., Nangia, A. K., & Shastri, N. R. (2019). Hepatoprotective Cocrystals of Isoniazid: Synthesis, Solid State Characterization, and Hepatotoxicity Studies. *Crystal Growth and Design*, *19*(9), 5161–5172. https://doi.org/10.1021/acs.cgd.9b00541

Yadav, A. V, Shete, A. S., Dabke, A. P., Kulkarni, P. V, & Sakhare, S. S. (2009). Co-crystals: a novel approach to modify physicochemical properties of active pharmaceutical ingredients. *Indian Journal of Pharmaceutical Sciences*, *71*(4), 359. https://doi.org/10.4103/0250-474X.57283

Yerly, S., von Wyl, V., Ledergerber, B., Böni, J., Schüpbach, J., Bürgisser, P., Klimkait, T., Rickenbach, M., Kaiser, L., Günthard, H. F., & others. (2007). Transmission of HIV-1 drug resistance in Switzerland: a 10-year molecular epidemiology survey. *Aids*, *21*(16), 2223–2229. https://doi.org/10.1097/QAD.0b013e3282f0b685

Zaffiri, L., Gardner, J., & Toledo-Pereyra, L. H. (2012). History of Antibiotics. From Salvarsan to Cephalosporins. *Journal of Investigative Surgery*, *25*(2), 67–77. https://doi.org/10.3109/08941939.2012.664099

References

Zaini, E., Rachmaini, F., Armin, F., & Fitriani, L. (2015). Preparation and characterization of binary mixture of efavirenz and nicotinamide. *Oriental Journal of Chemistry*, *31*(4), 2271–2276. https://doi.org/10.13005/ojc/310454

Žegarac, M., Lekšić, E., Šket, P., Plavec, J., Bogdanović, M. D., Bučar, D.-K., Dumić, M., & Meštrović, E. (2014). A sildenafil cocrystal based on acetylsalicylic acid exhibits an enhanced intrinsic dissolution rate. *CrystEngComm*, *16*(1), 32–35. https://doi.org/10.1039/c3ce42013b

Zhang, Y., Shi, W., Zhang, W., & Mitchison, D. (2014). Mechanisms of Pyrazinamide Action and Resistance. *Microbiology Spectrum*, *2*(4), 1–12. https://doi.org/10.1128/microbiolspec.mgm2-0023-2013

Zhang, Y., Wade, M. M., Scorpio, A., Zhang, H., & Sun, Z. (2003). Mode of action of pyrazinamide: disruption of Mycobacterium tuberculosis membrane transport and energetics by pyrazinoic acid. *Journal of Antimicrobial Chemotherapy*, *52*(5), 790–795. https://doi.org/10.1093/jac/dkg446

Zinner, R. G., Barrett, B. L., Popova, E., Damien, P., Volgin, A. Y., Gelovani, J. G., Lotan, R., Tran, H. T., Pisano, C., Mills, G. B., & others. (2009). Algorithmic guided screening of drug combinations of arbitrary size for activity against cancer cells. *Molecular Cancer Therapeutics*, *8*(3), 521–532. https://doi.org/10.1158/1535-7163.MCT-08-0937

Zumla, A., Abubakar, I., Raviglione, M., Hoelscher, M., Ditiu, L., Mchugh, T. D., Squire, S. B., Cox, H., Ford, N., McNerney, R., & others. (2012). Drug-resistant tuberculosis—current dilemmas, unanswered questions, challenges, and priority needs. *Journal of Infectious Diseases*, *205*(suppl 2), S228--S240. https://doi.org/10.1093/infdis/jir858

APPENDICES

Appendix A

Appendix A presents a list of all experiments done to screen and produce co-crystals and other solid-state hybrids of selected APIs.

Co-crystallization outcomes

API 1	API 2	Product	ratio	Method	Solvent	results
Nevirapine	Amantadine	NVAD	(1:1)	GR	none	NVP
			(1:2)	GR	none	NVP
			(1:3)	GR	none	NVP
			(1:4)	GR	none	NVP
			(1:1)	SE	Ethanol	mixture
			(1:1)	SE	Acetonitrile	NVP
			(1:4)	SE	Acetonitrile	NVP
			(1:1)	SE	Toluene	NVP
			(1:1)	SE	Methanol	Mixture
			(2:1)	SE	Methanol	mixture

	efavirenz	NEF	(1:1)	GR	None	Co-crystal
		NEF	(2:1)	GR	None	Co-crystal
		NEF	(3:1)	GR	none	Co-crystal
		NEF	(1:1)	AG	Toluene	Co-crystal
			(1:1)	SE	Butanol	NVP solvated
			(1:1)	SE	acetonitrile	NVP
			(1:1)	SE	Butanol	NVP
			(1:1)	SE	acetone	NVP
			(1:2)	SE	Ethanol	NVP
	isoniazid	NVISO	(1:1)	GR	none	Eutectic
		NVISO	(1:4)	SE	Methanol	Eutectic
		NVISO	(3:1)	SE	THF	solvated
		NVISO	(1:1)	GR	none	eutectic
		NVISO	(2:1)	GR	none	Eutectic
		NVISO	(3:1)	GR	none	Eutectic
		NVISO	(1:2)	SE	Ethanol	Solvate
		NVISO	(1:1)	LAG	Ethanol	eutectic

	NVISO	(1:2)	LAG	Ethanol	Eutectic
zidovudine	NVZA2	(1:1)	SE	1,4-Dioxan	Co-crystal
	NVZA2	(1:1)	SE	1,4-Dioxan	Co-crystal
		(1:1)	SE	Methanol	mixture
		(1:1)	SE	Propan-2-ol	solvated
	NVZA2	(1:2)	SE	1,4-Dioxan	Co-crystal
		(1:1)	SE	Acetonitrile	NVP
		(1:2)	SE	acetonitrile	-
		(1:3)	SE	actonitrile	-
		(1:1)	SE	dichloromethane	-
		(1:1)	SE	Toluene	-
		(1:1)	SE	THF- diethyl ether	-
		(1:1)	SE	butanol	NVP
	NVZA1	(1:1)	GR	None	eutectic
		(1:1)	SE	methanol	-
		(1:1)	SE	ether acetate	NVP
		(1:1)	SE	acetonitrile	NVP

			(1:1)	SE	water	Solvate
			(2:1)	AG	1,4-dioxan+THF	
			(1:1)	Slurry	1,4-Dioxane	AZT
			(1:2)	Slurry	1,4-Dioxane	AZT
			(2:1)	Slurry	1,4-dioxane+THF	Amorphous
		NVZA3	(1:3)	SE	1,4-Dioxane	Co-crystal
	Lamivudine	NL	(1:1)	SE	Cyclo6ne&EtOH	mixture
		NVP	(1:1)	SE	THF	solvate
			(1:1)	SE	Methanol	NVP
			(1:1)	SE	Ethanol	NVP
			(1:1)	SE	acetonitrile	NVP
			(1:1)	SE	THF +Methanol	NVP
			(1:1)	SE	Butanol	mixture
			(4:1)	SE	Butanol	mixture
		NL	(1:1)	GR	none	Binary eutectic NL
		NL	(1:2)	GR	none	Binary eutectic NL
		NL	(2:3)	GR	none	Binary eutectic NL

			(2:1)	GR	none	mixture
			(3:1)	GR	none	mixture
efavirenz	zidovudine	EFZA	(1:1)	GR	None	Co-crystal
		EFZA	(1:1)	GR	None	Co-crystal
		EFZA	(1:2)	GR	None	Co-crystal
		EFZA	(1:3)	GR	None	Co-crystal
		EFZA	(1:1)	LAG	Methanol	Co-crystal
		EFZA	(2:1)	GR	None	Co-crystal
			(1:1)	LAG	1,4-Dioxane	-
			(1:1)	SE	Acetonitrile	-
			(1:1)	SE	DMSO	-
			(1:1)	SE	Ethyl acetate	-
			(1:1)	SE	Butanone-dioxane	-
			(1:1)	SE	1,4-Dioxane	-
			(1:1)	SE	1-petanol	-
		EFZA	(1:1)	Slurry	Ethanol	Co-crystal
	Lamivudine	EL1	(1:1)	GR	none	Eutectic

			(1:1)	SE	acetonitrile	3TC
			(2:1)	SE	acetonitrile	3TC
		EL2	(1:2)	GR	None	Co-crystal
		EL2	(1:3)	GR	None	Co-crystal
		EL2	(1:4)	GR	None	Co-crystal
		EL1	(3:2)	LAG	Ethanol	Eutectic
		EL1	(2:1)	GR	None	Eutectic
	Amantadine	EFAD	(1:1)	GR	None	Amorphous
		EFAD	(1:2)	GR	None	Amorphous
			(1:1)	SE	toluene	-
			(1:1)	SE	acetonitrile	-
			(1:1)	SE	methanol	-
	Isoniazid	EFINH	(1:1)	GR	None	Co-crystal
			(1:2)	GR	None	Mixture
			(1:3)	GR	None	Mixture
Zidovudine	lamivudine	LMZT	(1:1)	GR	None	eutectic
			(1:1)	SE	Diethyl ether-methanol	-

			(1:1)	SE	Chloroform	-
			(1:1)	SE	1-propanol	-
			(1:1)	SE	Butane-1-ol	-
		LMZA	(2:1)	GR	None	eutectic
			(1:2)	GR	None	Mixture
			(1:3)	GR	None	Mixture
	Isoniazid	INHZA	(1:1)	GR	None	eutectic
		INHZA	(1:3)	GR	none	eutectic
		INHZA	(1:2)	GR	None	eutectic
	pyrazinamide		(1:1)	GR	None	eutectic
			(1:2)	GR	None	eutectic
Zidovudine	1-adamantylamine	ADZA	(1:1)	SE	acetonitrile	-
		ADZA	(1:1)	SE	Methanol	salt
1-adamantylamine	Lamivudine	LMAD	(1:1)	SE	Octanol	Lamivudine
	Nevirapine		(1:1)	SE	acetonitrile	NVP
			(1:1)	SE	acetonitrile	NVP
			(1:1)	SE	Toluene	NVP

			(1:1)	GR	None	NVP
			(1:2)	GR	None	NVP
			(1:3)	GR	None	NVP
			(1:4)	GR	none	NVP
	Efavirenz	EFAD	(1:1)	SE	Methanol	nothing
			(1:1)	SE	toluene	-
			(1:1)	SE	acetonitrile	-
Lamivudine	isoniazid	LMISO	(1:1)	GR	None	eutectic
		LMISO	(2:1)	GR	none	eutectic
Isoniazid	pyrazinamide	INHPZA1	(1:1)	DG	None	eutectic
		INHPZA2	(1:1)	SE	ethanol 96%	Solvate
		INHPZA2	(1:1)	SE	Propan-2-ol	Solvate
		INHPZA1	(1:1)	SE	Methanol	eutectic
			(1:1)	SE	Diethyl ether, TFE-MeOH	-
	Glutaric acid	INHGA(2:1)	(2:1)	DG	none	Co-crystal
		(INHGA(2:1)	(2:1)	LAG	ethanol 96%	Co-crystal

pyrazinamide	Glutaric acid	PGA(2:1) PGA(2:1)	(2:1) (2:1)	DG LAG	none ethanol 96%	Co-crystal Co-crystal

CC: co-crystal, DG= dry grinding, LAG= Liquid-assisted grinding, SE= solvent evaporation

Appendix B1

Accepted Review

Pharmaceutical Co-crystal: An alternative strategy for enhanced physicochemical properties and drug synergy.

Jean Baptiste Ngilirabanga, Halima Samsodien*

School of Pharmacy, Faculty of Science, University of the Western Cape, Cape Town, Bellville 7535, South Africa.

Correspondance: Halima Samsodien

Email: hsamsodien@uwc.ac.za

A growing number of co-crystals in the literature are proof of how significant the co-crystallization concept has become. Co-crystallization enhances physicochemical properties through the formation of intermolecular interactions between a drug and a co-former. A co-crystal is a single crystalline material consisting of at least two molecular components solid at room temperature and present in a definite stoichiometric ratio. Pharmaceutical co-crystals consist of the active pharmaceutical ingredient and the co-former selected from generally regarded as safe (GRAS) list of the United State Food and Drug Administration. Co-crystal formation requires an understanding of a drug target, a proper choice of a co-former and is only achieved experimentally after several trials. Other beneficial co-crystallization outcomes include binary eutectics, solid dispersions, amorphous forms, etc. Several key issues, including design strategies, co-former selection, and co-crystallization methods; tradition and newly synthetic methods that are more efficient and suitable for large scale have been briefly described. The co-crystal preference is demonstrated with a particular emphasis on multidrug co-crystals and their contribution to the drug combination strategies used for the treatment and management of drug resistance and adverse side effects in serious medical conditions that require the administration of high doses such as HIV/AIDS, tuberculosis, and others.

Keywords: Co-crystallization, pharmaceutical co-crystals, design, co-crystal development, preferences, synergistic co-crystals.

Appendix B2

A published research article

Mechanochemical synthesis and physicochemical characterization of isoniazid and pyrazinamide co-crystals with glutaric acid

Jean Baptiste Ngilirabanga[1], Marique Aucamp[1], Paulo Pires Rosa[2], and Halima Samsodien[1*]

[1] School of Pharmacy, University of the Western Cape, 7535 Cape Town, South Africa

[2] Faculty of Pharmaceutical Sciences, State University of Campinas, Sao Paulo, Brazil

*** Correspondence:** Halima Samsodien
hsamsodien@uwc.ac.za

Keywords: Antitubercular, co-crystallization, mechanochemistry, solid-state grinding, liquid-assisted grinding, characterization, saturation solubility

Abstract

The present work reports two novel pharmaceutical co-crystals 2:1 isoniazid-glutaric acid, and 2:1 pyrazinamide-glutaric acid. Isoniazid and pyrazinamide are key first-line drugs used for the treatment of tuberculosis. The co-crystals were produced *via* solid-state and solvent assisted grinding methods. Thermal characteristics of the samples were obtained using the differential scanning calorimetry, hot stage microscopy, and thermogravimetric analyses. The morphology of the powder samples by scanning electron microscopy, structural analysis by Fourier transform infrared spectroscopy, and powder X-rays diffraction ensured co-crystal formation. Thermal analyses confirmed the co-crystals with new melting transitions ranging between their respective starting materials. Unique morphologies of the co-crystal particles were clear in SEM micrographs. The formation of intermolecular interactions with the co-crystal former was confirmed by the FT-IR spectral band shifting and was supported by distinct PXRD patterns of co-crystals thereby authenticating the successful co-crystal formation. *In vitro* solubility evaluation of the synthesized co-crystals by HPLC suggested a remarkable increase in solubility of both INH and PZA in their respective co-crystals.

Appendix B3

A published research article

Dual-drug co-crystal synthesis for synergistic in vitro effect of three key first-line antiretroviral drugs

Jean Baptiste Ngilirabanga[a], Marique Aucamp[a], Paulo Pires Rosa[b], Yunus Kippie[a], Halima Samsodien[a]*

[a]School of Pharmacy, University of the Western Cape, 7535 Cape Town, South Africa

[b]Faculty of Pharmaceutical Sciences, State University of Campinas, Sao Paulo, Brazil

*** Correspondence:**
Halima Samsodien
hsamsodien@uwc.ac.za

Anti-HIV, Non-nucleoside reverse transcriptase inhibitors, Human immunodeficiency virus, Co-crystals, Mechanochemistry, Solubility

Abstract

Two pharmaceutical solid-state co-crystals EFZA and NEF of two non-nucleoside reverse transcriptase inhibitors (efavirenz, EFV and nevirapine, NVP) and a nucleoside reverse transcriptase inhibitor, zidovudine (AZT) were prepared. Currently, these drugs are essential in various front-line HIV treatment regimens due to their potential in the management of HIV infection. Solid-state principles and solvent-assisted grinding were used for screening of co-crystal preparation. Characterization was carried out using DSC, HSM and TGA, and then complimented by FTIR spectral data and powder X-ray diffraction. HPLC analysis was used for solubility assays. Both co-crystals indicated different thermal behaviour compared to the individual drug components. Differences in vibrational modes within the spectral region and the unique powder X-ray patterns confirmed the identity of EFZA and NEF as new molecular derivatives. Quantitative studies using HPLC indicated an enhanced solubility of the co-crystals at different pH values compared to the parent compounds; thus making these interesting candidates for future formulation.

Appendix B4

A research article (Manuscript Number: JDDST-D-20-00977 under review)

Mechanochemical Synthesis, Characterization and Solubility Evaluation of Zidovudine-Lamivudine Solid Dispersion (Binary Eutectic Mixture)

Jean-Baptiste Ngilirabanga, Marique Aucamp, Halima Samsodien*

School of Pharmacy, Faculty of Science, University of the Western Town, Bellville 7535, South Africa

*** Correspondence:**
Halima Samsodien
hsamsodien@uwc.ac.za

Abstract

Objective: In the present work, solid-state co-grinding, also known as mechanochemistry, is employed to investigate the co-crystal formation between two HIV nucleoside reverse transcriptase inhibitors lamivudine (3TC) and zidovudine (AZT).

Methods: Thermal analyses by DSC, HSM, and TGA provided thermodynamic parameters of the samples over the heating exercise. Infrared spectroscopy enabled evaluation of structural information of LMZT sample while its morphology was assessed using Scanning electron microscopy. Powder X-rays diffraction analysis confirmed the sample's identity.

Results: Eutectic LMZT was obtained from co-grinding. Its lower melting transition compared to pure lamivudine and zidovudine, was confirmed by HSM and DSC. Scanning electron microscopy micrographs indicated that the LMZT sample exhibits irregular, round-shaped particles with smooth surfaces. Infrared spectroscopy revealed weak interactions between 3TC and AZT and Powder X-rays diffraction pattern that's made of a summation of pure APIs diffraction peaks, confirming LMZT as a eutectic mixture. Solubility at 37 °C, in different buffered solutions, to mimic gastrointestinal, was established and the measurement by HPLC indicated that LMZT dual-API solid dispersion exhibited enhanced solubility for both active pharmaceutical ingredients.

Conclusion: Mechanochemistry is a potential and green method for co-crystal synthesis. Co-crystal formation attempt between 3TC and AZT, using solid-state co-grinding resulted in a eutectic LMZT. Characterisation revealed a lower melting transition and enhanced solubility associated with the resultant eutectic, making this an interesting dual-API delivery system.

Keywords: HIV; reverse transcriptase inhibitors; mechanochemical synthesis; co-crystallization; thermal analysis; spectral evaluation; in-vitro solubility

NB: Journal of drug delivery science and technology (Under review)

Appendix B5

A manuscript ready for submission

Screening for the co-crystal between two co-administered reverse transcriptase inhibitors nevirapine and zidovudine and characterization of resultant derivative hybrids

Jean-Baptiste Ngilirabanga, Halima Samsodien*

School of Pharmacy, Faculty of Science, University of the Western Town, Bellville 7535, South Africa

*** Correspondence:**
Halima Samsodien
hsamsodien@uwc.ac.za

Abstract

Screening for the co-crystal between nevirapine and zidovudine was conducted in this work. Multicomponent solid crystals NVZA1, NVZA2 and NVZA3, have been produced and characterized. Solid-state grinding, solvent evaporation, and slurry methods were used to screen for the co-crystals. The physicochemical characterization was carried out using thermal analyses, spectral, crystallographic and solubility measurements. Differential scanning calorimetric analysis, thermo-microscopic observation and thermogravimetric analysis provided thermal behaviors of multicomponent hybrids such as melting transitions, absence/presence of any volatile substances. Fourier-transform infrared spectroscopy and the powder X-ray diffraction respectively provided structural information and confirmed these multicomponent solid crystals. High-pressure liquid chromatography reverse-phase method enabled the quantification of the samples. NVZA1 was confirmed as binary eutectic and both NVZA2 and NVZA3 as dual-drug co-crystals of zidovudine and nevirapine. Eutectic NVZA1 exhibited a lower melting transition than both individual APIs, whereas co-crystals NVZA2 and NVZA3 showed a melting transition between AZT and NVP melting ranges. All three multicomponent solid forms have shown enhanced solubility, making these solid crystal forms potential targets for pharmaceutical formulators.

Keywords: Co-crystals synthesis, antiretroviral drugs, drug combination, characterization, enhanced solubility.

Status: To be submitted

Appendix B6

A research article

Efavirenz-amantadine co-amorphisation induced by the co-grinding method: Synthetic preparation and physicochemical characterization.

Jean-Baptiste Ngilirabanga, Halima Samsodien*

School of Pharmacy, Faculty of Science, University of the Western Cape, Bellville 7535, South Africa

*** Correspondence:**
Halima Samsodien
hsamsodien@uwc.ac.za

Status: Being finalised

Appendix B7

A research article

Non-covalent multicomponent crystals of efavirenz and lamivudine: Synthesis, physicochemical characterization and solubility evaluation

Jean Baptiste Ngilirabanga, Halima Samsodien*

School of Pharmacy, Faculty of Science, University of the Western Town, Bellville 7535, South Africa

*** Correspondence:**
Halima Samsodien
hsamsodien@uwc.ac.za

Abstract

Status: Being finalised

Appendix B8

A review article

Understanding HIV/TB infections, revolutionary treatment and future generation of anti-HIV/TB drugs

Jean Baptiste Ngilirabanga, Halima Samsodien*

School of Pharmacy, Faculty of Science, University of the Western Town, Bellville 7535, South Africa

*** Correspondence:**
Halima Samsodien
hsamsodien@uwc.ac.za

Status: Ready for submission

Appendix B9

Oral Presentation: J.Baptiste Ngilirabanga

Supervisor: Dr Halima Samsodien

Selected antiretroviral and anti-tubercular drug combinations by covalent and non-covalent approaches

Abstract

Introduction: HIV and TB are still a huge global challenge. Drug resistance makes the management of two infections very difficult or impossible in some cases. New treatment regimens are on demand. In this work novel solid-state adducts were prepared from selected nucleoside reverse transcriptase inhibitors viz. nevirapine and efavirenz, lamivudine and zidovudine, antitubercular drugs isoniazid and pyrazinamide, and adamantylamine.

Methods: Neat solid-state, solvent assisted grinding as well as solution co-crystallization of the mixtures in different molar ratio were used in the preparation of the adducts. Characterization was attained using differential scanning calorimetry, hot stage microscopy, thermogravimetric analysis, scanning electron microscopy, Fourier transform infrared spectroscopy and powder X-ray diffraction. High-pressure liquid chromatography was used to determine the solubility profile at 37 °C at varying pH values.

Results: Supramolecular adducts NEF, EFZA, NVZA, LMZT, NL, EL, EFINH, EFAD, INHZA, LMISO, AZTPZA, INHPZA, were successfully produced and show different melting ranges with respect to their respective parent compounds. The differences in vibrational modes within the spectral region as well as the unique powder X-ray patterns of adducts confirmed the newly derivatized adducts. Solubility studies suggested an enhanced solubility at different pH values.

Conclusion: Enhanced physicochemical properties; especially solubility critical for the drug performance, makes these multicomponent solid forms interesting candidates for future formulations.

Keywords: Anti-HIV drug, anti-tubercular, co-crystallization, supramolecular adducts, drug resistance.

Conference: First Conference on Biopharmaceutics Natural Science and Therapeutics (CoBNEsT)

Appendix B10

Oral presentation

SELECTED ANTI-RETROVIRAL AND ANTI-TB DRUG COMBINATIONS VIA NON-COVALENT APPROACHES

JB. Ngilirabanga1, H. Samsodien1

School of Pharmacy, University of the Western Cape, Bellville 7535, Cape Town, South Africa

3220742@myuwc.ac.za

Abstract

Co-crystallisation has shown the abilities to alter not only physicochemical properties but also bioavailability and other properties of the active substances including antiretrovirals and anti-tuberculosis drugs. Resistance as one of the main challenges encountered in HIV and TB treatment and the primary cause of the treatment failure is also related to poverty in properties of available drugs such as solubility. Despite the intervention of fixed-dose combinations (FDC) and Highly Active antiretroviral therapy (HAART), viruses are still able to survive and replicate. This leaves a gap for further search of more efficient drugs.

The study aimed to develop different complexes of four anti-retroviral, nevirapine (NV), efavirenz (EFV), Zidovudine (AZT) and lamivudine (NVP), two anti-TB drugs; isoniazid (INH) and pyrazinamide (PZA) selected from the first-line treatment available of the market and 1-adamantanamine (ADT) via covalent and non-covalent approaches also known as supramolecular chemistry. Using traditional methods of co-crystallisation such as solid-state grinding, liquid assisted grinding and liquid crystallisation, a set of than 20 multicomponent solid forms were prepared and so far analysed by HSM, DSC, TGA and FTIR. Further studies include XRD, SSNMR, and test on stability, dissolution, biological activity, toxicity studies and formulation of the most successful result.

Local interdepartmental seminar

Appendix C

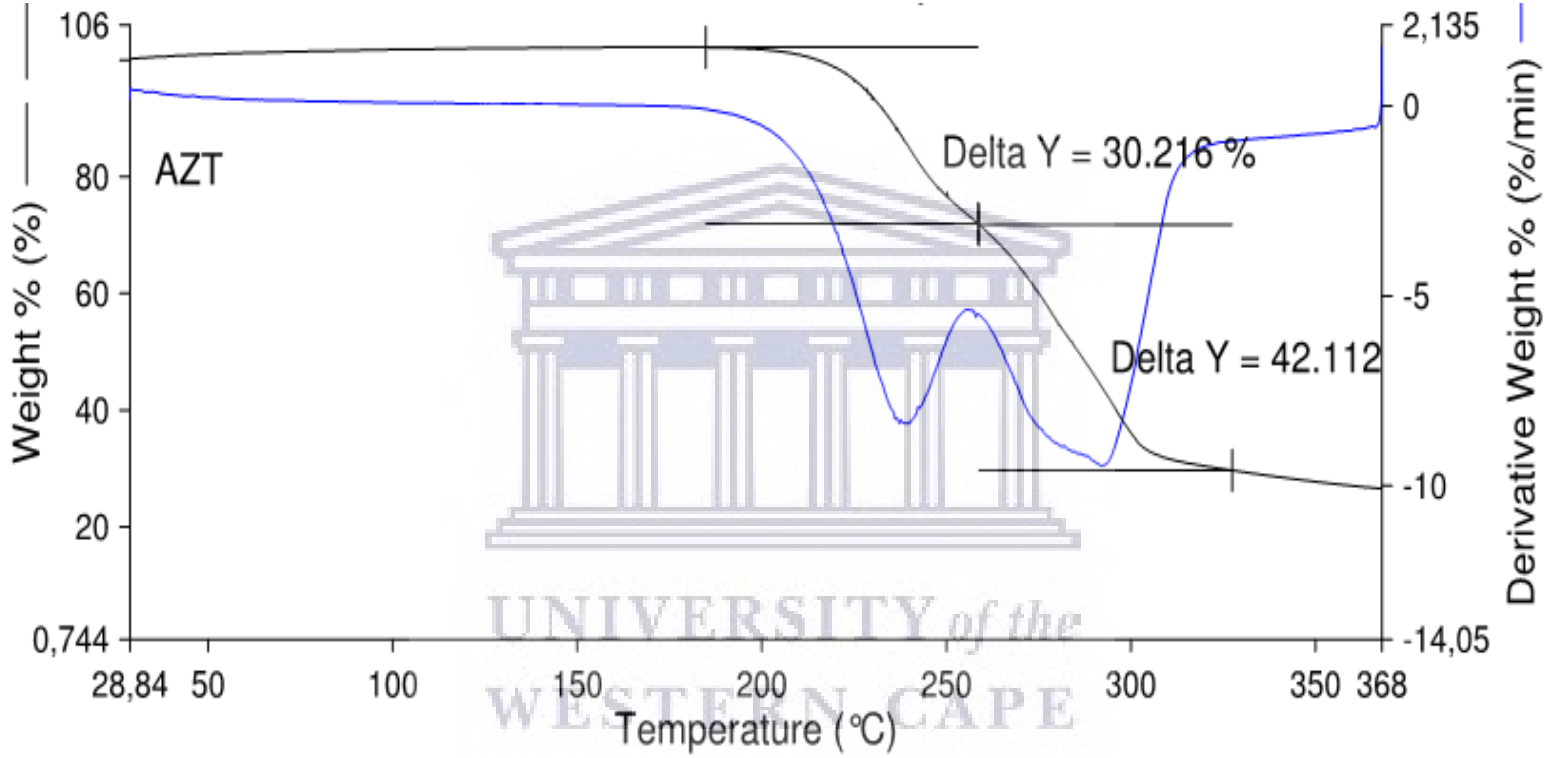

Supporting figure 1: TGA/DTA thermograms of zidovudine

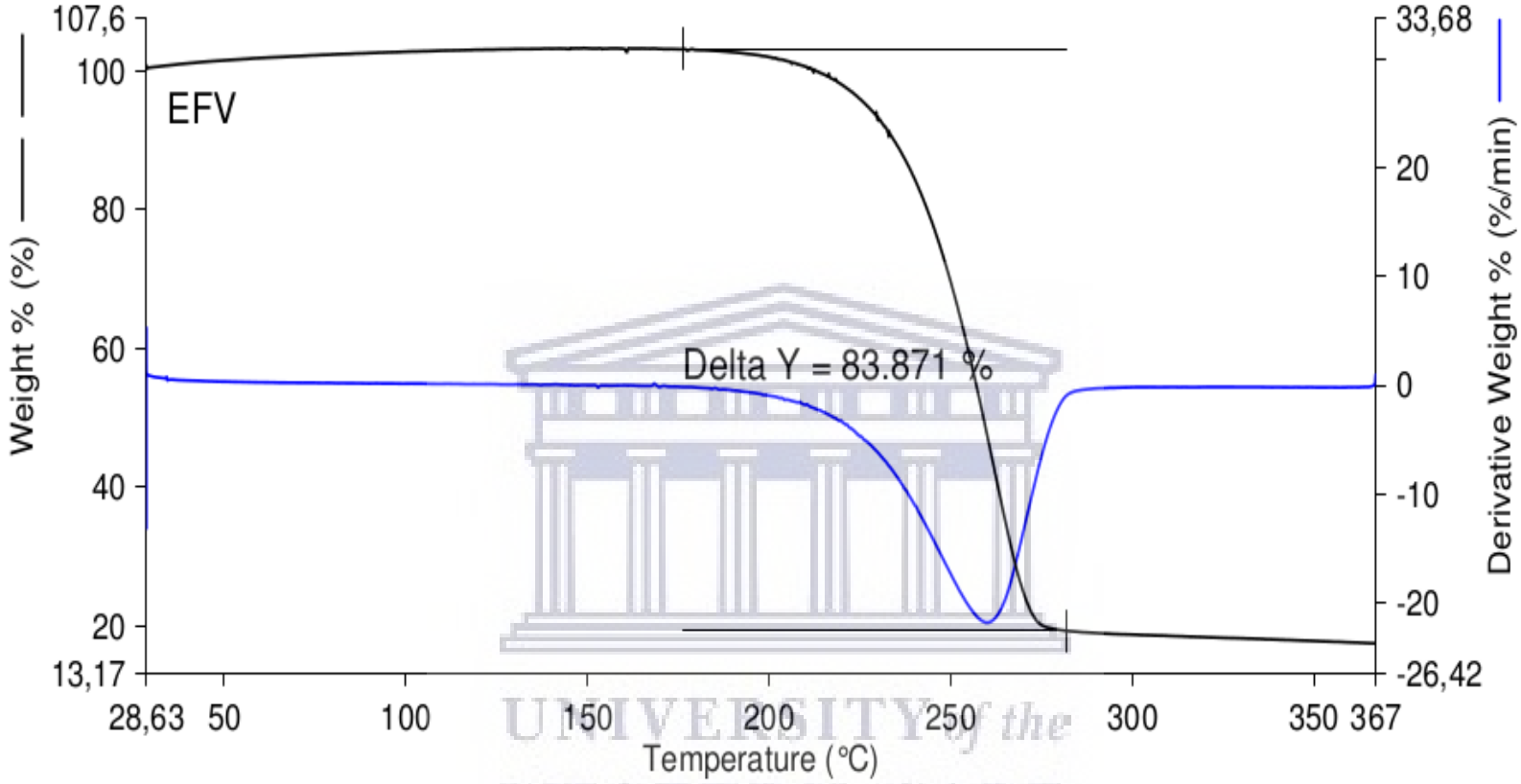

Supporting figure 2: TGA/DTA thermograms of Efavirenz

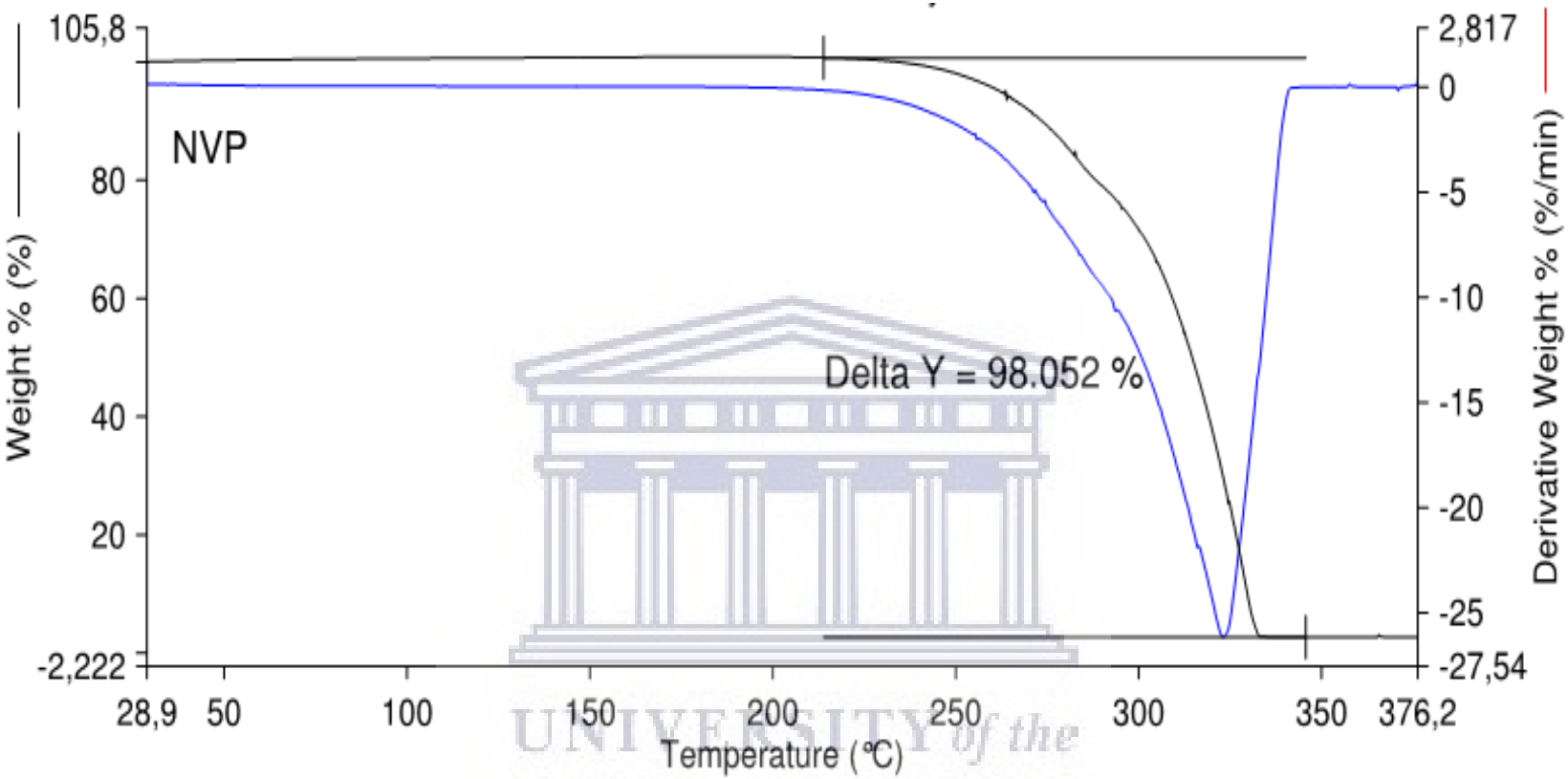

Supporting figure 3: TGA/DTA thermograms of nevirapine

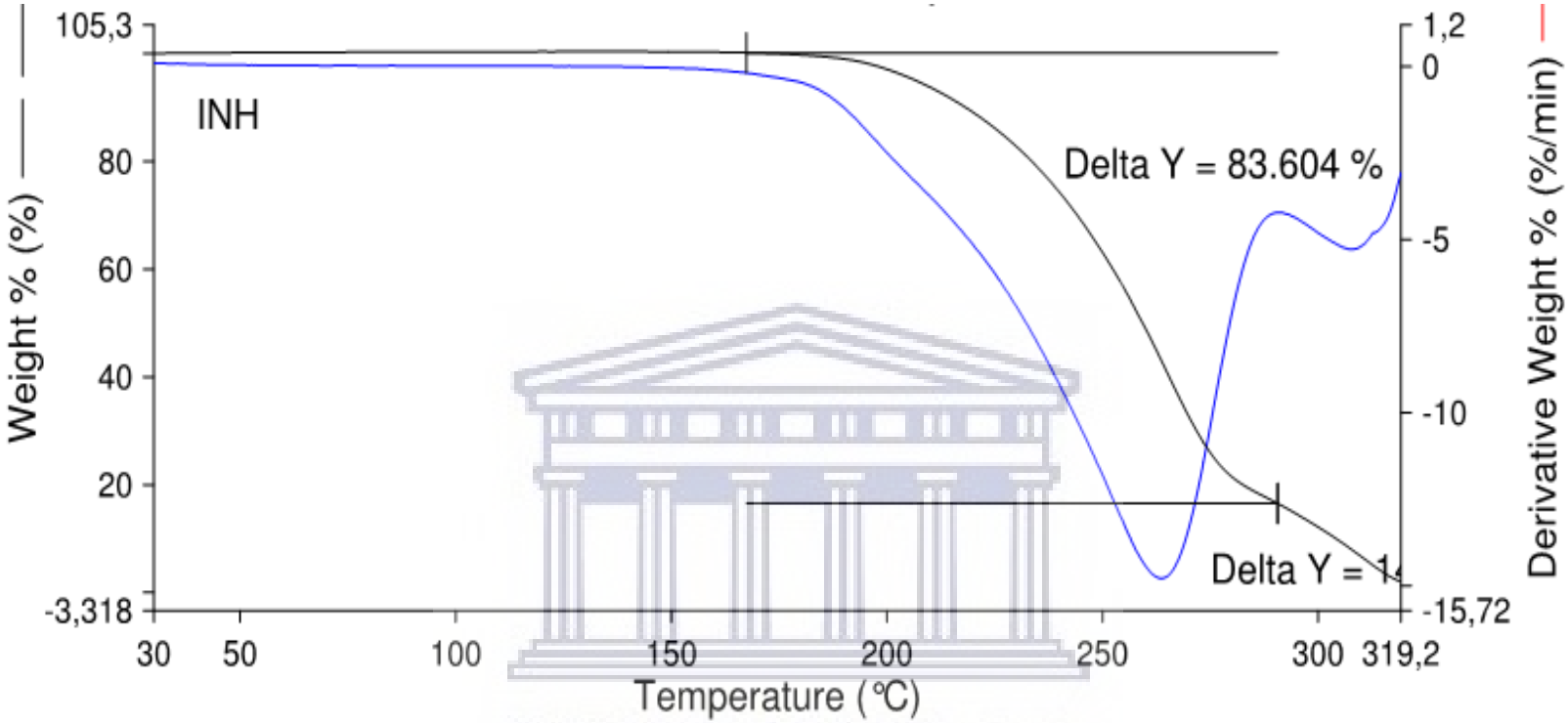

Supporting figure 4: TGA/DTA thermograms of isoniazid

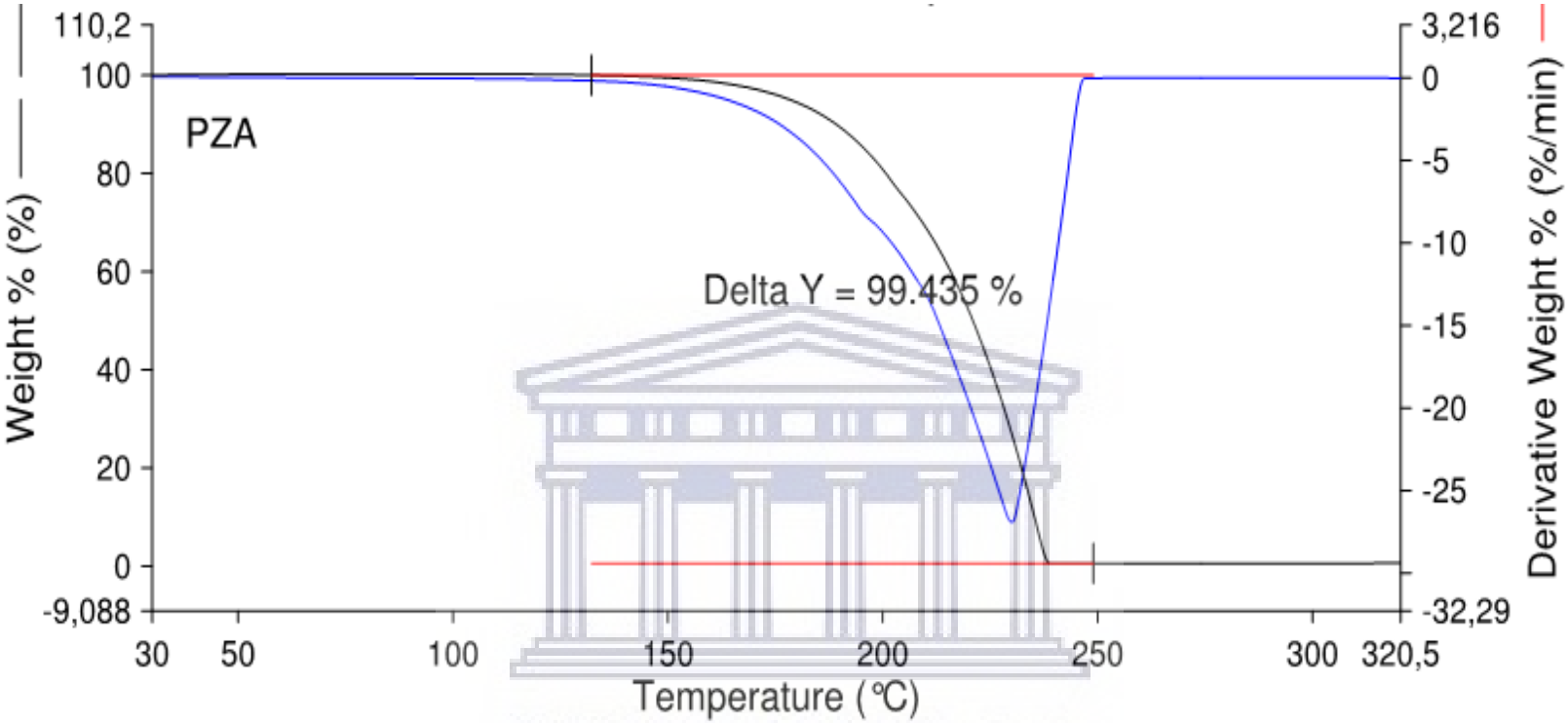

Supporting figure 5: TGA/DTA thermograms of pyrazinamide

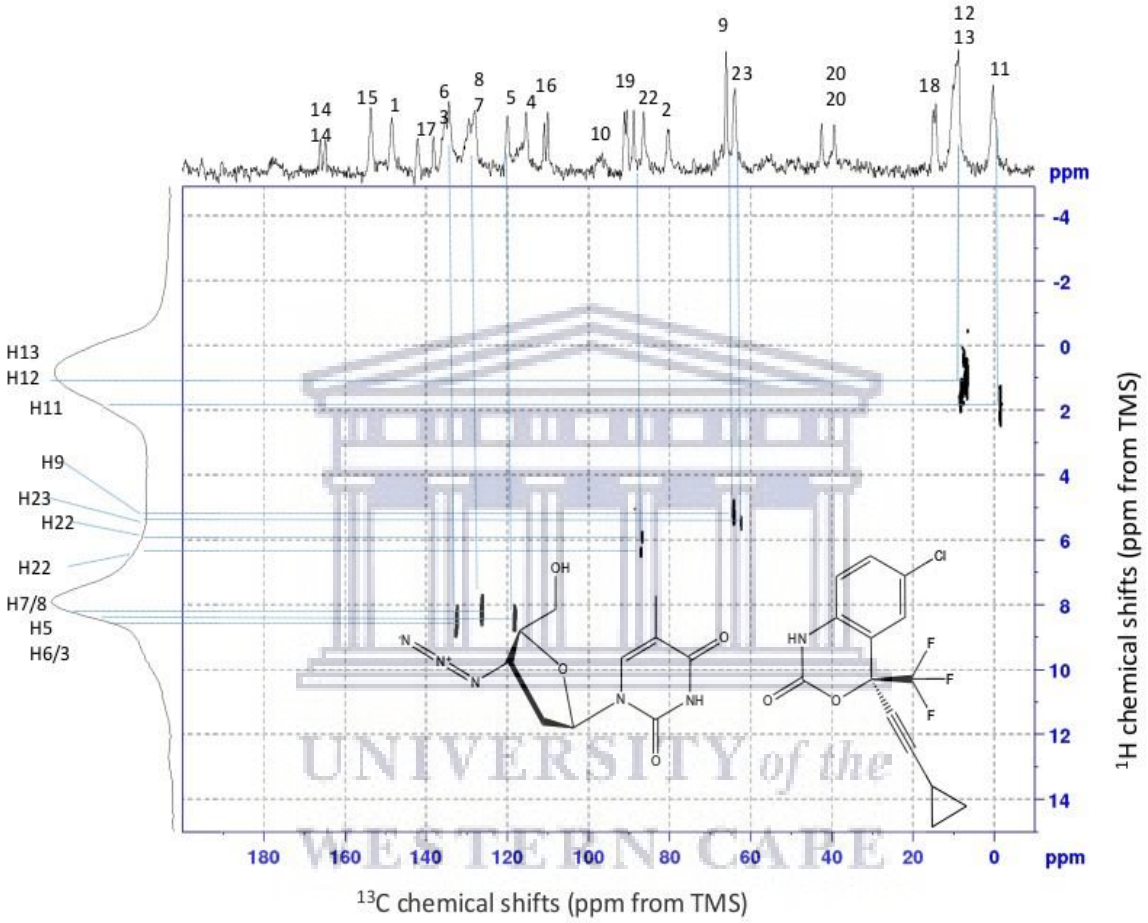

Supporting figure 6: The CP-HETCOR SSNMR experiment of EFZA supramolecular co-crystal

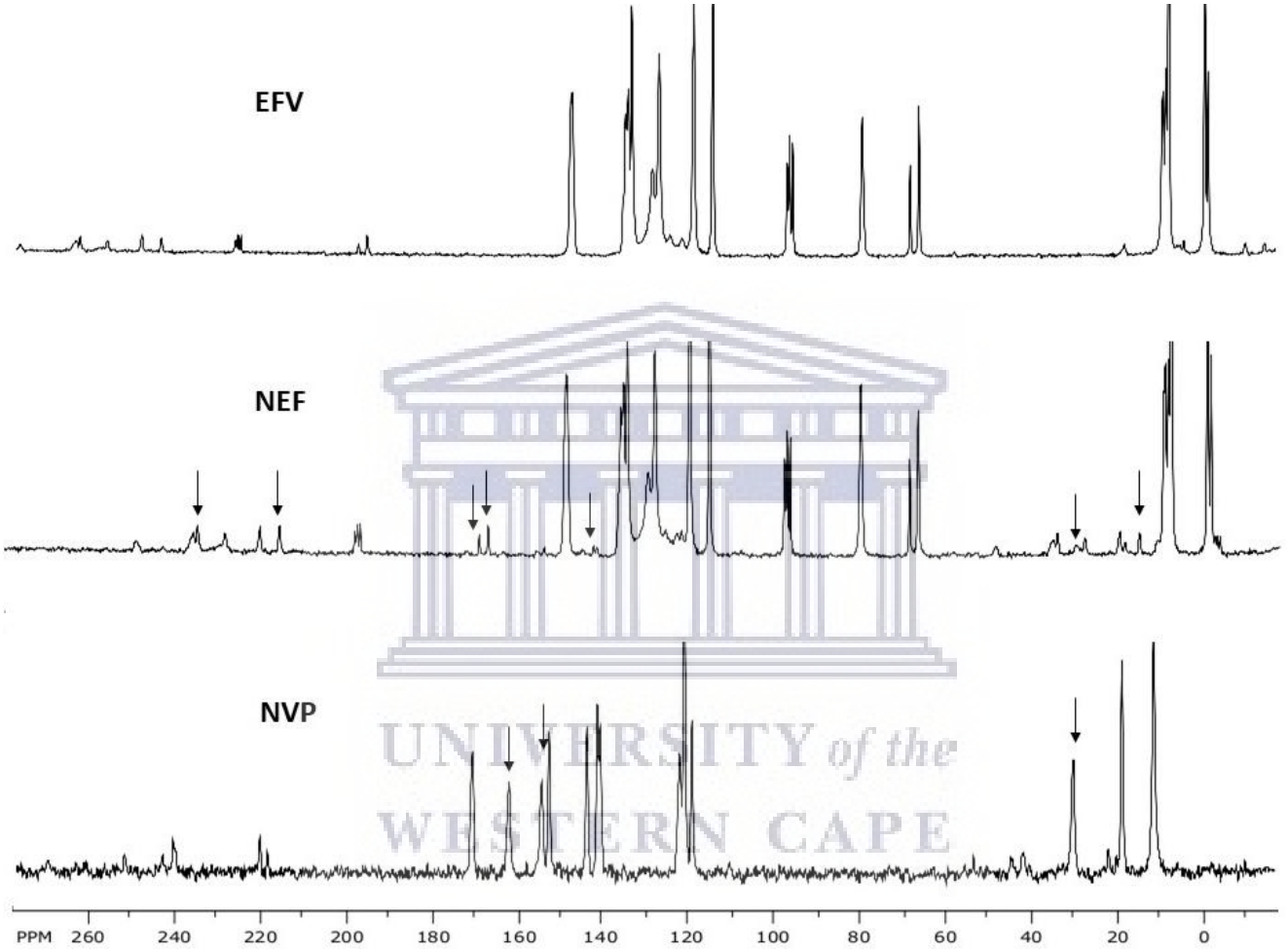

Supporting figure 7:C13 SSNMR spectra of EFV, NVP, and NEF co-crystal compared

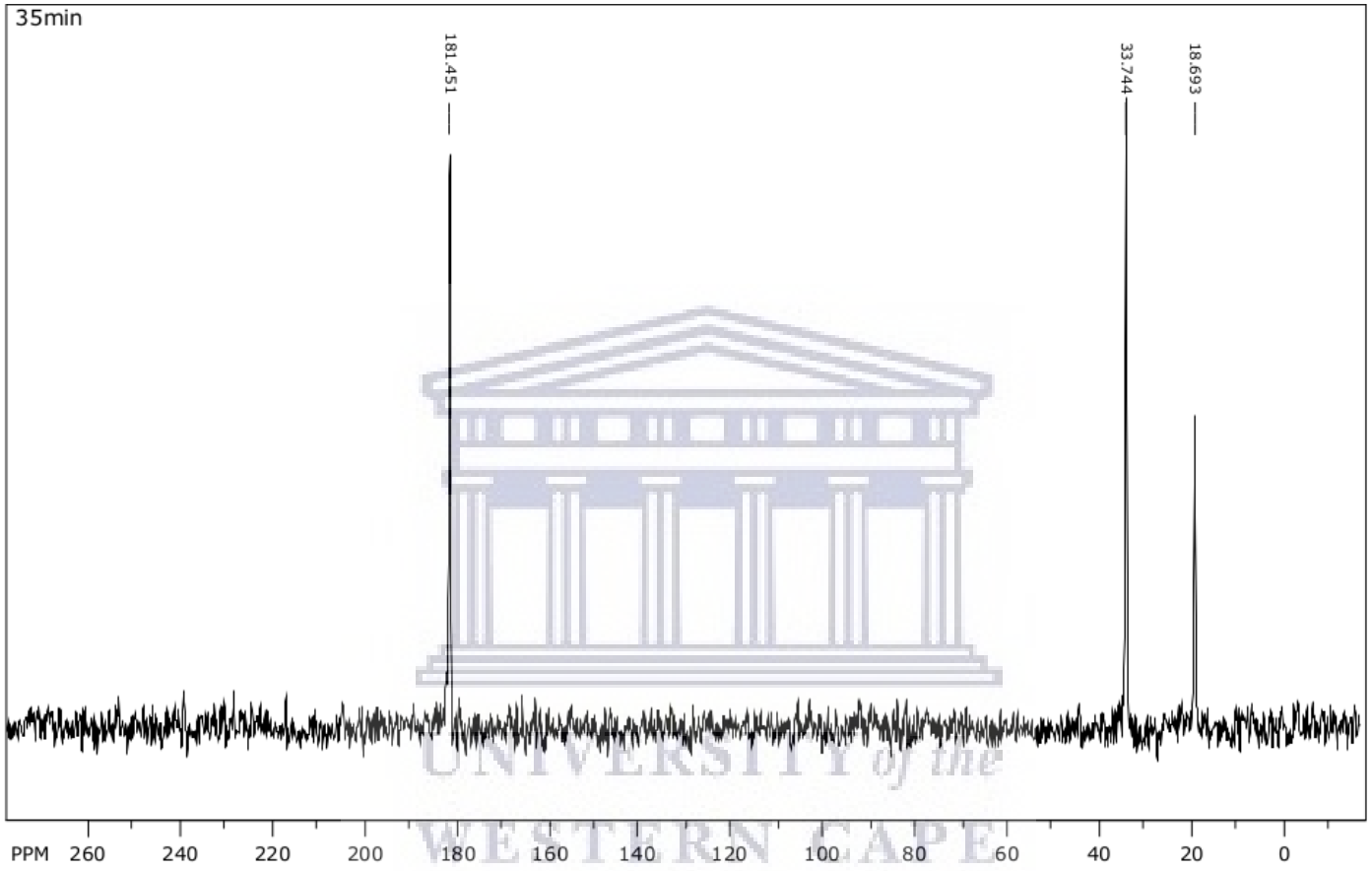

Supporting figure 8: C13 SSNMR spectrum of glutaric acid

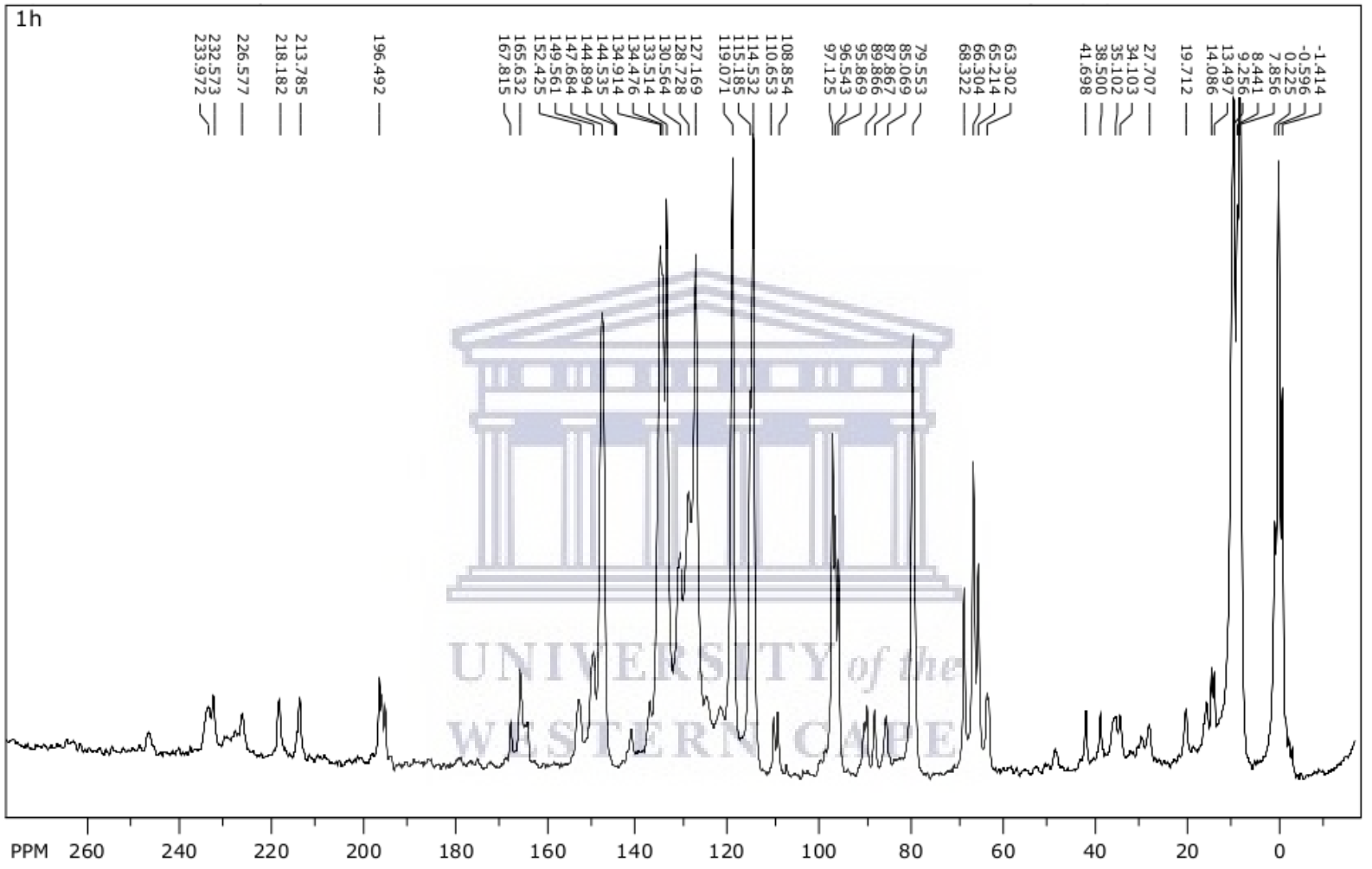

Supporting figure 9: C13 SSNMR spectrum of EFZA from solution crystallisation

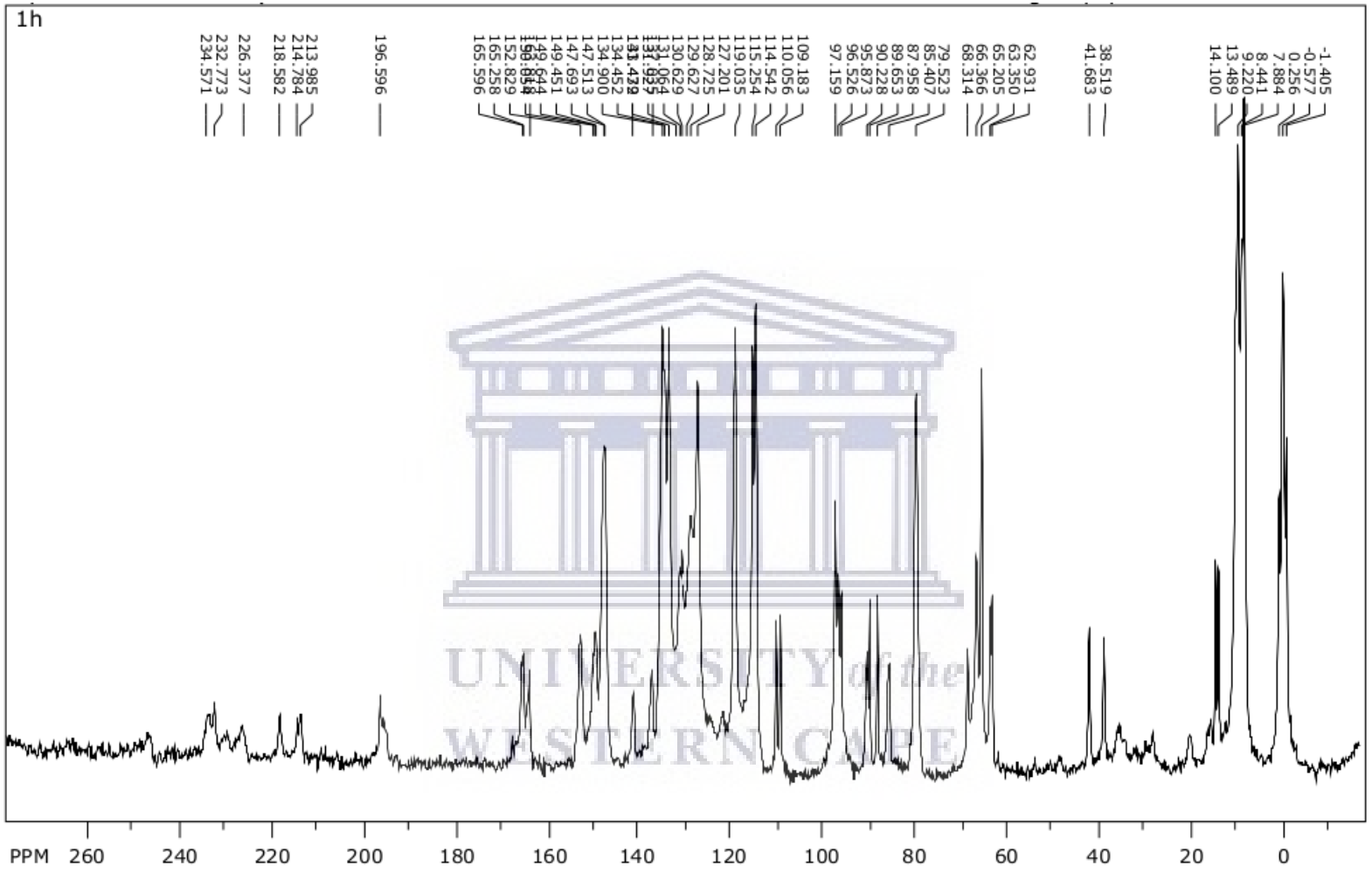

Supporting figure 10: C13 SSNMR spectrum of EFZA from dry grinding preparation

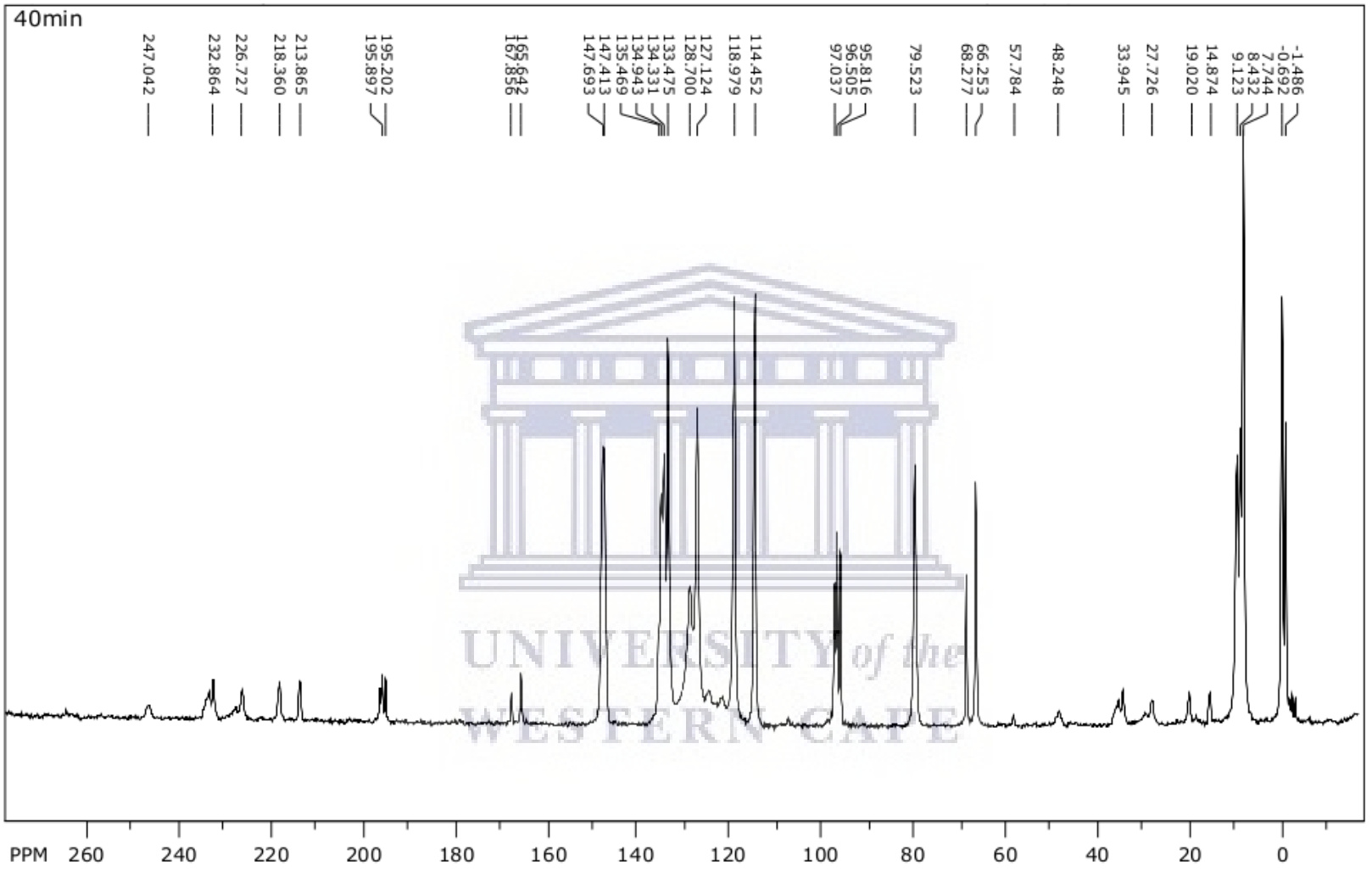

Supporting figure 11: C13 SSNMR spectrum of efavirenz

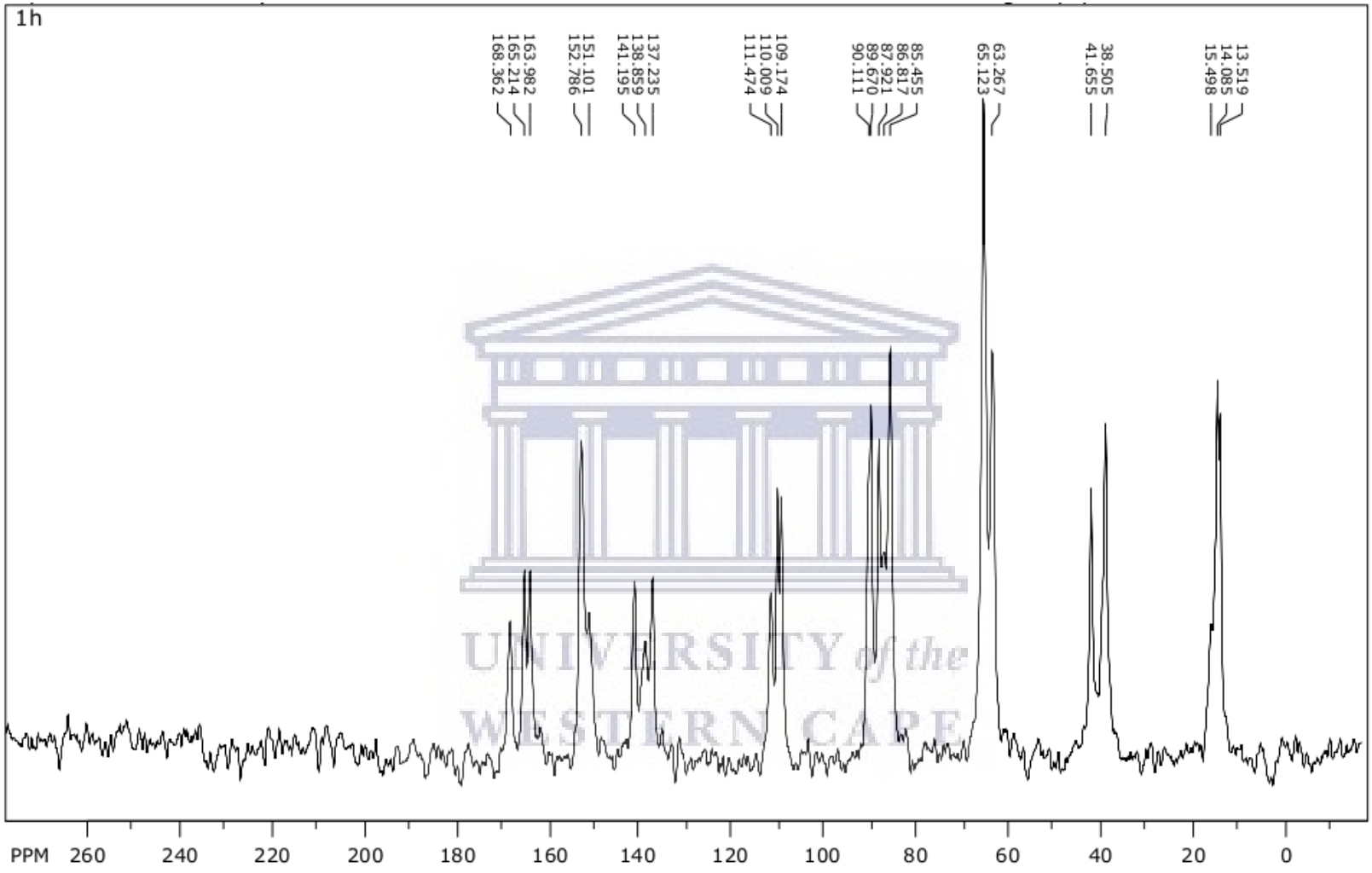

Supporting figure 12: C13 SSNMR spectrum of zidovudine (AZT)

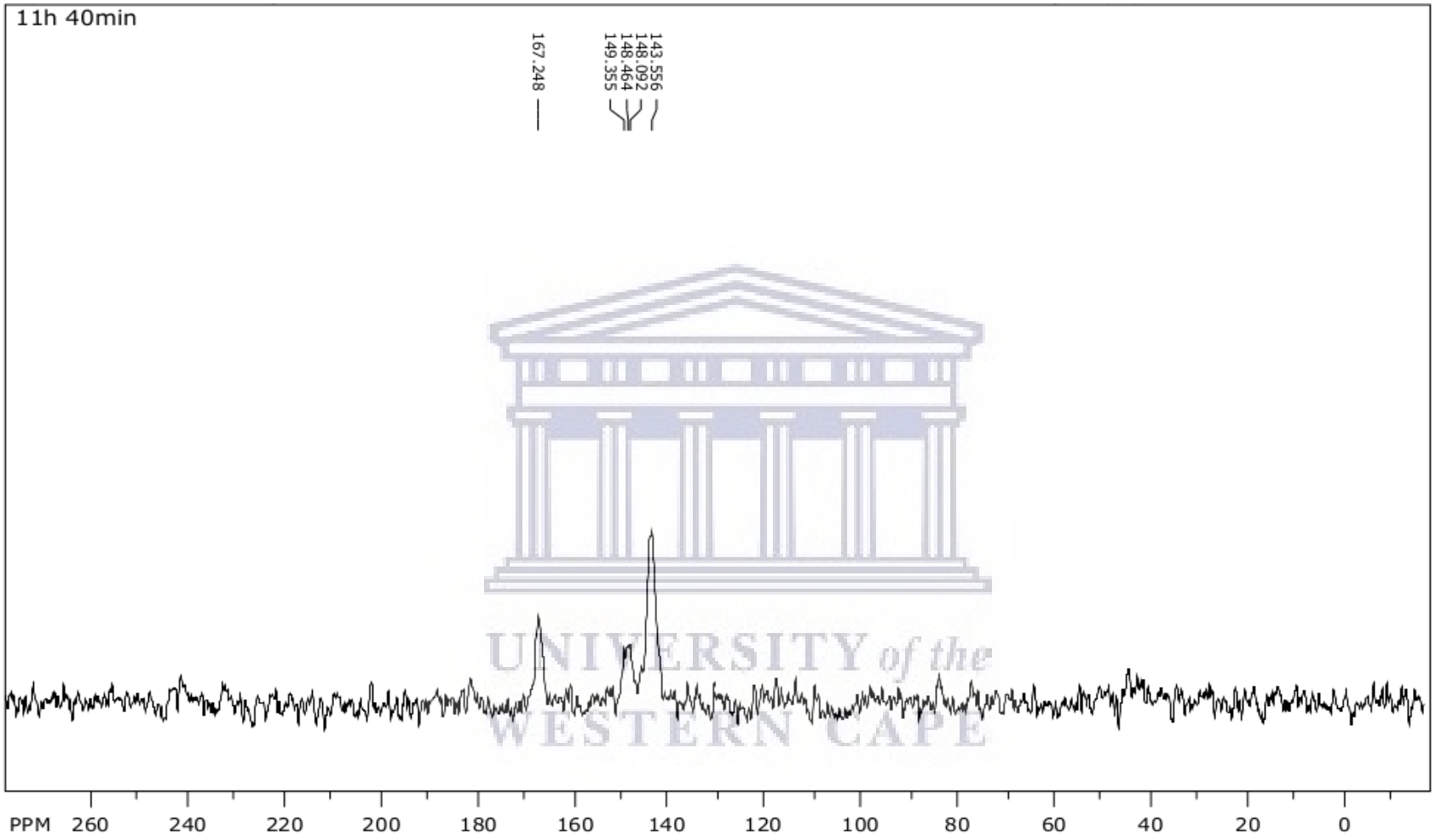

Supporting figure 13: C13 SSNMR spectrum of Pyrazinamide (PZA)

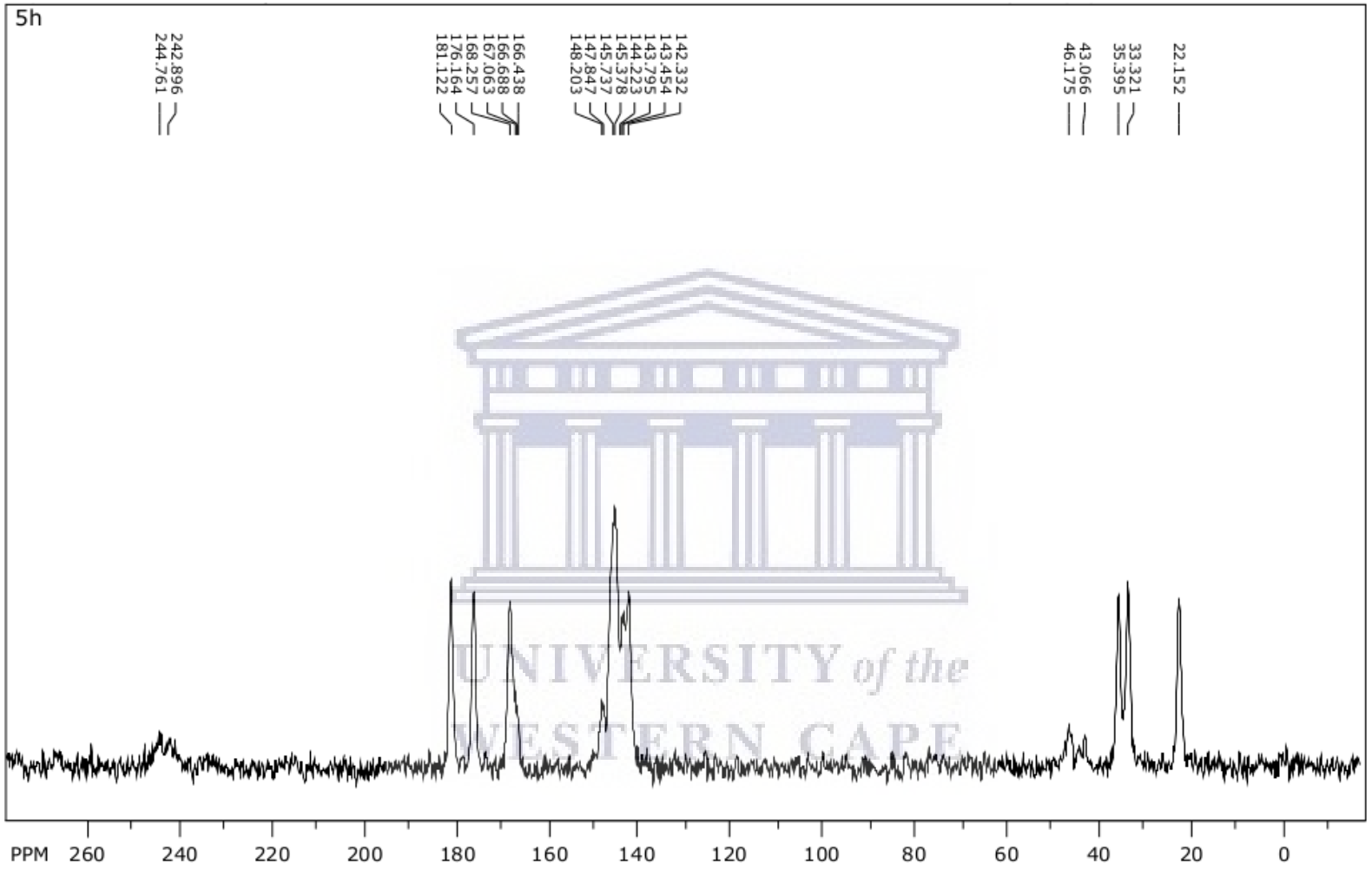

Supporting figure 14:C13 SSNMR spectrum of PGA (2:1) co-crystal

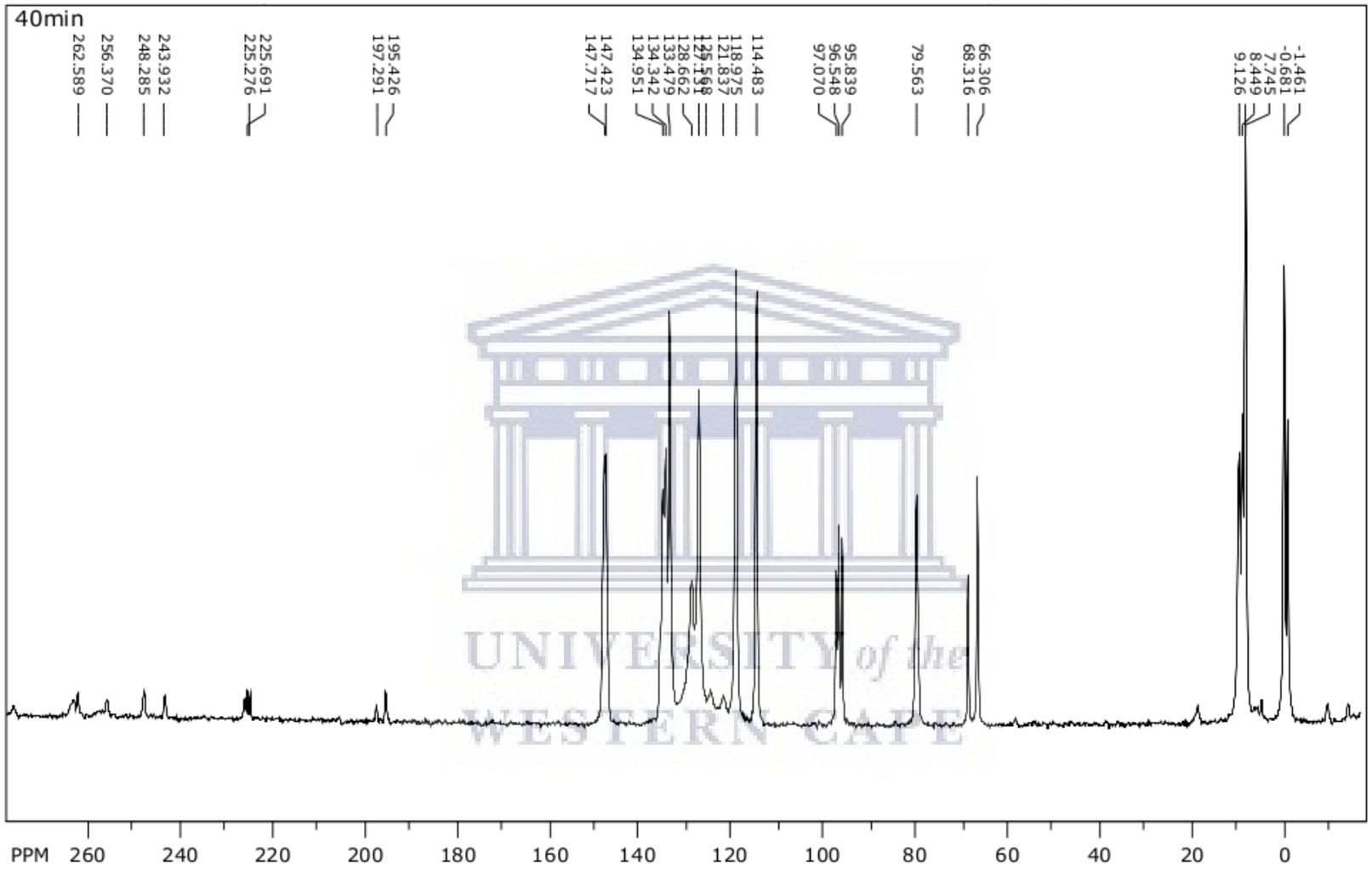

Supporting figure 15: C13 SSNMR spectrum of nevirapine-efavirenz co-crystal (NEF)

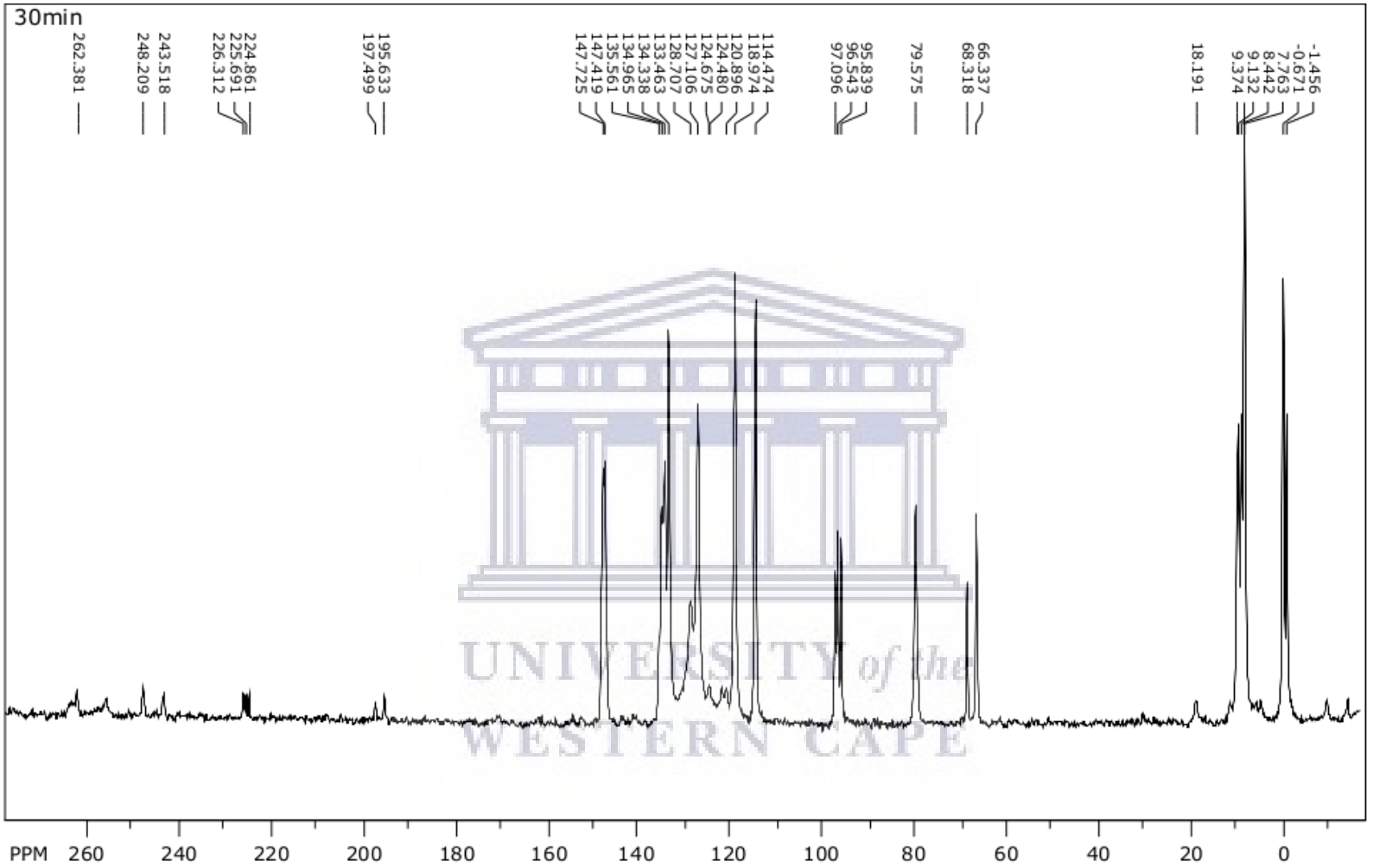

Supporting figure 16: C13 SSNMR spectrum of nevirapine-efavirenz co-crystal (NEF)

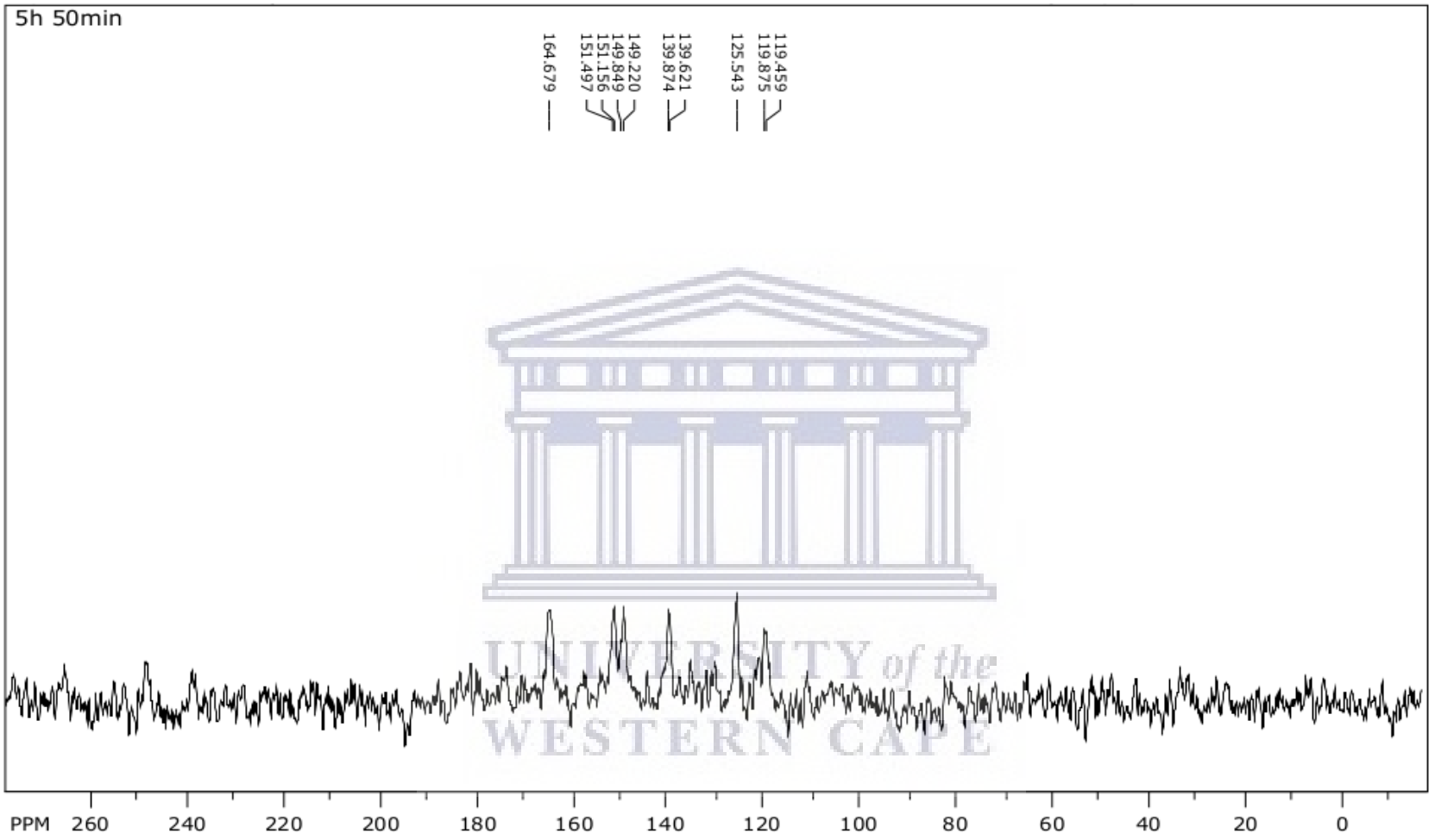

Supporting figure 17: C13 SSNMR spectrum of isoniazid (INH)

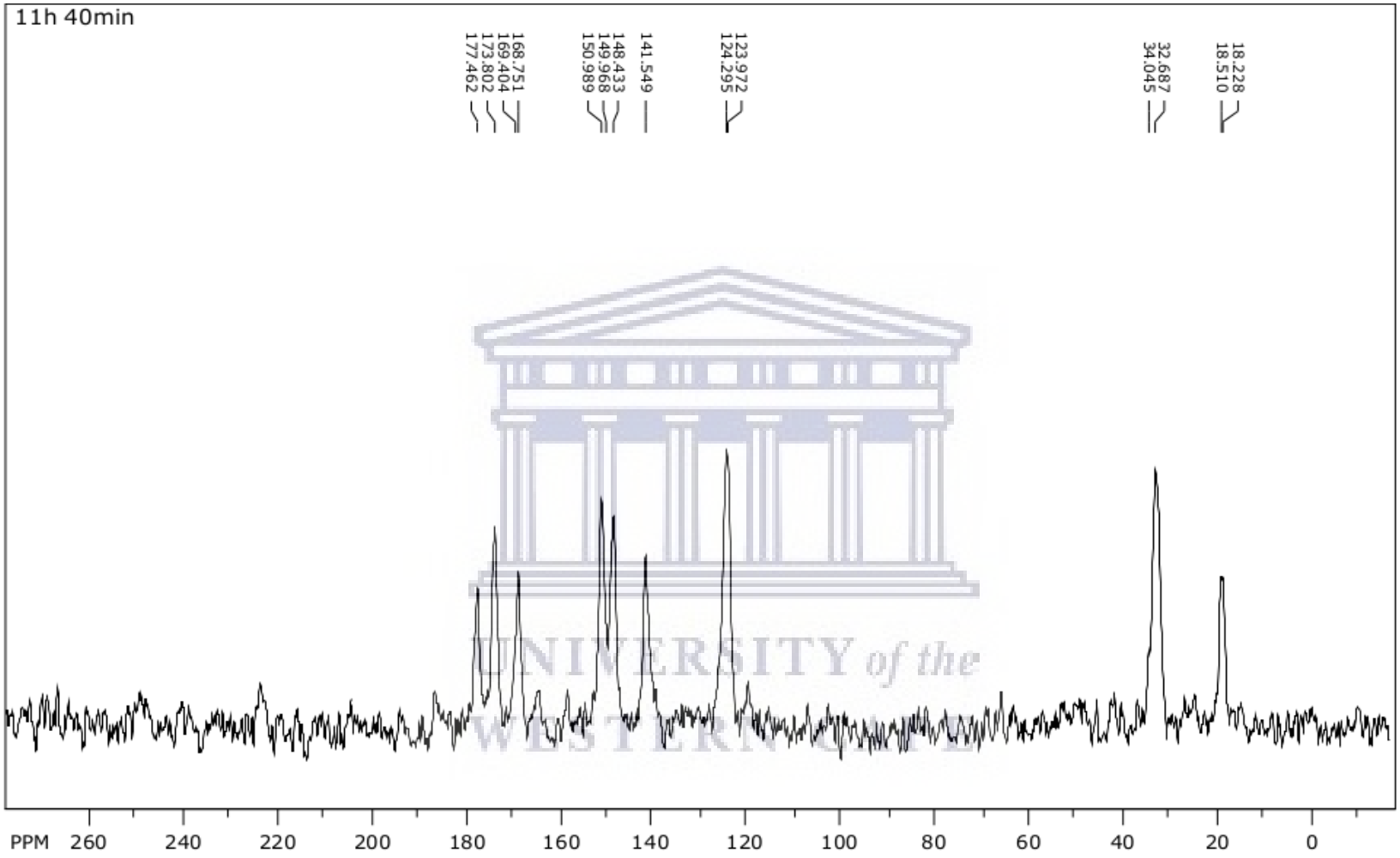

Supporting figure 18: C13 SSNMR spectrum of isoniazid-glutaric acid co-crystal (INHGA 2:1)